UNIVERSITÀ DEGLI STUDI DI PADOVA

DIPARTIMENTO DI FISICA E ASTRONOMIA "G. GALILEI"

CORSO DI DOTTORATO DI RICERCA IN ASTRONOMIA

CICLO XXXIV

STUDY OF VOLATILES ON PLANETARY SURFACES

Tesi redatta con il contributo finanziario di:

ISTITUTO NAZIONALE DI ASTROFISICA

OSSERVATORIO ASTRONOMICO DI PADOVA

Ph.D. School Coordinator: Ch.mo Prof. GIOVANNI CARRARO
Supervisor: GABRIELE CREMONESE
Co-Supervisor: Dr. MAURIZIO PAJOLA

Ph.D. Candidate: GIOVANNI MUNARETTO

External referees:
Dr. MATHIEU VINCEDON
Dr. ERNST HAUBER

Abstract

Planets Mars and Mercury represent two keystones for the current and future exploration of the Solar System. While the Red planet is an extremely interesting body for both its astrobiological and future human exploration potential, the exploration of Mercury is a promising path for answering many unresolved science questions about the formation and evolution of rocky planets and the occurrence of puzzling geological surface features. To investigate these topics, at the time of writing of this thesis, five new space missions begun their scientific activity at Mars, both from orbit and in-situ, and a new mission has been launched to Mercury, the third-one since the NASA's *Mariner10* probe in the 70s and the NASA's MESSENGER mission in 2011.

The scientific work presented in this thesis has been carried out in the framework of two of the above missions, the ExoMars/Trace Gas Orbiter (TGO) spacecraft currently orbiting Mars and the BepiColombo probe, currently *en-route* to Mercury, both supported by the European Space Agency (ESA).
In particular, we investigate currently not well understood landforms on Mars and Mercury, possibly related to the release of volatiles materials from the surface, with the aim of getting insights on their nature and characterise the formation mechanism. The rationale behind this choice was driven by the opportunity of analysing new and unique datasets from ExoMars/TGO and BepiColombo. In particular, the former started its scientific phase at the beginning of this Ph.D. project, allowing to investigate the surface of Mars with a novel perspective, while the launch of the latter prompted us to start identifying and investigating key science topics that will be specifically targeted once the Mercury orbit will be reached.
This body of work encompasses two planetary bodies each having his own, dataset and analytical techniques, and it is therefore presented in two parts: the first one concerning Mars, and the second one about Mercury.

On Mars, we specifically investigate the nature and formation mechanisms of martian Recurring Slope Lineae (RSL). Since 2010, RSL represented one of the major science questions concerning present-day Mars surface processes. Many studies brought up evidence that they could be related to the release of liquid water at the surface of Mars, while other reported that RSL could be best interpreted as dry processes. Their formation mechanism has been more tightly constrained only very recently. This was possible also thanks to the first observations of RSL performed by the Colour and Surface Science Imaging System (CaSSIS) instrument on board the ESA's ExoMars/TGO mission, together with coordinated images from the High

Resolution Imaging Science Experiment (HiRISE) camera on board the Mars Reconnaissance Orbiter (MRO) mission. Such observations and their analysis represent the core of the research work here presented on Mars. In addition, we could constrain the RSL nature and formation mechanism thanks to a novel methodology for the analysis of colour images of the surface of Mars, which development, validation and scientific application are presented in this thesis.

The second part of this thesis focuses on planet Mercury, where we investigate the nature and formation mechanism of hollows, i.e. puzzling bright, shallow, irregular depressions identified by the NASA's MESSENGER mission on the hermean surface. A well-established framework explaining the nature and formation mechanism of these features is still lacking. Therefore, hollows represent one of the major science topics about Mercury and its modern geological history. The nature of hollows will be one of the major science topics that the ESA/BepiColombo mission will investigate through the SIMBIO-SYS suite of instruments. By combining a high-resolution camera, spectrometer and stereo-camera, this instrument will allow to investigate the geomorphological, spectrophotometrical and 3D properties of hollows at high resolution, providing unprecedented datasets to analyse and interpret. In preparation for these unique datasets, we present a spectrophotometric characterisation of selected hollows sites based on data from the MESSENGER mission and we discuss its implication on their nature and formation mechanisms.

The structure of this thesis is organized as follows: in Chapter (1) we start with a general overview about planet Mars, its past and present aqueous environment, and we introduce RSL. In Chapter (2) we describe HiRISE and CaSSIS, the main instruments that have been used in our analysis, with a particular emphasis on the latter one. In Chapter (3) we present the analysis of the first CaSSIS observations of RSL at Hale crater, Mars. In Chapter (4) we present the spectrophotometric analysis of the RSLs at Horowitz crater, Mars. In Chapter (5) we present the development, validation and scientific applications of a novel methodology for the analysis of multiband images of Mars. In Chapter (6) we summarize all the research performed on Mars and discuss its future outlooks and perspectives. In Chapter (7) we move to Mercury, and we provide a general description of the planet, its geological history, its exploration and the landforms that were discovered on its surface. Particular detail is given to the description of hollows. The spectrophotometric analysis of two selected sites, the core of the part of the thesis concerning Mercury, and its implications for their origin and formation mechanisms are presented in Chapter (8). In Chapter (9) we describe the BepiColombo mission and the outstanding scientific questions that it aims to answer, with a particular focus on the SIMBIO-SYS suite of instruments. In addition, we specifically address the future potential of our analysis combined with the unique datasets from SIMBIO-SYS. Eventually, a general summary of the major key-points of both parts is provided in Chapter (10).

Contents

Chapter 1

Planet Mars

This chapter provides a very brief and general introduction about planet Mars and its past and present aqueous history, focusing on the problem of the current stability of liquid water on the martian surface. Aiming to provide just the basic knowledge and context of the topics treated in the next Chapters we just report here the most important facts, reminding the interested reader to more detailed references and sources if necessary.

Mars is the fourth planet from the Sun in the Solar System with and with a mass of ≈ 0.1 $M_\oplus$ (Earth Masses, 1 $M_\oplus = 5.97 \cdot 10^{27}$ g) and a radius of ≈ 0.53 $R_\oplus$ (Earth Radius, 1 $R_\oplus = 6.3781 \cdot 10^6$ m) it is the second smallest planet of the Solar System, after Mercury. Its gravity acceleration is 3.7 m/s^2, about the 38% of that of the Earth. Mars' rotation period is slightly longer than the Earth's one, resulting in a slightly longer solar day (or *sol*) of 24 hours, 39 minutes and 35.244 seconds. Its orbit has a semi-major axis of approximately 1.52 AU and an eccentricity of 0.09, resulting in a Martian sidereal year of about 686.98 Earth solar days, or 668.5991 sols. Mars orbits approximately 1.52 times as far from the Sun as Earth, hence it receives approximately the 43% of sunlight compared to Earth. Since it has an axial tilt of 25.19°, Mars experiences seasons, which are affected by its relatively large eccentricity.Seasons are indicated with the *Solar Longitude* angle, L_s, which is 0° at the northern vernal equinox, 90° at northern summer solstice, 180° at the northern autumn equinox, and 270° at the northern winter solstice (Clancy et al., 2000).

1.1 Internal structure and topography

Mars is differentiated into a inner, dense metallic core, with an estimated radius of approximately 1794 km and composed primarily of iron and nickel (Rivoldini et al., 2011), and an outer silicate mantle. Its 50 km (Wieczorek and Zuber, 2004) crust is mainly composed of basaltic material, i.e. silicon, oxygen and metals such as iron, magnesium, aluminum, calcium and potassium. The surface of Mars is characterized by relatively large variation in surface elevation, i.e. 29429 m (Carr, 2007), as we can see in Fig. (1.1). This is because the lowest point is located on the floor of the *Hellas* basin, at −8200 m and the highest one is the *Olympus Mons* summit at 21229 m above the reference elevation (i.e, the locus of points at which

atmospheric pressure is 6.1 mbar (Carr, 2007)). The most important topographic feature is the *global dichotomy*: the northern hemisphere is dominated by lowlands while the southern hemisphere is characterized by highlands. The relative elevation between the two hemispheres ranges from 3 to 6 km. This dichotomy is also expressed in crater densities, with the southern highlands being heavily cratered and the northern lowlands showing smoother terrains with few large craters and evident signs of more recent resurfacing. In addition, the *global dichotomy* also appears when considering crustal thickness, which is maximum the southern highlands (58 km) and minimum in the northern lowlands (32 km, Neumann et al. (2004)). Another important topographic features is the *Tharsis* bulge, a 10 km high, 5000 km diameter volcanic plateau which covers up to the 25% of the planet' surface. It hosts the largest known volcanoes on the Solar System, namely the *Asia Mons*, *Pavonis Mons* and *Ascreaeus Mons*, collectively called *Tharsis Montes*. At the western edge of the plateau, it is located the tallest volcano on the planet, the *Oympus Mons*. A much smaller bulge, the *Elysium* volcanic complex, is located West of the *Tharsis* region. Important negative topographic features are the *Hellas* and *Argyre* basins, two 9 km and $1-2$ km depressions, respectively, in the southern mid latitudes. All these features are indicated in Fig. (1.1).

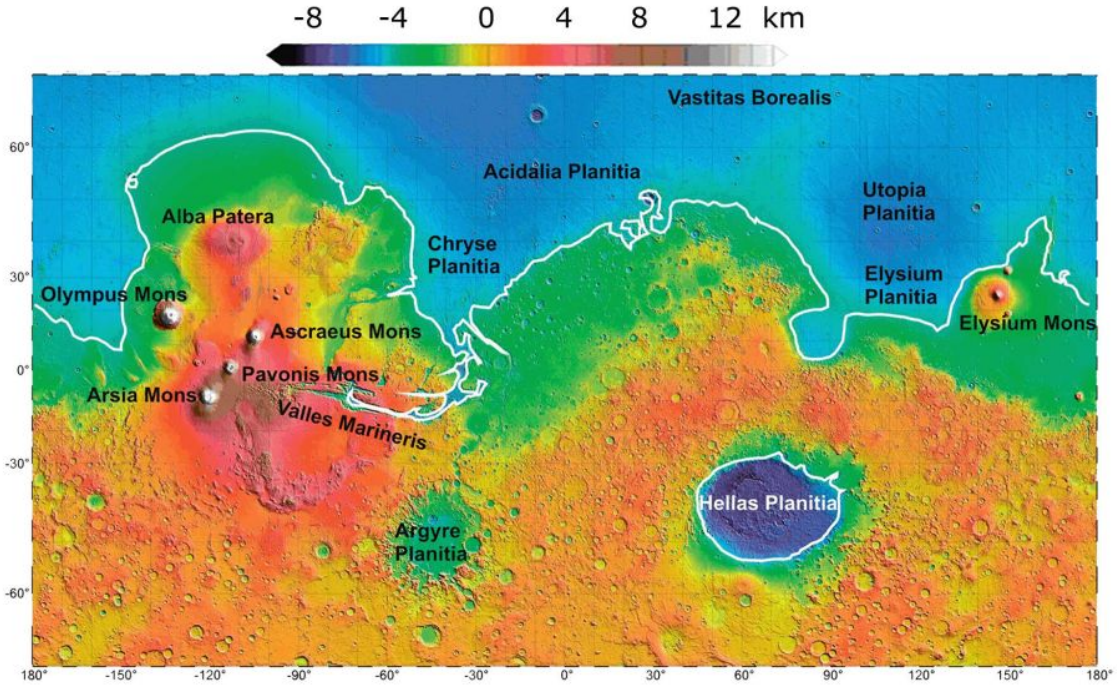

Figure 1.1: The global dichotomy is evident in this colourised elevation map: the northern hemisphere is dominated by smooth lowlands (blue) while the southern hemisphere is dominated by heavily cratered highlands (orange). The white line represents the hypothetical *sea level* isoheight.

1.2 Surface composition and mineralogy

As it can be appreciated from ground and space based observation at visible wavelengths, the surface of Mars is characterized by a distinctive reddish colour. This

is due to a fine layer of iron oxide dust deposited globally on the surface (Christensen et al., 2003). In particular, bright-red areas, like the *Arabia Terra*, *Tharsis* and *Hellas planitia* regions, are characterized by a thick dust cover. On the contrary in dark areas, like the southern mid latitudes, the northern *Acidalia Planitia* and the *Syrtis Major Planum* the amount of dust is relatively small and the darker colour is determined by the composition and mineralogy of the surface. Most of the surface is composed of igneous rocks formed by crystallization of different types of lavas: the southern highlands have a basaltic composition with high percentages of olivines, plagioclase feldspar and clinopyroxenes. The northern lowlands show instead a lower percentage of feldspars and clinopyroxenes and high percentages of high-silica phases (Bandfield et al., 2000; Poulet et al., 2009; Rogers and Christensen, 2007). Alhought the composition of the Martian surface is mostly basaltic, there are locations where its alteration by a variety of phenomena (meteorite impacts, water, erosion, weathering) resulted in different compositions. High-Mg olivines have been found in correspondence of large (>1000 km diameter) impacts, suggesting that they are either material excavated by the impact event and coming from the upper mantle (Mustard et al., 2009, 2007) or high-temperature lava emplaced and crystallized after the impact (Hamilton and Christensen, 2005; Tornabene et al., 2008). Clay minerals, i.e. hydrated silicates resulting from aqueous alteration, have been detected in correspondence of exposed Noachian crust (Bibring et al., 2005; Carter et al., 2013; Poulet et al., 2005) and in fluviodeltaic deposits inside paleolakes and craters (Dehouck et al., 2010; Ehlmann et al., 2008a; Grant et al., 2008; Milliken et al., 2010; Murchie et al., 2009) in association with salts such as sulfates (Wray et al., 2010) and chlorides (Osterloo et al., 2010, 2008). Carbonates have also been identified in some impact craters (Ehlmann et al., 2008b; Niles et al., 2013) and within the martian dust (Bandfield et al., 2003).

Visible images of Mars also highlight the presence of bright polar features. These are $1 - 3$ km-thick water ice caps, covered by a variable layer of CO_2 ice. Their estimated volume is of approximately one million of km^3 each.

1.3 Atmosphere

Mars has a very thin and rarefied atmosphere primarily composed of CO_2 (95%) and small quantities of Nitrogen (2.8%) and Argon (2%) (Franz et al., 2017). Water vapour, oxygen, carbon monoxide, hydrogen and noble gases are also present, even though in traces. As a consequence, surface pressures on Mars are on average of 6 mbar (i.e., less than 1% of the Earth pressure), depending also on season and elevation. The thermal interaction between the surface and the atmosphere is responsible for two main phenomena. On large spatial scales, the high thermal contrast between the surface and the atmosphere during summer on the southern hemisphere tends to lift dust and produce dust storms(Toigo et al., 2018). They may happen as regional events or grow to global scales encircling the whole planet for several weeks. During dust storms, typical values of the optical depth may rise over 9, obscuring the surface at visible wavelengths (Chen-Chen et al., 2021). One of the effects of dust storms is a net transfer of dust from the southern hemisphere to the low northern latitudes. On small scales, local turbulence is responsible of dust-devils, i.e. martian whirlpools, which lift and redistribute dust in the surroundings

leaving the so-called *dust-devil tracks* (Reiss et al., 2013).

1.4 Martian geological ages

The geological history of Mars is divided in four ages: the pre-Noachian, the Noachian, the Hesperian and the Amazonian ages.

The pre-Noachian age

The pre-Noachian age extends from 4.5 Gyr ago to approximately $4.1 - 3.8$ Gyr ago, i.e. to the formation of the Hellas basin. In this phase the differentiation of the planet into crust, mantle and core and the formation of the global dichothomy occurred. The Tharsis volcanic province began to accumulate and the large impact basins severely reworked the surface (Carr and Head, 2010).

1.4.1 The Noachian period

The Noachian period dates from 4.1 to 3.7 Gyr ago and refers to the age in which the Martian crust was experiencing a high rate of modification by several geologic processes (i.e. impacts, erosion) that rapidly declined at the end of the Noachian (Craddock and Howard, 2002; Golombek et al., 2006). In particular, the high rate of impact crater bombardment, occurring at an approximate frequency of one 100 km diameter impact every million years (Carr, 2007; Ivanov, 2001), had the effect of comminute the surface materials, allowing them to be moved and transported by water and winds, generate hydrothermal activity at the impact sites, and break the surface materials increasing their porosity and allowing groundwater to infiltrate. Another process that was eroding most of the Noachian terrain was water, which resulted in the incision of valley networks, deposition of sediments, formation of stable bodies of water called *paleolakes* and episodic flooding events. All these features left important geomorphological and mineralogical markers that are discussed in Section (1.5.1).

1.4.2 The Hesperian period

The Hesperian period extends from the end of the Noachian, 3.7 Gyr ago, to approximately 3 Gyr ago (Hartmann and Neukum, 2001). The most important process occurring during this age was a phase of widespread volcanism that formed extensive lava plains and a low number of shield-like central edifices known as *paterae*. This volcanic activity resulted in a resurfacing of $\approx 30\%$ of the planet' surface (Carr and Head, 2010). The valley formation rate was extremely low, resulting in only few incisions. In contrast, most of flooding events, leading to the formation of *outflow channels* (c.f. Section 1.5.1) formed in this age, including the Kasei, Tiu, Simud Ares Mangala and Maja systems. Surface conditions also changed such that the production of phyllosilicates (c.f. Section 1.5.1) declined in favour of sulfate-rich deposits. The latter may be formed either by the evaporation of water or by the weathering of basalts by acid fluids, such as acid fogs, fumarolic condensates or groundwater affect by magmatic volatiles (Madden et al., 2004). This picture again suggests the decline of a warm and wet atmospheric environment towards a more dry, cold

and acidic one. The most striking feature of the Hesperian age is the formation of Valles Mariners, the biggest Martian canyon system. The presence of large bodies of water, i.e. seas or oceans, during this age is also a highly debated topic. While it is supported by several, tentatively identified shorelines in the northern plains and in Hellas (Carr and Head, 2010), other evidence like the lack of minerals generated by the evaporation of such water (Bibring et al., 2006) and the absence of material that should have been deposited by it (Carr and Head, 2010) tend to disprove it, leaving this topic as an open question. Finally, the identification of the remnants of a Hesperian cold trap at the south circumpolar latitudes, called the *Dorsa Argentea Formation*, suggests that some of the water lost via outflow channels and/or evaporation was trapped into an Hesperian, possibly planet-wide, global cryosphere (Carr and Head, 2010).

1.4.3 The Amazonian period

The Amazonian is dated from 3 Gy ago to the present day. It is characterised by a minimal rate of surface geomorphological changes. Volcanic activity was confined to growth of shields and lava plains accumulations in the Tharsis and Elysium provinces. Without significant surface modifications by impacts or erosion, the action of ice is one of the main processes at play during the Amazonian. In particular ice-related processes such as, glaciations (Head and Marchant, 2003), the buildup of the polar caps, and the formation of ice-related glacial surface features such as *lobate debris aprons*, *lineated valley fills* and glaciers occurred during the Amazonian. More details are given in Section (1.5.2). Fluvial activity ended with the Hesperian period, but young, Amazonian-aged outflow channels have been discovered in Tharsis and in Elysium and very few valley networks have been identified in Echus Chasma (Mangold et al., 2004), on the Alba Patera volcano (Fassett and Head, 2008a) and in Lyot crater (Dickson et al., 2009). Aeolian activity has been pervasive during the whole Amazonian period and resulted in the redistribution of loose materials across the surface.

Despite its cold and arid environment, the present-day surface of Mars experience a variety of dynamic processes. Dark slope streaks (Morris, 1982) and dust devil tracks (Reiss et al., 2013) are related to the downslope movement and redistribution of dust on the surface, and are recognizable as flow-like and fuzzy/curvilinear dark streaks, respectively. A variety of processes is instead thought to be formed by the release of a volatile from the surface, either CO_2 or water ice, with a varying degree of confidence. A well established and documented process is the sublimation of CO_2 ice and water ice frost during early spring, which has been observed in a variety of location, especially on top of defrosting dunes. The rapid release of pressurized CO_2 and dust grains through slabs is responsible for the formation of polar *spiders* (Schwamb et al., 2018) and a variety of low albedo, fan-shaped or haloed surface features (Hansen et al., 2013). A slightly less understood process is the one responsible for the formation of the so-called *gullies*, i.e. mass wasting features that are formed by an alcove (i.e., an arched, hollowed depression formed in a cliff wall), a channel through which material is transported and a depositional apron (i.e., a fan shaped deposit) that contain the material removed from the alcove (Malin and Edgett, 2000). While it is well established that gullies are granular flows generated

by CO_2 frost (Diniega et al., 2013; Dundas et al., 2012), recent studies also suggest that they could be generated by melting H_2O ice (Rai Khuller and Russel Christensen, 2021), making the overall picture somewhat unclear. Eventually, the most puzzling Amazonian surfaces feature at the time of writing of this thesis are the so-called *Recurring Slope Lineae* (RSL, McEwen et al., 2011), i.e. dark narrow linear low albedo features that are seen lengthening down Martian steep slopes during local summer, fading during cold season and recurring annually at approximately the same locations. Many theories for RSL formation have been proposed, ranging from liquid flows on the surface on Mars to dry granular flows. A detailed, state of the art description of RSL is given in Section (1.6).

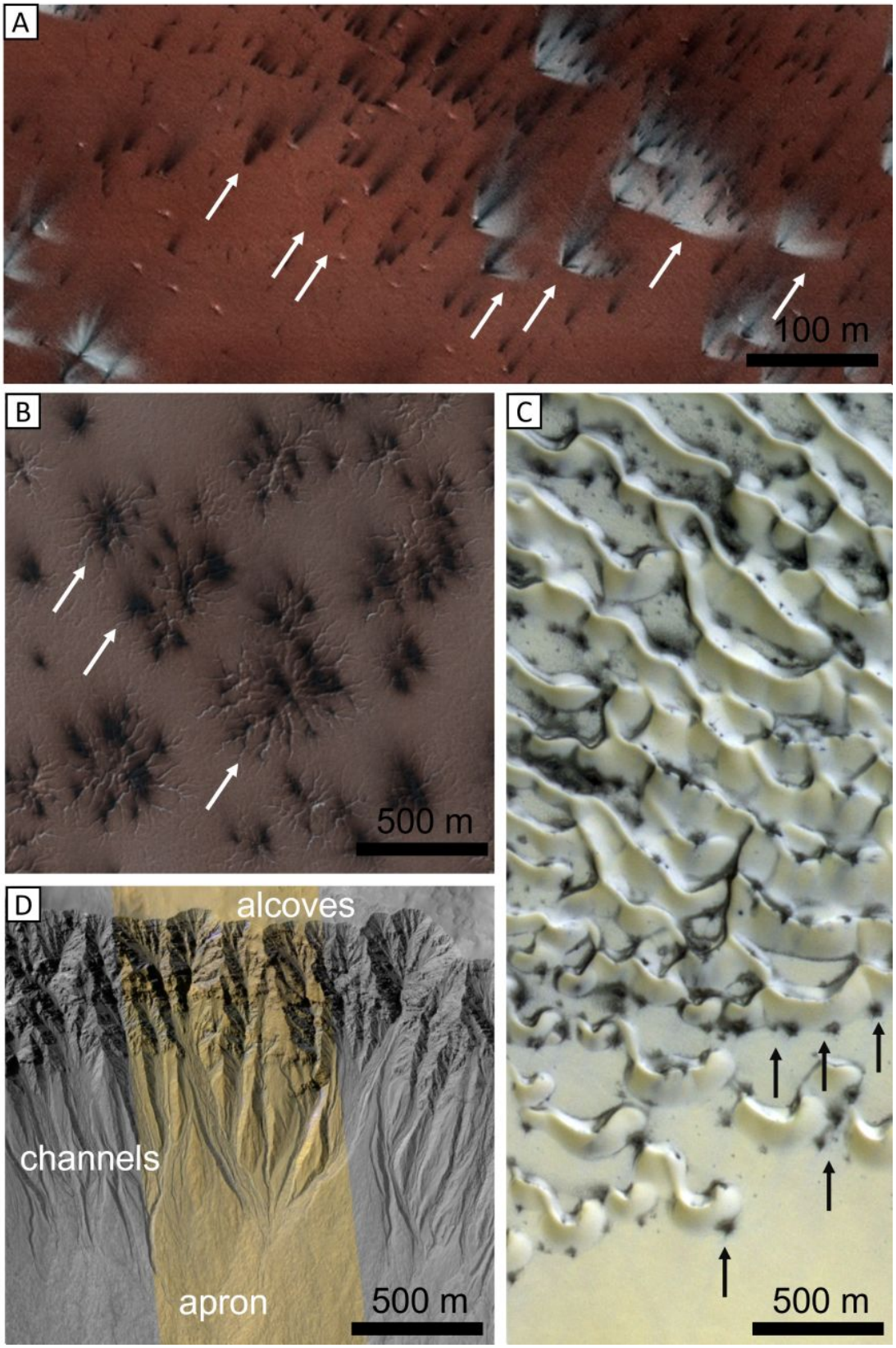

Figure 1.2: HiRISE colour images showing examples of polar fans (A, white arrows) and martian spiders (B, white arrows). C) CaSSIS colour image showing snow-covered dunes with dark spots due to the defrosting ice (black arrows). D) HiRISE image showing typical alcove-channel-apron gullies.

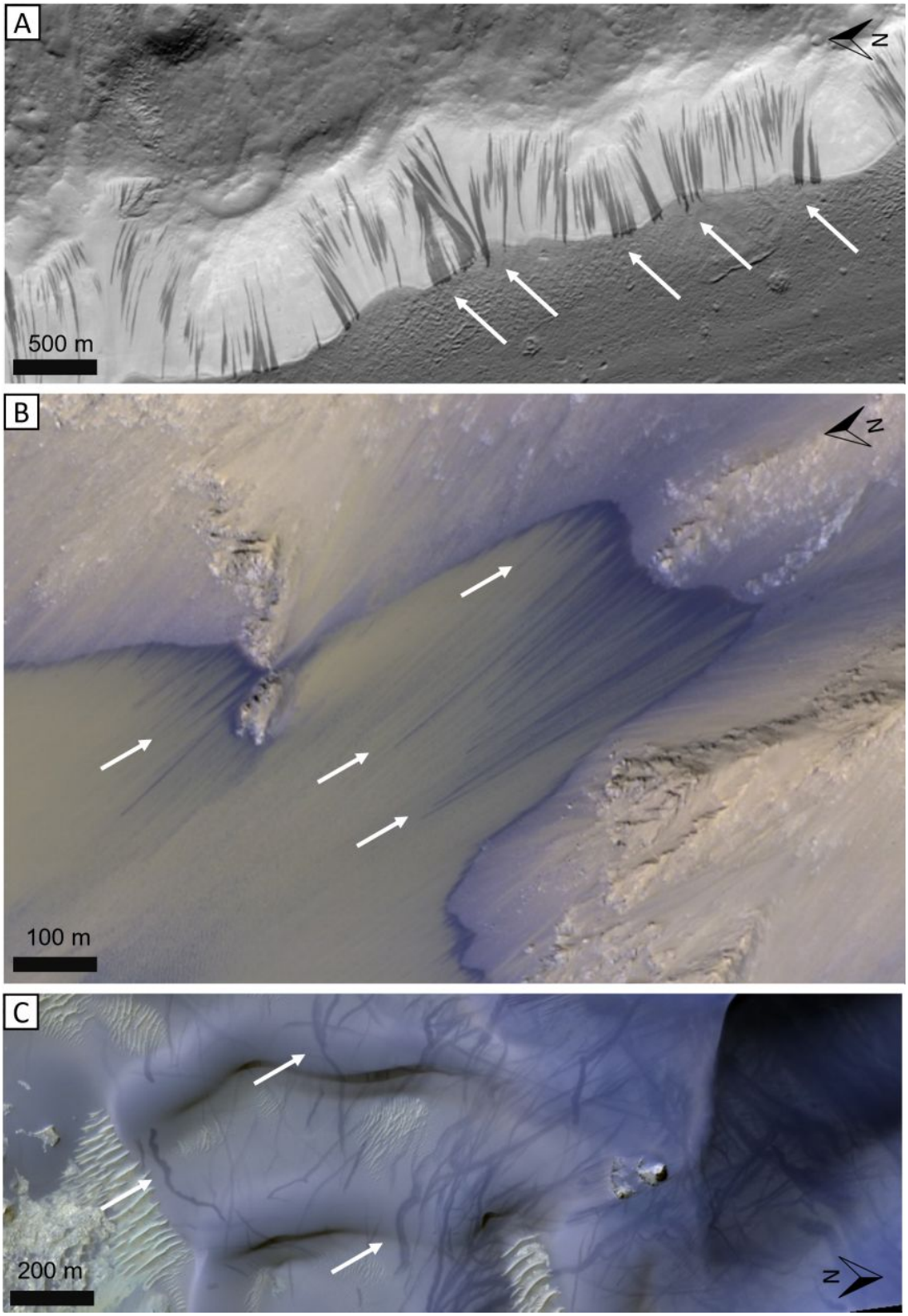

Figure 1.3: A) HiRISE image showing examples of dark slope streaks (white arrows). HiRISE colour images showing example of RSL (B, white arrows) and dust devil tracks (C, white arrows).

1.5 Past and present water on Mars

Given the relevance of water in explaining several present-day Mars surface features, including RSL, and its important implications for biologic processes and human exploration, we here provide an overview about the past and present water inventories on Mars, we discuss its stability, both in solid and liquid phases and we review the main processes that may trigger liquid flows on the surface of Mars.

1.5.1 Evidences of past liquid water

The surface of Mars records multiple evidences that the planet was much wetter and warmer in its ancient past (Pollack et al., 1987). Evidences of ancient stable bodies of standing water and of surface runoff come from observations of geomorphic features attributed to the action of water in the early Martian history, like paleolakes, river valleys and deltas, from the detection of aqueous alteration of minerals and from the analysis of Martian meteorites.

Geomorphic evidences of water

Analysis of images of the Martian surface showed the extensive presence of surface features that are attributed to the erosion of the crust by water.
Valley networks, like the one depicted in Fig. (1.4A,B,C), were formed by the eroding action of liquid water, similarly to terrestrial valleys. The presence of valley networks with both a high and low density of tributaries suggest that both groundwater sapping (Carr and Clow, 1981; Gulick, 1998; Pieri, 1980) and precipitation and surface runoff have occurred. In particular, the latter landforms are more common on older terrains and progressively transition into the former. This suggest that during this age there was an initial wet climate with at least episodic precipitation that transitioned at the end of the Noachian to a more arid and locally wet environment (Carr, 2007).

Several depressions with *inlet* and outlet *valleys* have been also observed (1.4D), indicating that stable bodies of water once occupied topographic lows (Fassett and Head, 2008b). These depression also show deltas and fans observed at locations where water entered into the paleolake, as well as sediments transported by water. Remarkably, these sediments have a highly rhythmic layering, suggesting multiple episodes of deposition driven by orbital forcing (Malin and Edgett, 2000).These geomorphic features are characteristic of terrestrial lakes and have been interpreted as the presence of *paleolakes* in the Martian past history.

Outflow channels appear as huge, long, isolated channels lacking a dendritic network (Fig. 1.4E) and are characterized by the presence of teardrop-shaped islands, signs of the eroding action of flowing liquid water. Most of outflow channels are thought to be formed by the rapid release of large volumes of water from upstream reservoirs (Carr, 2007; Pajola et al., 2016a).

Inverted reliefs have been detected in correspondence of paleo-river beds (1.4G). These positive-relief features were built by the accumulation of sediments on the

river bed, which later underwent cementation resulting in a competent (i.e., resistant to erosion) material and were buried by a capping unit, like lava flows. Later on, erosion by aeolian agents removed the less resistant capping unit until the inner, cemented layer of sediments is exposed. The latter, more resistant to erosion, remains relatively more preserved and therefore shows the "*negative*" of the (paleo) river bed.

Evidences from alterations of surface minerals

The Martian surface is mostly composed of igneous minerals, which react with water to form hydrated minerals, in particular phyllosilicates. The detection of aluminium phyllosilicates, called clays, is therefore an evidence of the presence and activity of past liquid water on the Martian surface (Bibring et al., 2006; Zolotov and Mironenko, 2007). Moreover, the detection of clays with salts (sulfates, chlorides, carbonates) in sedimentary environments is an evidence that these minerals were generated by the deposition of sediments in aqueous environments (Mastropietro et al., 2020; Pajola et al., 2016b). Another kind of alteration is due to the upward migration of subsurface hydrothermal fluids, heated by the residual heat produced by large impacts (Abramov and Kring, 2005). In particular, when water migrates through the basaltic crust, its interaction results in the formation of *serpentinite*, which has been detected on Mars (Ehlmann et al., 2010).

Evidence from meteorites

Evidence of the presence of water in the past Martian history comes also from the chemical analysis of Martian meteorites, which shows the alteration of olivine by water (Treiman,2005).

1.5.2 Contemporary water inventory

The low average Martian surface temperatures and pressures are currently not favorable to the formation of stable liquid water, which is hypothesized to form only in transient anomalous conditions. Stable liquid water has only been detected below the surface using the Mars Advanced Radar for Subsurface and Ionosphere sounding (MARSIS, Orosei et al., 2018). It was first identified in a 1.5 km deep, 20 km wide subglacial lake located in the southern pole region of *Planum Australe* (193°E, 81°S) (Orosei et al., 2018), but some studies argued that other mechanisms not involving water could explain the bright reflectivity of that area (Bierson et al., 2021; Smith et al., 2021; Sori and Bramson, 2019). Further detections by Lauro et al. (2021) strengthen the claim of a stable liquid water body under the south pole of Mars.

On the contrary, water ice is commonly available on present-day Mars. The biggest reservoir is located in the polar caps, but detection of hydrogen with the Mars Odyssey Gamma Ray Spectrometer and Neutron Spectrometer (Boynton et al., 2002, 2007; Wilson et al., 2018) revealed that water ice is also abundant and widespread below the uppermost meters of Martian soil. In particular, ice is very abundant polewards of ±50°, but it also is present in lower concentrations in mid-latitude and equatorial locations, notably the slopes of *Tharsis Montes*, *Elysium Mons* and at the *Medusae Fossae* formation (Feldman et al., 2004; Wilson et al., 2018). Several

geomorpholgical evidences of ice-rich materials have been documented so far, like viscous flow features, lobate debris aprons, concentric crater fill, lineated valley fill, scalloped depressions, expanded craters and polygonal ground (Dickson et al., 2012, 2010; Head et al., 2005; Milliken et al., 2003; Viola and McEwen, 2018; Zanetti et al., 2010). Some of these features were also confirmed to be ice-rich from subsurface radar measurements (Bramson et al., 2015; Holt et al., 2008; Plaut et al., 2009). In addition, a possibly ice-rich, 1-10 m thick mantling unit convering at least 23% of Mars has been observed over the mid-latidues (Kreslavsky and Head, 2002; Mustard et al., 2001). Eventually, patches of "pasted-on" smooth mantles containing possibly 46-95% ice have been observed on pole-facing slopes in the midlatitudes (Conway and Balme, 2014; Gulick et al., 2019). Several > 100 m thick exposed and nearly pure water ice sheets have been directly imaged poleward of $\pm 50^{\circ}$ by HiRISE (Dundas et al., 2018).

1.5.3 Stability of water on Mars

As discussed in the previous section the presence of ice on the surface of Mars is widespread, and could possibly represent a high potential resource for shallow liquid water production, possibly explaining the origin and formation mechanism of some surface features mentioned above like it has been proposed for RSL. To better understand the theoretical framework and the models employed in this context, in this section we briefly describe the problem of liquid water stability on present-day Mars and the possible mechanism that may generate surface or subsurface liquid flows.

Thermodynamics of ice and brine melting on Mars

From a thermodynamical perspective, the phase (i.e. liquid, gas, solid) of water is determined by its temperature and partial pressure. In particular, if the temperature is above the water freezing point (i.e., 273K) and the partial pressure of water is above the 6.1 mbar, then liquid water is stable against freezing and/or boiling. By considering these constraints, 29% of the surface of Mars could host liquid water, provided that there is available ice to melt (Haberle et al., 2001). However, even thought the total pressure of the Martian atmosphere can exceed the saturation partial pressure of water (6.1 mbar), the partial pressure of water vapour is approximately 4000 times lower, i.e. 0.0015 mbar (Schorghofer, 2020). This means that even when water ice is at temperatures and pressures near the melting point, it will quickly diffuse into the very thin atmosphere rather than melt and form a liquid solution. In addition, when temperatures and pressure are approaching the melting point, the heat loss through evaporation exceeds the heat coming from the solar radiation, hence preventing temperature to increase further (Ingersoll, 1970). In summary, evaporation prevent pure ice to melt and form liquid solutions on the surface of Mars, even at locations where temperature and pressure would be above those at the triple point. In contrast, pure liquid water is predicted to be stable against evaporation in the subsurface, even as shallow as 5 cm to the surface, where a regolith layer would prevent evaporation (Möhlmann, 2011, 2010) and in groundwater aquifers as shallow as 100 m (Goldspiel and Squyres, 2011). In particular conditions with favourable topography, such as with boulders, and where the formation of CO_2 frost occurs, however, the cooling by evaporation is minimized by a dust lag left by the complete sublimation of CO_2. Here temperatures can get close to the melting point, hence allowing the transient formation of particular liquid *saline* solutions Schorghofer (2020). These are called *brines*, i.e. are mixtures of ice and salts. Having lower freezing point temperatures and evaporation rates than liquid water (Altheide et al., 2009; Brass, 1980; Chevrier and Altheide, 2008), they have a more favourable thermodynamical behaviour with respect to melting, either at the surface or in the subsurface.

Deliquescence of salts

Brines are interesting liquid water sources candidates because, in addition to having a low freezing temperature, which for brines is called *eutectic temperature* (T_e), they can absorb moisture from air and generate liquid solutions (Gough et al.,

2016). This process is called *deliquescence*, and it occurs when the temperature is above the eutectic temperature and the air humidity is higher than a threshold called *deliquescence relative humidity* (DRH). For example, the temperature and relative humidity conditions that allow the formation of liquid $Ca(ClO_4)_2$ are shown in Fig. (1.7). Once a liquid phase is formed, it remains stable until the relative humidity falls below the *efflorescence relative humidity* (ERH) (Gough et al., 2016). Several laboratory studies have identified chlorides (Gough et al., 2016; Wang et al., 2019), perchlorates (Nuding et al., 2014) and chlorates (Toner and Catling, 2018) as potential candidate deliquescent salts. Numerical modeling by Gough et al. (2016) showed that atmospheric water vapor could sustain the deliquescence of hydrated chlorides ($CaCl_2$) brines at 3-cm depth at the Phoenix landing site. Indeed, these brines have require DRH from 12.9% at $T = 273$ K to $\sim 20.9\%$ at $T = 233$ K (Gough et al., 2016), while their eutectic temperature is $T = 223K$. The deliquescence of Ca-perchlorates is also interesting because of their lower DRH (from $10 \pm 4\%$ at 273 K to $55 \pm 4\%$ at 223 K (Nuding et al., 2014)) and eutectic temperature of $T = 200$ K. Recent modeling by Rivera-Valentin et al. (2020) predict that Ca and Mg perchlorates brines can form and persist from equatorial to high latitudes on the surface for a few (i.e. ≤ 2) percent of the year and up to six consecutive hours. Finally, chlorates may be even more interesting candidates as they have a lower DRH than perchlorates (Toner and Catling, 2018). Experimental evidence of liquid brines on Mars has been scarce so far, but Renno et al. (2009) showed that from a thermodynamical point of view they could form at the Phoenix landing site and they proposed that the droplet-shaped features observed on the lander struts were liquid brines. This picture is also supported by detection of perchlorate salts ($Mg(ClO_4)_2$ and $NaClO_4$) at the landing sites.

1.6 Martian Recurring Slope Lineae (RSL)

Recurring Slope Lineae (RSL) are narrow, low-albedo dark streaks that are seen to incrementally lengthen down Martian steep slopes during local late spring and summer and subsequently fade and often completely disappear during cold seasons. These are also found to recur at approximately the same locations every Martian Year, indicating a strong seasonal influence on their formation and evolution (Levy, 2012; McEwen et al., 2014; McEwen et al., 2011; Ojha et al., 2014; Stillman et al., 2014).

This global pattern however becomes more complicated at certain locations, that show concurrent RSL lengthening and fading (Stillman and Grimm, 2018; Vincendon et al., 2019)), or multiple pulses of activity within a single Martian Year (Stillman and Grimm, 2018). This seasonal dependence suggests that temperature is the main driver of RSL activity, triggering it at thresholds at which water (often salty) may be liquid, hence hinting at a water-related origin. Consequently, RSL were thought to have been formed by liquid water or brine flows (Chevrier and Rivera-Valentin, 2012; Huber et al., 2020; Levy, 2012; McEwen et al., 2011; Ojha et al., 2014, 2015; Stillman et al., 2017, 2016; Stillman et al., 2014) possibly fed by subsurface, briny aquifers (Abotalib and Heggy, 2019; Stillman and Grimm, 2018). Results from numerical modelling, however, suggests that the water volume requirements to explain RSL activity are larger than what could be reasonably available on present-day Mars

locations (Grimm et al., 2014); moreover, many RSL form in ridge crests or peaks, where the presence of an aquifer is unlikely (Chojnacki et al., 2016). Another study (Edwards and Piqueux, 2016) reports on the non-detection of thermal signatures of liquid water at some active RSL locations, including Garni crater, although Stillman et al. (2017) argue that this may either be due to non-coordination in time of these observations with RSL activity, or simply the small scale of the features themselves which prevents them from generating a detectable infrared signal.

Another water-dominated process that has been proposed to explain RSL formation is the deliquescence of salts, i.e. the absorption of large quantities of water vapor by hygroscopic salts until they turn into liquid solutions (Gough et al., 2016). In particular, Wang et al. (2019) proposed that the deliquescence of subsurface hydrated chlorides may be a thermodynamically viable, although not necessarily a sufficient process to trigger RSL activity. (Gough et al., 2019) reported that some hygroscopic salts, including perchlorates and calcium chlorides, absorb water vapor from the atmosphere too slowly to explain RSL formation, hence requiring an already hydrated brine deposit. While previous spectral detections of hydrated salts at RSL locations have been reported (Ojha et al., 2015), recently identified challenges in accurately mapping hydrated mineral compositions from absorptions beyond $2\mu m$ may render these detections unreliable (Leask et al., 2018; Vincendon et al., 2019). Other options envision an indirect role of water: Massé et al. (2016) and Raack et al. (2017) proposed that boiling liquid water and water-induced sediment levitations may trigger downslope transport of dry sediments. Although requiring minimal amounts of water, this mechanism still requires more water than available from the atmosphere, and RSL activity has been observed even at temperatures lower than the boiling point of water (Stillman et al., 2017). The roles of surface CO_2 and H_2O frost have also been investigated as potential triggers, but they do not form in all RSL locations, and sublimate completely before the onset of RSL activity (Schorghofer et al., 2019).

The fact that all proposed volatile-related models have issues identifying a robust mechanism for RSL activity has led authors to consider dry alternatives. Dundas et al. (2017) invoke dry granular flows to explain the observed correlation between RSL termination slope angles and the angle of repose of dry sand. Recent works report that some RSL may propagate on even lower slopes (Stillman et al., 2020; Tebolt et al., 2020), but Stillman et al. (2020) consider their observations consistent, within error, with dry flows. In addition, Tebolt et al. (2020) measured some slopes where RSL have not been seen (Dundas, 2020). Despite not requiring a water source, the identification of a process that could produce dry flows recurring yearly at the same locations has been challenging. Schmidt et al. (2017) proposed that RSL could be granular flows triggered by a Knudsen pump enhanced by shadows, but this model has difficulties with predicting RSL activity on some slopes (Stillman and Grimm, 2018) and at sites without sources for shadows (Vincendon et al., 2019). On the basis of the observed temporal correspondence between dust, aeolian and RSL activity seasonality, Vincendon et al. (2019) suggest that RSL could be dry, dust-removed features triggered by aeolian processes such as slope winds. Further, Schaefer et al. (2019) analysed the relative albedo of RSL, boulder and dust-devil tracks at Tivat crater, finding that all such features fade at the same time. They proposed that RSL fading may be due to widespread dust deflation, and that RSL

are indeed dry features resulting from a dust-lifting process, hence appearing as dark streaks. Dundas (2020) also proposed an aeolian grainflow model in which RSL are explained as flows of sand that remove dust. The recently reported correlation between fresh dust deposits from the most recent planet-encircling dust event (PEDE) and RSL activity is another indication that the latter is consistent with dry, dust-related features (McEwen et al., 2021). Aeolian and dust transport processes are also supported by high resolution local thermal (Millot et al., 2021) and photometric analyses (Munaretto et al., 2020, 2021a,b).

Although several lines of evidence towards a dry RSL interpretation built up during the development of this Ph.D. project, a complete and detailed description is still lacking. Novel and independent analyses of these features are therefore still helpful for better establishing and characterizing the nature and formation mechanism of RSL. In particular, imaging of RSL through HiRISE, traditionally the only camera able to observe RSL, is possible approximately at the same local time, preventing a characterization of their diurnal behaviour. However, if RSL are related to volatile release (either brine melting of deliquescence) their surface expression is expected to have a diurnal modulation, with a more intense activity at times of day when these processes are favoured. Comparing morning vs afternoon observation is therefore one promising path, now possible thanks to the CaSSIS stereocamera orbiting Mars, to better characterize the RSL nature and formation mechanism. Another promising research field to better understand the RSL puzzle is the characterization of their spectral properties. Indeed, spectral datasets of RSL are traditionally available at resolutions lower than 18 m/px, which is larger than the typical RSL width (a few meters), hence preventing robust analyses of these features. Although providing only four bands, the higher spatial resolution offered by CaSSIS allows to investigate and discriminate the spectral behaviour of RSL and understand more of their composition. The research work carried out in this Ph.D. project and presented in this thesis goes in these two directions and it is described in detail in Chapters (3) and (4), respectively.

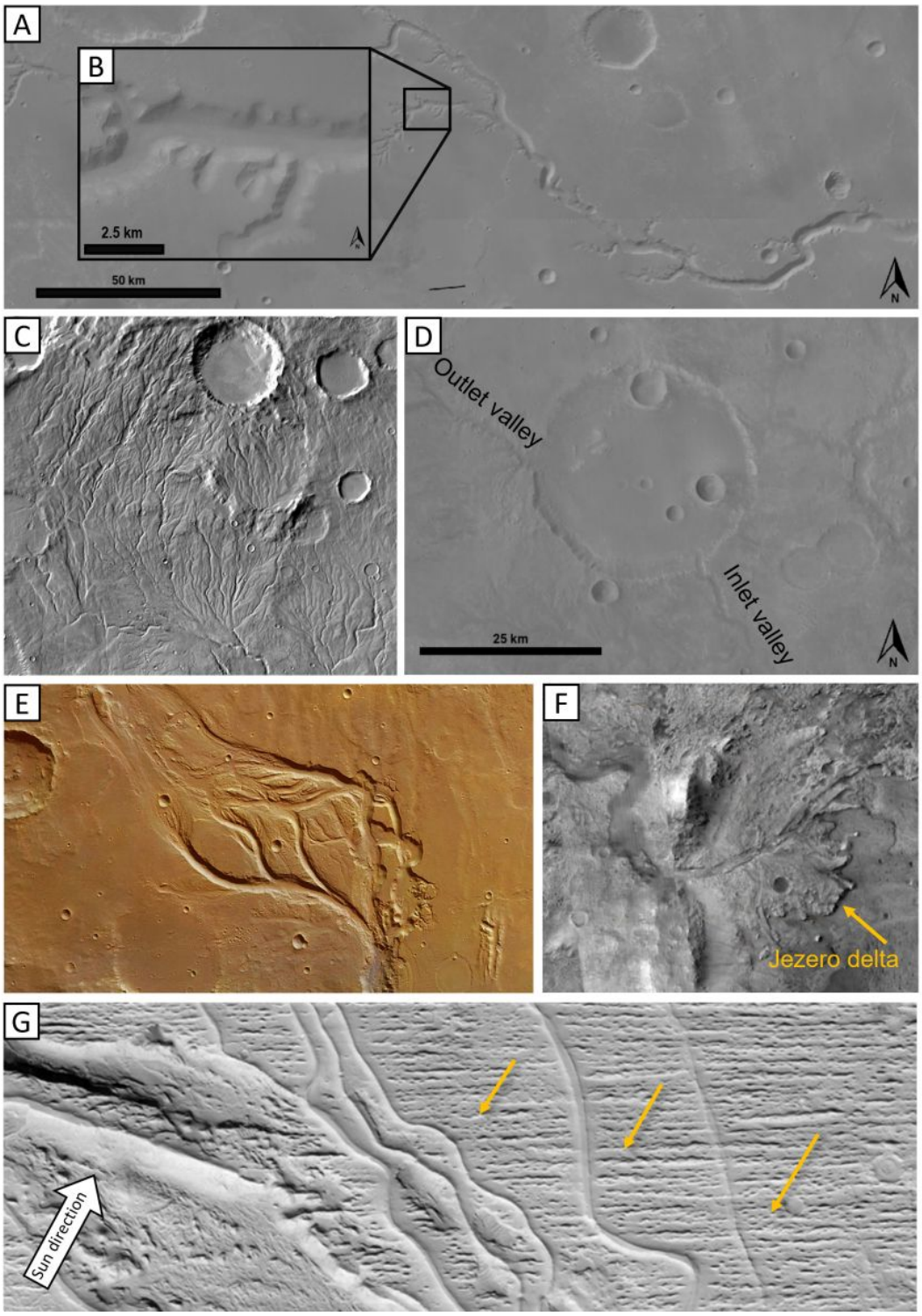

Figure 1.4: Geomorphic evidences of water. A) CTX mosaic of Nirgal vallis with groundwater sapping-related landforms highlighted in panel B). C) Example of a valley network with a high density of tributaries. D) Example of paleolake with an *inlet* and *outlet* valleys which breach the crater rim, suggesting that water flew into the crater from the bottom part of the figure and flew out from the breach in the crater in the top of the figure. E) HRSC image The Osuga valley outflow channel. F) CTX image of the Jezero crater delta. G) HiRISE image of *inverted relief* features (orange arrows).

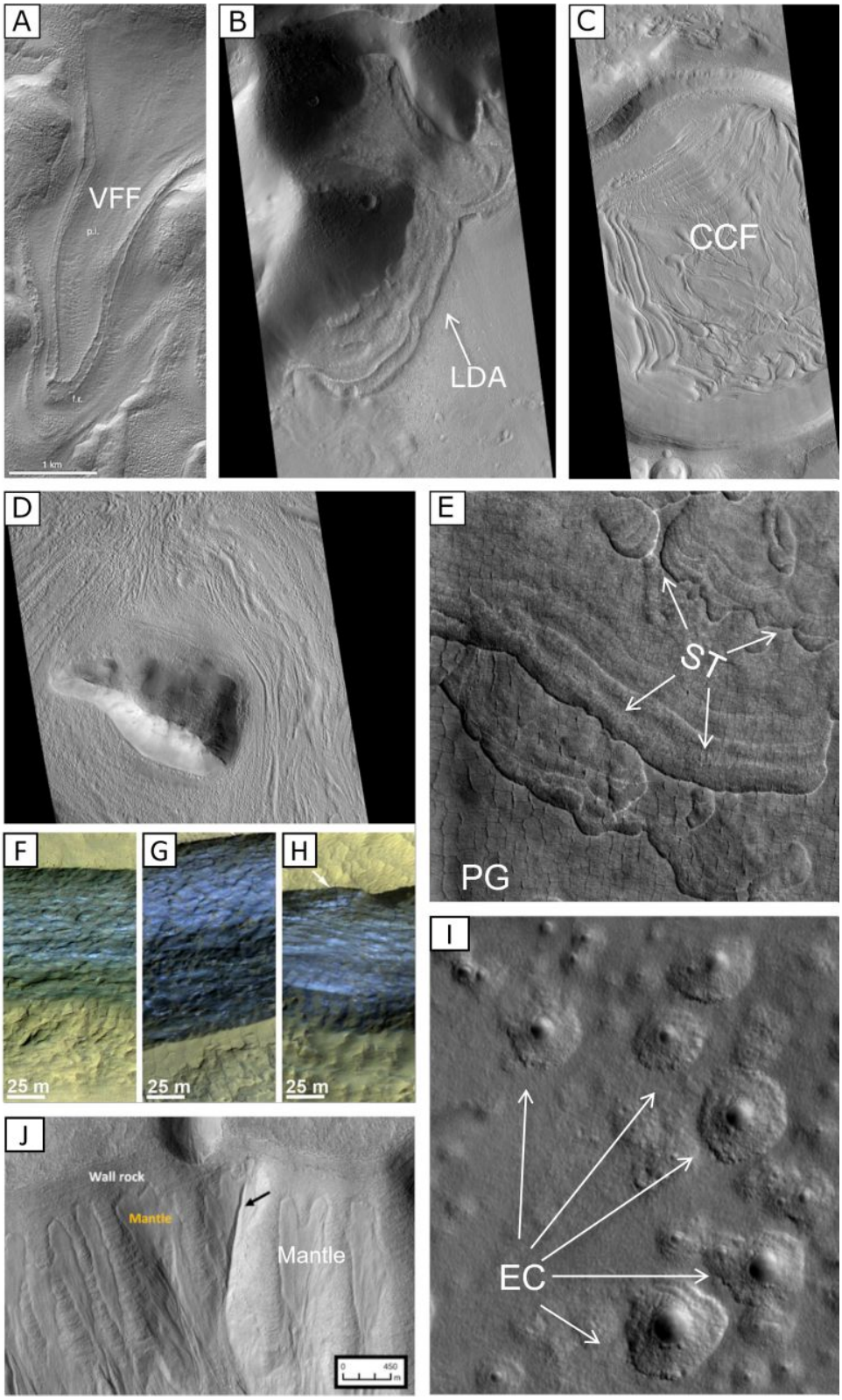

Figure 1.5: A) Mars Orbiter Camera (MOC) image of a Viscous Flow Feature (VFF). B) HiRISE images showing a Lobate debris Apron (LDA). C) Concentric crater fill (CCF). D) lineated valley fill (LVF). E) scalloped topography and polygonal ground (ST and PG). F,G, H) Exposed nearly pure water ice sheets. I) Expanded craters (EG, white arrows). J) pasted-on smooth mantle (labeled as mantle).

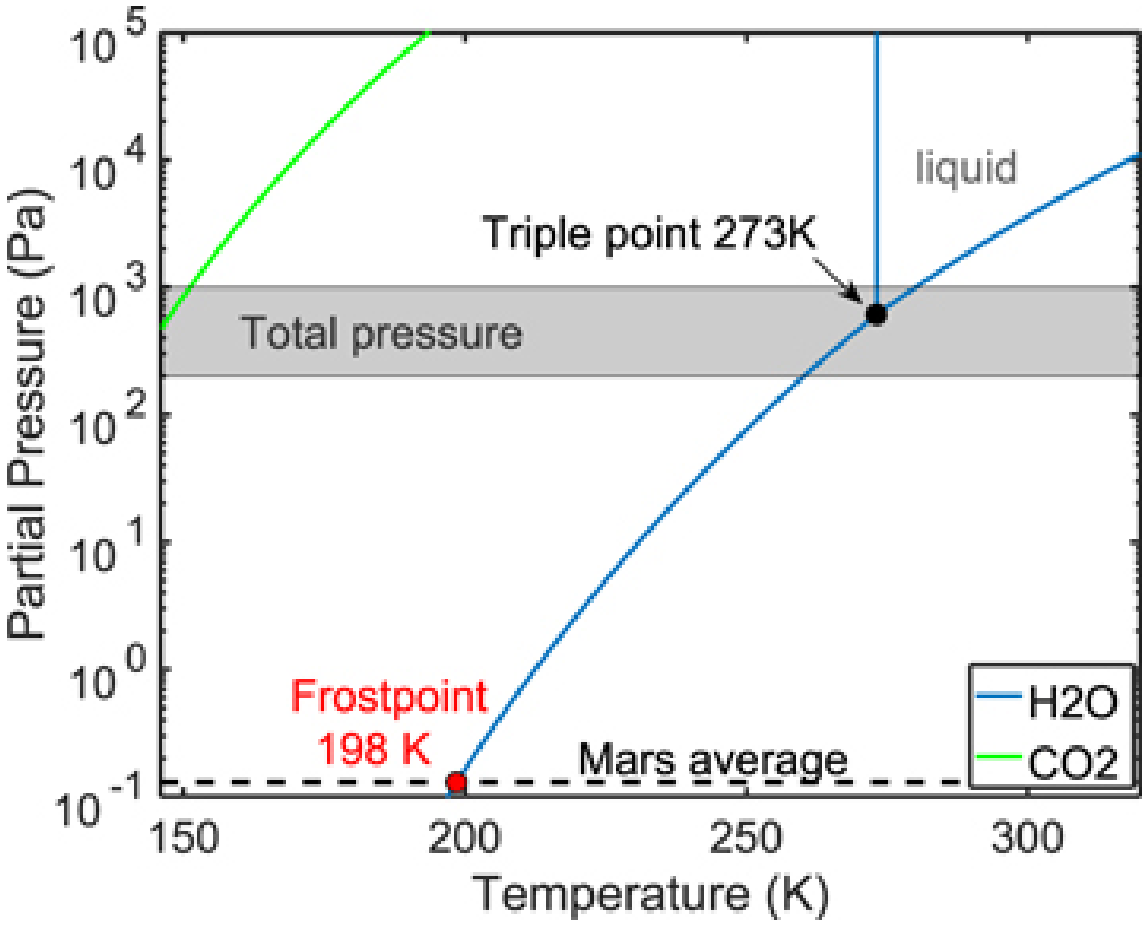

Figure 1.6: Phase diagram of water at present-day Mars conditions from (Schorghofer, 2020).

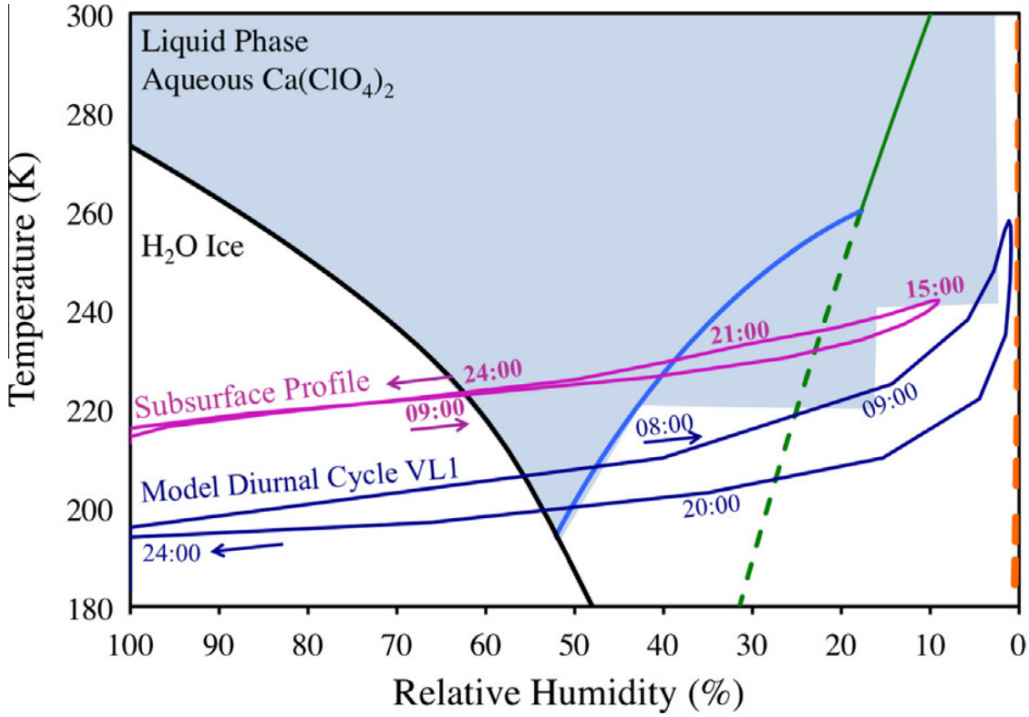

Figure 1.7: Figure 10 of Nuding et al. (2014) showing the stability diagram for the $Ca(ClO_4)_2$+H_2O system with a simulated surface diurnal profile at the VL1 landing site (dark blue line) and subsurface diurnal profile (pink line). The solid lines indicates predicted thermodynamically stable phase transitions and dashed lines represents metastable phase transitions. The blue shaded region represents the upper limit of the stable and metastable liquid phase of $Ca(ClO_4)_2$ based on the experimental results.

Chapter 2

Datasets and instruments: imaging of Mars through ExoMars TGO/CaSSIS and MRO/HiRISE

In this chapter, we introduce the two main instruments and related datasets that will be used in the Mars-related part of this thesis. In particular, we will first introduce the HiRISE camera and its related datasets in Section (2.1). In Section (2.2) we will describe the CaSSIS camera and its related 3D products, highlighting the importance of this instruments for studying the Martian surface and for investigating RSL, the prime topic of this thesis.

2.1 High resolution imaging of Mars with HiRISE

Launched in 2005 on board the NASA Mars Reconnaissance Orbiter (MRO) mission, the HiRISE instruments is the highest resolution camera currently orbiting Mars (McEwen et al., 2007). It provides images at a resolution as high as 25 cm/px, meaning that $\approx$ 80 cm sized object are resolved, in three broadbands: the red (RED, i.e. 570–830 nm), blue (BG, i.e. $<$ 580 nm) and near-infrared (NIR, i.e. $>$ 790 nm) visible wavelengths. The field of view is $\approx$ 6 km large and of variable length in the RED filter. The central 20% ($\approx$ 1.2 km across) is also acquired with the color filters. All the images acquired by HiRISE are available through the HiRISE catalog (`https://www.uahirise.org/catalog/`). The MRO orbits Mars in a sun-synchronous orbit, meaning that it will pass over a specific location at approximately the same local time throughout all the martian year. This orbital configuration has been exploited to acquire stereo observations of the surface from close-by orbits. The resulting highly similar illumination conditions of the stereo pair allowed to derive high resolution digital elevation models (DEM) of the surface through photogrammetry (Kirk et al., 2008). These are publicly available through the PDS or the HiRISE DTM catalog (`https://www.uahirise.org/dtm/`) at spatial resolution as high as 1 m/px. In addition, orthorectified images (i.e. corrected from parallatic distortions due to the terrain topography) overlapping these DEMs are also available for specific locations.

2.2 Color imaging and 3D mapping of Mars with CaSSIS

CaSSIS is the main imaging system of the ESA's TGO mission. Launched in March 2006, it is currently in its scientific phase. It provides high resolution (4.6 m/px) images of Mars over typically $\approx$ 9.5 km by $\approx$ 45 km swaths (see Fig. (2.1) and in four colour bands (Thomas et al., 2017). In addition, it implements a novel rotation mechanism that allows to acquire stereo observation for 3D reconstruction purposes. This design allowed to fill the gap left by other imagers and spectrometers orbiting Mars. While HiRISE, the MRO Context Imager (CTX, Malin et al., 2007) and the Mars Observer Camera (MOC, Malin et al., 1992 have superior or comparable resolution, their have no or very restricted colour capabilities. In particular, colour imaging with HiRISE, although possible only in the narrow central 20% of the observation swath, revealed that Mars has an impressive colour diversity at small spatial scales (Delamere et al., 2010). In addition, stereo imaging of Mars with these instruments is restricted and requires two different passes on the same target with favourable illumination and observation geometries. Other instruments orbiting Mars that provide stereo and colour imaging but at lower resolutions. The High Resolution Stereo Camera (HRSC, Jaumann et al., 2007) on board the Mars Express mission provides colour and stereo images of Mars, but at resolutions of 10 m/px at best, and DTMs with an average grid size of 200 m, up to 50 m in particular cases. The Compact Reconnaissance Imaging Spectrometer for Mars (CRISM, Murchie et al., 2007) provides hyperspectral datasets, but at resolution of 18 m/px at best. In summary CaSSIS fills the current gaps left by other instruments in terms of resolution, colour and stereo coverage. More importantly, the 74°-inclination circular orbit of the TGO allows CaSSIS to image a given location at different times of day. This capability is pivotal for studying dynamic processes on Mars, that can be observed at the precise local time when the release of volatiles from the surface is more probable according to theoretical predictions.

2.2.1 Image acquisition details

CaSSIS uses the same focal plane assembly of the SIMBIO-SYS instrument (Cremonese et al., 2020) on board the ESA's BepiColombo mission . In particular, the light sensing element is a Raytheon Osprey 2k hybrid CMOS detector. It is based on Hybrid Silicon PIN (Si PIN) CMOS technology. The Si PIN diodes, have a 100% fill factor and very high quantum efficiency up to near-IR wavelengths, ranging from 4% at 400 nm up to 91% at 800 nm at 293 K The detector array is composed of 2048×2048 pixels with 10 μm × 10 μ m pixel pitch and a full well capacity of about 90000 electrons (Thomas et al., 2017). A filter strip assembly is placed directly on top of the detector, and contains four colour filters similar to the ones used by HiRISE. In particular, the CaSSIS BLU (effective wavelength = 499.9 nm, equivalent bandwidth = 118.0 nm) and PAN (effective wavelength = 675.0 nm, equivalent bandwidth = 229.4 nm) corresponds to the BG and RED HiRISE filters, providing photometric consistency between the two instruments. In addition the CaSSIS RED (effective wavelength = 836.2 nm, equivalent bandwidth = 94.3 nm) and NIR (effective wavelength = 936.7 nm, equivalent bandwidth = 113.7 nm) split the HiRISE IR filter in two. This filter setup has been optimized for discriminating different sur-

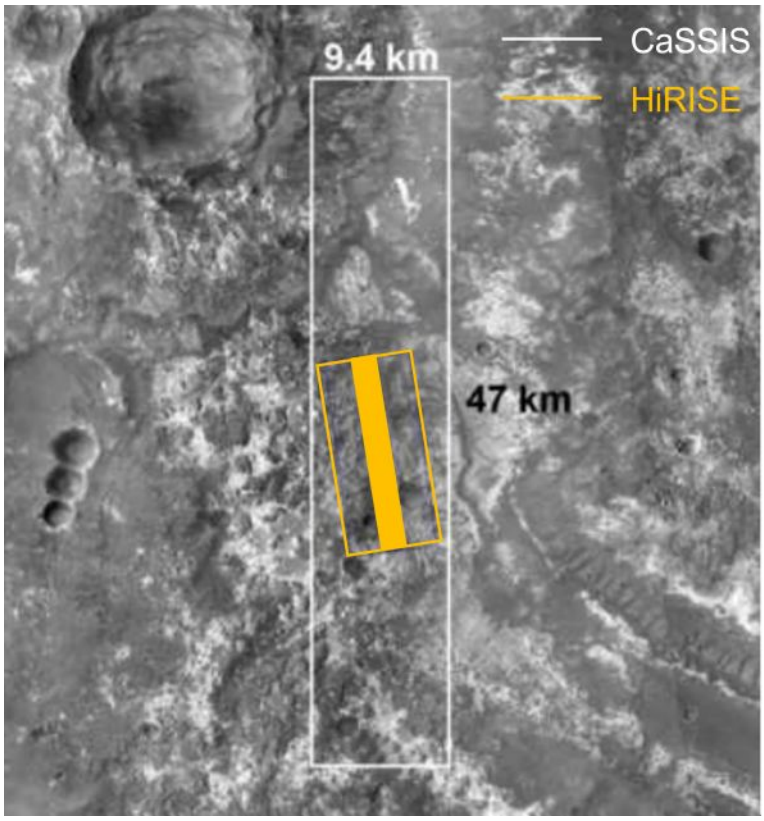

Figure 2.1: White polygon: footprint of a CaSSIS observation. Orange polygon: footprint of a HiRISE observation. The filled polygon is the HiRISE colour swath.

face minerals on Mars. Fe-bearing minerals, in particular ferrous (Fe^{2+}-bearing, i.e. olivine and pyroxene) and ferric (Fe^{3+}-bearing, like hematite and goethite) minerals display an absorption between $0.7 - 1.1$ μ m, which is captured by the RED and NIR filters. These minerals also have an absorption in the UV, which is captured by comparing the BLU and the PAN signals. Ices and surface frosts are also highly reflective in the BLU and PAN filters, making CaSSIS very sensitive to the presence of these materials on the surface. The CMOS technology allows to acquire up to six simultaneous windows on the detector. In the CaSSIS imaging strategy four windows are defined, each one below a filter, and acquired simultaneously. These windows (one for each filter) are called "framelets". The number of acquired filters, framelets and their sizes can be commanded from Earth, but they may be up to 2048×280 pixels in the PAN filter and 2048×256 pixels in the other filters (Thomas et al., 2017). With the push-frame approach, a single observation (full frame image) is made of multiple "framelets" that are acquired with a time interval between each other, called repetition time. The repetition time depends on the ground track velocity of the satellite and it is such that the location imaged at the top of a given framelet is located at the bottom of the next one. This overlap is necessary when all framelets for each filter are collected and mosaicked to produce the final image.

2.2.2 Stereo imaging system

The main feature of the CaSSIS camera is the capability of imaging the surface of Mars in stereo mode in a single pass. Avoiding to rely on a second pass with favourable illumination and observation conditions, this translates in a larger stereo coverage with respect to instrument of comparable or higher spatial resolution. To accomplish this, CaSSIS implements a rotation mechanism that, as soon as an image is acquired, rotates the camera of 180° with respect to the along-track direction. After this movement, the camera is "looking back" at the location that has been imaged prior to the rotation. Another image is therefore acquired, which will have very similar illumination conditions with respect to the first one. The parallattic angle introduced by the two different looking direction (one forward, one backward) makes the two images of the sequence a stereo pair. Stereo-photogrammetric routines can be therefore applied to reconstruct the imaged surface in 3D and obtain a digital terrain model (DTM) of the surface. Details about the 3D reconstruction are given in Simioni et al. (2021) and summarized here. A sketch showing the geometry of a stereo acquisition is presented in figure (2.3). Each image of the pair is radiometrically calibrated (i.e., converted from Digital Numbers to radiances). Using well established computer vision techniques, a net of interest point is extracted from each image of the stereo pair. Each interest point on an image is matched with the corresponding one on the other image. This allows to estimate the parallax at each point, called "disparity", which is extrapolated to all the point of the image producing a "disparity map". The disparity map is further refined, outliers are removed and "holes" where the algorithm did not find suitable matches are filled using the information in the neighboring regions. At last, the triangulation of the disparity map allows to derive a DTM of the surface with a vertical resolution comparable with the CaSSIS pixel size ($\approx$ 5m) and a grid size from 1 to 3 CaSSIS pixels (i.e., from 4.6 m/px to 13.8 m/px) (Simioni et al., 2021).

2.2.3 Image reductions and calibrations

Once a raw image is acquired, it is reduced and converted to physical values (radiances) and map-projected on the surface of Mars. Details about all the steps are provided in (Pommerol et al., 2021). A bias level (i.e, a constant offset) is estimated from night-side observation of Mars and is subracted from the framelets. To correct the pixel to pixel variability of the instrument response, the bias-subtracted framelets are divided by a flat-field image. The latter is derived by summing multiple images of Mars, which "blurs" the signal of the surface and highlights the fixed pattern signal intrinsic of the instrument. Finally, the stray-light of the instrument is also modeled and removed. After the flat-field and stay-light corrections, the image is converted from raw values to physical units of radiance factor (I/F) relying on a radiometric model of the instrument that takes into account the filter transmission curves, the mirror reflectivity and the detector quantum efficiency (Roloff et al., 2017) (see Fig. 2.2) and on observations of standard stars, Phobos and Jupiter (Thomas et al., 2021, *in review*).

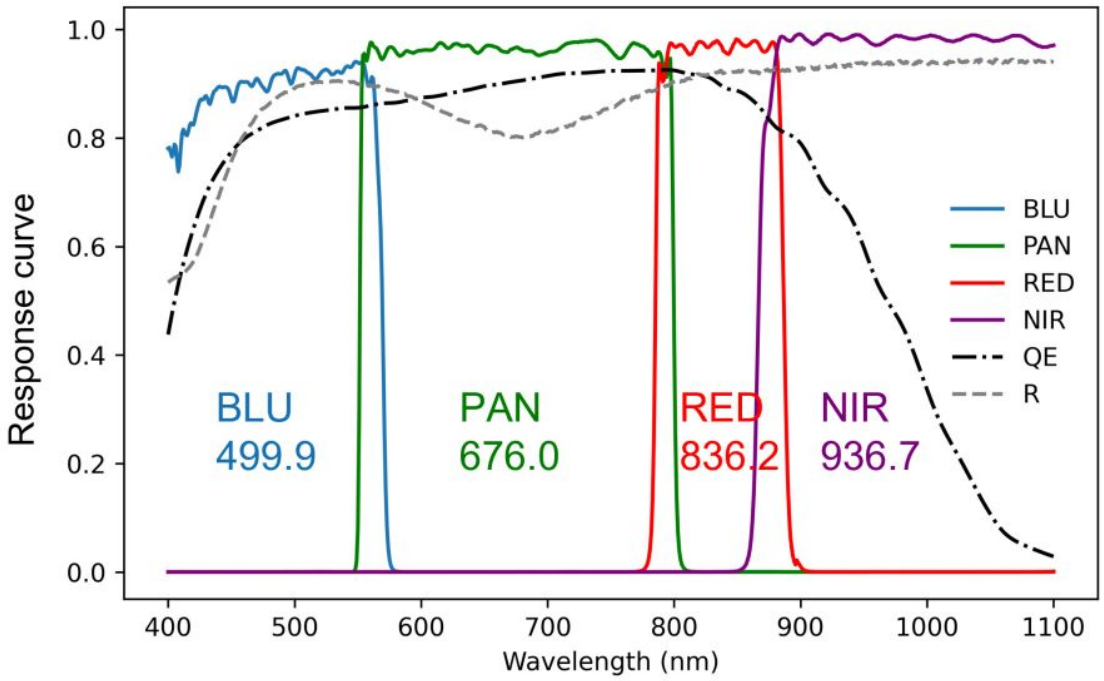

Figure 2.2: Filter transmission, mirror reflectivity and detector quantum efficiency functions as a function of wavelength. Also reported are the filters central wavelengths.

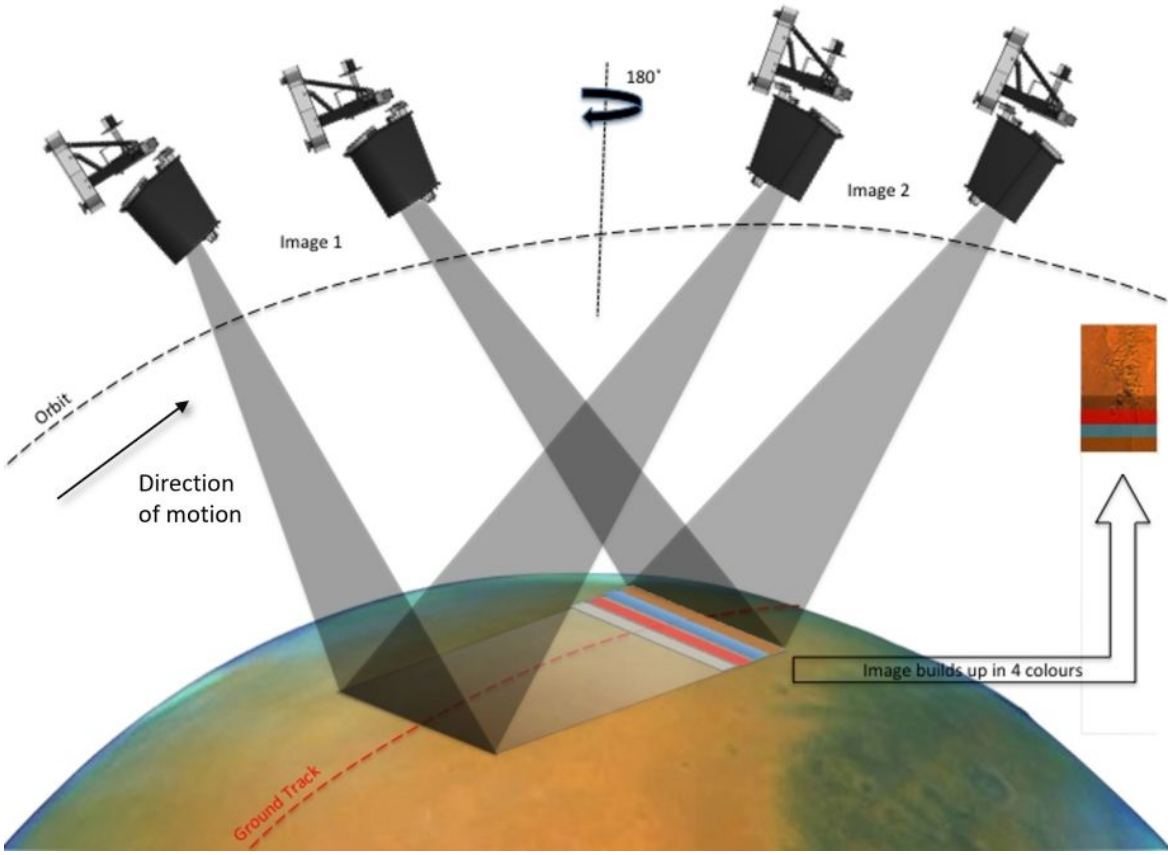

Figure 2.3: Sketch depicting the geometry of a stereo acquisition. Credits: University of Bern.

Chapter 3

Analysis of Martian Recurring Slope Lineae at Hale crater through CaSSIS and HiRISE observations

As already discussed in Chapter (1.6), the origin of Recurring Slope Lineae (RSL) is one of the most controversial scientific questions regarding present-day surface activity on Mars. Many models have been proposed to explain their origin, for which a detailed description has been given in Section (1.6), but a definitive explanation is still elusive. In particular, some studies point to a water-related origin, either through deliquescence or brine melting, while other studies propose dry origins such as granular flow or dust-removed aeolian features.

Each scenario (water-related vs dry) has implications on the diurnal activity of RSL. Laboratory studies (Gough et al., 2016) and analyses of data from both the Rover Environmental Monitoring Station (REMS) on board Curiosity and the Thermal and Electrical Conductivity Probe (TECP) on the Phoenix lander shows that daily maximum RH values occur during the early morning of local summer (Fischer et al., 2019; Steele et al., 2017), suggesting that these local hours are the most favourable for deliquescence. Therefore, if RSL are liquid-based flows, their activity should increase in the morning, when both temperature and air humidity are high enough to favor the deliquescence of salts and increase the stability of brines. Under this scenario, dehydration would occur in the afternoon, so we would also expect RSL to be darker in the morning than in the afternoon. Instead, if RSL are caused by the melting of shallow subsurface ice (such as from a deep groundwater source), then they should be darker in the afternoon. This assumes that the quantity of water or brines at play is relatively small, so that evaporative losses exceed the supply of water (Hillel, 2004). If instead RSL have a high water content, its concentration within the pores of the regolith would not be affected by evaporation and there wouldn not be any albedo change (Levy et al., 2014; Pommerol et al., 2013). The latter case, however, may not be in agreement with the very low water content of RSL estimated at Garni crater (Edwards and Piqueux, 2016). Finally, if RSL are dry flows, then we do not expect any albedo change between the observations. Therefore, the combined analysis of morning and afternoon observations is a promising and novel tool to further investigate the RSL nature and formation mechanism. This is now

possible by analyzing coordinated CaSSIS and HiRISE observations, and it is the main topic of this Chapter.

The CaSSIS camera, described in section (2.2), is at the moment the only satellite instrument that can acquire RSL observations at different times of day, such as in the local morning, thanks to the 74° inclined orbit of the TGO. This capability is pivotal for RSL studies, since morning observations of these features are not possible otherwise. The only exceptions are extremely early morning views by Mars Odyssey, with poor SNR and much lower spatial resolution. On the contrary, HiRISE (see section 2.1) images are instead taken between $\sim$ 2-4 PM, due to the sun-synchronous orbit of the MRO satellite, at a much higher spatial resolution ($\sim$ 0.26 m/px).

In this study we present the first observations of RSL performed by CaSSIS during the local morning and compare them with HiRISE observations acquired one month earlier in the afternoon. We focus on three main analyses. We first search for any geomorphological difference (i.e. length, slope, aspect) that may be interpreted with a water-related or dry model. We investigate the relative photometry of RSL performed on morning and afternoon images. We perform a thermal modeling of the surface and shallow sub-surface at the time of the CaSSIS observation to assess whether temperatures would either allow melting of brines or deliquescence of salts.

This Chapter is organized as follows: in Section (3.1) we describe our study region and the dataset that we used. In Section (3.2) we describe the RSL identification, mapping and comparison (3.2.1), the relative photometry approach (3.2.2) and the thermal modeling approach (3.2.3). In Sections (3.3,3.4) we report and discuss our results, respectively. Finally, in Section (3.5) we draw our conclusions.

3.1 Data

The study region is the central peak of Hale crater (−35.7° N, 323.5° E, see Fig. 3.2a, b), where several areally extensive RSL have been discovered so far, making it an ideal site to be investigated with CaSSIS. RSL in Hale were first reported by Ojha et al. (2014) and then analyzed by different authors (Dundas et al., 2017; Stillman and Grimm, 2018; Stillman et al., 2014). Stillman and Grimm (2018) reported that RSL activity in general may occur in one or two pulses, where RSL fade partially or completely and then re-appear in the same year. The RSL at Hale crater are peculiar because they seem to experience three pulses of activity (Stillman and Grimm, 2018), unlike any other sites analyzed on Mars so far. Our RSL observations span an L_s range between 331.5° and 347.4°, within the third pulse proposed by Stillman and Grimm (2018), allowing us to confirm its presence at Hale crater. In order to study whether there is a diurnal dependence in the activity of RSL, an ideal dataset would include two observations of an RSL site acquired during the same Martian day, the first one with CaSSIS in the morning and the second one with HiRISE in the afternoon. In our case, the observations were acquired during late southern summer, one month apart. The HiRISE image was acquired on L_s = 331.5° at 14:06 local time, while the CaSSIS image was acquired on L_s = 347.4° at 11:13 local time. This time interval may be too big to minimize seasonal changes between images, such as fading of RSL, which typically

happens during this season at southern hemisphere sites. However, this issue may not be important for Hale crater, where fading was reported to occur only after $L_s > 7°$ for both MY 30 and 31 (Stillman and Grimm, 2018), well after the L_s of our observations. For this reason, we are confident that fading is not influencing our analysis. Moreover, RSL at Hale crater are "rejuvenated" by a third pulse of activity which occurs just before $L_s = 331.5°$. The occurrence of this third pulse of activity is illustrated in Fig. (3.1). HiRISE image ESP_057_569_1440, acquired at $L_s = 286.6°$, shows dense RSL coverage (see Fig. 3.1a), while the subsequent HiRISE image ESP_058618_1445, acquired at $L_s = 331.5°$, shows smaller RSL in the same places (see Fig. 3.1b). These further lengthened in the subsequent CaSSIS image MY34_005640_218_2, acquired at $L_s = 347.4°$ (see Fig. 3.1c). This means that the RSL had completely faded and had started lengthening again between the first two images (3.1a,b) and continued lengthening between $L_s = 331.5°$ and $L_s = 347.4°$. This is also confirmed by the analysis of HiRISE images of Hale crater in previous Martian Years reported by Stillman and Grimm (2018). In particular, from figure S9 of Stillman and Grimm (2018) we see that RSL lengthening occurs between $341.9° < L_s < 7°$ in MY 31 and $326.5° < L_s < 7°$ MY 32. This means that despite the HiRISE and CaSSIS images analyzed here being taken 30 days apart, the mechanisms responsible for RSL lengthening are active during this period and any seasonal fading can be considered negligible, allowing us to compare RSL albedos between the two images. In the following sections we will describe our dataset, summarized in Fig. (3.2), which combines HiRISE (section 3.1.1), CaSSIS (section 3.1.2) and Thermal Emission Imaging System (THEMIS, Christensen et al., 2004) (section 3.1.3) observations.

3.1.1 HiRISE data

We downloaded the latest publicly available HiRISE image of the central peak of Hale crater, ESP_058618_1445, acquired on 27 January 2019 at 14:06 Mars local time and with a $L_s = 331.5°$, as well as the corresponding HiRISE DTM and orthophoto of the region. The RED channel (McEwen et al., 2007) of the HiRISE image was orthorectified on the DTM using the NASA Ames Stereo Pipeline (Moratto et al., 2010). To obtain reliable slope and aspect measurements, we adapted the technique of Schaefer et al. (2019) to reduce noise and systematic artifacts present in the DTM and calculated slope and aspect maps using ArcGIS (Burrough and McDonell, 1998). In particular, the DTM was resampled at 2m resolution and smoothed with a 10 m radius moving average as in Schaefer et al. (2019). The aligned HiRISE DTM, image, aspect and slope maps are shown in Fig. (3.2).

3.1.2 CaSSIS data

The central peak of Hale crater was imaged by CaSSIS on 26 February 2019 at 11:13 Mars local time, with a $L_s = 347.4°$, in stereo mode and with the near infrared (NIR), red (RED), panchromatic (PAN) and blue (BLU) filters (Thomas et al., 2017). From the CaSSIS stereo pair MY34_005640_218_1, a DTM and radiometrically calibrated orthophoto of the PAN channel of the second image in the stereo pair (i.e. MY34_005640_218_2) were obtained using the 3DPD photogrammetric pipeline described in Simioni et al. (2017). The CaSSIS orthophoto was then

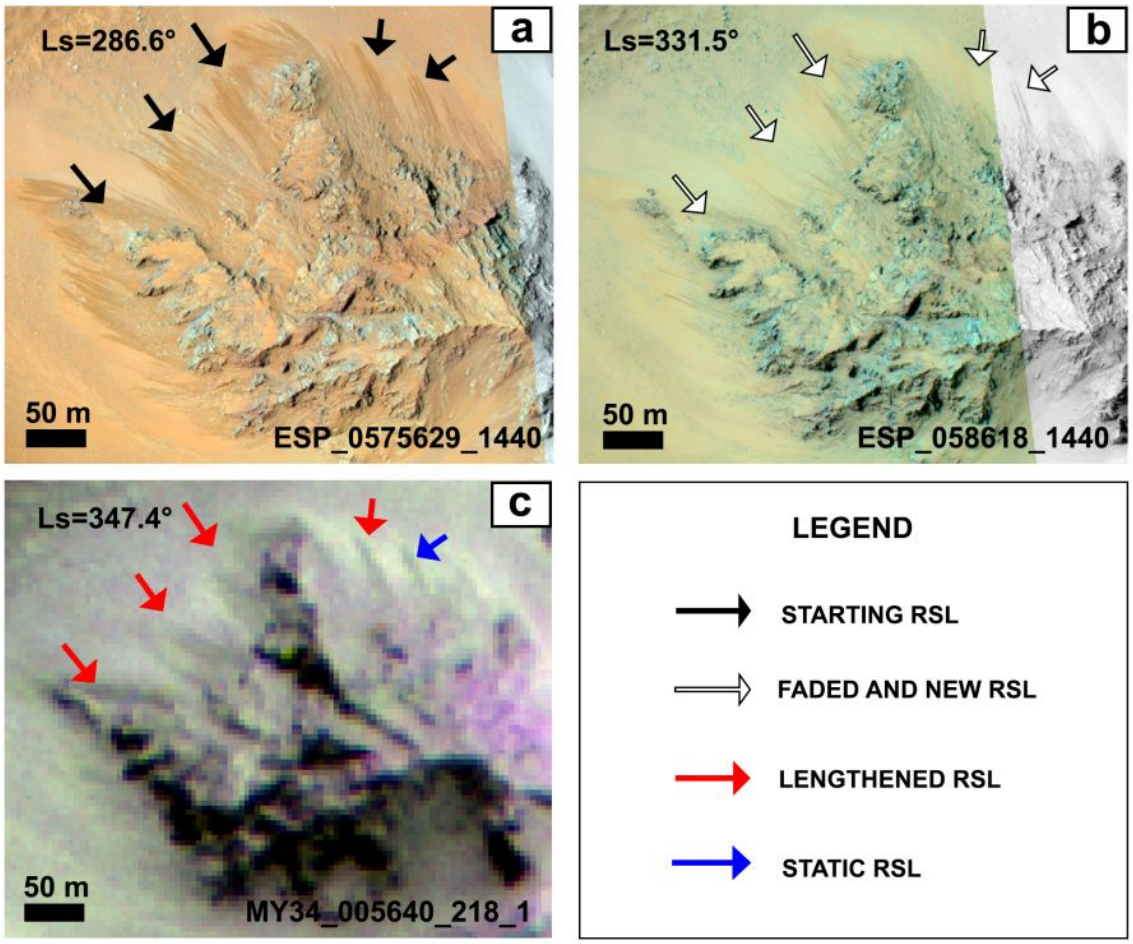

Figure 3.1: RSL activity during the 3rd pulse at Hale crater. a) HiRISE image showing areally extensive RSL, indicated by black arrows, at $L_s = 286.6°$. b) The same area but observed at $L_s = 331.5°$. White arrows indicate the same RSL in a) that faded and restarted their lengthening phase. c) Colour composite of the RED, PAN and BLU filters of CaSSIS image MY34_005640_218_2 taken at $L_s = 347.4°$ and showing that some a RSL in n) remained static (blue arrow) while others (red arrows) further lengthened with respect to the previous image. Areal extents of RSL in this area are mapped in Fig. (3.9).

manually co-registered to the aligned HiRISE dataset in ArcGIS. The footprint of the CaSSIS stereo pair is shown in Fig. (3.2b) and a color composite image obtained by combining the overlap of the RED, PAN and BLU channels is shown in Fig. (3.2c).

3.1.3 THEMIS data

We used the MARSTHERM web interface (Putzig et al., 2013) to process THEMIS infrared observations within $\pm$ 5° of L_s of the CaSSIS image and derive thermal inertia maps of Hale crater at 100 m resolution. As is customary for Martian thermal modeling studies (Edwards and Piqueux, 2016; Fergason et al., 2006), we considered only nighttime observations. The final thermal inertia map was obtained by computing the median thermal inertia value at each pixel from all the selected observations. The thermal inertia map was then used to simulate surface and subsurface temperatures at Hale crater, as described in section (3.2.3).

3.2 Methods

3.2.1 General properties

We first identified all RSL that were resolved in both the HiRISE and CaSSIS images. Sometimes the RSL identified on the HiRISE image occurred in clusters of several lineae, spanning multiple CaSSIS pixels, but separated by distances lower than the CaSSIS resolution. In these cases we did not consider the single RSL, not resolved by CaSSIS, but the whole cluster. We mapped the envelope of each RSL, or cluster of RSL, in both images. To better compare the two images and cross-check any detected lengthening, we also resampled the HiRISE image at the CaSSIS resolution by summing all HiRISE pixels within a CaSSIS pixel and mapped the RSL envelopes on the resampled image. Examples of "changed" and "static" RSL, including their mapped envelopes are seen in Fig. (3.3). If a significant RSL lengthening could be detected using both the original and resampled images, we labeled the RSL as "changed", otherwise as "static". To take into account uncertainties in the comparison from any residual misalignment and/or differences in resolution and illumination between the two images, we considered a lengthening to be statistically robust only if greater than 1 CaSSIS pixel. This threshold is much lower than the typical lengthening that should occur between the two images, $\sim 60 - 100$ m given the average RSL advance rates (Levy, 2012; Stillman et al., 2016). To distinguish darkening caused by illumination conditions (i.e. topographic shading) from real RSL in the CaSSIS image we also considered the relative orientation between the slopes and the direction of the Sun, and avoided comparison of albedo features within highly shaded regions. Finally, we measured the mean slope and aspect at the termination point of every mapped RSL in the HiRISE image.

3.2.2 Relative albedo

The relative albedo is the ratio between the reflectance (I/F) of two atmospherically corrected regions of the surface that have the same illumination conditions (Daubar et al., 2016). Our goal is to assess if RSL are darker, and thus potentially wetter, in

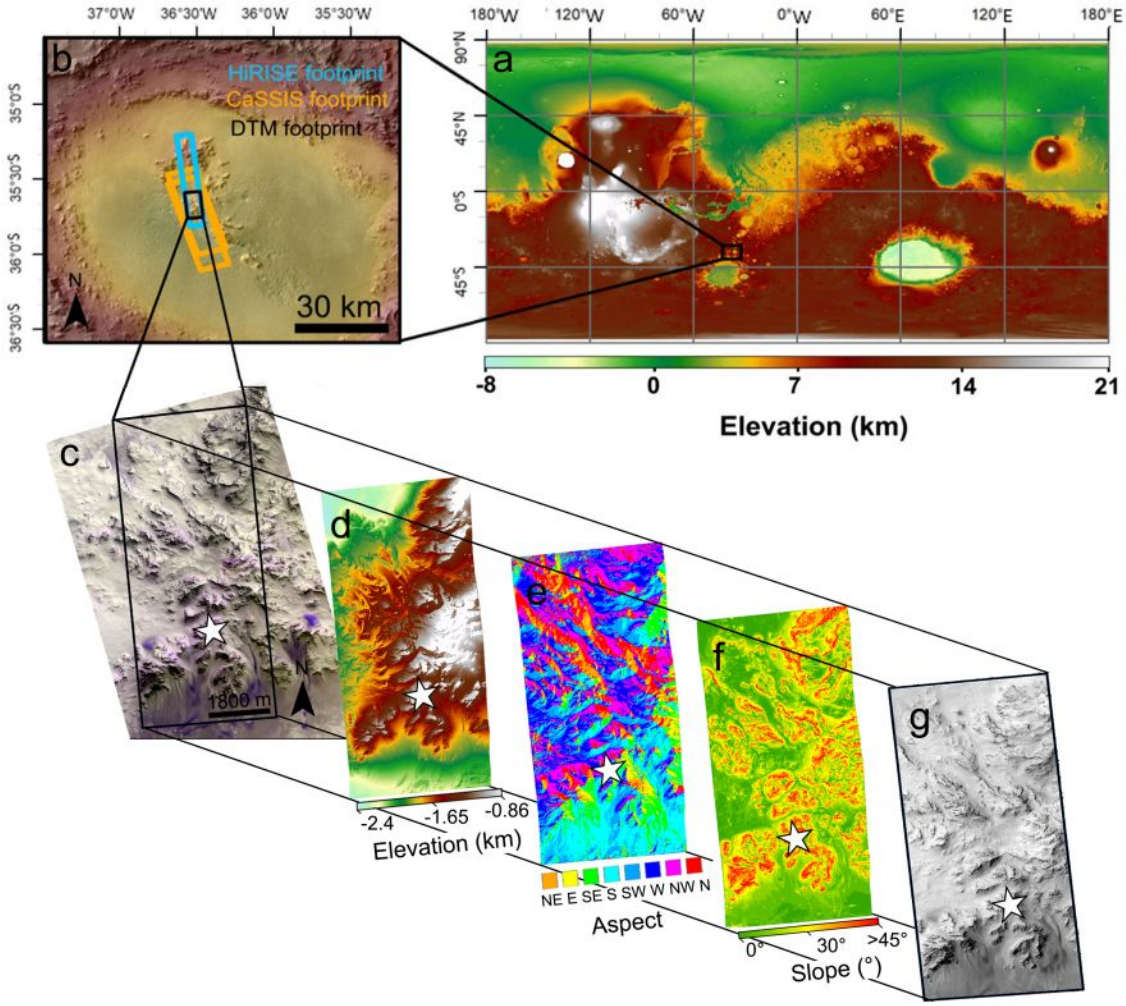

Figure 3.2: Schematic description of our dataset. a) Mars Orbiter Laser Altimeter (MOLA) colorized elevation map of Mars showing the location of Hale crater (black rectangle). b) MOLA colorized elevation map overlaid on THEMIS infrared daytime mosaic showing the central peak of Hale crater and the footprints of our observations. c) RGB color composite of the RED, PAN and BLU filters of CaSSIS image MY34_005640_218_2 depicting the central peak of Hale crater. d) HiRISE DTM, e) aspect and f) slope maps generated from the HiRISE DTM and g) HiRISE image ESP_058618_1445 projected onto the HiRISE DTM.The white star indicates the location of Fig. (3.1).

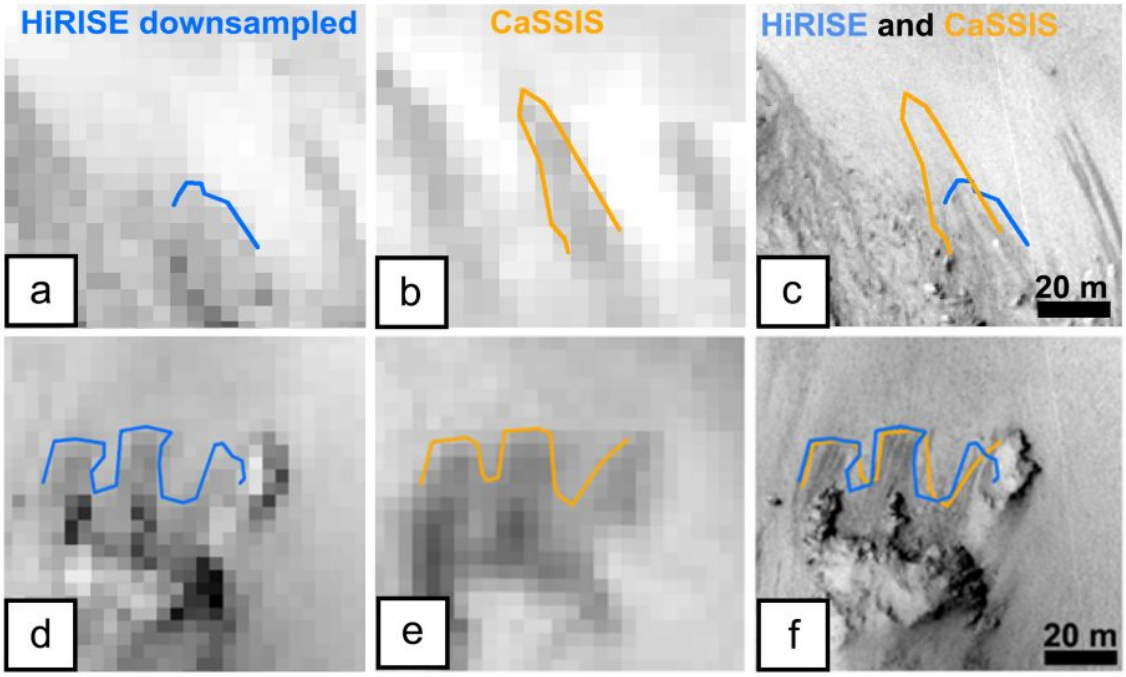

Figure 3.3: Examples of "changed" (upper row) and "static" (lower row) RSL envelopes mapped in blue on the downsampled afternnon HiRISE image (a,d) and in orange on the morning CaSSIS image (b,e). Panels (c) and (f) Show their comparison on top of the original HiRISE image.

the morning with respect to the afternoon. We compute the RSL relative albedo as the ratio between the reflectance of an RSL region and the reflectance of a nearby RSL-free region with the same illumination conditions, that is assumed to not have "changed". We only compare the CaSSIS PAN channel with the HiRISE RED channel. As these two filters closely correspond one to each other, the consistency between HiRISE and CaSSIS measurements is granted (Thomas et al., 2017). A complete multi-band analysis taking into account for differences between the CaSSIS RED and NIR and the HiRISE IR filters is left for a future work. In order to perform relative albedo measurements, it is necessary to first identify regions with similar slope and aspect, and in turn similar incidence angles. To do this, we first selected a set of regions of interest (ROI) from the previously identified RSL in both images (RSL ROI). To ensure that each RSL ROI is dominated by RSL signal, we used the HiRISE image for the selection and kept that same ROI in the CaSSIS image. Their mean slope and aspect were measured using ArcGIS. For each RSL ROI, we defined a corresponding background (BK) ROI in a nearby region, with similar mean slope and aspect but without RSL in either images. Where a suitable BK ROI could not be found, we did not include the RSL in the relative albedo analysis. Figure (3.4) shows examples of some selected ROIs. We extracted the mean I/F and its standard deviation for each BK and RSL ROI and applied a first order atmospheric correction by subtracting the I/F value of the darkest pixel within shadows in the overlapping region of the two images from IF_{RSL}. To take into account the different resolutions of the two images, for HiRISE we used the mean I/F in a 4.6×4.6 m square area around the darkest pixel within shadows. Although this kind of atmospheric correction can

be inaccurate in steep topography, it is often adopted when performing relative photometry (Daubar et al., 2016; Schaefer et al., 2019). In addition, more precise use of shadows areas for this purpose could be performed if required (Hoekzema et al., 2011). In our case, however, we only apply the atmospheric correction to the RSL ROIs and not to the BK ones. The rationale behind this approach is to take into account the non-linear effect of aerosols on the apparent reflectance of a surface, meaning that low-albedo surfaces are more brightened by diffuse light than high albedo ones (Vincendon et al., 2007). We finally computed the relative albedo as:

$$RA_* = \frac{IF_{RSL} - IF_D}{IF_{BK}} \qquad * \in \{H, C\} \tag{3.1}$$

where RA_* is the RSL relative albedo, computed either from the original HiRISE ($* = H$) or CaSSIS ($* = C$) images. IF_{RSL} is the mean I/F extracted from an RSL ROI. IF_D is the I/F of the darkest shadowed pixel and IF_{BK} is the I/F of a BK ROI. We compute uncertainties for the HiRISE and CaSSIS relative albedos applying standard error propagation. The significance of any difference between the HiRISE and CaSSIS relative albedos is established applying standard statistical tests. We use the Kolmogorov-Smirnov (KS, Massey, 1951) and Wilcoxon (W, Wilcoxon, 1945) signed-rank statistical tests to assess if the HiRISE and CaSSIS relative albedos are sampled from the same distribution. We apply the Anderson-Darling (AD, Anderson and Darling, 1954) and Shapiro-Wilk statistical tests (SW, Shapiro and Wilk, 1965) to assess if the differences between the two distributions are stochastic. From each test, a $p-$value is computed and compared with the customary 0.05 threshold. All tests and the $p-$value computations are performed using routines implemented in the `nortest` library (Gross and Ligges, 2015), a common and well established package for statistical calculations implemented in the R (`https://CRAN.R-project.org/package=nortest`) programming language (R Core Team, 2019).

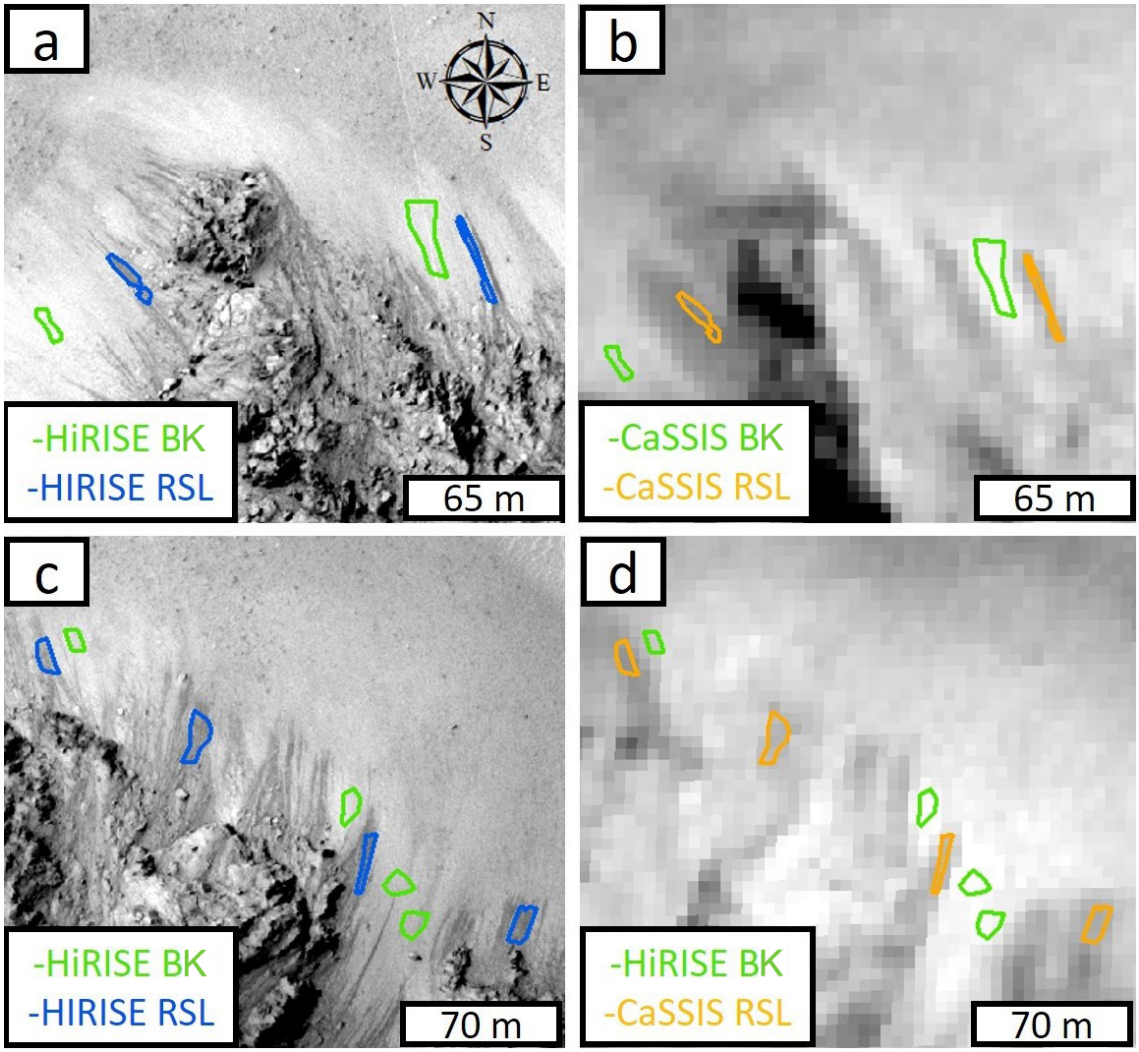

Figure 3.4: a,c): examples of RSL ROI (blue) and BK ROI (green) used to extract the mean I/F of RSL and RSL-free regions and their uncertainty from the HiRISE image. b,d): examples of RSL (orange) and BK (green) ROIs used to extract the mean I/F of RSL and RSL-free regions and their uncertainty from the CaSSIS orthoimage.

3.2.3 Thermal analysis

We simulated diurnal surface and subsurface temperatures on the region depicted in Fig. (3.5a) at the time of the CaSSIS observation using the thermal model of Schorghofer et al. (2019). This model solves the 1D thermal balance and diffusion equations in a rough surface, taking into account the contribution of 3D topography to the surface energy balance. Examples of modeled diurnal surface and subsurface temperature maps are shown in Fig. (3.6). We focused only on this region because it hosts many large RSL on multiple slope orientations and allowed us to reduce computation time. Within this region we defined different study zones, as depicted in Fig. (3.5b). To account for the different thermal behavior of different materials within our region, we distinguished between zones composed of exposed bedrock (i.e. those starting with "B" in Fig. 3.5d and zones composed of finer material, like

regolith (i.e. those starting with "S" in Fig. 3.5d). For the former we estimate a mean thermal inertia of 772^{+188}_{-130} TIU, and for the latter we estimate a mean thermal inertia of 540^{+128}_{-122} TIU (TIU is thermal inertia units, i.e. J m^{-2} s$^{-0.5}$ K^{-1}). Thermal inertia and 3σ uncertainties were estimated by computing the mean, maximum and minimum values of pixels within the "BEDROCK" and "SLOPE" ROIs defined in the thermal inertia map and depicted in Fig. (3.5d). These estimates are used, along with a DTM of the region, to simulate the mean, maximum and minimum diurnal temperature profiles at the surface and at 10 and 20 cm depth, as in (Chevrier and Rivera-Valentin, 2012). Although the thermal model has already been validated by Schorghofer et al. (2019) at Palikir crater, we also checked that the simulated temperatures of our zones agreed with the nighttime THEMIS IR observation I59655010, acquired at a $L_s = 348.8°$, close to the CaSSIS image L_s. THEMIS surface temperatures were obtained using the `https://www.thmproc.mars.asu.edu` website and are reported in Fig. (3.8).

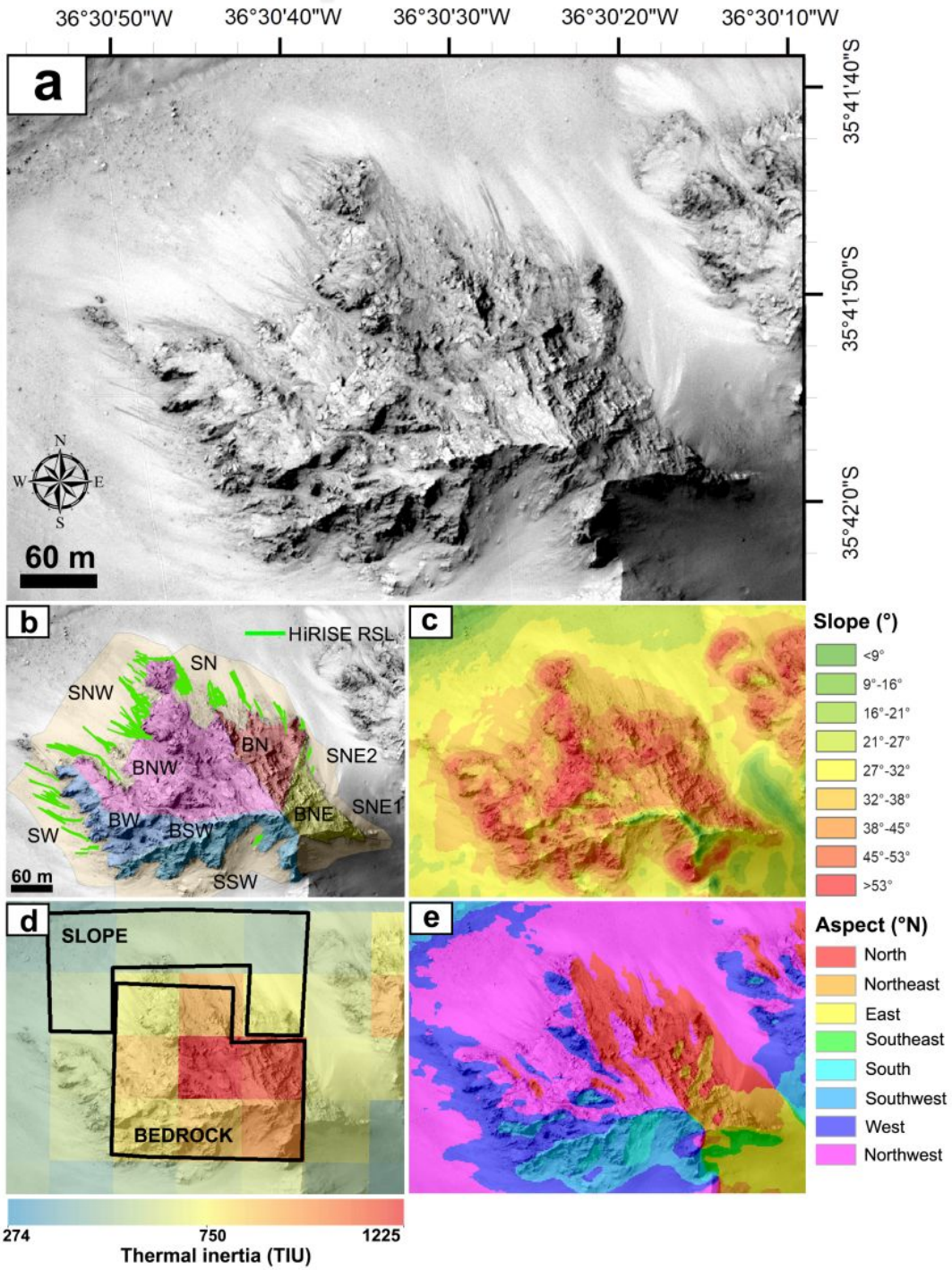

Figure 3.5: a) HiRISE image ESP_058618_1445 showing the selected region for the thermal analysis. b) Definition of zones where we simulated temperature profiles. c) Slope map. d) THEMIS-derived thermal inertia map. Black polygons represent the "BEDROCK" and "SLOPE" ROIs used to extract the thermal inertia of the bedrock material and the regolith, respectively. e) Aspect map.

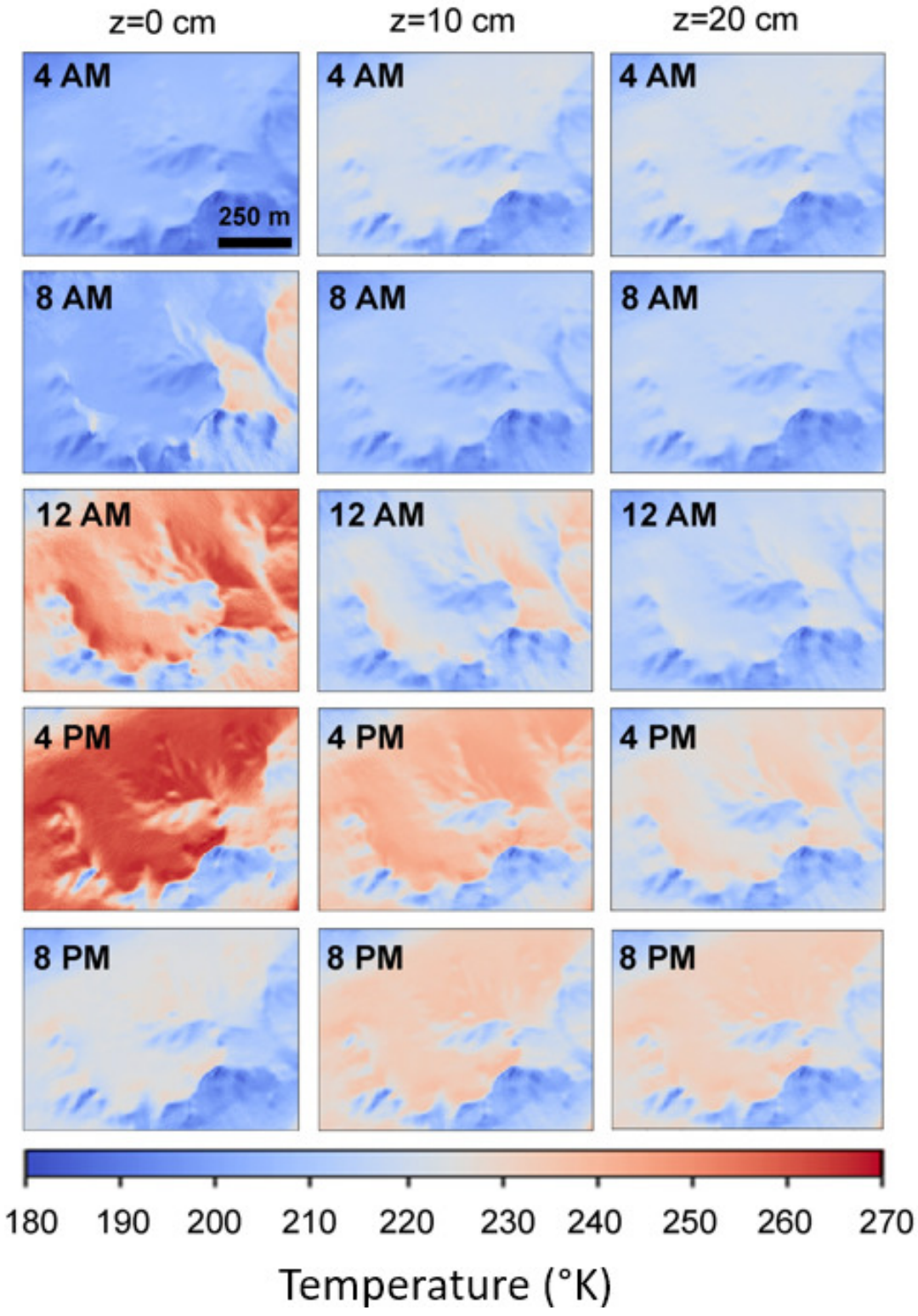

Figure 3.6: Example of diurnal temperature maps simulated at the surface (left), 10 cm depth (middle) and 20 cm depth (right). The simulations were performed using a THEMIS-derived thermal inertia of 770 TIU and used to extract diurnal temperature profiles for the bedrock.

3.3 Results

3.3.1 General properties

We identified 125 RSL, or groups of RSL in some cases, that were visible in both the HiRISE and CaSSIS images. Figures (3.7b,c and d) show examples of RSL as observed by CaSSIS. All the mapped RSL and their classification in terms of significant or absent lengthening between the morning and afternoon image are shown in Fig. (3.7a), while their slope and aspect distribution are in Fig. (3.7e,f) . In particular, the aspect distribution in Fig. (3.7f) shows that the considered RSL are found on north, north-west and west facing slopes and that there is no significant difference between the aspect of "static" and "changed" RSL. On the contrary, the slope distribution shows a dichotomy between the two classes. Most of the "static" RSL are found at slopes $< 30° - 32°$ while most of "changed" RSL are found at slopes $> 30° - 32°$.

3.3.2 Relative albedo analysis

We performed the relative albedo analysis on a selected sample of 11 RSL. The relatively low number of RSL considered for the relative albedo analysis is determined by the selection criteria discussed in section (3.2.2), i.e. we selected only RSL ROIs for which we could identify nearby BK ROIs having their same slope and aspect. In table (3.1) we report the CaSSIS (RA_C) and HiRISE (RA_H) RSL relative albedos, their difference and their 1σ uncertainties. We obtain average relative albedos of $\bar{R}A_H = 0.792 \pm 0.032$ for HiRISE and $\bar{R}A_C = 0.790 \pm 0.029$ for CaSSIS. These are broadly consistent with the relative albedo values measured by Schaefer et al. (2019) between $L_s = 330°$ and $L_s = 343°$ at Tivat crater, prior to the fading of RSL, confirming that any possible seasonal pattern is not influencing our measurements. The RSL relative albedo values reported for each ROI in table (3.1) show that there are no significant differences between the HiRISE and CaSSIS observations. The uncertainty on the relative albedo differences in table (3.1) is given by the sum of the uncertainties on RA_C and RA_H and gives us an idea of the minimum albedo difference detectable by our methodology. We obtain a mean absolute uncertainty on $RA_C - RA_H$ of 0.09, corresponding to an average relative uncertainty of 11%. The relative albedo differences reported in table (3.1) are fully consistent with stochastic variability in the two datasets. To demonstrate this, we checked whether the differences between the HiRISE and CaSSIS relative albedos follow a normal distribution, applying both an Anderson-Darling and a Shapiro-Wilk test of normality. We obtained $p-$values of $P_{AD} = 0.48$ and $P_{SW} = 0.50$. These are greater than the customary $\alpha = 0.05$ threshold, so we cannot reject the null hypothesis that the relative albedo differences come from a normal distribution, i.e that they are stochastic. To further cross-check our results, we also applied a Kolmogorov-Smirnov and a Wilcoxon signed-rank test and assessed the hypothesis that the HiRISE and CaSSIS relative albedos are drawn from the same distribution. Both tests failed to reject the null hypothesis, resulting in $p-$values of $P_{KS} = 0.99$ and $P_W = 0.90$ both greater than the $\alpha = 0.05$ threshold, confirming that the detected differences between the HiRISE and CaSSIS relative albedos are stochastic.

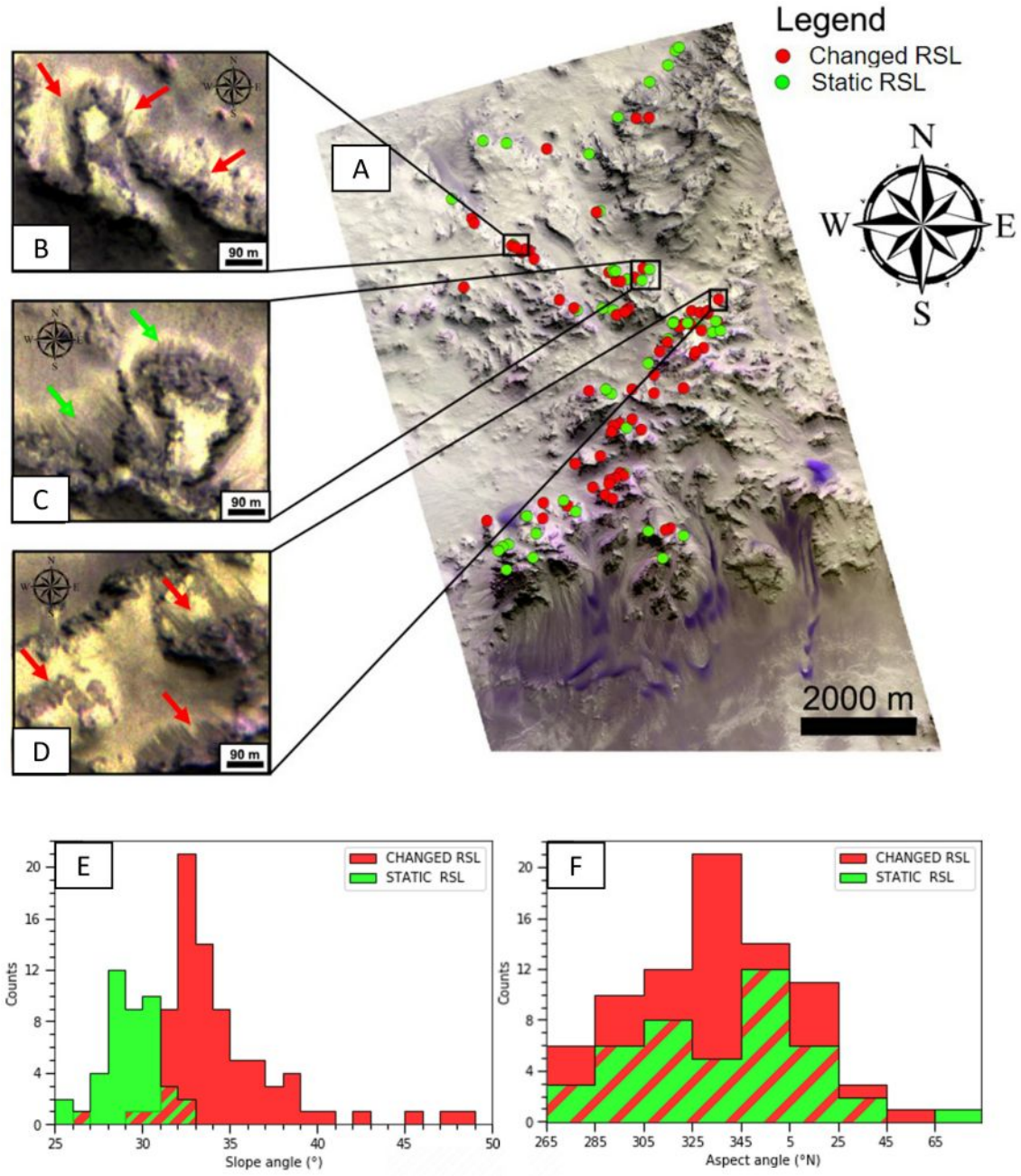

Figure 3.7: A) RGB color composite of the RED, PAN and BLU filters of CaSSIS image MY34_005640_218_2 depicting the central peak of Hale crater. Red dots indicate "changed" RSL. Green dots indicate "static" RSL. B), C) and D): examples of identified RSL, indicated by arrows. Distributions of E) slope and F) aspect of the termination points for "static" (green) and "changed" (red) RSL. The red-green striped part highlights where the two distributions overlap.

ROI	RA_C	RA_H	$RA_C - RA_H$
1	0.76 ± 0.03	0.79 ± 0.06	-0.03 ± 0.09
2	0.73 ± 0.03	0.76 ± 0.05	-0.03 ± 0.08
3	0.79 ± 0.02	0.77 ± 0.06	0.02 ± 0.09
4	0.80 ± 0.02	0.75 ± 0.05	0.05 ± 0.07
5	0.78 ± 0.03	0.75 ± 0.05	0.03 ± 0.08
6	0.83 ± 0.04	0.80 ± 0.06	0.03 ± 0.10
7	0.82 ± 0.03	0.85 ± 0.06	-0.02 ± 0.08
8	0.76 ± 0.02	0.81 ± 0.08	-0.05 ± 0.10
9	0.83 ± 0.04	0.79 ± 0.06	0.04 ± 0.10
10	0.79 ± 0.02	0.79 ± 0.06	0.00 ± 0.08
11	0.81 ± 0.03	0.82 ± 0.07	-0.01 ± 0.10

Table 3.1: Relative albedo analysis results. RA_C and RA_H are the relative albedos of RSL with respect to nearby RSL-free slopes measured on CaSSIS and HiRISE images, respectively. $RA_C - RA_H$ is the difference between the CaSSIS and HiRISE relative albedo. Errors are reported as 1σ uncertainties.

3.3.3 Thermal analysis

We simulated the thermal environment in a small region within Hale crater, shown in Fig. (3.5). Diurnal surface and subsurface temperature profiles and their uncertainties for each of the zones in Fig. (3.5) are shown in Fig. (3.8). In the same figures, we also show the eutectic temperatures of water ice, $CaCl_2$ brine (Gough et al., 2016) and Ca-perchlorate (Marion et al., 2010), as well as mean THEMIS surface temperatures for each ROI. From the temperature profiles in Fig. (3.8) we can see that both north-west, north and north-east regions transiently reach temperatures higher than the melting temperature of water ice only at the regolith surface, and not on bedrock or in the subsurface. In contrast, the transient melting of $CaCl_2$ or $Ca(ClO_4)_2$ frozen brines is generally supported in all these zones. In particular, from the temperature profiles in Fig. (3.8a) we see that north-east facing slopes allow the melting of $CaCl_2$ at 10 cm in the subsurface from $\sim$ 10:00 local time until $\sim$ midnight, and at 20 cm depth from $\sim$ 12:00 to $\sim$ 14:00. On north facing slopes (see Fig. 3.8b) melting could occur from $\sim$ 11:00 to $\sim$ midnight at 10 cm depth and from $\sim$ 13:00 to $\sim$15:00 at 20 cm depth. On north-west facing slopes (see Fig. 3.8c) melting happens from $\sim$ 12:00 until $\sim$ midnight at 10 cm depth and from $\sim$ 14:00 to $\sim$ 3:00 at 20 cm depth. West facing slopes (see Fig. 3.8d) allow melting of from $\sim$ 13:00 until $\sim$ 23:00 local time at 10 cm depth, and from $\sim$ 15:00 to $\sim$ midnight at 20 cm depth. Finally, south-west facing slopes permit melting of $CaCl_2$ mostly on the regolith and from $\sim$ 15:00 to 20:00 at 10 cm depth. At 20 cm depth, temperatures are mostly below the eutectic temperature of $CaCl_2$ brines (see Fig. (3.8e)). In all these cases, melting of $Ca(ClO_4)_2$ is allowed at any hour of the day at all depths, except for north-west, west and south-west facing slopes where early morning surface temperatures are very close to 200 K and can reach values as low as 190K, below the eutectic temperature of this brine.

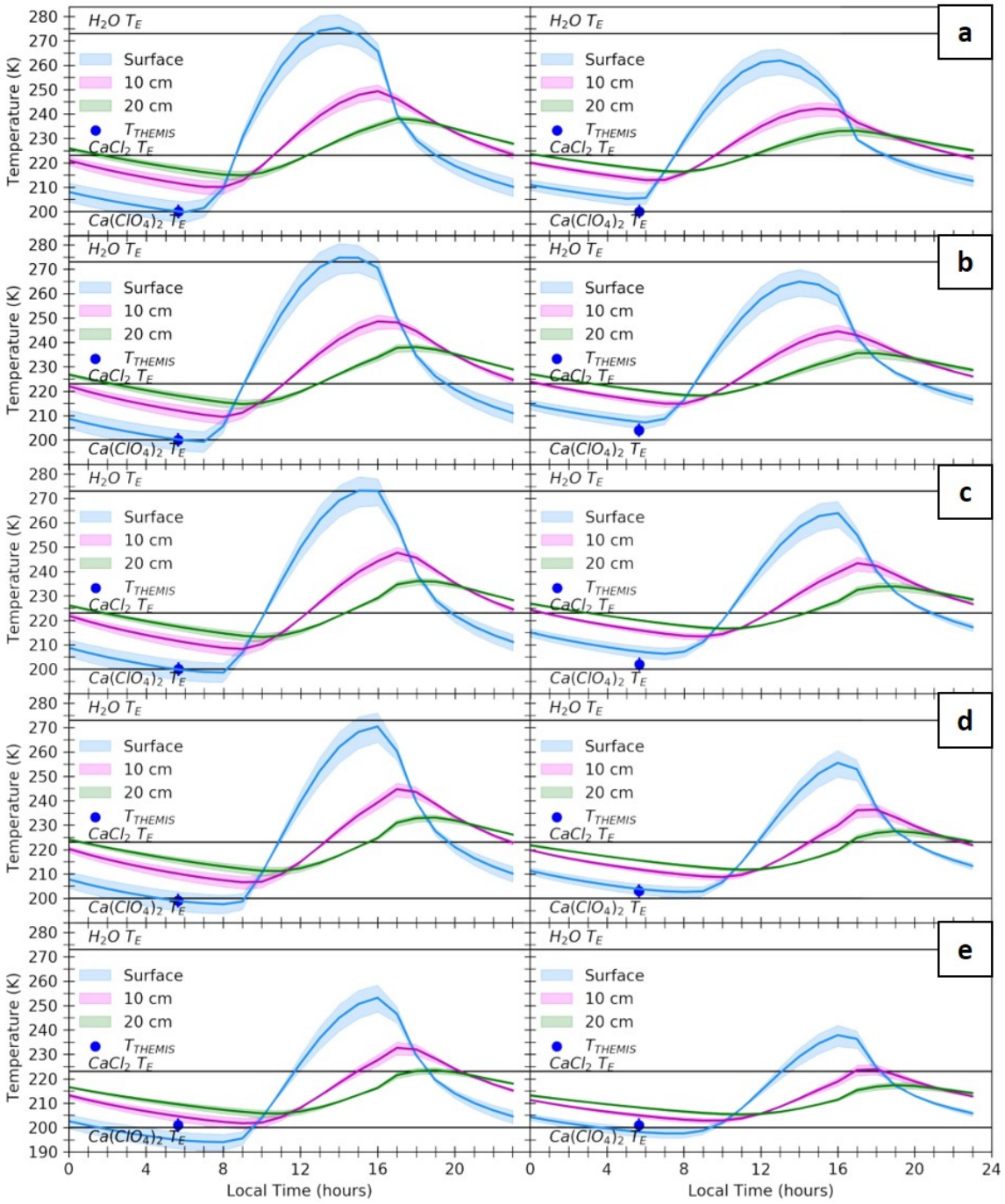

Figure 3.8: Diurnal temperature profiles (solid lines) with 3σ uncertainties (shaded areas) simulated at the surface (light blue), at 10 cm (magenta) and 20 cm depth (green) for ROIs a) SNE (left) and BNE (right), b) SN (left) and BN (right), c) SNW (left) and BNW (right), d) SW (left) and BW(right), e) SSW (left) and BSW (right). These ROIs are defined in Fig. (3.5). Blue dots are mean THEMIS surface temperature of each ROI with 3σ uncertainties of 2.8 K (Fergason et al., 2006).

3.4 Discussion

Since at Hale we observe RSL starting on bedrock outcrops (Fig. 3.9c), which generally have lower temperatures than the freezing point of water ice but higher than the considered brines, the latter are more likely than flows of seeping water. Moreover, exposed water ice is not predicted to form on equator-facing slopes at latitudes comparable to that of Hale crater (Schorghofer et al., 2019), and it is not observed by spectral instruments sensitive to micrometer-thick surfaces of water frost (Vincendon et al., 2010). Liquid brines may form via a) melting of a subsurface reservoir or b) deliquescence of salts. In the first case, either a reservoir near the surface or a subsurface deposit, which would be exposed by fractures, are necessary. The fractured rocky outcrops in the central peak of Hale crater might host these shallow brine reservoirs. In such a case, brine melting would occur when subsurface temperatures rise above their eutectic temperature, i.e. from mid-afternoon to evening hours, depending on its depth and slope orientation. This is because ice is more likely to be found in the shallow subsurface than at the surface at these latitudes. In particular, our thermal analysis suggests that melting of $CaCl_2$ brines should be favored on north-east, followed by north, north-west, west and south-west facing slopes. Melting of $Ca(ClO_4)_2$ is generally possible on all slopes, as it can occur over most of a Martian day. However north-east, north and north-west facing slopes are favored since their subsurface temperature is always higher than 200K at $L_s = 347.4°$. This picture also suggests that if RSL are formed through melting of shallow subsurface brines, they should form preferentially from noon and early-afternoon to evening hours, depending on ice depth, slope orientation and salt composition.

In the case of deliquescence, the main parameters constraining RSL activity are surface temperature and relative humidity. As shown in Fig. (3.8) surface temperatures are above the eutectic temperature of $CaCl_2$ from $\sim$ 8:00 to $\sim$ 19:00-20:00 Mars local time, depending on the slope orientation and thermal inertia. However, the RH may not be high enough during these hours. In particular, (Steele et al., 2017) and (Fischer et al., 2019) show that from $\sim$ 8:00 to $\sim$ 19:00-20:00, RH values are below 5% both at Gale crater and at the Phoenix landing site during local summer. This makes perchlorates more interesting candidates, because surface temperatures are above their eutectic temperature at any time of day, except for north-west, west and south-west facing and slopes during early morning. If RSL are deliquescence-related features, we should see a similar aspect preference as that expected for the melting of brines, but more shifted towards north-east facing slopes. In fact, these slopes reach higher surface temperatures at earlier local times, at a time when air relative humidity is higher (Fischer et al., 2019; Gough et al., 2016; Steele et al., 2017), which enhances deliquescence. The aspect distribution in Fig. (3.7e) suggests quite a different picture, showing a preference for north, north-west and west facing slopes over north-east facing slopes. An example of this behavior is also illustrated in Fig. (3.9) where RSL sourcing from north-east facing slopes are fewer in number and less extensive than on north, north-west and even west facing slopes. This aspect distribution may be an indication that RSL lengthening is not associated with surface moisture, deliquescence of salts nor melting of brines. Another option may instead be that deliquescence occurs during sunset instead of early morning when temperatures fall and relative humidity rises, as suggested by (Tebolt et al., 2020). In this

case, west-facing, north-west and north facing slopes may be favoured as they have slightly higher evening surface temperatures, possibly explaining the aspect distribution at Hale crater. While this is in principle consistent with our aspect distribution, it is not supported by either laboratory experiments (Gough et al., 2016), REMS (Steele et al., 2017) or TECP data (Fischer et al., 2019), which suggest, instead, that early morning hours should be more favourable for deliquescence than evening hours.Moreover, it may not be in agreement with the very low water content of RSL estimated from nighttime IR observations (Edwards and Piqueux, 2016). Detailed, high-resolution modeling may be necessary to further explore the precise interplay between temperature and relative humidity at RSL locations and quantify the best periods for deliquescence. An indication that RSL at Hale crater may be dry flows is that their lengthening stops at slope angles $\sim 30°$ (Dundas et al., 2017). We also detect this behavior in our slope distribution in Fig. (3.7e) and in Fig. (3.9), which show that RSL lengthening is generally correlated with the presence of slopes steeper than $\sim 30° - 32°$. On the contrary, RSL that already reached slopes within this range or shallower remained static. This dichotomy is shown in Fig. (3.7e), where there is a significant difference between the "changed" and "static" slope distributions. This dichotomy is expected for dry flows that stop when they reach the angle of repose, producing the observed sample of "static" RSL, and lengthen on steeper slopes, producing the observed sample of "changed" RSL. In one case, we also detect a RSL that lengthened at a slope angle of $\sim 26°$. A similar behaviour has also been detected by Stillman et al. (2020) and Tebolt et al. (2020). Although, in principle, this would support wet-based flows, the fact that they occur with a very low frequency suggests that these RSL could be statistical outliers (Stillman et al., 2020). As such, it is possible that additional and/or different mechanisms may be at play in this sample of RSL. Dedicated analyses considering statistically significant occurrences of these RSL and consideration of uncertainties in the DTM used for computing the slope values may be necessary to reach a definitive conclusion.

Our comparison of HiRISE and CaSSIS RSL relative albedo indicates that there are no significant diurnal variations between 11:13 and 14:06 local time, a result expected for dry flows. However, it may be also possible that significant dehydration has already occurred at 11:13, producing the observed result independently from how RSL form, or that the relative albedo differences at play are lower than 11%. If RSL are formed through deliquescence, the importance of this issue depends on salt composition and its interaction with the regolith, as these both affect the DRH and ERH (efflorescence relative humidity) of the solution (Nuding et al., 2014). In particular, Nuding et al. (2014) showed that liquid $Ca(ClO_4)_2$ brines persist with very low RH values. Therefore, if liquid brines form on early morning they may persist until late morning in a metastable state and dehydrate during the afternoon. Again, detailed near-surface relative humidity modeling should be performed to determine whether these processes are occurring at RSL sites. Another interpretation of our relative albedo measurement, which is not supported by thermal studies (Edwards and Piqueux, 2016), is that the water supply exceeds evaporative losses. In this case dehydration does not occur and there is no significant albedo variation (Hillel, 2004). Future observations acquired during early morning will help to better characterize the diurnal albedo of RSL. Nevertheless, the relative albedo measurements reported here could provide a useful validation for modeling and experimental studies of RSL.

In summary, our result collectively support dry flows as responsible for RSL lengthening. The triggering mechanisms which initiate these flows may involve thermal creep (Schaefer et al., 2019; Schmidt et al., 2017), or aeolian processes (Vincendon et al., 2019). In particular, the latter would also be able to describe the temporal evolution of RSL activity during the third pulse shown in Fig. (3.1) (Vincendon et al., 2019). While our results support dry flows models, brines and more generally volatiles may still play and indirect and concurrent role in RSL formation by triggering dry mass fluxes (Bishop et al., 2019; Massé et al., 2016; Wang et al., 2019), but our data does not provide any additional insight on RSL triggering.

3.5 Summary and Conclusions

We presented the first CaSSIS observation of RSL obtained during local morning at Hale crater, Mars. We identified a set of 125 RSL and studied their overall morphology, slope and aspect distributions and analyzed their thermal environment. We performed an initial comparison of their relative albedo using morning CaSSIS and afternoon HiRISE observations. Our comparison of RSL, as viewed through HiRISE and CaSSIS, 30 days later, reveals that most RSL lengthening occurred where slopes $> 30° - 32°$ were available. Instead, RSL on slopes $< 30° - 32°$ remained generally static. This result supports a dry granular flow origin, as suggested by other authors (Dundas et al., 2017; McEwen et al., 2019; Schaefer et al., 2019; Vincendon et al., 2019). The simulated diurnal surface and subsurface temperature profiles at Hale crater suggest that melting of brines and deliquescence of salts would be both favoured on north-east facing slopes, followed by north and north-west facing slopes. However, this pattern is different from our observed aspect distribution of "changed" RSL at Hale crater, suggesting that RSL lengthening is not controlled by surface moisture, deliquescence of salts or melting of brines. We compared HiRISE and CaSSIS RSL relative albedo between 11:13 and 14:06 local time, respectively, and found no significant differences, another result expected for dry flows. Our measurements could provide a useful validation for future models and experimental studies on RSL formation and lengthening. We conclude that the RSL at Hale crater are best explained as dry flows, in agreement with the conclusions of other authors (Dundas et al., 2017; McEwen et al., 2019; Schaefer et al., 2019; Vincendon et al., 2019). These may be triggered through thermal creep (Schaefer et al., 2019; Schmidt et al., 2017), aeolian processes (Vincendon et al., 2019), or very limited brine activity (Bishop et al., 2019; Massé et al., 2016; Wang et al., 2019). Future CaSSIS observations of RSL sites acquired earlier in the morning, in combination with same-day afternoon HiRISE images, will be pivotal in improving the characterization of the diurnal activity of RSL and will provide a clearer picture of their formation mechanism.

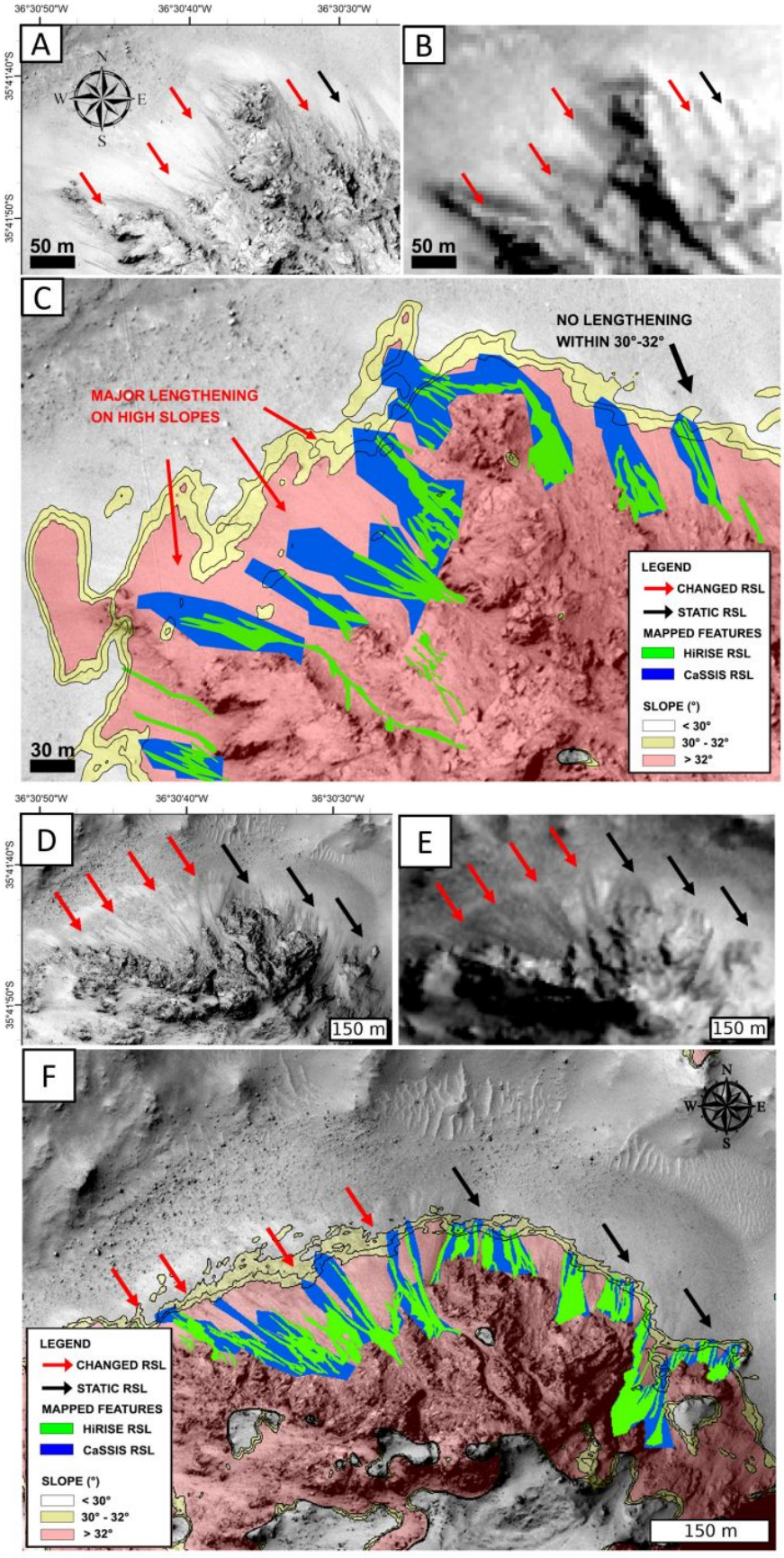

Figure 3.9: A,D) HiRISE "static" (black arrows) and "changed" RSL (red arrows) over two location on the central peak of Hale crater. B,E) CaSSIS image showing the same RSL as in panels A,D), respectively. C,F) Mapping of HiRISE (green) and CaSSIS (blue) RSL overlain on a discretized slope map. Red indicates slope $> 32°$, yellow is for slopes between 30° and 32°.

Chapter 4

Multi-band CaSSIS photometry of RSL at Horowitz crater

In this chapter we present a complementary analysis to the one in Chapter (3). In addition to the diurnal variability of RSL, because of the small scale of RSL, the small colour swath HiRISE and the lower resolution of the CRISM spectrometer, the spectrophotometric properties of RSL are not significantly constrained yet. For this reason and to improve our knowledge about RSL origins and formation mechanisms, we began to investigate their color properties through multiband photometry obtained from 4-filter Colour and Surface Science Imaging System (CaSSIS, Thomas et al. (2017)) observations at Horowitz crater (140.8° E, -32.0° N, Fig. 4.1,4.2). We adopt both a comparative and a modelling approach. In particular, we extend the analysis of Chapter (3) to all the CaSSIS filter to perform multiband photometry and compare the spectral properties of RSL with dust-devil tracks (DDTs, c.f. Section 1.4.3, i.e. dark marks left by the passage of Martian whirlwinds) and regions where there is evidence of a localized depletion of surface dust that we call "dust-poor" areas (DP, Fig. 4.1 and Section 4.1). Since DDTs and DPs are well-established as being formed by the removal or disturbance of brighter ferric dust and the exposure of underlying, typically darker, ferrous material, the comparative multiband photometry provided by CaSSIS may help us understanding whether the RSL observed in this location are consistent with being formed by the removal of dust, as suggested by recent papers (Dundas, 2020; McEwen et al., 2021; Schaefer et al., 2019; Vincendon et al., 2019).
To quantitatively support our comparative photometry, we also compare our results with laboratory spectral measurements of dust deposition on Martian terrain analogs (Wells et al., 1984) and wet and dry Martian soil photometric models (Gunderson et al., 2007). The structure of this Chapter is the following: first we describe our dataset, the study site and the relevant terminology (Section 4.1). Next we present the methods (Section 4.2) applied to derive multiband relative photometry of RSL and DDTs (4.2.1). We report the convolution and modeling of dust-fallout laboratory spectra in the CaSSIS photometric system in Section (4.2.2) along with the description of the photometric models of dry and wet Martian soil analogs that have been considered in Section (4.2.3). We present the comparative photometry of RSL and DDTs in Section (4.3.1), comparing it with both dust-fallout models (Section 4.3.2) and soil-wetting models (Section 4.3.3). Finally we discuss our results in Section (4.4) and draw our conclusions in Section (4.5).

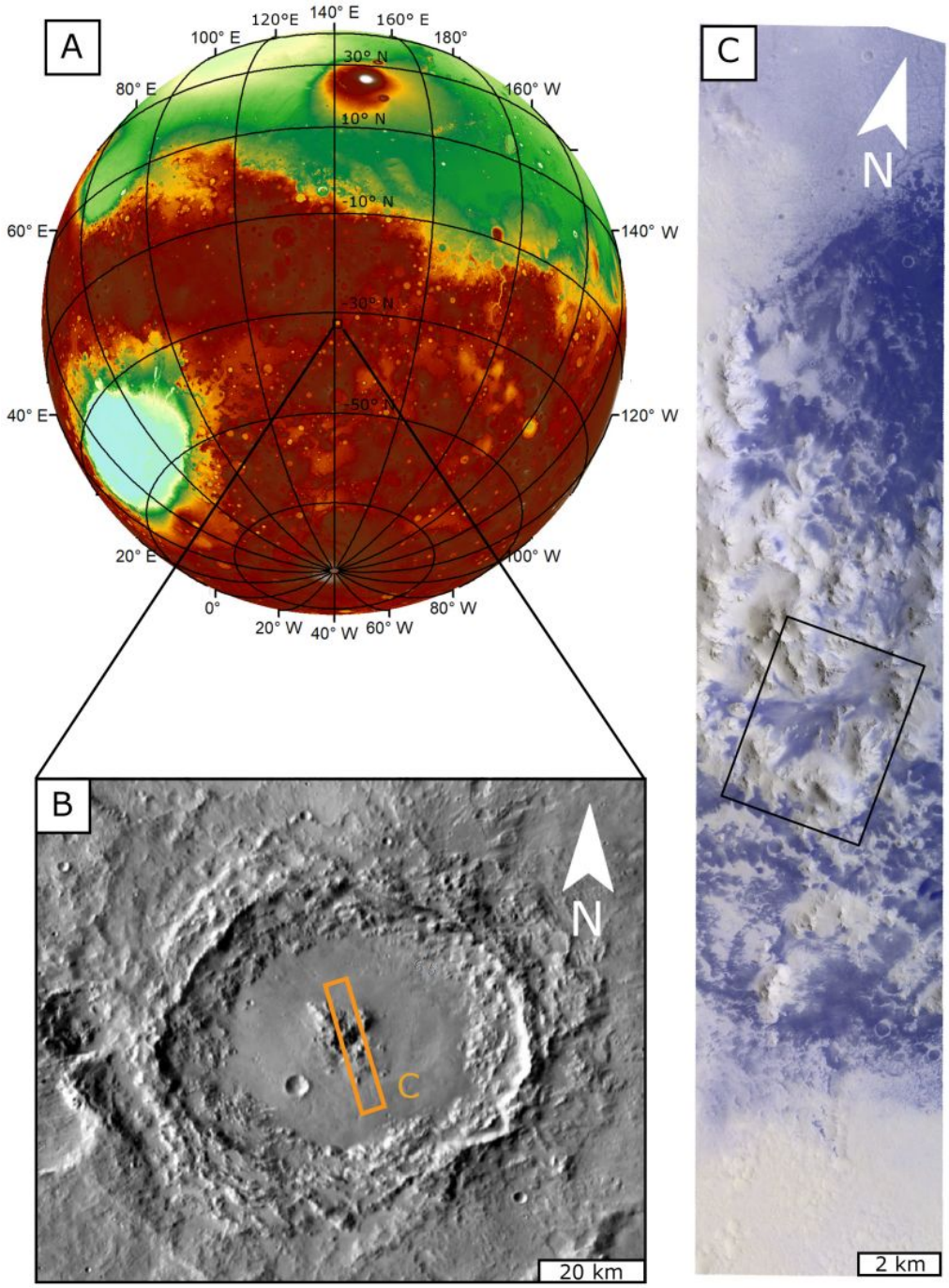

Figure 4.1: A) Mars Orbiter Laser Altimter (MOLA) colorized elevation map in orthographic projection showing the position of Horowitz crater. B) Thermal Emission Imaging Spectrometer (THEMIS) infrared daytime global mosaic showing Horowitz crater and the footprint of the CaSSIS image (orange polygon). C) CaSSIS NIR-PAN-BLU (NPB) color composite of MY34_005696_214_0 showing the central uplift of Horowitz crater. The black rectangle shows the location of Fig. (4.2)

4.1 Dataset and terminology

Our study site is the central uplift of Horowitz crater (140.8° E, -32.0° N, Fig. 4.1), Mars. This location was selected because it shows RSL large enough to be resolved at the CaSSIS resolution (i.e. 4.6 m/px) and displays DDTs, the presence of which is pivotal for our comparative photometry. In addition, based on previous studies of Horowitz RSL (McEwen et al., 2011) we expect them to be actively growing at Ls=321.8°. We analyse the CaSSIS image MY34_005696_214_0, which was acquired during the local morning (10 AM LTST) and southern summer (Ls=321.8°) with all the four color filters (NIR, RED, PAN, BLU). A NIR, PAN and BLU (hereafter NPB) color composite of the image is shown in Fig. (4.1C) and (4.2). To facilitate our spectral analysis of the scene, we used a dark subtraction-corrected Colour Band Ratio Composite (CBRC) product, as originally defined by (Tornabene et al., 2018). CBRCs are R-G-B composites that combine band ratios that have been devised to highlight ferric- and ferrous-iron bearing materials (i.e., in this case, dusty and dust-poor surfaces). In particular, we used the CBRC-ALL product (formerly referred to as the CBRC1 product in (Tornabene et al., 2018)). This composite combines ratios using all four CaSSIS bands as follows in R-G-B: RED/PAN, PAN/BLU and PAN/NIR. This combination effectively highlights the presence of dust-rich areas in yellows and dust-poor surfaces in blues (Fig. 4.3). The combined analysis of the CaSSIS NPB (Fig. 4.2A) and the CBRC-ALL products (Fig. 4.3) facilitates an assessment of the relative dust contents of the surface materials in the scene. In particular, we use these images to identify and define three types of regions, i.e. “dust-rich”, “dust-poor” and “dust-enriched” surfaces. The rationale of this identification is just to provide a broad, first order classification of different terrains, characterised by different amounts deposited dusts, in the surroundings of our study area (Fig. 4.2A) to better support the subsequent spectral analysis. A yellow CBRC color is consistent with ferric dust, which has relatively high PAN/BLU and RED/PAN ratios, due to the presence of the “red edge” caused by a strong ferric absorption near 550 nm (Tornabene et al., 2018). Dust-rich (“DR” in Fig. 4.2A and Fig. 3) regions display strong beige and yellowish hues in the NBP and CBRC-ALL products, respectively, meaning that a relatively large amount of dust is present. Relatively dust-poor (“DP”, white-dashed polygons in Fig. 4.2A and Fig. 4.3) regions are consistent with basaltic ferrous-bearing materials, which are relatively lower in PAN/BLU and RED/PAN ratios with a relatively strong absorption in the CaSSIS NIR band, and thereby a relatively high PAN/NIR ratio; as such, these deposits are characterised by bluish hues in both the NPB and CBRC-ALL products with the strongest blue colored surfaces representing the most dust-poor ferrous-bearing surfaces in the scene. Departures from blue tones towards purplish hues indicate a mixture with relatively thin sheets of dust. Materials with moderately beige and yellowish colors and with a slight purplish hue in the CBRC-ALL product are labelled as “dust-enriched” (c.f., “DE” in Fig. 4.2A and Fig. 4.3), and represent an intermediate case between DP and DR regions. In particular, the surface immediately outside DDTs is an example of “dust-enriched” surface. We recall that these definitions and the examples outlined in Fig. (4.3) are meant to provide only a broad classification and do not represent an extensive and complete mapping of these surface units. DDTs have a well-established photometric signature that is due to dust removal and subsequent exposure of an underlying basaltic ferrous-bearing

surface material (Mushkin et al., 2010). While RSL show qualitatively similar color attributes to DDTs in the CaSSIS NPB products, it remains to be seen if they can be explained as dust-removed features. In this context, DDTs and DPs are used here as independent cross-checks for assessing the robustness of our analysis and interpretation of the RSL color and spectral signatures.

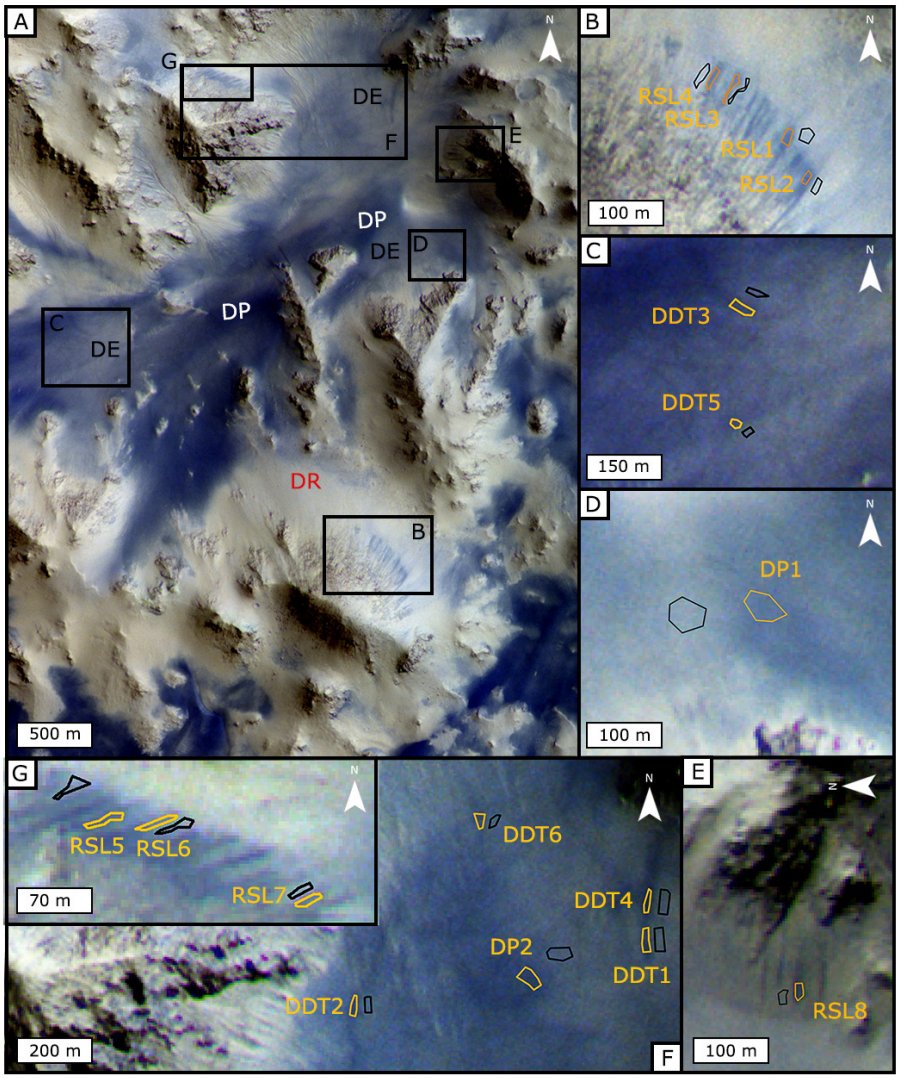

Figure 4.2: Crop of CaSSIS NPB color composite of image MY34_005696_214_0 showing a portion of the central uplift of Horowitz crater. The full image with the extent of panel A is shown in Fig. (4.1). "DR" indicate examples of "dust rich" areas. "DP" labels provide examples of regions where some surface dust has been removed. "DE" labels provide examples of regions where there is an intermediate deposit of dust between "DR" and "DP" regions. See text for more details about the definitions of these regions. Panels B) to E), indicated by black boxes in panel A), show the RSL, dust-devil tracks (DDT) and dust-poor (DP) ROIs considered in this analysis (orange polygons). Nearby black ROIs are used as background areas for the relative albedo analysis in Section (4.2.1)

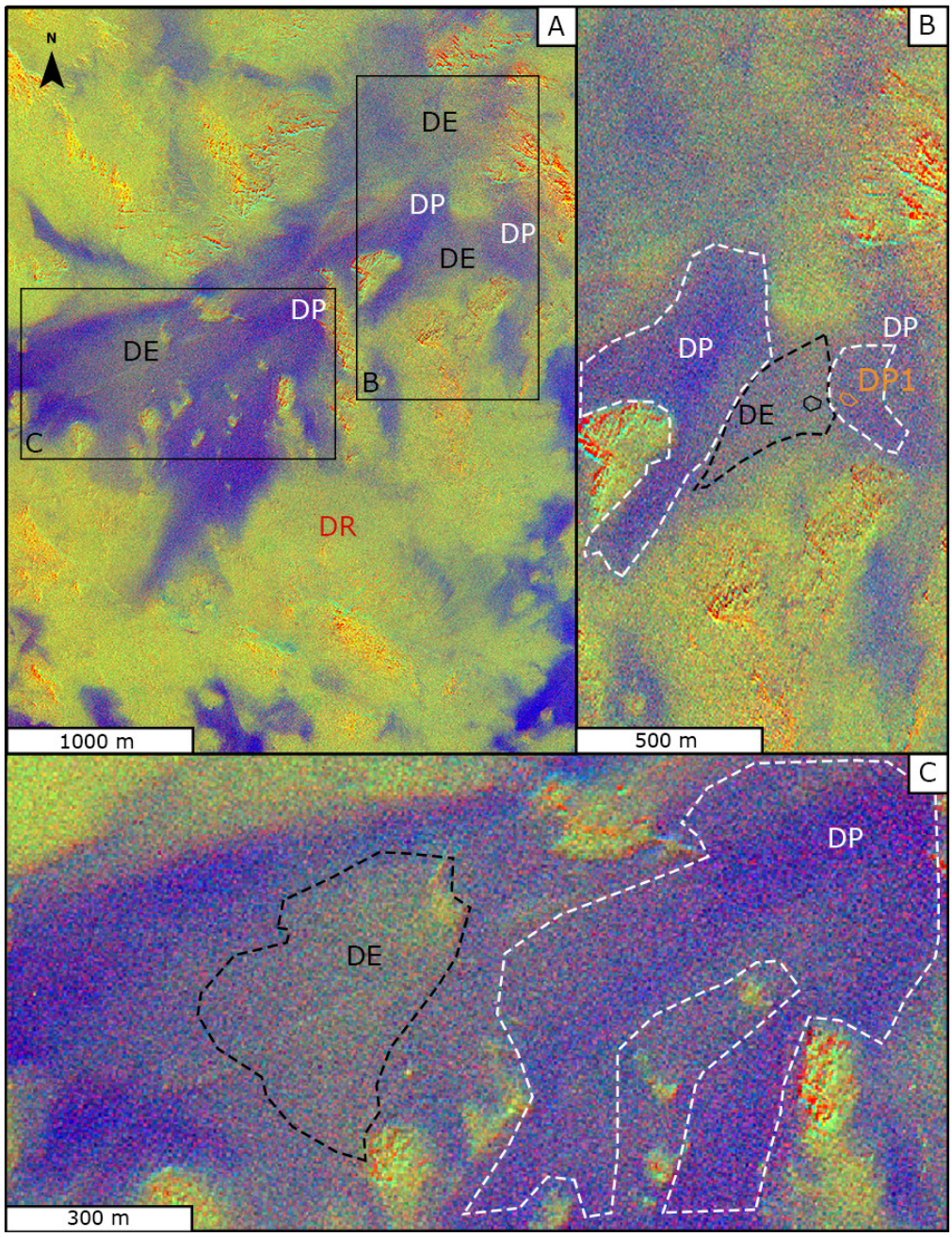

Figure 4.3: A) CaSSIS CBRC1 product of the study area in Fig. 4.2A. B) and C) provide examples of "dust-enriched" (DE) and "dust poor" (DP) areas discussed in the text. The orange polygon in B) is the DP1 ROI and the black polygon nearby is its corresponding BK ROIs used for the relative albedo analysis (see Section 4.2.1).

4.2 Methodology

In this section we present the methodology that we applied. In particular, in Section (4.2.1) we describe the relative photometry approach, which is derived from the analysis in Chapter (3). Further developments of such methodology are presented in Section (4.2.2), which describes the laboratory spectral dataset that we used, modeled and converted them into the CaSSIS photometric system with the aim of simulating the relative albedo that would be detected when observing two Martian soils with a different amount of deposited dust from one another. Finally, Section (4.2.3) describes which models of wet and dry Martian soil we adopted and how we simulated the relative albedo of a wet Martian soil with respect to a dry one.

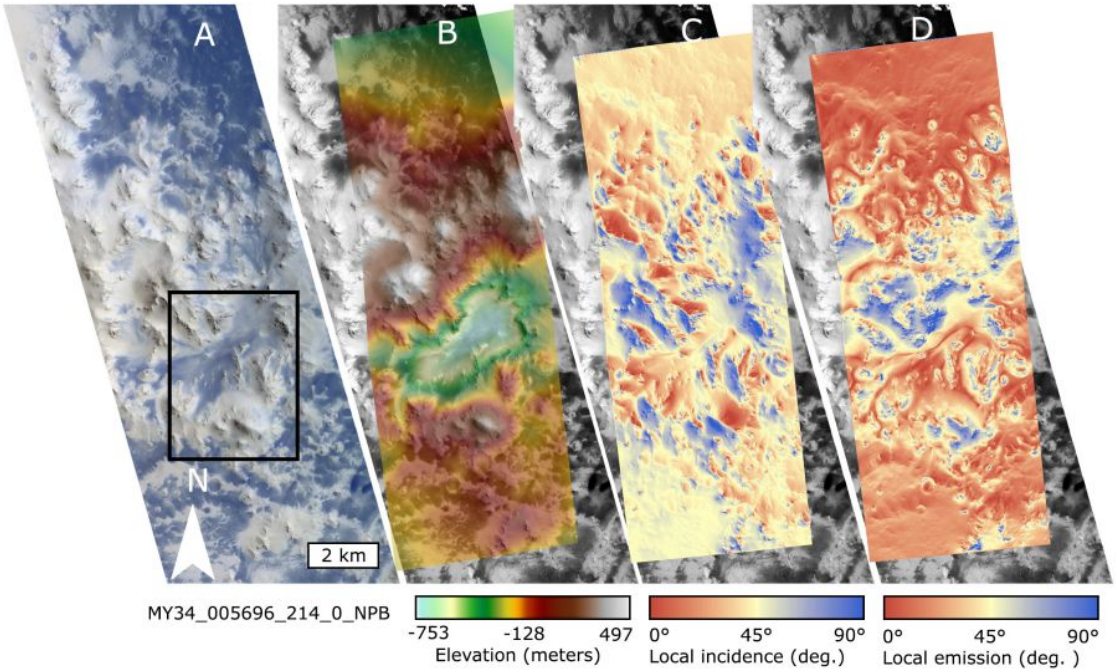

Figure 4.4: A) CaSSIS NPB colour composite of image MY34_005696_214_0 showing the central peak of Horowitz crater. B) HiRISE DTM of the site. C) local incidence map and D) local emission map derived from the DTM. The background of panels B, C and D is the PAN band of image MY34_005696_214_0

4.2.1 Relative photometry of RSL and dust-removed features at Horowitz crater

The relative albedo is defined as the ratio between the atmospherically corrected surface reflectance (I/F) of two regions of the surface that have the same illumination and observation conditions, i.e. the same local incidence and emission angles (Daubar et al., 2016). To avoid too many repetitions of the term "relative albedo", we will also refer to it as "relative reflectance". The computation of the relative albedo is a well-established (Daubar et al., 2016; Munaretto et al., 2020, 2021a,b; Schaefer et al., 2019) technique for photometric studies of Martian surface features. We follow the approach presented in Munaretto et al. (2021b) and use the publicly

available HiRISE DTM DTEEC_021689_1475_020832_1475_A01 at 1 m/px resolution to compute the local incidence (Fig. 4.4C) and emission (Fig. 4.4D) angles of the surface at the time of the CaSSIS observation. We use the local incidence and emission angle maps and the CBRC-ALL product to select regions of interest (ROIs) located within the RSLs (RSL1 to RSL8, orange polygons in Fig. 4.2B, G, E), DDTs (DDT1 to DDT6, orange polygons in Fig. 4.2C, F) and DP (DP1 and DP2, orange polygons in Fig. 4.2D, F) materials and in corresponding nearby materials (BKRSL, BKDDT, BKDP, black polygons in Fig. 4.2B to F). The main criteria driving the definition of RSL, DDTs and DP ROIs was ensuring the same average local incidence and emission angles as the corresponding BK ROIs. Where this constrain could be satisfied, the CRBC-ALL product was then used to slightly optimize each ROI position and shape. In particular, where possible, we maximized the presence of bluish materials within each RSL, DDT and DP ROIs and beige-yellowish materials for the corresponding BK ones. For each CaSSIS filter, as is customary for Martian relative photometry studies (Daubar et al., 2016; Munaretto et al., 2020, 2021b; Schaefer et al., 2019) we compute the relative albedo using equation 3.1.

4.2.2 Convolution and modeling of laboratory dust-fallout spectra in the CaSSIS filters

The spectral signature of dust-deposition on terrains that are photometrically similar to bright and dark Martian soils has been studied in detail through laboratory experiments by Wells et al. (1984). We here focus on the spectral measurements of dust-fallout on a substrate of 150 to 250 μm size particles of Mauna Kea volcanic soils, which has a similar spectrum to Martian dark areas i.e., where RSL are located, reported in Fig. 3 of Wells et al. (1984). They measured the relative reflectance of the substrate after depositing varying amounts of dust as well as the relative reflectance of an optically thick layer of dust, from 400 to 1200 nm. The resulting reflectance spectra and the associated dust deposit are shown in Fig. (4.5). Since the dust deposit for "Deposit 6" was not reported in Wells et al. (1984), the reported value is an estimate based on the following approach. RSL, DDT and DP ROIs and nearby surfaces may however be characterised by a smaller relative difference of deposited dust than the measurements in the original dataset. For example, nearby slopes could be optically thick deposits and RSL could have more dust than the maximum, non-optically thick one investigated in Wells et al. (1984), i.e. $6.3 \cdot 10^{-4}$ g/cm^2 ("Deposit 5" in Fig. 4.5). For this reason, we decided to model at each wavelength the reflectance as a function of the dust deposit thickness and simulate the reflectance spectra on a much finer range of dust deposits. Wells et al. (1984) identified a model for the change in reflectance at 750 nm due to the deposition of dust given by the following formula:

$$r(m) = r_f - (r_f - r_i)\, e^{-Am} \tag{4.1}$$

Where $r(m)$ is the reflectance associated to a dust deposit thickness m (which has areal density units g/cm^2, but we keep the nomenclature of Wells et al. (1984) for consistency). r_f is the reflectance of an optically thick layer of dust, r_i is the reflectance of the substrate without dust and A is a parameter defined as a "mass absorption coefficient" (units cm^2/g). r_f and r_i are the "Deposit 6" and "Deposit 1" black profiles of Fig. (4.5). We decided to use this model and fit the value of A for

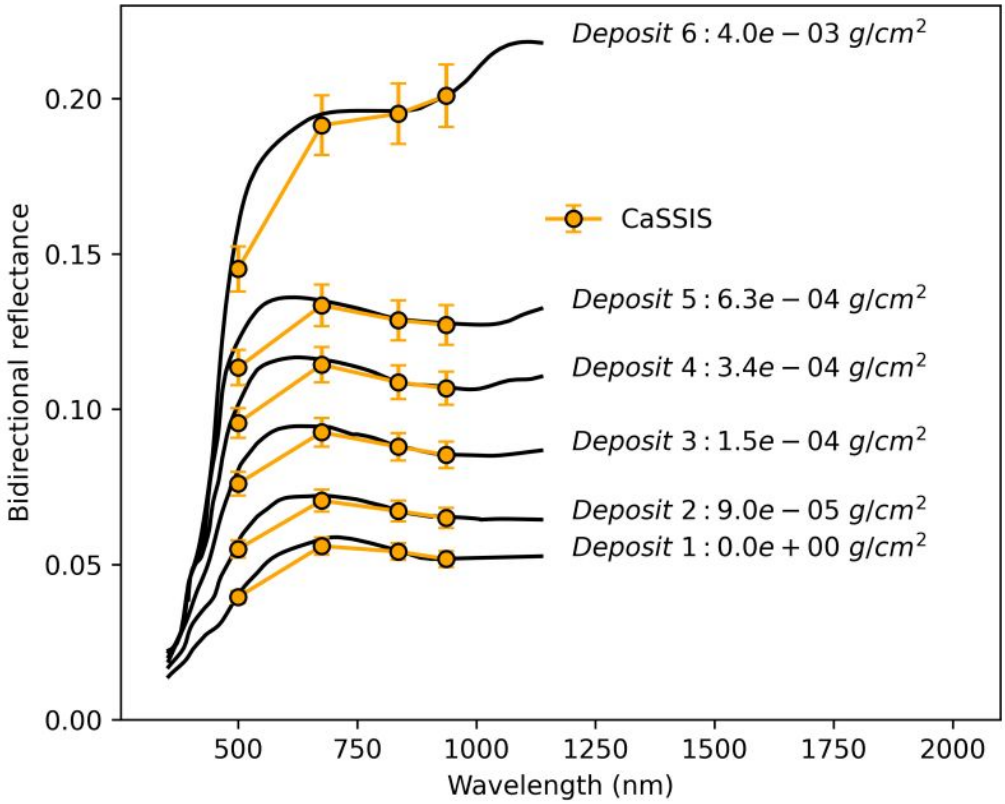

Figure 4.5: Black lines are digitized data from Wells et al. (1984) converted to bidirectional reflectance units. The labels next to each profile indicate the amount of deposited dust. Orange markers with associated error bars represent their convolution into the CaSSIS photometric system and conversion to bidirectional reflectance units. The amount of deposited dust for "Deposit 6" was estimated in this work and not reported in (Wells et al., 1984).

each wavelength. This strategy is illustrated in Fig. (4.6,4.7). By focusing on Fig. (4.6), at each wavelength we have 6 reflectance values. The first from the bottom of the figure is r_i, then we have the reflectance r associated with the first measurement of m and so on until we reach the optically thick deposit, r_f, which was not associated to a deposit thickness in the original data. If we collect these measurements, we can fit the relation between r and m in equation (4.1) and find a least square estimate of A. Our fits and the corresponding measurements are shown in Fig. (4.6) for an arbitrary sample of wavelengths. With the estimated value A, we identified the areal dust coverage of an optically thick deposit (units g/cm^2) by selecting the smallest value of m for which the reflectance did not change by more than 1%. This value is shown with a filled square in Fig. (4.6), as well as the modeled dust-fallout spectral reflectance, which we will hereafter call "dust models". An example of dust models for a wider and finer range of values than the original ones (shown in Fig. 4.5), is provided in Fig. (4.7). Through the dust models derived above, we simulate the signal that would be detected by CaSSIS when observing a material illuminated by

the Sun and presenting such modeled spectral reflectance. Further details on the convolution of spectra within the CaSSIS photometric system are given in Thomas et al. (2021). The signal (units DN/s where DN is Digital Number) that is generated through a given CaSSIS filter in a second can be expressed as:

$$F = \frac{A}{G \cdot hc} \int_{\Delta\lambda} r\left(i, e, \alpha\right) I_{\odot}\left(\lambda\right) \cos\left(i\right) R\left(\lambda\right) F\left(\lambda\right) QE\left(\lambda\right) \lambda d\lambda \tag{4.2}$$

Where A is the effective area of the primary mirror, $G = 7.2$ e/DN (Thomas et al., 2017) is the gain, i.e. number of electrons that corresponds to 1 DN, h is Planck's constant and c is the speed of light in vacuum. Since we will deal with relative quantities, these terms will cancel out and will not affect our results, but we report them for clarity. $I_{\odot}\left(\lambda\right)$ is the solar spectral irradiance reaching the surface of Mars and has been computed by scaling the solar spectral irradiance of (Thuillier et al., 2003) to the heliocentric distance of Mars during the observation. The $\cos\left(i\right)$ factor takes into account the incidence angle of the surface. $r\left(i, e, \alpha\right)$ is the reflectance of the surface, which in our case is computed from our dust models. $R\left(\lambda\right)$ is the mirror reflectivity function. $F\left(\lambda\right)$ is the filter response function and $QE\left(\lambda\right)$ is the quantum efficiency of the detector as a function of wavelength. These three functions are shown in Fig. 8 and further details are given in (Thomas et al., 2017). Pixel values in the radiometrically calibrated CaSSIS data products are in I/F units, defined as the ratio of the observed surface radiance, and the radiance of a 100% Lambertian reflector with the Sun and camera orthogonal to the observing surface. I/F values can be converted to bidirectional reflectance units dividing by π. The signal computed with (4.2) is converted from DN/s to I/F units by dividing it for the signal that we would be detected observing a 100% reflecting surface, which can be obtained applying (4.2) with $r\left(i, e, \alpha\right) = 1$. At this point we can simulate the signal detected by CaSSIS when observing a surface characterised by a given dust deposit m and illuminated by the Sun. This is, however, not yet directly comparable with our observations because it still depends on the lighting and observation geometry. We therefore consider the ratio IF_{ij} between the I/F of two surfaces characterised by dust deposits m_i and m_j. Inserting (4.1) in (4.2) we obtain:

$$IF_{ij} = \frac{\int_{\Delta\lambda} \left[r_f - \left(r_f - r_i\right) e^{-Am_i}\right] I_{\odot} R(\lambda) F(\lambda) QE(\lambda) d\lambda\lambda}{\int_{\Delta\lambda} \left[r_f - \left(r_f - r_j\right) e^{-Am_j}\right] I_{\odot} R(\lambda) F(\lambda) QE(\lambda) d\lambda\lambda} \tag{4.3}$$

Where r_f and r_i are already known and are the "Deposit 1" and "Deposit 6" profiles shown in Fig.(4.5). We now aim to find the values of m_j and m_i that best reproduce our relative photometry. Since equation (4.3) has a rather complex mathematical expression, we use a grid-search approach. We test all the combinations of m_j and m_i in a 100 by 100 evenly spaced grid. For each combination, we compute IF_{ij} in the four CaSSIS filters using (4.3) and compare it with our relative albedo measurements for each band. The pair of m_i and m_j giving the lowest sum of the squared residuals between IF_{ij} (Fig. 4.9 dashed lines) and the observed relative albedo (Fig. 4.9 solid lines and markers) is selected as the best fit solution.

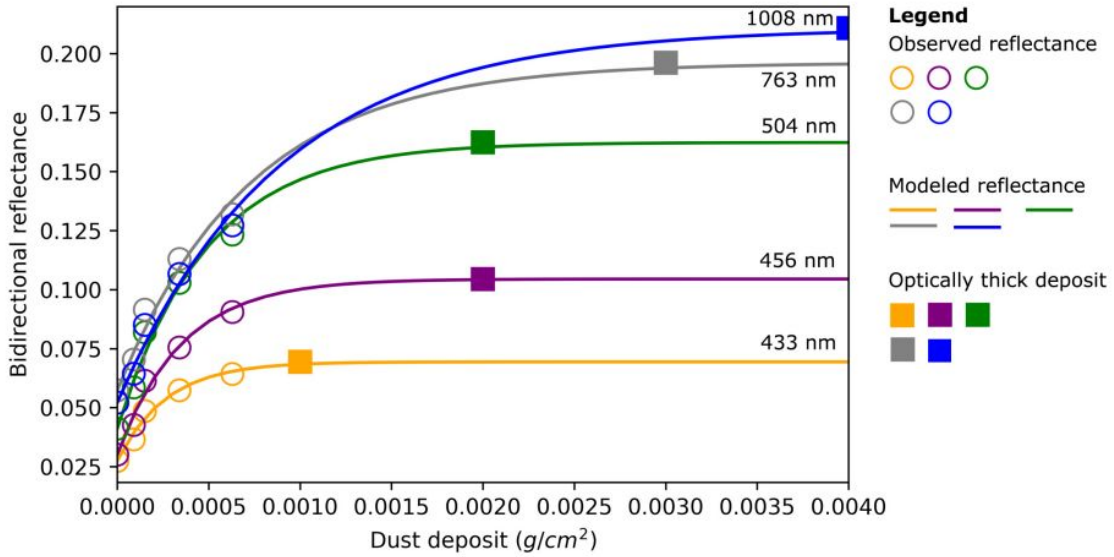

Figure 4.6: Figure 6. Observed reflectance vs dust deposit thickness (circles), fitted reflectance model (solid lines) and estimated optically thick deposit (filled squares) at various wavelengths.

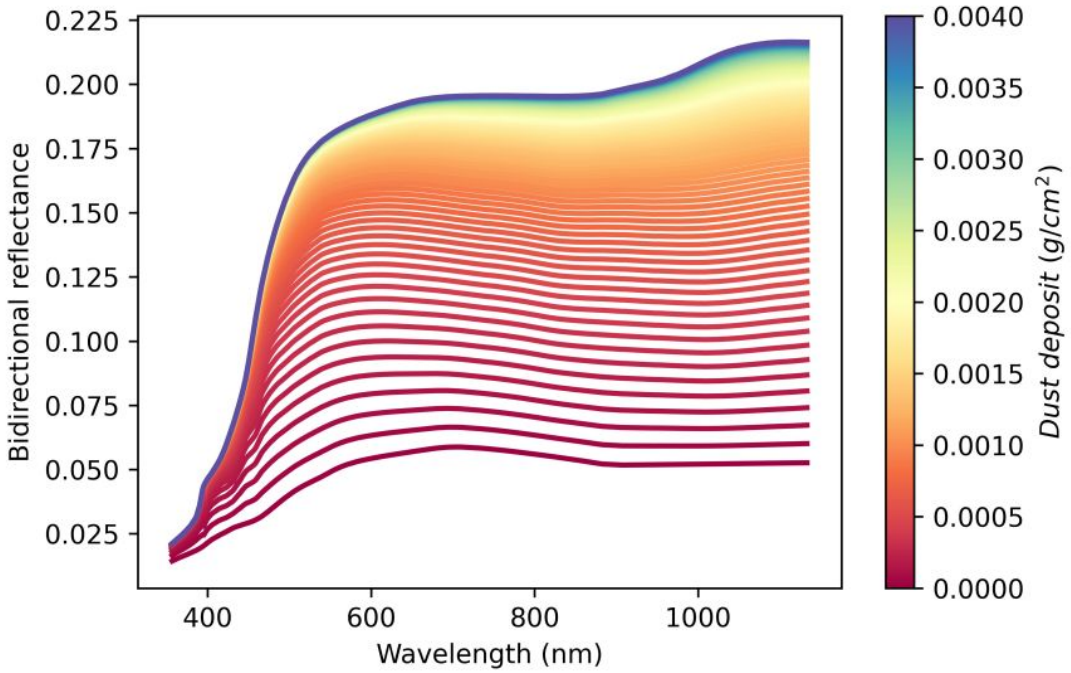

Figure 4.7: Modelled dust-fallout spectral reflectance ("dust models" in the text) as a function of the dust deposit thickness.

4.2.3 Photometric models of wet and dry Martian soil analogs

To assess if our measurements could be consistent with the relative reflectance of a wet vs dry Martian soil, we relied on the photometric modeling results published by Gunderson et al. (2007), that provide Hapke parameters (Hapke, 1993) for both dry and wet samples of the JSC-1 Martian regolith simulant in several filters, reported in Table (4.1). In particular, the B_{HR} and V_{HR} filters have a similar bandpass to the HiRISE BG and RED bands (Delamere et al., 2010), respectively, which are also similar to the CaSSIS BLU and PAN ones (Thomas et al., 2017). The Hapke parameters for these two filters can be therefore used to predict the relative albedo of a wet vs dry Martian regolith and compare it with our relative albedo measurements. For each filter in Table (4.1), we model the relative reflectance of a mixture composed by a variable percentage of wet (w) and dry soil ($1-w$), referred as "water model", as:

$$IF_w = \frac{w \cdot r_w + (1-w)\, r_d}{r_d} \tag{4.4}$$

Where r_w is the reflectance of the wet material, computed from the Hapke parameters in the left-most cells of each column in Table (4.1) and r_d is the reflectance of the dry soil, computed from the Hapke parameters in the right-most cells of each column in Table (4.1). As we did for the dust models, we test all values of w from 0 to 100% at increments of 1% and select the one giving the lowest sum of square residuals between IF_w (Fig.(4.7)G, H, I dashed lines) and the observed relative albedo (Fig.(4.7) solid lines). In this computation we only consider the CaSSIS BLU and PAN and the B_{HR} and V_{HR} filters, as these are the only ones characterised by a good wavelength correspondence. For the other filters, the IF_w vs observed I/F is considered just at a qualitative level.

	B_J	B_{HR}	V_J	R_J	V_{HR}	R_{KC}	I_J	I_{HR}
ω	0.131 ± 0.003	$0.157^{+0.003}_{-0.004}$	0.169 ± 0.001	$0.2673^{0.00009}_{-0.0010}$	0.3013 ± 0.0009	0.334 ± 0.002	0.359 ± 0.001	0.373 ± 0.001
	0.200 ± 0.001	0.211 ± 0.005	0.270 ± 0.004	0.442 ± 0.002	0.472 ± 0.004	0.501 ± 0.004	$0.5238^{+0.0009}_{-0.0008}$	0.536 ± 0.002
b	$0.399^{+0.006}_{-0.005}$	0.37 ± 0.01	0.287 ± 0.005	0.217 ± 0.002	0.215 ± 0.02	0.204 ± 0.003	0.208 ± 0.002	0.211 ± 0.002
	0.25 ± 0.02	0.12 ± 0.01	$0.07 + 0.01_{-0.02}$	0.102 ± 0.006	0.08 ± 0.1	0.06 ± 0.02	$0.0003^{0.008}_{0.003}$	$0.0003^{+0.0006}_{0.0004}$
c	-0.87 ± 0.02	-0.75 ± 0.02	-0.55 ± 0.01	0.316 ± 0.007	-0.292 ± 0.006	$0.292^{+0.090}_{-0.010}$	0.401 ± 0.005	-0.468 ± 0.006
	$-0.41^{+0.06}_{-0.08}$	0.45 ± 0.04	$1.6^{+0.4}_{-0.3}$	$1.84^{+0.09}_{-0.10}$	2.2 ± 0.3	$3.3^{+1.3}_{-0.9}$	54^{+142}_{-61}	522^{+2860}_{-539}
h	$0.07^{+0.03}_{-0.02}$	$0.03^{+0.03}_{-0.02}$	0.05 ± 0.01	0.081 ± 0.006	0.079 ± 0.005	0.098 ± 0.009	0.098 ± 0.005	0.111 ± 0.006
	0.07 ± 0.03	0.11 ± 0.01	0.120 ± 0.008	0.106 ± 0.004	0.130 ± 0.008	$0.138^{+0.009}_{-0.008}$	0.144 ± 0.003	$0.158^{+0.007}_{-0.006}$
$B0$	0.9 ± 0.1	$0.8^{+0.3}_{-0.2}$	0.81 ± 0.04	0.72 ± 0.01	0.63 ± 0.01	0.69 ± 0.02	0.66 ± 0.01	0.67 ± 0.01
	$1.6^{0.3}_{-0.2}$	1.8 ± 0.1	$1.66^{+0.08}_{-0.07}$	1.09 ± 0.02	1.20 ± 0.04	$1.18^{+0.05}_{-0.04}$	$1.19^{+0.009}_{-0.010}$	1.22 ± 0.02
θ	< 5.9	< 4.7	< 4.7	< 6.5	$8.5^{+0.4}_{0.4}$	$6.2^{0.9}_{-1.2}$	$5.5^{+0.5}_{-0.7}$	$7.6^{+0.8}_{-0.9}$
	< 7.0	< 7.1	< 4.3	< 3.6	< 3.7	$5.1^{+0.5}_{-0.6}$	$3.7^{+0.6}_{-1.0}$	4.9 ± 0.3

Table 4.1: Hapke parameters for wet (upper row) and dry (lower row) samples of JSC-1 Martian soil simulant from (Gunderson et al., 2007). B_J, B_{HR}, V_J, R_J, V_{HR}, R_{KC}, I_J and I_{HR} are Johnson blue, HiRISE "BG" analogue, Johnson visible and red, HiRISE RED, Kron-Cousins red, Johnson infrared and HiRISE NIR filters, respectively

4.3 Results

This section reports our results and it is organized as follows: first, we present the comparative photometry of DDT, RSL and DP ROIs at Horowitz crater (Section 4.3.1). Then we compare it with simulated relative albedo measurements of dusty materials (Section 4.3.2) and eventually we compare it with simulated relative albedo measurements of dry and wet martian soils (Section 4.3.3).

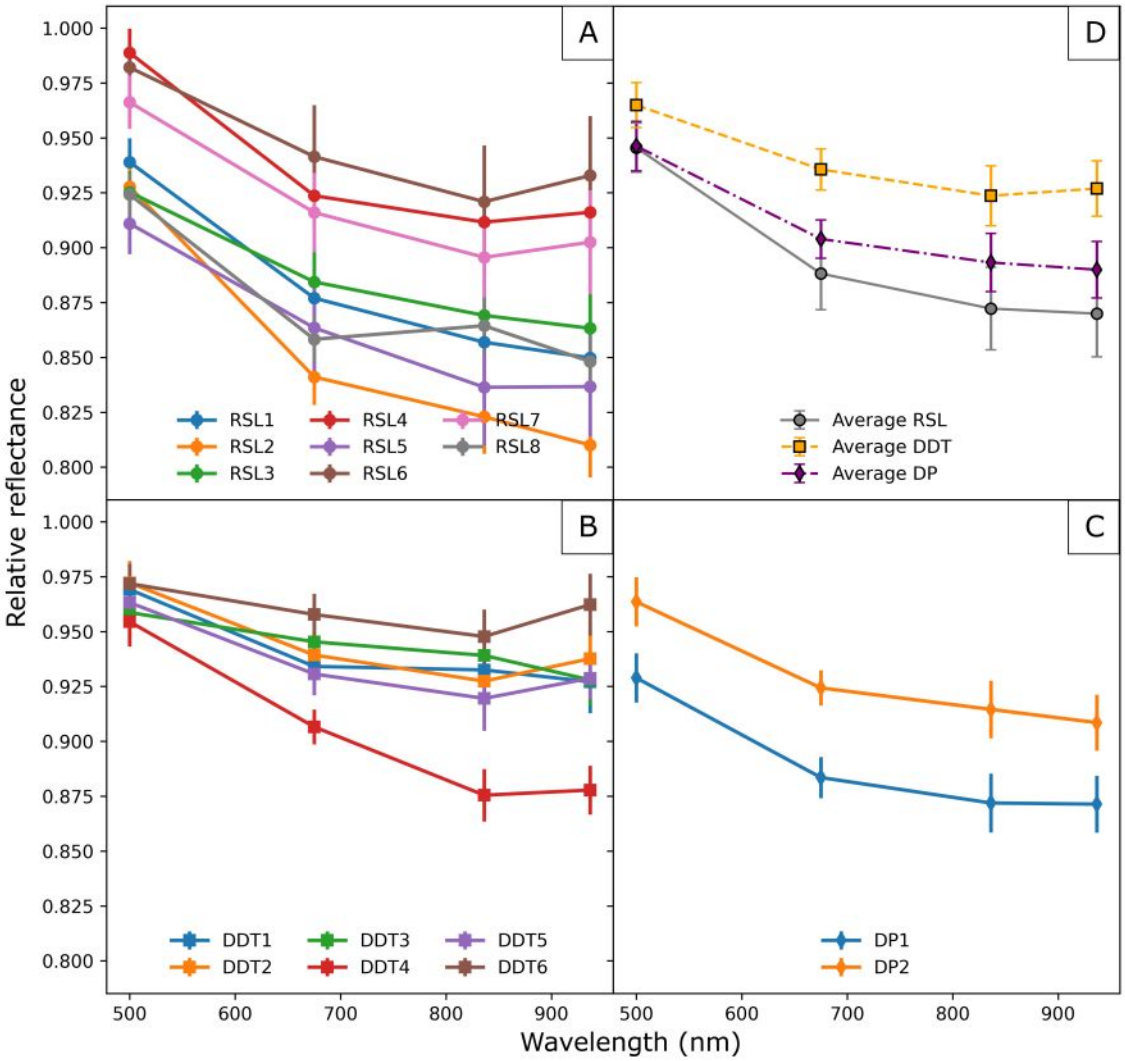

Figure 4.8: Relative albedo of A) RSL B) DDTs and C) DP ROIs with respect to nearby materials and D) corresponding average profile.

4.3.1 Comparative photometry of albedo features

The relative albedo of DDT, RSL and DP ROIs with respect to nearby, RSL and DDT free materials having the same illumination and observation geometries are reported in panels A, B and C of Fig. (4.8), respectively. It is clearly seen that all features have a similar relative reflectance, greater than 80% in all filters, and relatively similar colors. In all the studied features, the PAN, RED and NIR filters that show similar (within error bars) relative reflectance. The only prominent spectral

trend is a slightly higher relative reflectance in the BLU compared with the other channels. This trend is present in all three features, although with variable levels of significance, but it is more common for RSLs and DPs. A breakdown of the relative albedo measurements of each feature and comparison with dust and water models is provided in the next sections.

4.3.2 Comparison with dust-fallout models

The best-fit dust models to the DDT, RSL and DP ROIs relative reflectance are reported in Fig. (4.9). The dust model (dashed lines) usually provides a good fit to the observations (solid line and markers). The dust thickness (g/cm^2) of the DDT, RSL and DP ROIs (numerator) and nearby material (denominator), estimated as detailed in Section 3, are also reported in the legend. The statistical distributions of the dust deposits thicknesses for the DDT and DP ROIs (collectively called "DUST"), RSL ROIs and nearby materials (referred as "BK/DUST" and "BK/RSL") are shown through boxplots in Fig. (4.11A, B). In particular, as reported in Fig. (4.11A), DUST and RSL ROIs have statistically comparable deposits, although RSL have a slightly wider distribution. DUST ROIs have on average $1.090 \cdot 10^{-3} \pm 0.158 \cdot 10^{-3}$ g/cm^2 of deposited dust vs $1.08 \cdot 10^{-3} \pm 0.354 \cdot 10^{-3}$ g/cm^2 for RSL. On the other hand, Fig. (4.11B) shows that materials near the DUST features are characterised by a slightly lower dust deposit ($1.590 \cdot 10^{-3} \pm 0.459 \cdot 10^{-3}$ g/cm^2) than the materials nearby the RSL ROIs ($2.080 \cdot 10^{-3} \pm 0.837 \cdot 10^{-3}$ g/cm^2).

4.3.3 Comparison with wet martian soils

The comparison between our observed relative albedo for RSL, DDTs and DP ROIs and predictions by a mixture of wet and dry martian soil is shown in Fig. (4.10). We notice that water models predict a rather flat relative albedo, while our measurements have a higher relative reflectance in the BLU than in the PAN. However, we point out that our comparison is the most accurate in correspondence of the BLU and PAN filters, while it is only qualitative in the others. Nonetheless, these filters are those which provide most of the spectral information in this case, as the NIR and RED channels have relative reflectance values similar to the PAN, within error bars. This being said, the water models provide a rather poor fit to the observations and the prediction is often outside the error bars. Best-fit values of w, i.e. the percentage of wet soil in the mixture, are reported in each panel legend.

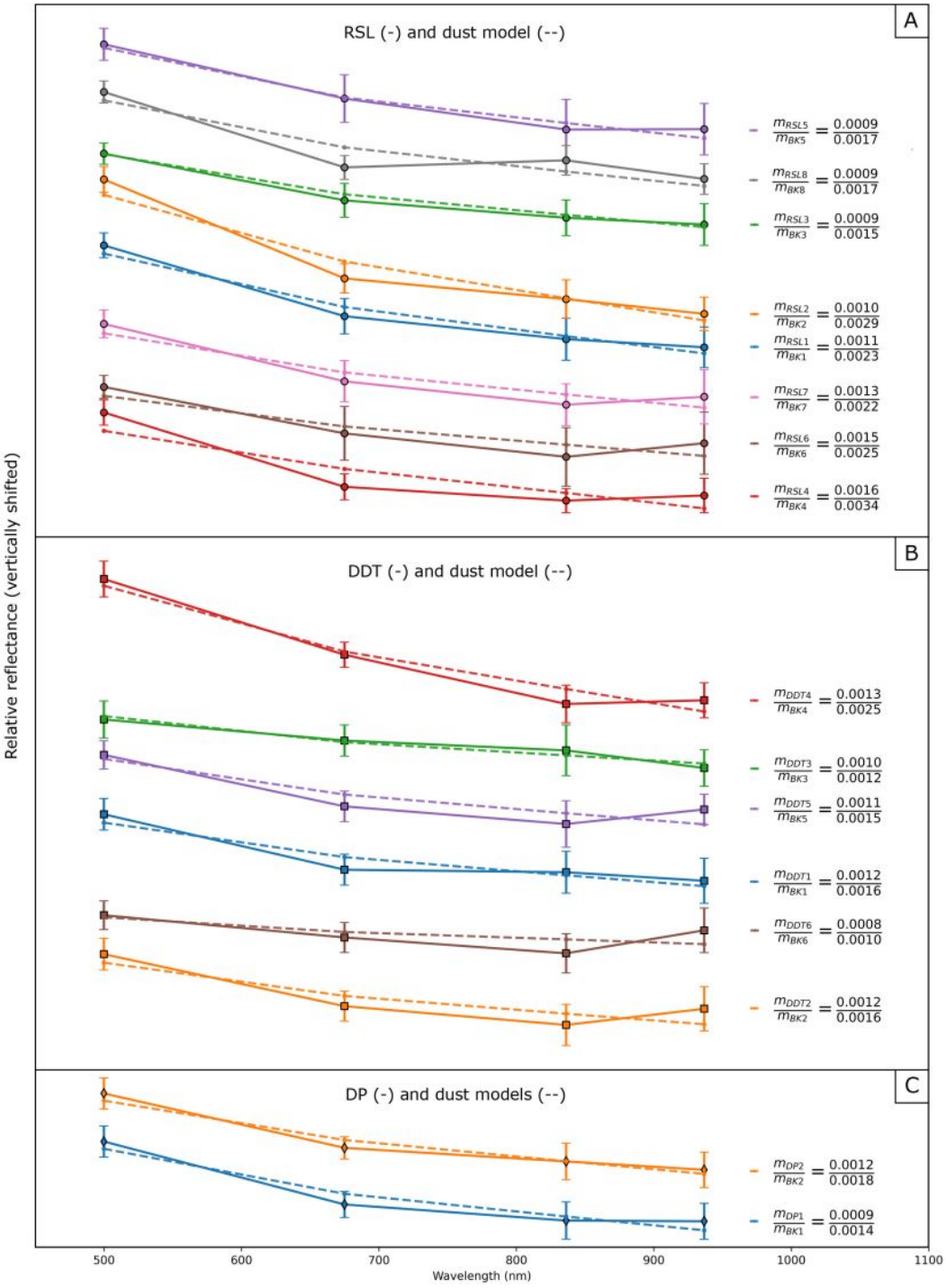

Figure 4.9: Vertically shifted relative reflectance measurements of A) RSL B) DDTs and C) DP ROIs (markers and solid lines) and best-fit dust model (dashed lines). The legend reports the dust thickness of each ROI (numerator) and the corresponding BK ROI (denominator). Each profile is vertically shifted in order to better show all the individual measurements

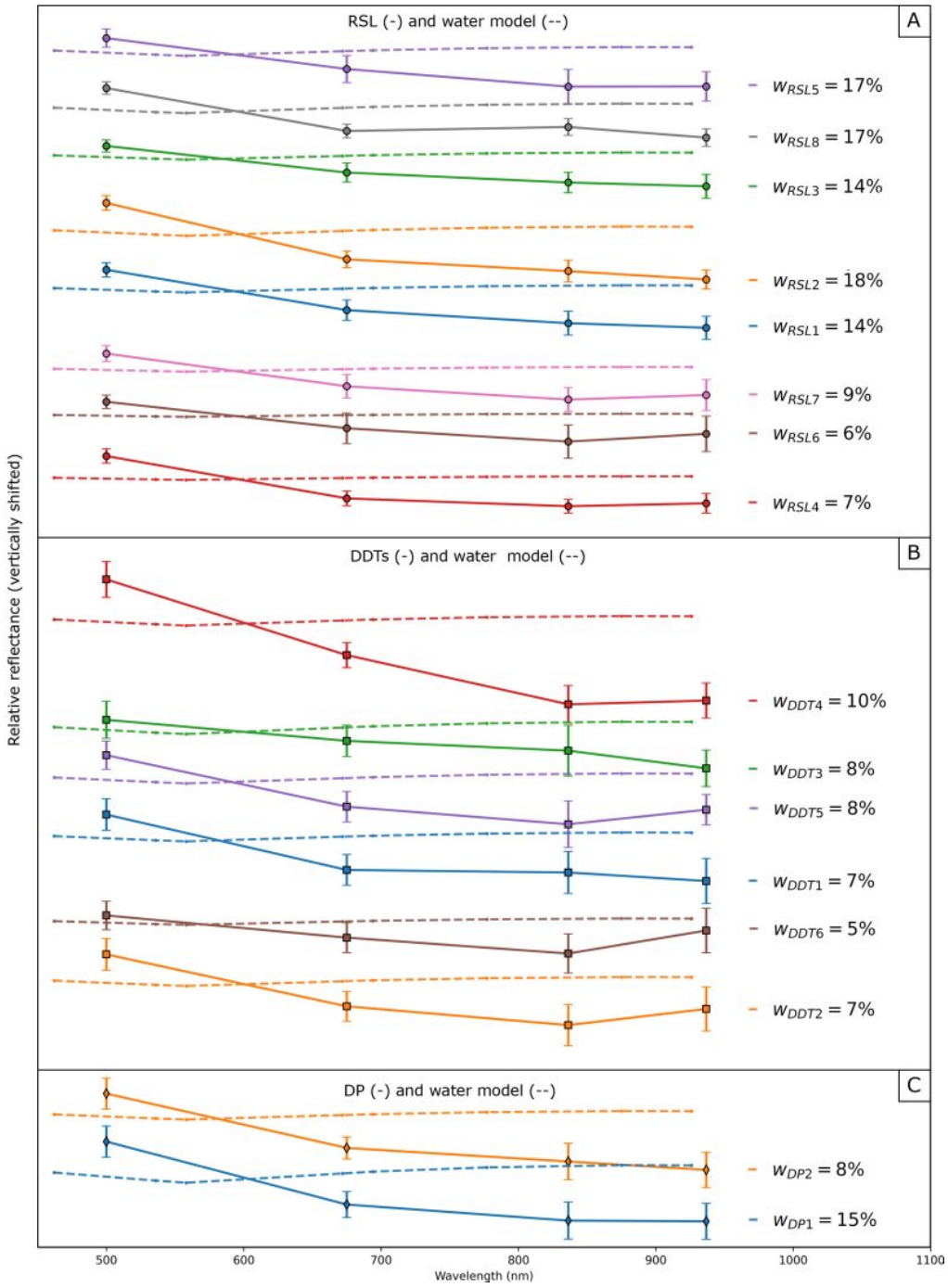

Figure 4.10: Vertically shifted relative reflectance measurements of A) RSL B) DDTs and C) DP ROIs (markers and solid lines) and best-fit water model (dashed lines). Also reported are the fitted percentages of water for each ROI. Each profile is vertically shifted in order to better show all the individual measurements.

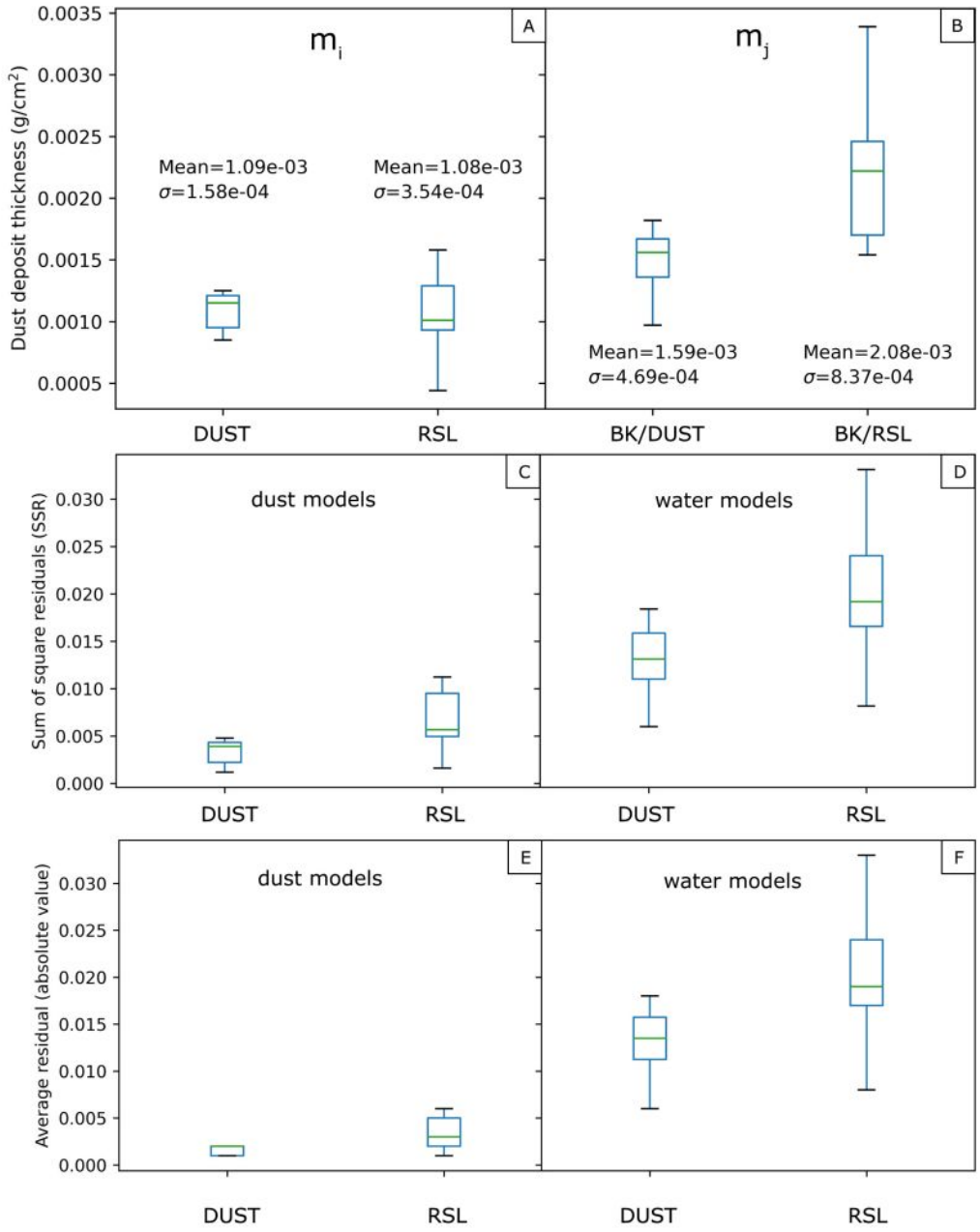

Figure 4.11: A) Box plots showing the statistics of the dust deposit thickness of DDT and DF (hereafter referred as "DUST") and RSL ROIs and B) corresponding nearby material: "BK/DUST" for the DUST ROIs and "BK/RSL" for the RSL ROIs. Mean values and standard deviations are also reported. C) Box plots of the sum of squared residuals, evaluated on the BLU and PAN filters for the DUST and RSL ROIs, of the best-fit dust models C) and water models D). E) and F) are the same as C) and D) respectively, but with the average absolute residual of each model.

4.4 Discussion

We characterised the spectrophotometric behavior of RSL and features known to be related to dust removal, i.e. DDTs and DP materials. Our relative reflectance measurements in Fig. (4.8) show a remarkable photometric similarity between these three features, characterised by a higher relative reflectance in the BLU and the same relative reflectance in the PAN, RED and NIR. This pattern shows some variability. For example some RSL (RSL1,2,3,5,8) display a larger difference in BLU relative reflectance with respect to the other filters than most (but not all) DDTs and DP ROIs, which show flatter profiles. However, since in some cases also the inverse is true, this is probably because of the intrinsic variability of these features, maybe due to slight compositional differences of the material. We propose that the photometric similarity between the relative reflectance of RSL, DDTs and DPs may indicate that they have a similar origin, i.e. they are dust-removed features, even though not necessarily formed by exactly the same mechanisms. To assess this hypothesis, we compare our measurements with the predictions by models of dust fallout and mixtures of dry and wet soils derived from laboratory experiments. In particular, we find that our measurements are well fitted by dust models returning a lower dust-thickness for the RSL, DDT and dust-poor ROIs and a higher one for the nearby materials. This agrees with the well-established physical interpretation of DDTs and DPs, hence validating our approach and confirming that Horowitz RSL are photometrically consistent with being dust-removed features. In particular, the relative spectral signature detected here are in principle consistent with ratios between a ferrous and ferric material (i.e. dust). The latter ratio would imply a decreasing relative albedo from BLU to NIR, that we detect in some RSLs (RSL1,2,3,5), in the DP ROIs and in DDT4, while the others have either more or less the same RED and NIR values or an upturn in the NIR. However, this variability in the RED and NIR bands is also comparable with the error bars. Nevertheless, the fact that some features have similar RED and NIR relative reflectance or an upturn in the NIR may be explained by considering that the material in the RSL, DDT and DP ROIs could not be a perfectly, dust-free ferrous material but may be contaminated by dust. This is consistent with our modeling that shows a significantly greater than zero best-fit dust-deposit in all the studied ROIs. A possible flaw in this interpretation may be that CaSSIS could be spectrally insufficient for distinguishing the photometric signature of dust depletion from other mechanisms, because it provides color information in only four broadbands. In particular, darkening by wetting the soil may be responsible for the observed spectrophotometric signatures. To assess this, we relied on photometric models of wet soils available in literature. Even if our comparison is formally accurate only for the BLU and PAN, we recall that in our case these two bands are the ones that show the most difference between each other, and thus provide the main spectral contrast to be fitted by any model. In general, at the observation and lighting geometries investigated in this study, a mixture of wet and dry materials exhibits a rather flat relative reflectance when ratioed to a dry material, meaning that it is not possible to fit the higher BLU relative reflectance with respect to the PAN for either DDTs, RSLs or DP ROIs. As a consequence, the best-fit water models are not able to reproduce our measurements within errors. A further quantitative comparison of both models is presented by the distributions of Fig. 4.11. In particular, we report the sum of squared residuals (SSR) distri-

bution, which is a metric of the goodness of fit, for both the dust models (Fig. 4.11C) and for the water models (Fig. 4.11D). For both DUST and RSL ROIs, dust models consistently provide lower, statistically significant, SSR values than water models, hence achieving a better fit. The same is true even if we consider another metric, which is the average residual (in absolute value) committed by each model (Fig. 4.11D, E). The fact that dust models provide a better fit than water models is also found in Fig. (4.12) where we perform a different assessment. We consider all measurements globally, regardless of the feature, and evaluate both models on the basis of the well-established χ_r^2 (i.e. the reduced chi square) metric. The χ_r^2 is computed as the square root of the sum of the square residuals divided by each measurement uncertainty. This value is then divided by the number of observations. Values close to 1 indicate that the model errors are comparable with the measurement uncertainties, hence suggesting a good fit. Values higher than 1 indicate that the errors of the model are bigger than what would be expected by the measurement uncertainties. Values lower than 1 means that the model prediction are closer to the measurements than what would be expected considering the measurements uncertainty, suggesting that either the latter were overestimated or that the model is "overfitting" the dataset. We note that for the dust models we now use all filters for the ${\chi_r}^2$ computation, allowing it to be potentially influenced by model errors in the RED and NIR filters. This would in principle favor the water models, but it also helps to assess if there is any bias in considering only the BLU and PAN filters This would in principle favor the water models, but it also helps to assess if there is any bias in considering only the BLU and PAN filters. In Fig. (4.12) we compare the predicted (x-axis) vs observed (y-axis) relative reflectance for the dust (orange) and water (blue) models. The former achieves a ${\chi_r}^2 \approx 1$ while the latter produces a 5 times higher value, hence again confirming a worse fit. This is consistent with the results of Fig. (4.11), confirming also that adding or removing the RED and NIR filters does not influence our ability to assess the goodness of fit of each model. The fact that water models return a larger ${\chi_r}^2$ can be also qualitatively recognized in Fig. (4.11). Indeed, the modeled reflectance is always "in between" the observed reflectance in the BLU and PAN filters, typically higher in the latter and lower in the former. When considering the observed/modeled ratio, this implies two clusters, one below a 1:1 relationship and one above it. This behavior can be seen in Fig. (4.12) and implies that errors will be not distributed in a gaussian way. As a consequence, they will be consistently higher than expected by a gaussian error distribution and hence the ${\chi_r}^2$ will return a larger value. These three checks (SSR distribution in Fig. 4.11B, C, average absolute residual in Fig. (4.11)D, E and ${\chi_r}^2$ in Fig. 4.12) support our hypothesis, suggested by the qualitative comparative analysis in Fig. (4.8), that RSL, DDTs and DP terrains at Horowitz have the same origin as dust removed features, hence bringing new evidence for a dry origin for RSL. Our estimated dust deposit thicknesses provide a constraint on the process forming RSLs. The similar, and greater than zero, fitted dust deposits of RSL, DDTs and DP materials suggests that the amount of deposited dust on these ROIs is similar. However, the amount of dust deposited outside the RSLs is greater than outside the other features. An explanation of this may be sought in terms of aeolian processes: both dust-devils and winds could first lift some dust from the surface (Reiss et al., 2013). This dust is then redeposited, possibly either over the whole crater or a large, less localized area. This would happen in a more uniform way, hence explaining the same dust

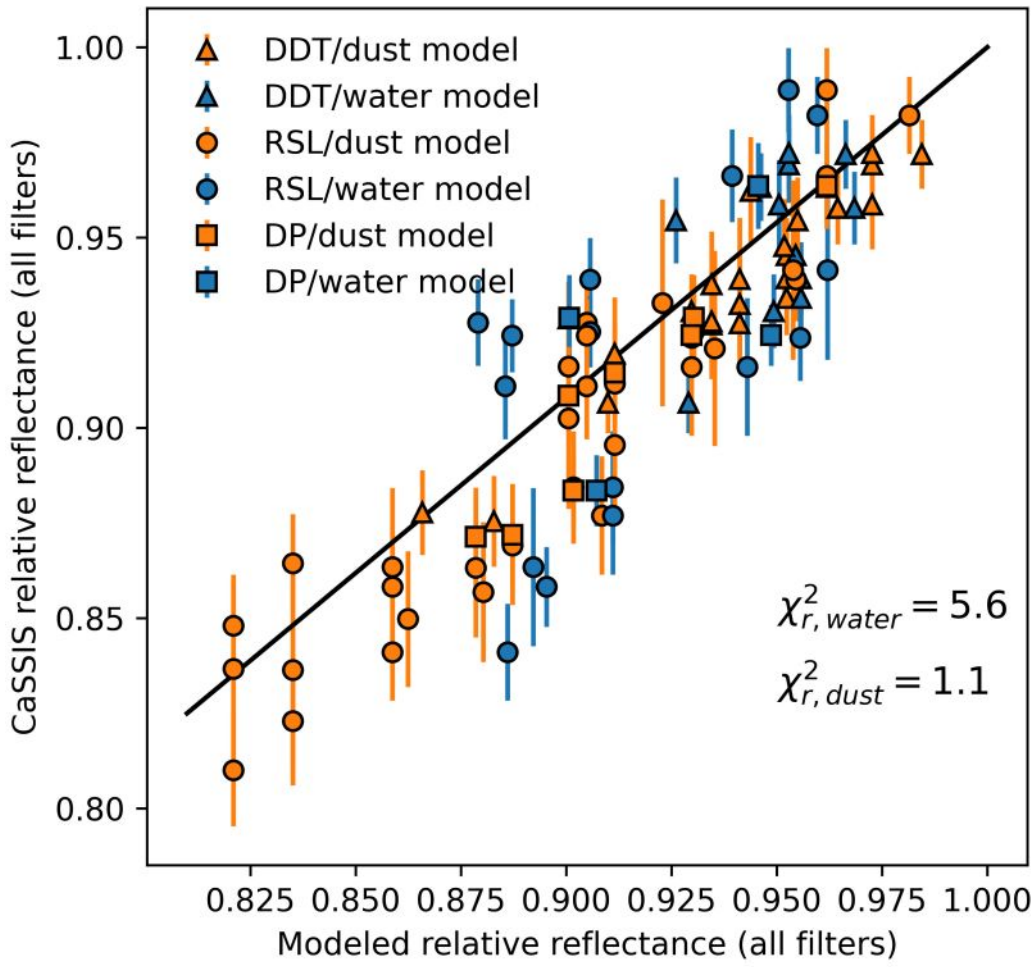

Figure 4.12: Modeled (x axis) vs measured relative reflectance for dust models (orange, all filters) and water models (blue, only BLU and PAN filters). The black line indicates the perfect 1:1 line that would be expected for an ideal model.

content within the DDTs, DP and RSL ROIs. The higher predicted dust content nearby RSLs is consistent with the beiger hue of materials near RSL that can be seen in the CaSSIS NPB composite in Fig. (4.2), against the relatively bluer tone of regions nearby dust-devil tracks. It is also consistent with the more yellow tone of materials nearby RSLs in the CaSSIS CBRC-ALL product displayed in Fig. (4.3). The physical process responsible for this dust excess may be explained in different ways, which are difficult to discriminate in this analysis: it may be a peculiarity of the RSL-forming process that may not only lift dust (as for dust devils) but also displaces it laterally, hence enriching in dust the nearby slopes. This dust could then be lifted by widespread dust deflation processes, like those occurring at Tivat crater (Schaefer et al., 2019), hence explaining the lack of a visible lateral deposit at RSL locations. Another possibility is that RSL on Horowitz could form on slopes that are already relatively richer in dust with respect to DDTs and DFs regions, prior to the RSL formation. This pre-existing excess may be due to dust falling from the upslope part of the steep rocky outcrops of Horowitz crater and depositing where it is more dynamically stable, i.e. near RSL locations where the slope angle matches the angle of repose of dry granular flows. Winds may then locally redistribute dust grains, but those that are brought back upslope will fall again while those that are moved downslope will remain there. As a consequence, a net excess of dust could accumulate near RSL locations and downslope. In contrast, the lower slopes in the DDT and nearby the DP material regions do not allow this scheme, implying that dust is on average the same everywhere, with only minor excesses in local topographic sinks. Another option is that dust is more efficiently depleted by aeolian activity at the DDT and DP material locations than at RSL sites. As we can see from Fig. (4.13), DDT3 and DDT5 are in a region that presents aeolian ripples, otherwise absent from the RSL ROIs. The presence of aeolian ripples implies a significant wind activity that can blow away dust particles, forbidding their accumulation and explaining the lower dust-deposit at the surface nearby the DDTs and DP ROIs. Neither of these three options is specifically favoured by our analysis, but they nevertheless offer a justification and physical explanation of the dust deposit thickness derived from our modeling. The dry, dust removed nature of Horowitz RSL implied by our photometric analysis agrees with recent works outlining that RSL are aeolian features Dundas (2020) correlated with the availability of dust on the surface (McEwen et al., 2021; Vincendon et al., 2019). The most recent models of aeolian RSLs invoke slope winds (Vincendon et al., 2019) or dry sandy flows that displace dust (Dundas, 2020). In general, both options appear consistent with our analyses and are supported by it, because the main spectrophotometric signature would be dust-removal, which is detected here. We can however discuss some implications of these two models that may be directly probed with future spectrophotometric analyses. In the full aeolian scenario where RSL are dark tracks left by localized wind activity (Vincendon et al., 2019), we may have a photometric dependency on the location where RSL are formed. If a slope wind removes dust and forms RSL, their reflectance depends on the exposed material, while the reflectance of a nearby surface would be more or less the same (i.e. the reflectance of a dusty soil). As a consequence, if this analysis would be repeated at other sites we could therefore possibly see different RSL relative reflectance. However, it is also possible that a thin layer of dust covering the RSL, which is detected in our analysis, could mask any spectral differences. Nevertheless, we shall discuss here another possibility. RSL

at Horowitz form on steep scarps immediately downslope of rocky outcrops. DP and and DDT ROIs are instead found in a central "pool" of dark material (see for example Fig. 4.2A). As noted above, this material also has small aeolian ripples, visible in the HiRISE imagery in Fig. (4.13), that together with its low albedo suggests that it could be an aeolian sandy deposit. The same ripples are not seen in the vicinity of RSL, meaning that these occur in a different geomorphological environment. A putative slope wind would remove the deposited dust and expose the underlying material, which in this case would be different for RSL. Hence, if RSL are formed via dust removal by slope winds, we shall not expect such a similar spectral trend between the RSL, DP and DDT materials at Horowitz crater. Again, the implied relative albedo differences can be under our detection capabilities or masked by the amount of deposited dust estimated through our modeling. Therefore, we do not discard the full aeolian RSL hypothesis and defer a more detailed assessment to a time when a larger sample of CaSSIS color images at multiple locations on Mars will be available. If RSL are the result of dust removal by winds and deposition of sand grains, then the relative reflectance of RSL should be similar even at different locations, and similar to DFs and DDTs when these are located on sandy deposits, which is indeed the case at Horowitz crater. While this analysis may not be able to fully discriminate between these two similar formation mechanisms for RSL, we provide new and independent evidence supporting them and outline possible ways to discriminate one from the other. Further observations are required to disentangle these effects and discern between these two aeolian models of RSL, which are therefore both supported by this analysis.

4.5 Conclusions

We investigated the relative reflectance of RSL, DDTs and DPs at Horowitz crater, Mars, in the BLU, PAN, RED and NIR CaSSIS filters. Our comparative photometry of these features revealed that they have a similar relative reflectance, higher in the BLU and more or less constant in the other filters. Since DDTs and DFs are well-established dust-removed features, this suggest that RSL may have the same origin. To assess this hypothesis, we analysed laboratory spectral measurements of dust deposition on a Martian soil analog to simulate the relative reflectance that would be detected by CaSSIS when observing a dust-removed surface. We also considered photometric models of wet and dry Martian soils to check if our relative photometry could be explained by a mixture of wet and dry materials. We find that dust deposition models provide a good fit to the relative reflectance of DDTs and DPs, in agreement with their physical origin, and also of RSLs. This adds new evidence that RSL are dry features generated by the removal of dust and possibly the deposition of sand by aeolian processes. In contrast, mixtures of dry and wet soil cannot explain our observations, and therefore are not supported by the current analysis. This study supports both the recently proposed aeolian and grainflow models for RSL formation. Even though our evidence does not allow us to discriminate clearly between these two models, future observation of different RSL sites on Mars by CaSSIS may help us provide a clearer picture of their precise formation mechanism.

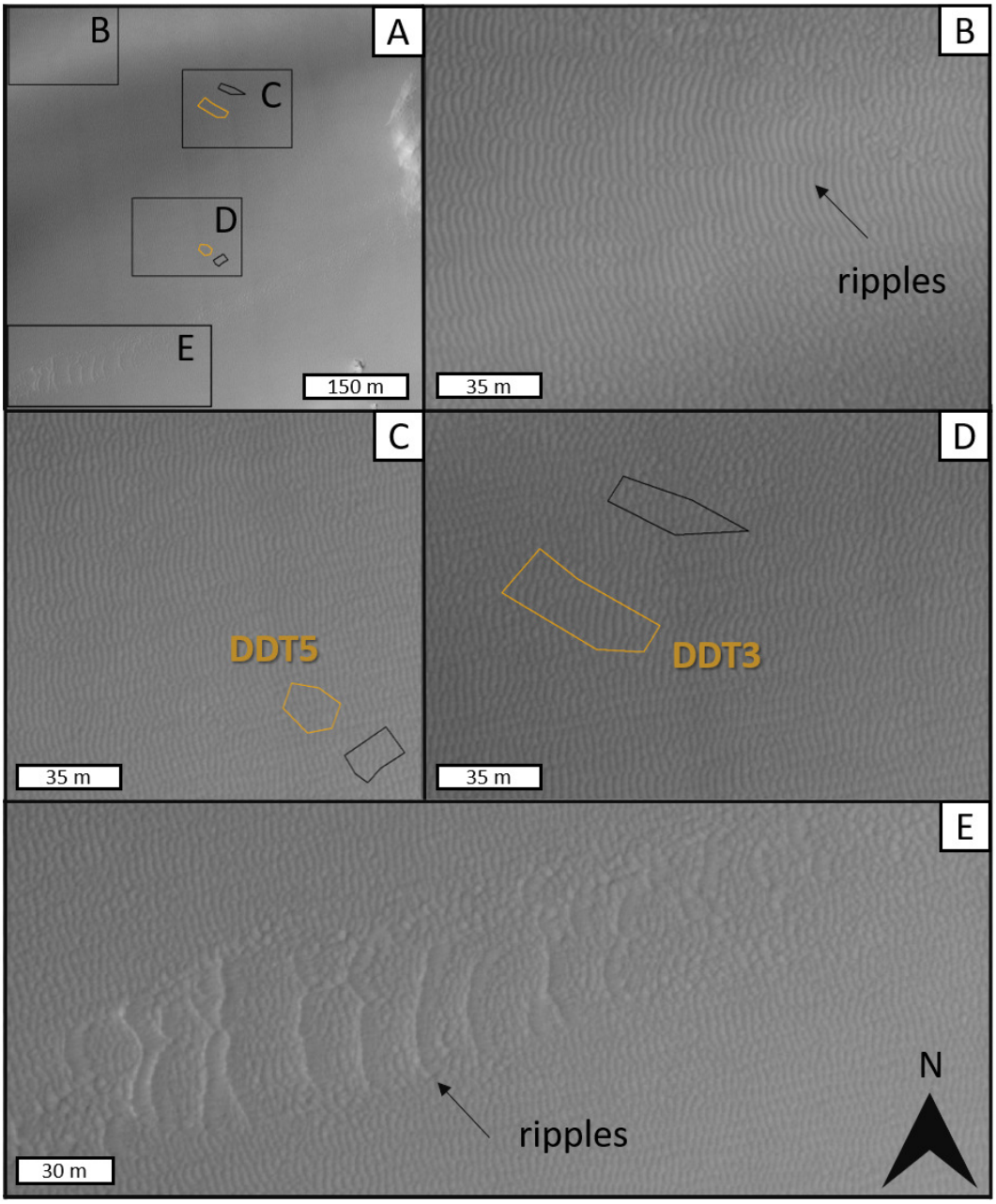

Figure 4.13: HiRISE image ESP_020832_1475 showing A) the region in Fig 1C. B) An example of aoelian ripple. C) Further examples of ripples near DDT5 and DDT3 (D). E) Bigger and widely spaced ripples.

Chapter 5

Topographic correction of HiRISE and CaSSIS images: validation and application to colour observations of Martian albedo features

The apparent brightness of a planetary surface depends on the illumination and observation geometries and on the composition and texture of the reflecting material. The determination of a mathematical function that can accurately model the reflected radiation at given illumination and observation angles enables quantitative comparisons between photometric measurements of planetary surfaces, laboratory experiments and different spectrophotometric datasets. Such modeling allows to highlight and investigate differences in the scattering properties of the reflecting medium, discriminating albedo variations from illumination effects. If the model depends on physical properties of the regolith, such as composition, grain size and shape, porosity and roughness, it may also be used to indirectly probe such properties. The modeling and removal of brightness variations induced by topography, also referred as topographic shading, are therefore pivotal for the spectrophotometric study of planetary surfaces. For instance, this is required for the production of image mosaics and the analysis of the surface spectral reflectance. In this context, a variety of mathematical functions, or photometric models, have been proposed so far (Fairbairn, 2005; Hapke, 1993; McEwen, 1991; Schröder et al., 2013). Some of these are simple combinations of functions of the illumination and observation angles and contain few or no parameters, as the Lambert, Lommel-Seelinger, Minnaert and Akimov models (Fairbairn, 2005; Hapke, 1993; Minnaert, 1941; Schröder et al., 2013). Other formulations consider shadow-hiding effects too and more advanced optical phenomena that depend on the phase angle (i.e. the angle between the observation and illumination directions). In particular, the Kaasalainen–Shkuratov (KS) model allows to couple any of the above simple functions with phase angle ones (Schröder et al., 2013; Shkuratov et al., 2011; Velikodsky et al., 2011; Wu et al., 2013). Finally, the Hapke photometric models (Hapke, 1993, 2002a,b, 2012) possibly provides the most detailed and complete description of the scattering properties of a reflecting medium, but it implies a relatively complex mathematical expression. In this work, we will test the performances of the Lambert, Lommel-Seeliger, Min-

naert and Akimov photometric functions to model and remove topographic shading from HiRISE (McEwen et al., 2007) and CaSSIS (Thomas et al., 2017) images of the surface of Mars. The choice of using simple photometric models is motivated by the potentially large uncertainties and source of errors that may arise from using complex, multi-parameter models. Indeed, a single HiRISE or CaSSIS image is characterised by a relatively low coverage of illumination and observation angles, preventing an accurate and robust estimation of complex models parameters from a single image (Schmidt and Fernando, 2015). On the contrary, complex models are usually employed when multi-angular observations are available. For example, accurate estimates of the parameters of the Hapke model for Mars from orbit have been performed trough the multi-angular nature of CRISM (Murchie et al., 2007) "emission phase function" (EPF) observations (Ceamanos et al., 2013; Fernando et al., 2013). Alternatively, they were also achieved by analysing multiple (≥ 13) repeated low resolution observations (i.e. above 1 km/px) of the same locations taken with the "Observatoire pour la Minéralogie, l'Eau, les Glaces, et l'Activité" (OMEGA, Bibring et al., 2004) hyperspectral imager (Vincendon et al., 2007). While these approaches are very accurate in recovering surface reflectance, they require a high number of images of the same site with different observation geometries, and without significant surface changes between the images. For high-resolution (<5 m/px) datasets, this requirement may restrict their applicability to few very well monitored sites (i.e. landing locations), preventing the analysis of more common regions with a low number of observations. Complex models also require an accurate, radiative transfer based atmospheric correction to remove the contribution of aerosol to the observed reflectance, which is out of the scope of this analysis. For these reasons, we opted for an initial, simplified treatment of the surface reflectance function, leaving a more detailed analysis for a future work. To validate our method, we compare the resulting topographically corrected (i.e. topographic-shading removed) reflectance with the relative albedo measurement of Martian RSL (see Section 1) reported in Schaefer et al. (2019) in the RED HiRISE channel (Delamere et al., 2010). We also highlight its scientific benefits by applying it to HiRISE colour observations of albedo features, including RSL and dust-devil tracks. Both RSL and dust-devil tracks have been described in detail in Section (1), but we provide here a very brief description for clarity. Dust devils tracks are dark or bright-toned lineaments left by the passage of Dust Devils (i.e. turbulent whirlwinds) that lift deposited dust and expose the underlying surface (Reiss et al., 2016). RSL are narrow (< 5 m) low-albedo linear features, often sourcing from bedrock outcrops and lengthening hundreds of meters down warm Martian steep slopes (McEwen et al., 2011). The nature of RSL is still debated, although an increasing body of work suggest that they may be dry granular flows (Dundas et al., 2017; Gough et al., 2020; Munaretto et al., 2020, 2021a,b; Schaefer et al., 2019; Schmidt et al., 2017) possibly of aeolian nature (Dundas, 2020; Vincendon et al., 2019). Both dust-devil tracks and RSL show a different albedo from nearby surfaces, hence representing an interesting scientific application of our method. The only previous photometric analysis of RSL in all HiRISE filters highlighted that the ratios between RSL colours and adjacent areas are the same, within uncertainties (McEwen et al., 2011). By focusing on ratios between regions with the same illumination conditions, these measurements do not require a topographic correction: for this reason, it provides another benchmark to further validate our method. Nevertheless, the relatively small HiRISE colour

swath implies a small probability of finding a common "normalisation" region with the same illumination and observation conditions as the features of interest, such as in our case RSL, dust-devil tracks and their nearby slopes. In most cases the absence of the topographic correction prevents the investigation and comparison of relative albedo of many different features in the HiRISE filters. For this reason, we extended our method to the blu-green (BG, from 400 to 600 nm) and near infrared (NIR, from 800 to 1000 nm) channels of HiRISE colour orthoimages depicting both RSL and dust-devil tracks. This allows us to investigate and compare the relative albedo of these features in multiple bands. While absolute photometry would in principle permit a comparison of the RSL reflectances with wetting of dry Martian simulants (Pommerol et al., 2013) or dust fallout (Wells et al., 1984) laboratory measurements, it would require both a convolution of these datasets with the HiRISE bandpasses and a more accurate atmospheric correction (Ceamanos et al., 2013; Fernando et al., 2013; Vincendon et al., 2007), which are out the scope of this work. On the other hand, relative photometry analysis is often the preferred approach when considering HiRISE data (Daubar et al., 2016; Munaretto et al., 2020; Schaefer et al., 2019). Hence, we adopt this simpler approach and compare the relative albedo of dust devil tracks, which are well accepted dust-removed features (Klose et al., 2016), with RSL for all the HiRISE filters. We apply our method to correct a CaSSIS panchromatic image of the Ascraeus Mons summit caldera complex. This location features multiple terraces, a dense fracture network and several faults (Byrne et al., 2012), resulting in a rich variety of slope orientations that allow to better showcase the potential of our methodology in removing topographic shading.

In section (5.1) we describe the photometric models tested in this work. In section (5.2) we describe our dataset and methodology. In section (5.3) we validate our methods and in section (5.4) we present a few examples of scientific applications. In section (5.5) we discuss our results and finally in section (5.6) we draw our conclusions

5.1 Photometric modeling

The reflectance (r) of a planetary surface illuminated by the Sun is defined as the ratio between the observed radiance (I, units: W m^{-2} µm^{-1} sr^{-1}) and the normal solar irradiance (J, units: W m^{-2} µm^{-1}) (Hapke, 1993; Schröder et al., 2013) and depends on the local incidence angle of sunlight (i_l), the local emission angle (e_l), the phase angle (α) and the wavelength. The local incidence angle is defined as the angle between the direction of the incoming sunlight and the normal to the surface. The local emission angle is the angle between the observation direction and the normal to the surface. In this study we will consider the "radiance factor", or "I/F" ratio, which is defined as (Hapke, 1993):

$$I/F = \pi r\left(\mu_0, \mu, \alpha, \lambda\right) = \pi \frac{I\left(\mu_0, \mu, \alpha, \lambda\right)}{J\left(\lambda\right)} \tag{5.1}$$

where $\mu_0 = \cos\left(i_l\right)$ and $\mu = \cos\left(e_l\right)$. Throughout the article, we will use the term "reflectance" to refer to the radiance factor. Since we focus on images taken at the same wavelength, we will omit the λ symbol. As in (Schröder et al., 2013), we will consider r as the product of a phase function, or equigonal albedo A, and a

disk function, D:

$$I/F = A(\alpha)\, D(\mu_0, \mu, \alpha) \tag{5.2}$$

The phase function $A(\alpha)$ describes the phase dependence of the normal albedo of the surface. The disk function $D(\mu_0, \mu, \alpha)$ describes the dependence of the surface brightness from the local incidence and emission angles at constant phase. This term accounts for the surface brightness variations induced by local topography, or topographic shading, whose modeling and correction are the main focus of this work. The simplest disk function here considered is the Lambert disk function (Hapke, 1993), which describes the reflectance of an isotropically scattering surface:

$$D_L(\mu_0, \mu, \alpha) = \mu_0 \tag{5.3}$$

The second disk function examined is the Lommel-Seeliger law (L.S.) (Fairbairn, 2005; Hapke, 1993), which can be derived from the radiative transfer theory applied on a particular medium:

$$D_{LS}(\mu_0, \mu, \alpha) = \frac{2\mu_0}{\mu_0 + \mu} \tag{5.4}$$

Another widely used disk function is the Akimov law. For simplicity, we use the parameter-free formulation of (Schröder et al., 2013):

$$D_A(\mu_0, \mu, \alpha) = cos\Big(\frac{\alpha}{2}\Big) cos\left[\frac{\pi}{\pi - \alpha}\left(\gamma - \frac{\alpha}{2}\right)\right] \frac{(cos\beta)^{\frac{\alpha}{\pi-\alpha}}}{cos(\gamma)} \tag{5.5}$$

where β and γ are the photometric latitude and longitude, depending on incidence, emission and phase angles as follows:

$$\begin{aligned} \mu_0 &= cos(\beta) cos(\alpha - \gamma) \\ \mu &= cos(\beta) cos(\gamma) \end{aligned} \tag{5.6}$$

The fourth and final disk function considered here is the Minnaert law (Minnaert, 1941):

$$D_M = \mu_0^k \mu^{k-1} \tag{5.7}$$

where k is an empirical parameter that depends on wavelength and phase. Its value can be estimated by fitting the Minnaert law to the observed surface reflectance. For k = 1, the Minnaert law becomes the Lambert Law.

5.2 Dataset and methodology

We initially apply the topographic correction (i.e. modeling and removal of topographic shading) to HiRISE images of Tivat Crater (−45.5°N,9.5° E), Mars. This location was selected because it is covered by multiple HiRISE images (see Table 5.1) and a digital terrain model (DTM) which is required for the application and validation of our method. All these datasets are publicly available through the Planetary Data System (PDS). In addition, orthorectified versions of the HiRISE images are also available. Indeed, these are pivotal for our analysis because they ensure the coregistration between images and the DTM, which is used to derive the local observation and illumination conditions of the surface. Most importantly, Schaefer et al. (2019) recently performed several relative albedo measurements of albedo features within Tivat crater, including RSL and dust devil tracks. Their measurements offer a benchmark for validating our methodology and proving its applicability to photometric studies of the Martian surface.

5.2.1 Data processing

To be able to compare our results with those of Schaefer et al. (2019), where we refer for further details, we analysed their same dataset. DTM and orthoimages of Tivat crater were pre-processed following their same methods. In particular, the DTM was resampled at 2 m resolution with cubic convolutions and smoothed with a 20 m diameter moving average. Orthoimages were atmospherically corrected by subtracting the Digital Number (DN) of the darkest, shadowed pixel and radiometrically calibrated to I/F units with the offset and gain factor included in their PDS label. Moreover, following the approach of Schaefer et al. (2019), the mutual alignment between the orthoimages was further enhanced using the automatic registration tool in ArcGIS and affine transforms. To use the disk functions described in Section (5.1), estimates of the local incidence, emission and phase angles for each pixel and for each observation are required. The latter is not influenced by local topography and it is reported within the PDS label of each image. On the contrary, local incidence and emission angles must be computed considering both the effects of topography and the illumination and observation geometries. Following (Hapke, 1993), the local incidence (i_l) and emission (e_l) angles of a surface, tilted of angles θ (i.e. the slope angle, computed from the DTM) with respect to the local normal to a reference surface and ζ (i.e. the difference between the aspect direction, computed from the DTM, and the subsolar ground azimuth [1]) with respect to the source of illumination, are given by:

$$\begin{aligned} \cos(i_l) &= \cos(i)\cos(\theta) + \sin(i)\sin(\theta)\cos(\zeta) \\ \cos(e_l) &= \cos(e)\cos(\theta) + \sin(e)\sin(\theta)\cos(\zeta - \psi) \end{aligned} \tag{5.8}$$

where i and e are and the incidence and emission angles computed with respect to the normal to a reference surface, in our case the standard IAU2000 Martian ellipsoid (polar radius = 3376.20 km, equatorial radius = 3396.19 km). ψ is the azimuth angle between the subsolar and subspacecraft points [2] . All angles and the relevant geometric quantities are sketched in Fig. (5.1). To apply (8) we must first compute i, e, ζ and ψ. To do so, we first re-process each HiRISE observation through the `hiedr2mosaic.py` script of the Nasa Ames Stereo Pipeline (ASP, Shean et al., 2016). This script processes the Experimental Data Records (EDR, McEwen et al., 2007) of each observation and outputs a radiometrically calibrated and map-projected image. In particular, it uses the Integrated Software for Imagers and Spectrometers (ISIS) `spiceinit` tool to attach the information contained in the SPICE kernels of the observation to the output image. This step allows the output image to be processed through other ISIS tools to extract additional observation details, including i, e, ζ and ψ. We edited the `spiceinit` command by specifying the standard IAU2000 Martian ellipsoid as the shape model of the surface. The resulting

[1] The subsolar ground azimuth is the clockwise angle between the true North (90° latitude) and the subsolar point, which is defined as the intersection between the line connecting the Sun to the target body's (i.e. Mars) center and the body's surface, specified through a shape model. A more detailed explanation is given at `https://isis.astrogeology.usgs.gov/documents/Glossary/Glossary.html`.

[2] The subspacecraft point is the point where the look vector from the spacecraft (i.e. the direction at which the spacecraft is pointing to) intersects the target body's (i.e. Mars) surface. Its azimuth angle is defined as the subspacecraft ground azimuth. A more detailed and complete explanation is given at `https://isis.astrogeology.usgs.gov/documents/Glossary/Glossary.html`

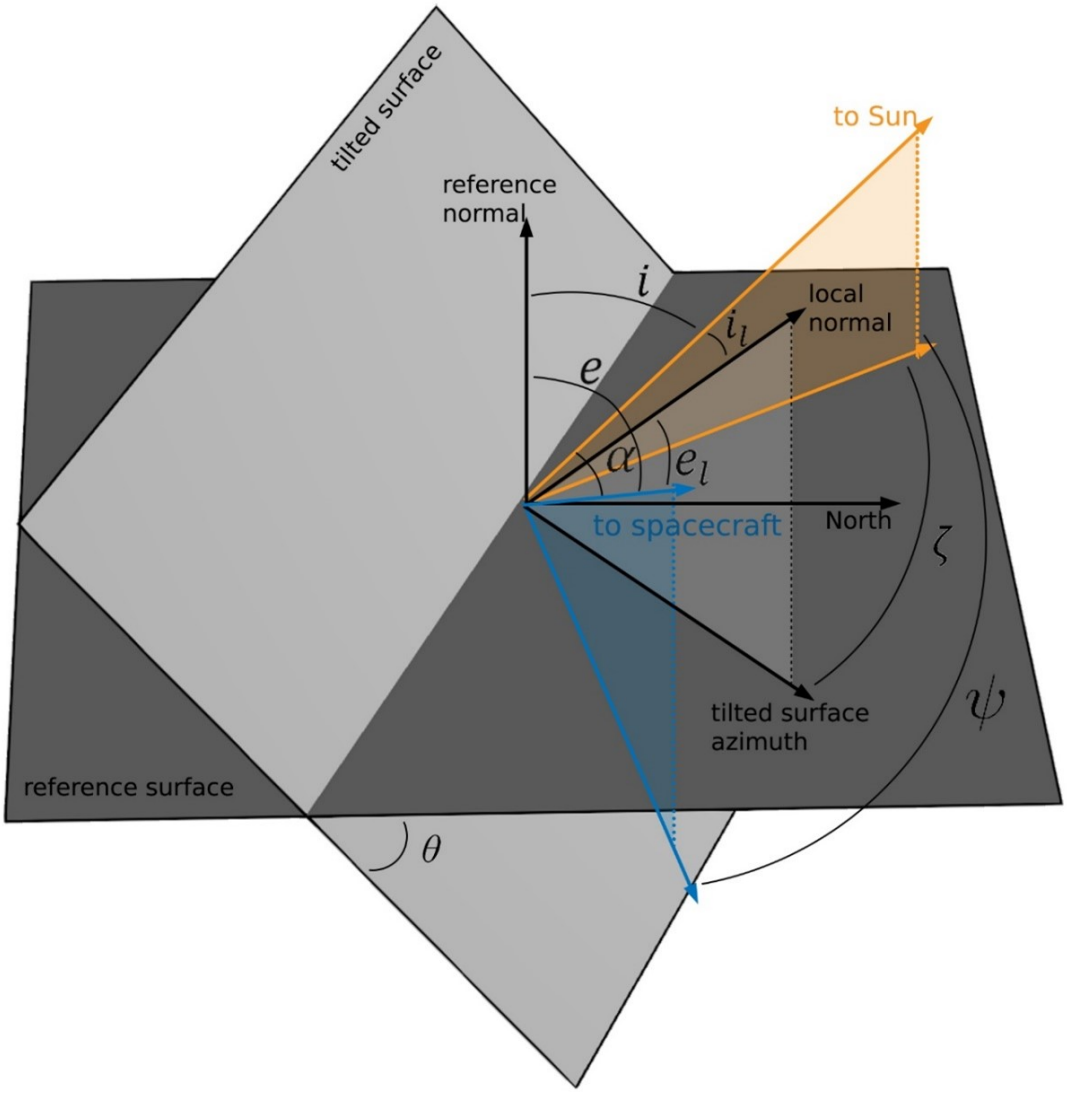

Figure 5.1: Sketch depicting all angles and relevant geometrical quantites referenced in the text. "Reference surface" (dark grey) is the standard Mars IAU ellipsoid. "Tilted surface" (light grey) represents the orientation of an arbitrary pixel of the DTM. Cyan arrows represent vectors pointing to the spacecraft position and sub-spacecraft point. Orange arrows are vectors pointing to the Sun and the subsolar point. "Reference normal" is a vector orthogonal to the reference surface. "Local normal" is a vector orthogonal to the titled surface. "Tilted surface azimuth" represents the direction that the tilted surface is facing. All angles are defined in the text.

image is then processed with the ISIS `campt` package to compute the incidence (i) and emission (e) angles with respect to the normal to the standard Martian ellipsoid. The same package also provides the subspacecraft and subsolar ground azimuths, whose difference gives us ψ. At this point, the local incidence and emission angles are computed with equation (5.8) and each disk function is evaluated by applying equations (5.3-5.7). We note that with this approach, the effect of planetary curvature on the local incidence and emission angles in not taken into account. This is reasonable for high-resolution datasets, such as HiRISE or CaSSIS, where planetary curvature is not significant. Should this not be the case, as for example in wide-angle camera datasets, a more precise methodology for computing the local incidence and emission angles should be adopted. For example, the ISIS `phocube` command could be used after running the `spiceinit` task with a digital terrain model of the surface (instead of an ellipsoid) as a shape model. In our case, the latter procedure took significantly longer to process a single image and did not improve our final results. Therefore, we decided to adopt the former approach. Finally, the radiometrically calibrated and atmospherically corrected orthoimage is divided by each disk function to obtain a topographically corrected image for each disk function. Fig. (5.2) reports an example of original and corrected images and local incidence and emission angle maps for HiRISE image ESP_021628_1335. For the Minnaert disk function, we apply the statistical bootstrap method (Efron, 1979; Press et al., 2002) to obtain the distribution of the k parameter and estimate its median value, which is then used for the correction. The performance of each disk function is evaluated by assessing whether the dependence of the corrected reflectance from the local incidence angle is removed. We only focus on the dependence from the local incidence angle because it was the most significant one in our case. An ideal, perfect correction would yield a constant I/F for all local incidence angles, i.e. a horizontal corrected reflectance profiles, which corresponds to the normal albedo of the surface at the phase angle of the observation. The presence of different materials having slightly different albedo, combined with uncertainties in the DTM will result in a spread around a global mean value, independently from the incidence angle. We use the statistical bootstrap technique to fit a linear model for each corrected reflectance profile to quantitatively compare each function. Among all disk functions, the lowest linear slope is selected as the best topographic correction. An example of original and corrected reflectance profiles obtained from HiRISE image ESP_021628_1335, including median linear slopes resulting from 500 bootstrap iterations, is shown in Fig. (5.3). This procedure is repeated for all the HiRISE images analysed in Schaefer et al. (2019). Image IDs and the final disk function used for the topographic correction are listed in Table (1).

5.3 Validation and scientific applications

To validate our method, we reproduce the relative albedo measurements of RSL reported in Schaefer et al. (2019) using topographically corrected (hereafter "corrected") images. Relative albedo is defined as the ratio between the I/F of two atmospherically corrected regions with the same illumination and observation conditions (Daubar et al., 2016). The relative albedo of two RSL are computed in Schaefer et al. (2019) by dividing the mean I/F of two region of interest (ROI) having 100% RSL pixels (RSL1 and RSL2 in Fig. 5.4) by the mean I/F of a "normalisation re-

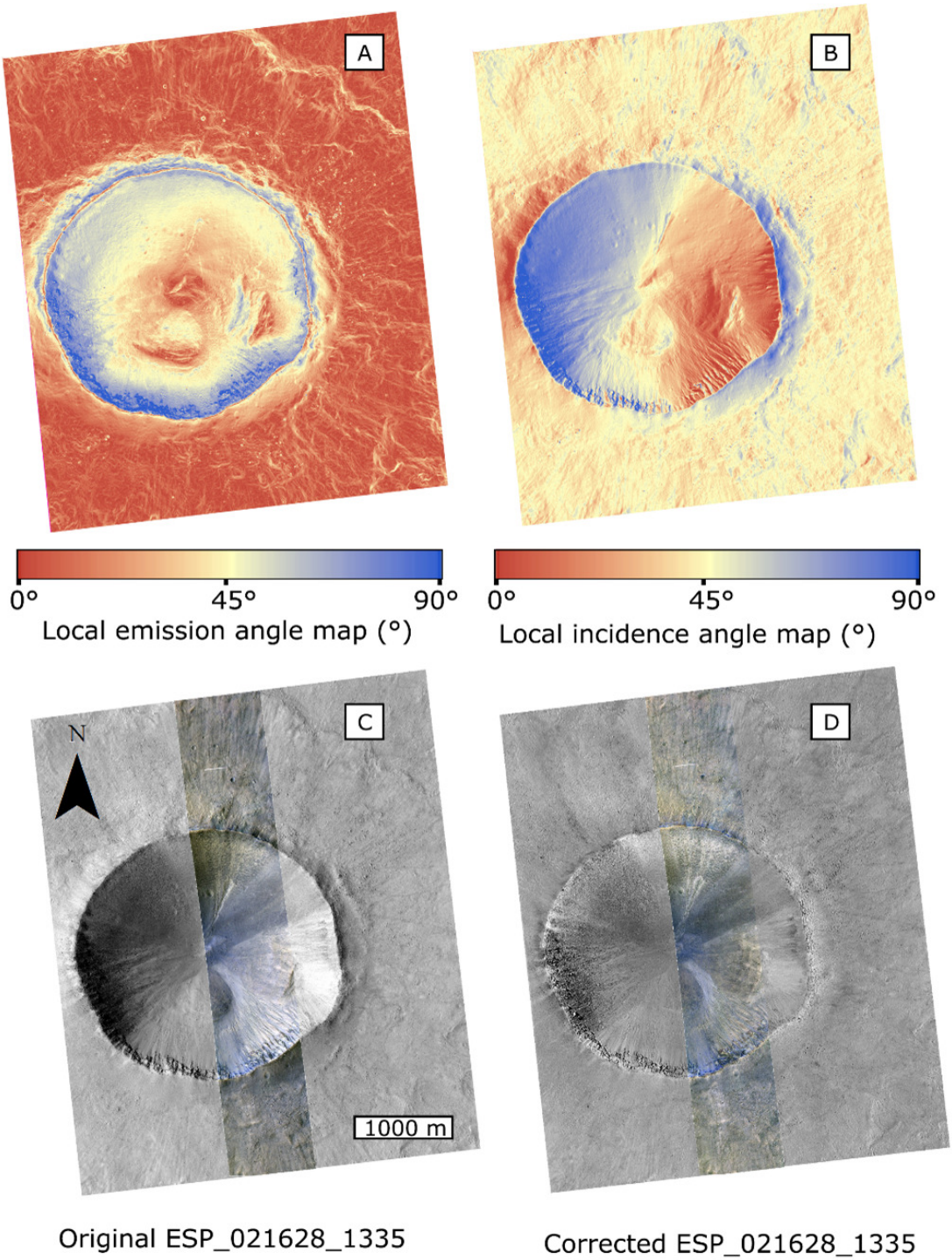

Figure 5.2: Topographic correction of HiRISE image ESP_021628_1335. A) Local emission angle map. B) Local incidence angle map. C) Original and D) Minnaert-topographically corrected HiRISE RED and IRB products.

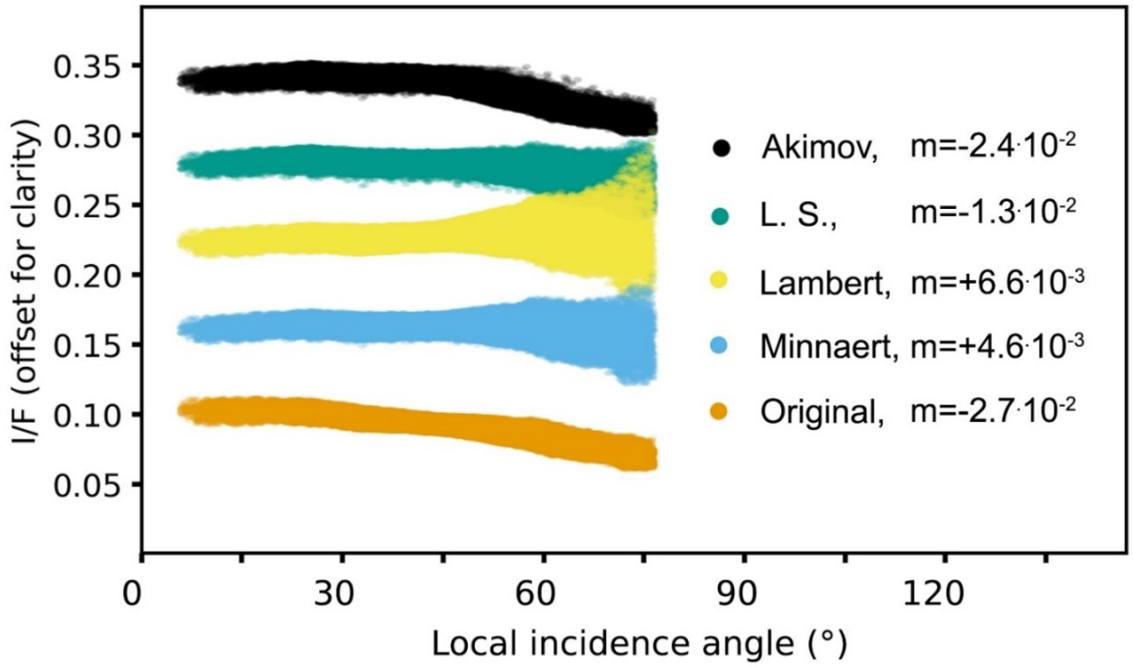

Figure 5.3: Original and corrected reflectance profiles (offset for clarity) for HiRISE image ESP_021628_1335 for each disk function and fitted linear slopes (median of 500 bootstrap iterations).

Image ID	Date	i_l^{min} (°)	$\langle i_l \rangle$ (°)	i_l^{max} (°)	e_l^{min} (°)	$\langle e_l \rangle$ (°)	e_l^{max} (°)	α (°)	Ls (°)	Band	Disk function
										IR	Minnaert, k=0.736±0.010
ESP_021628_1335	8/3/2011	17	29	48	19	28	31	43	250.6	RED	Minnaert, k=0.725±0.005
										BG	Minnaert, k=0.868±0.008
ESP_021773_1335	20/03/2011	14	27	45	30	34	39	50	257.8	RED	Lambert
ESP_022195_1335	21/04/2011	10	22	41	20	29	31	38	278.5	RED	Minnaert, k=0.798±0.004
ESP_022406_1335	8/5/2011	9	21	39	14	26	32	32	288.6	RED	Minnaert, k=0.783±0.008
ESP_022762_1335	5/6/2011	7	18	35	21	29	32	38	305.3	RED	Minnaert, k=0.847±0.01
ESP_022973_1335	21/06/2011	9	19	35	14	26	32	35	314.9	RED	Minnaert, k=0.809±0.009
ESP_023184_1335	8/7/2011	12	21	35	11	26	34	36	324.3	RED	Minnaert, k=0.836±0.009
ESP_023329_1335	19/07/2011	14	21	34	27	32	37	48	330.5	RED	Lambert
ESP_023540_1335	4/8/2011	17	24	35	18	28	31	45	339.4	RED	Lambert
ESP_024318_1335	4/10/2011	30	35	45	21	29	31	45	10.2	RED	Lambert
ESP_024885_1335	17/11/2011	40	44	54	17	27	31	60	31	RED	Lambert
ESP_027219_1335	17/05/2012	53	57	67	26	32	36	67	111.7	RED	Lommel-Seeliger
ESP_028551_1335	29/08/2012	41	49	61	19	28	31	87	162.7	RED	Minnaert, k=0.943±0.058
ESP_030819_1335	21/02/2013	14	26	44	8	25	35	71	269.1	RED	Minnaert, k=0.730±0.008
ESP_031254_1335	27/03/2013	6	19	36	34	43	50	28	290.2	RED	Lambert
ESP_032454_1335	29/06/2013	19	25	37	19	28	31	55	343.5	RED	Lambert
ESP_033021_1335	12/8/2013	29	34	44	15	27	32	48	5.9	RED	Minnaert, k=0.803±0.014
ESP_033944_1335	23/10/2013	43	48	58	18	28	31	55	39.6	RED	Lommel-Seeliger
MY34_004324_169_1	18/03/2018	0	41	120	0	17	60	39	285.8	PAN	Lambert

Table 5.1: Details of the images used in our analysis, acquisition date, Ls (°), filter and disk function that used for the topographic correction. i_l^{min},i_l^{max},$\langle i_l \rangle$ are the minimum, maximum and average local incidence angles for all considered ROIs (see Fig. 5.4) for each image. e_l^{min},e_l^{max},$\langle e_l \rangle$ are the minimum, maximum and average local emission angles for all considered ROIs for each image. α is the phase angle, which is constant for each image. Statistics for the CaSSIS image (last row) refer to the whole image.

gion" located far away and having the same illumination and observation conditions (CON in Fig. 5.4) of the RSL ROIs. The relative albedo of two nearby, RSL-free slopes (NEAR1 and NEAR2 in Fig. 5.4) is computed in the same way. Finally, the TEST ROI (see Fig. 5.4) has the same illumination and observation conditions of the CON ROI and it is used to check whether the latter has a constant albedo. To validate our correction, we perform additional relative albedo measurements on the corrected images using further control ROIs with a different geometry than the RSL and NEAR ROIs. Hence, we define six additional CON ROIs (CON1, CON2, CON3, CON4, CON5, CON6) located at the north-west, north and north-east facing portion of Tivat crater's rim, as shown in Fig. (5.4). To ensure the maximum possible consistency between our dataset and the one analysed by Schaefer et al. (2019), we used both the publicly available shapefile of their ROIs, which are shown in Fig. (5.4), and the same atmospheric correction, i.e. the subtraction of the darkest shadowed pixel from each image. We computed the relative albedo of the RSL1, RSL2, NEAR1, NEAR2 and TEST ROIs by dividing their mean I/F by the mean I/F of the CON region (see Fig. 5.4). We estimated 1σ uncertainties applying standard error propagation. We performed their same analysis on the uncorrected original images, and then on the corrected ones. In particular, the former is necessary to evaluate any residual, subtle difference, as those introduced by the possibly different coregistration of the images and ROIs. Our relative albedo measurements are reported in Fig. (5.5) for each ROI and for the original (green dots) and corrected (yellow dots) images, along with the relative albedo values reported in Schaefer et al. (2019) (solid lines). We notice that in some cases our measurements on the original images (green dots) are not perfectly equal to those previously obtained, nevertheless the differences are smaller than the measurements uncertainties and, hence, not significant. These are possibly due to a small relative misregistration between the ROIs and the underlying images. Indeed, while we used the same method to smooth and resample the DTM and to register the images, the relative coregistration between them depends on the selected control points and the reference image, which may be different in our case. If we compare our measurements on the original images with those on the corrected images (yellow dots in Fig. 5.5), we notice also in this case small, and not significant, differences between the two datasets, again below the uncertainties. These may be due to small differences in incidence and emission angles between the ROIs. In Fig. (5.6) we report our relative albedo measurements of the RSL1, RSL2, NEAR1 and NEAR2 ROIs using both the original (grey markers) and topographically corrected (yellow markers) images and the CON6 ROI as normalisation. We compare them with the relative albedo measurement obtained with the CON ROI (blue line and light-blue shaded band) as normalisation. Since the RSL and NEAR ROIs have the same illumination condition, the CON ROI normalisation provides reliable relative albedo measurements even using the original images: it can be therefore used to validate other normalisations. As shown in Fig. (5.6), for all ROIs, the relative albedo measurements obtained using the CON6 control region on the corrected images are consistent (yellow markers), within the estimated uncertainties, with those derived on the original images using the "CON" ROI (light-blue shaded band). The relative albedo measurements on the original images (using CON6 control region, grey markers), on the contrary, are significantly different from those obtained on the original image using CON ROI, as expected. This shows that the application of our method allows to correct for the topographic

shading and perform relative albedo measurements even when there are no ROIs with the same orientation of the features of interest (in our case, RSLs). To better highlight this point, in Fig. (5.6e) we recreate Fig. (5.11) of Schaefer et al. (2019) but using the CON6 ROI as normalisation, obtaining their same relative albedo evolution over time. In particular, we also find that RSL fading occurs when the neighboring RSL-free slopes (NEAR1 and NEAR2) darken until matching the RSL relative albedo.

The same conclusion also applies to all the other normalisation ROIs (CON1 to CON5) displayed in Fig. (5.4). The relative albedo measurements obtained with these ROIs are displayed in Fig. (5.7). To use a more compact visualisation, we plot on the x-axis of each panel the relative albedo values normalised with the CON region. Since the CON region has similar illumination conditions to the RSL and NEAR ROI, the corresponding relative albedo values are not affected by topographic shading and provide the most reliable measurement possible. Therefore, we will now refer to them as "true" relative albedo measurements. On the y-axis we plot relative albedos computed on both the topographically corrected images (yellow markers) and the original images (grey markers) for each normalisation ROI. We will refer to the former as "corrected" and to the latter as "original" relative albedo measurements. In the case of a perfect topographic correction, the y and x values would be identical showing a 1:1 relationship, and a linear regression of y vs x would yield the cyan solid line, which is displayed in each panel of Fig. (5.7). The "original" measurements (grey markers) are instead affected by topographic shading and they do not show a 1:1 relationship with the x-axis. As a consequence, the grey-dashed regression line, obtained by fitting a straight line to the "original" datapoints, has a significantly different slope and intercept with respect to the cyan solid line. When applying the topographic correction, the "corrected" measurements (yellow markers) result very close to the 1:1 relationship. Indeed, the resulting red-dashed regression line is enclosed to the cyan one, which would be ideally obtained with a perfect correction. In Table (1) we also report the minimum, maximum and the average incidence and emission angles as well as the phase angle (which is constant) of all the analysed ROIs for each image. This is useful for estimating the range of angles in which our correction has been validated. In particular, the incidence angle ranges from 6° to 67°. The emission angle ranges from 8° to 50°. The phase angle ranges from 28° to 87°. Outside these ranges, our methodology shall be applied very carefully for quantitative analyses. For example, the quality of the correction could be assessed by evaluating the shape of the corrected reflectance profile, that should be horizontal in the area of interest. For low phase angles observation, instead, more complicated functions that incorporate opposition effects, as the Hapke model, should be applied and validated.

5.4 HiRISE and CaSSIS case studies

5.4.1 Topographic correction of HiRISE colour images of Tivat crater

We apply the topographic correction to all filters of the HiRISE colour orthoimage ESP_021628_1335 of Tivat crater, obtaining the results in in Fig. (5.8). As we already considered the RED HiRISE filter in section (3.2), we now extend our anal-

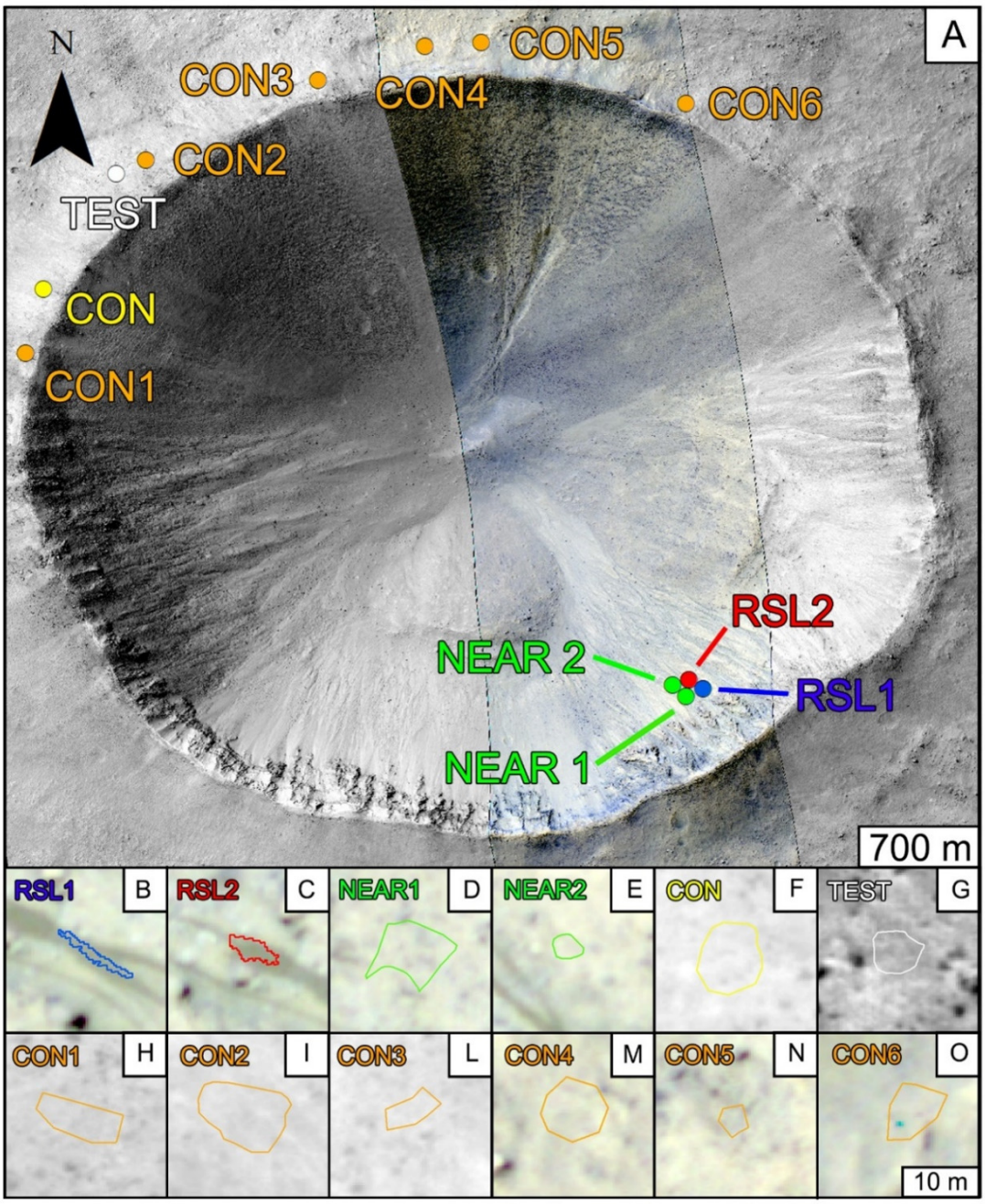

Figure 5.4: A) HiRISE image ESP_022973_1335 of Tivat crater showing the ROIs used for the relative albedo analyses. B) to G) ROIs used both in Schaefer et al. (2019) and in our analysis. H) to O) are additional ROIs that are used to validate our topographic correction.

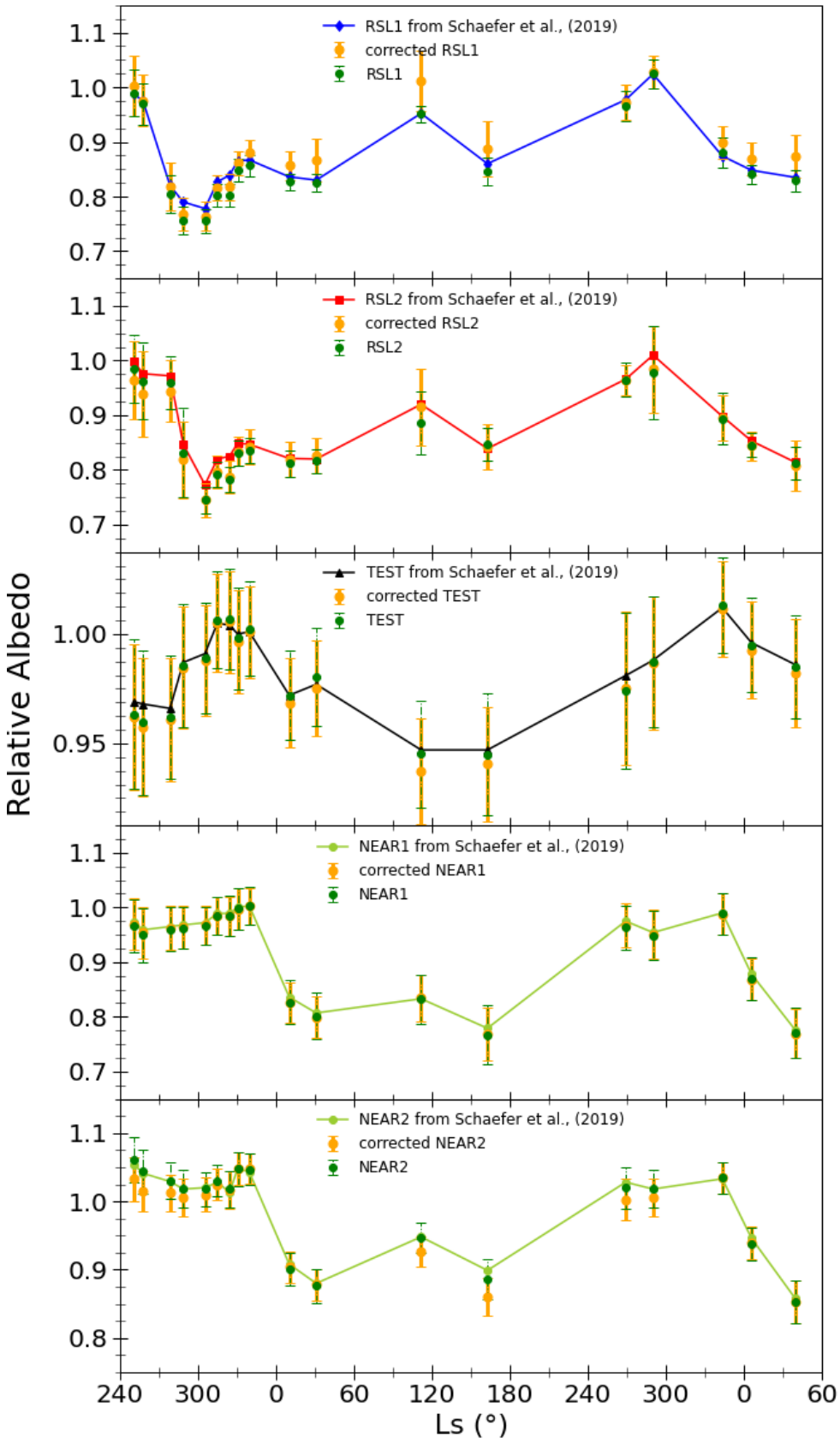

Figure 5.5: Comparison between our relative albedo measurement and those obtained by Schaefer et al. (2019). In each panel, solid profiles represent the measurements from Schaefer et al. (2019). Our measurements on the original images are displayed with green dots, while our measurements on the corrected images are shown with yellow dots. Error bars represent 1σ uncertainties.

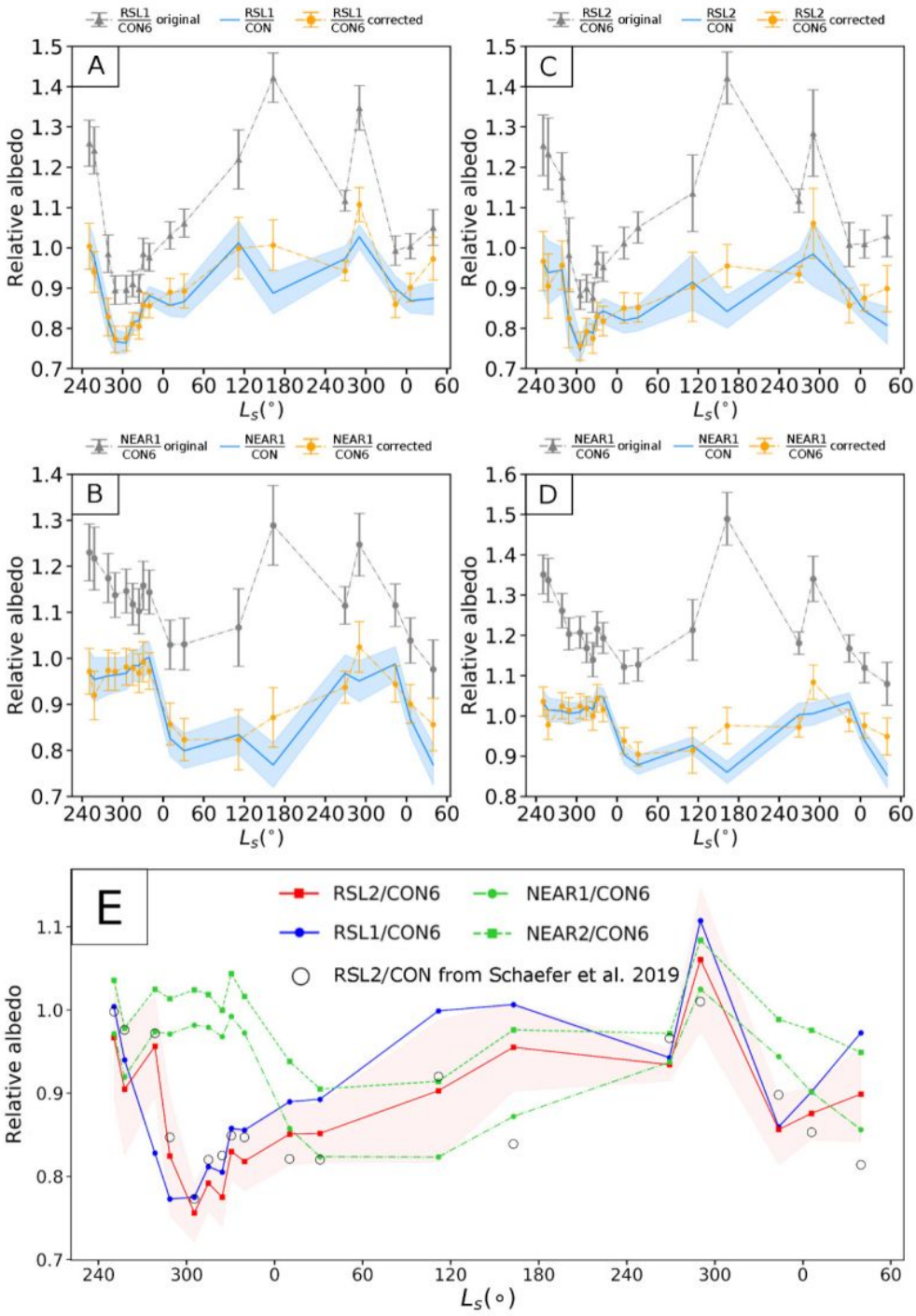

Figure 5.6: Relative albedo measurements of the A) RSL1, B) NEAR1, C) RSL2 and D) NEAR2 ROIS. The light-blue solid lines represent the relative albedo values obtained with the CON ROI as normalisation. Grey and yellow markers are measurements on the original and corrected images, respectively, using the CON6 ROI as normalisation. Error bars and the light-blue shaded region represents 1σ uncertainties E) Relative albedo measurements on corrected images using CON6 as normalisation. Circles are RSL2/CON from Schaefer et al. (2019). The red shaded band represents the uncertainty on RSL2/CON6. Error bars for the other profiles are omitted for clarity.

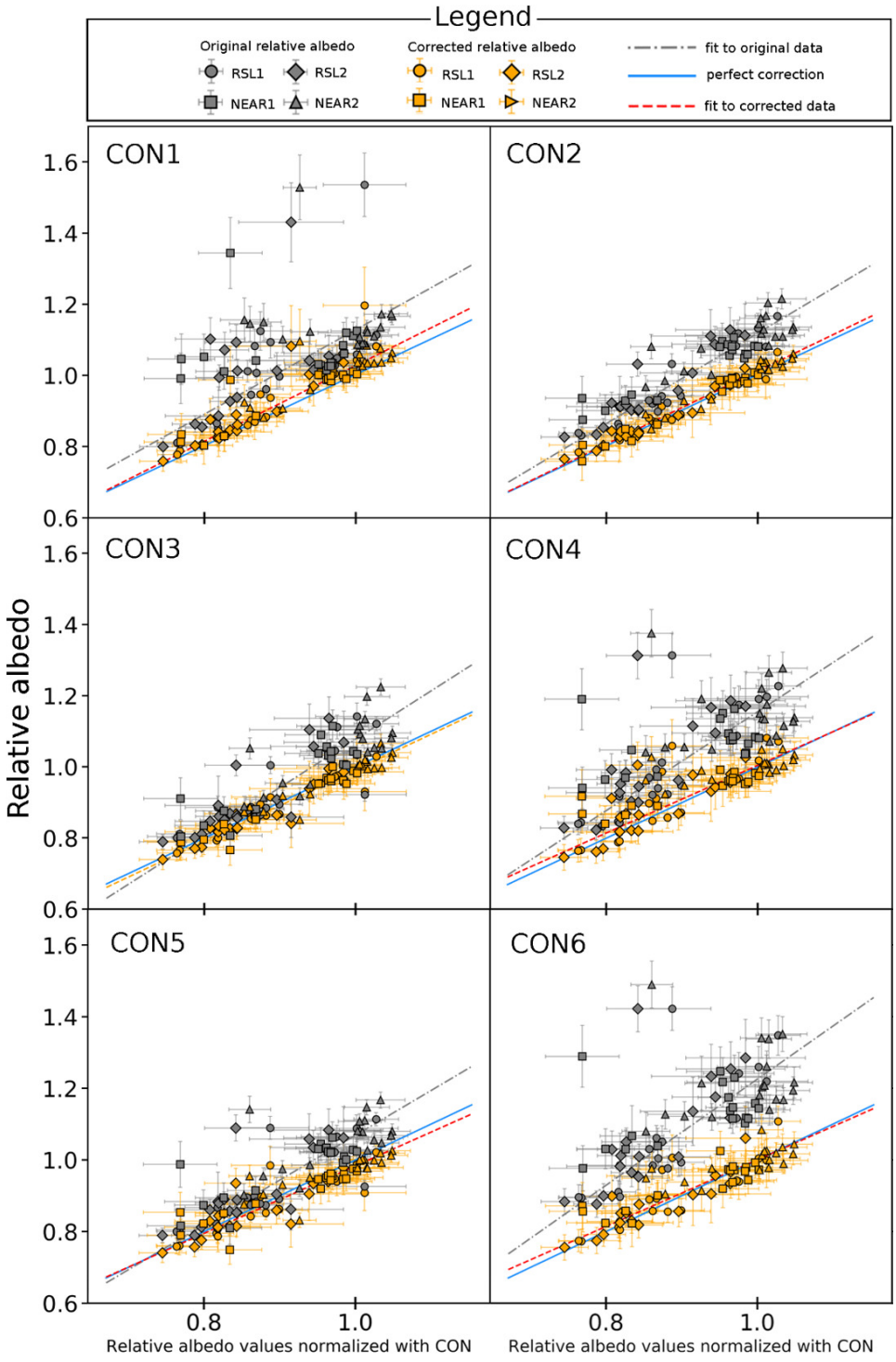

Figure 5.7: On the x-axis of each panel we plot relative albedo values normalised with the CON ROI and on the y-axis the relative albedo values normalised with the CON1 to CON6 ROIs. Grey and yellow markers are measurements performed on the original and topographically corrected images, respectively. The grey dashed line is a linear fit of the "original" data. The red dashed line is a linear fit of the corrected data. The cyan solid line is the linear fit that would be ideally obtained for a perfect correction

ysis to the NIR and BG bands. The local incidence and emission angles maps were already computed in section (3.1) and are depicted in Fig. (5.2). The original and corresponding corrected IRB images are shown in Fig. (5.8a,b). Qualitatively, the corrected image has a more uniform surface brightness and allows to better identify regions with different colours. The visibly more uniform brightness of the corrected images cannot be attributed to an "ad-hoc" stretching of the image but, instead, to the removal of most brightness variation induced by topographic shading resulting from the applied correction. This is quantitatively shown in Fig. (5.8), where we compare surface reflectance profiles extracted from the two regions defined by the black rectangles A1 and B1 in the original IRB image (Fig. 5.8a) with their counterparts A2 and B2 in the topographically corrected IRB image (Fig. 5.8 8b). Both regions are compositionally homogenous and should have a constant surface brightness, once topographic shading has been removed. Panels A1 and A2 show the line profiles used to extract the surface reflectance in the original (light-blue line) and corrected images (orange line), respectively, for the first region. Panels B1 and B2 show the line profiles used to extract the surface reflectance in the original (light-blue line) and corrected image (orange line), respectively for the second region. Panels A3, A4 and A5 show the reflectance profiles extracted from the original (light blue solid line) and corrected (light blue solid line) images in the NIR, RED and BG filters, respectively, for the first region (panels A1 and A2). Panels B3, B4 and B5 show the reflectance profiles extracted from the original (light blue) and corrected (orange) images in the NIR, RED and BG filters, respectively, for the second region (panels B1 and B2). For both regions and in all filters, the corrected reflectance profiles always yield a lower slope, meaning that surface brightness variation induced by topography have been successfully removed.

5.4.2 Comparison of RSL and dust-devil tracks colour properties at Tivat crater

We apply our method to a further HiRISE image, the ESP_022762_1335 orthoimage, that provides an interesting scientific case because it shows both dust devil tracks and RSL. To achieve our goal, we applied the topographic correction to the BG, RED and NIR filters of HiRISE orthoimage ESP_022762_1335. For the RSL and neighboring slopes, we used the RSL1, RSL2, NEAR1, NEAR2 ROIs already defined in Section (3.2) and displayed in Fig. (5.4). For the dust devil track and the nearby surface, we define the DD1 and NEARDD1 ROIs, as displayed in Fig. (5.9). Relative albedo was computed as in Section (3.2) using the CON5 ROI as normalisation. The latter was selected because it was well within the colour swath of ESP_022762_1335. To cross-check our calculations, we also computed DD1/CON4 and NEARDD1/CON4, obtaining similar results. In contrast, CON6 was outside the colour swath. As demonstrated in Section (3.2) and Fig. (5.7), despite having different illumination conditions than the other ROIs, this region allows to recover "true" relative albedos when using topographically corrected images. The obtained relative albedo in all HiRISE filters are reported in Fig. (5.9) and show that RSL are darker than the material within the dust-devil tracks, moreover, there are no significant colour differences. The same behaviour is also seen between RSL and RSL-free material (RSL1,2 vs NEAR1,2), and between the dust-devil track and the nearby surface outside the track (DD1 vs NEARDD1). We also notice that both

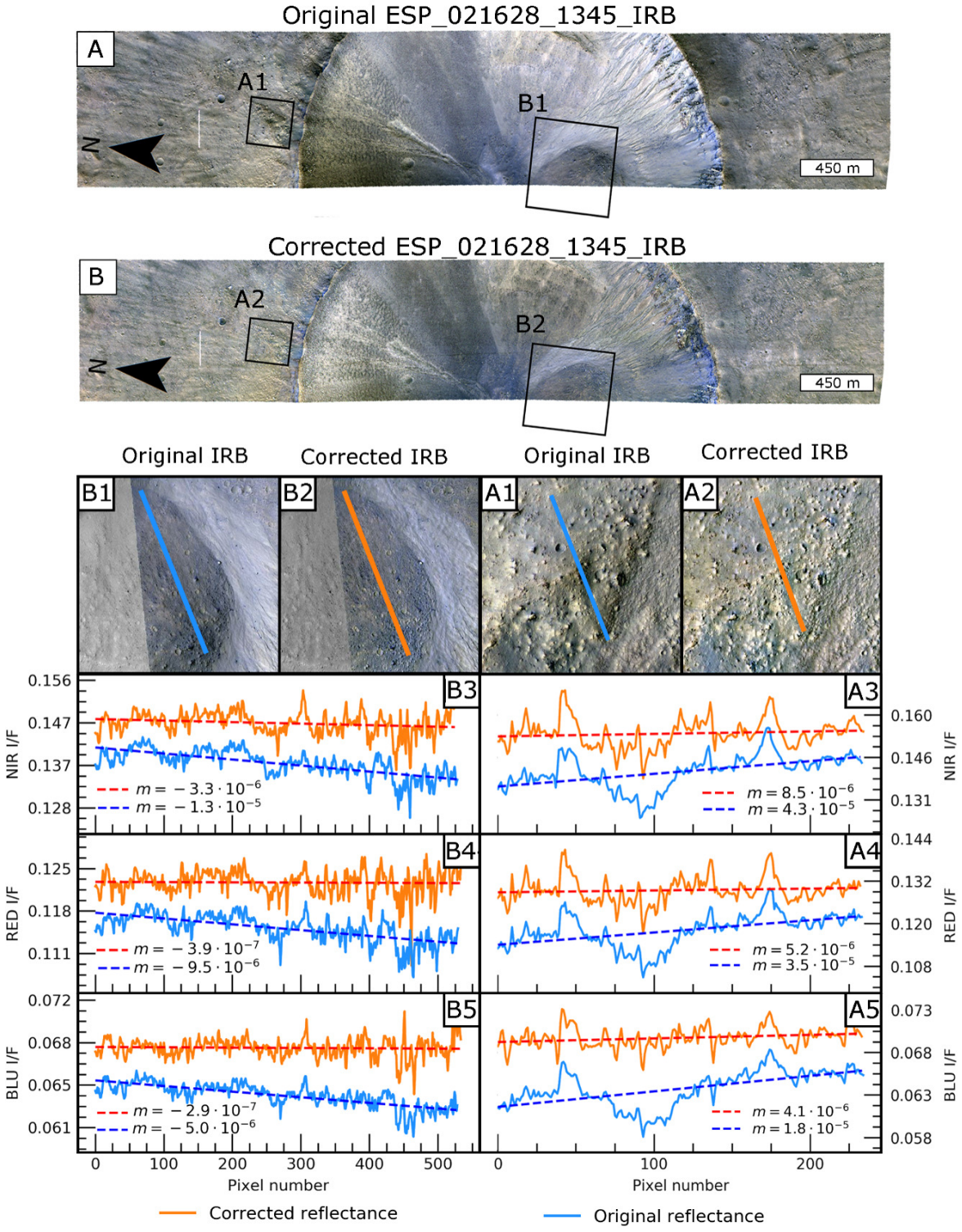

Figure 5.8: Topographic correction of BG, RED and NIR filters of HiRISE image ESP_021628_1335_IRB. A) Original image. B) Corrected image. A Minnaert correction was applied for all the filters with the coefficients in Table (1). A1, A2, B1, B2) Zoom of the black rectangles in panels A) and B) and line profile used to extract surface reflectances. A3) Original (light blue) and corrected (orange) reflectance profiles extracted from A1 and A2, respectively, in the NIR filter. B3) Same as A3 but for B1 and B2). A4 and B4) Same as A3 and B3 but for the RED filter. A5 and B5) Same as A3 and B3 but for the BG filter.

RSL, dust-devil tracks and the surface outside the dust-devil track have the same colour trend, i.e. they have the lowest relative albedo in the NIR and BG bands, but the highest relative albedo in the RED. However, we recall that these differences are within the measurement uncertainties, so they may therefore be not robust.

5.4.3 Topographic correction of a CaSSIS panchromatic image

The third application of our method is the topographic correction of a CaSSIS orthoimage depicting the north-eastern part of the summit caldera complex on Ascraeus Mons (11.2° N, 255.9° E). Since it has a very complex topography, this site shows a significant topographic shading and it is an interesting target to showcase the performances of our correction. The observations were performed in stereo mode, allowing the production of both DTM and orthoimages through the 3DPD photogrammetric pipeline (Simioni et al., 2021). These products are shown in Fig. (5.10) along with the computed local incidence and emission angle maps. The resulting topographically corrected dataset is shown in Fig. (5.11). In particular, Fig. (5.11B) depicts the corrected image, where a Lambert model provided the best correction. Again, the corrected image displays a more uniform surface brightness, compatibly with the removal of topographic shading. This is quantitatively shown by comparing surface brightness profiles in Fig. (5.11): in all the example regions (black rectangles in Fig. (5.11A,B) the corrected reflectance profiles (orange lines in panels A3 to C3) are always flatter than their original counterparts (light blue lines in panels A3 to C3). This means that most brightness differences induced by the different pixels orientation are corrected by the photometric model. The clearest example is shown in panel (C3) of Fig. (5.11), where a relative darkening of $\approx 30\%$ in the original profile (light blue solid line) is successfully corrected, resulting in a uniform, straight corrected reflectance profile (orange solid line).

5.5 Discussion

We tested and evaluated a method to correct satellite images from brightness differences induced by topographic shading. The aim of the topographic correction is to exploit the resulting corrected images to perform photometric studies of surface features. In this work, we focus on the topographic correction of images of the Martian surface obtained by the HiRISE and CaSSIS visible cameras. We highlight that this method could be applicable to any satellite image if a high-resolution DTM of the surface, required for an accurate computation of the local incidence and emission angle maps, is available. We compared the performance of four disk functions and, for each analysed image, we selected the one producing the flattest corrected reflectance profile. We validated our approach using relative albedo measurement of RSL at Tivat crater. The site was already studied by Schaefer et al. (2019), whose dataset was used as "ground truth" for assessing our method. As shown in Figures (6) and (7), the corrected relative albedo measurements, normalised with regions of arbitrary illumination conditions (CON1 to CON6 in Fig. 5.4), are consistent with the "true" ones, computed by ratioing regions having the same illumination conditions (i.e. by CON in Fig. 5.4). On the contrary, when using the original images, the different illumination conditions between the RSL and normalisation ROIs result in significantly

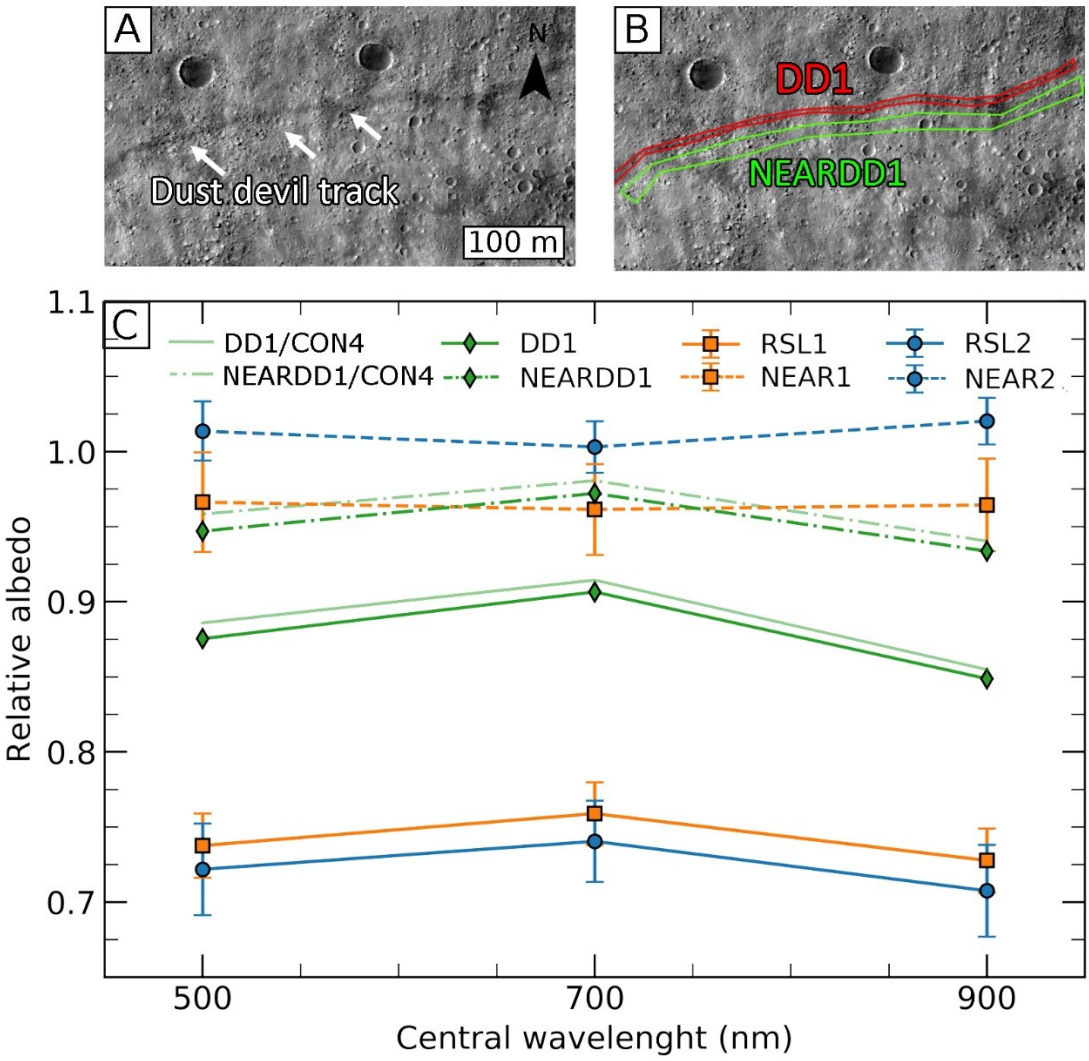

Figure 5.9: A) Dust devil track considered for the relative albedo analysis. B) DD1 and NEARDD1 ROIS, used for extracting the mean I/F from of the dust devil track and the nearby material. C) Comparison of relative albedo between the RSL1 and NEAR1 (yellow squares), RSL2 and NEAR2 (light-blue circles) and DD1 and NEARDD1 (green diamonds) ROIs in the HiRISE bands. The x-axis shows the central wavelength of each filter. Shaded green profiles are obtained with the CON4 normalisation ROI, while all others with the CON5 normalisation ROI.

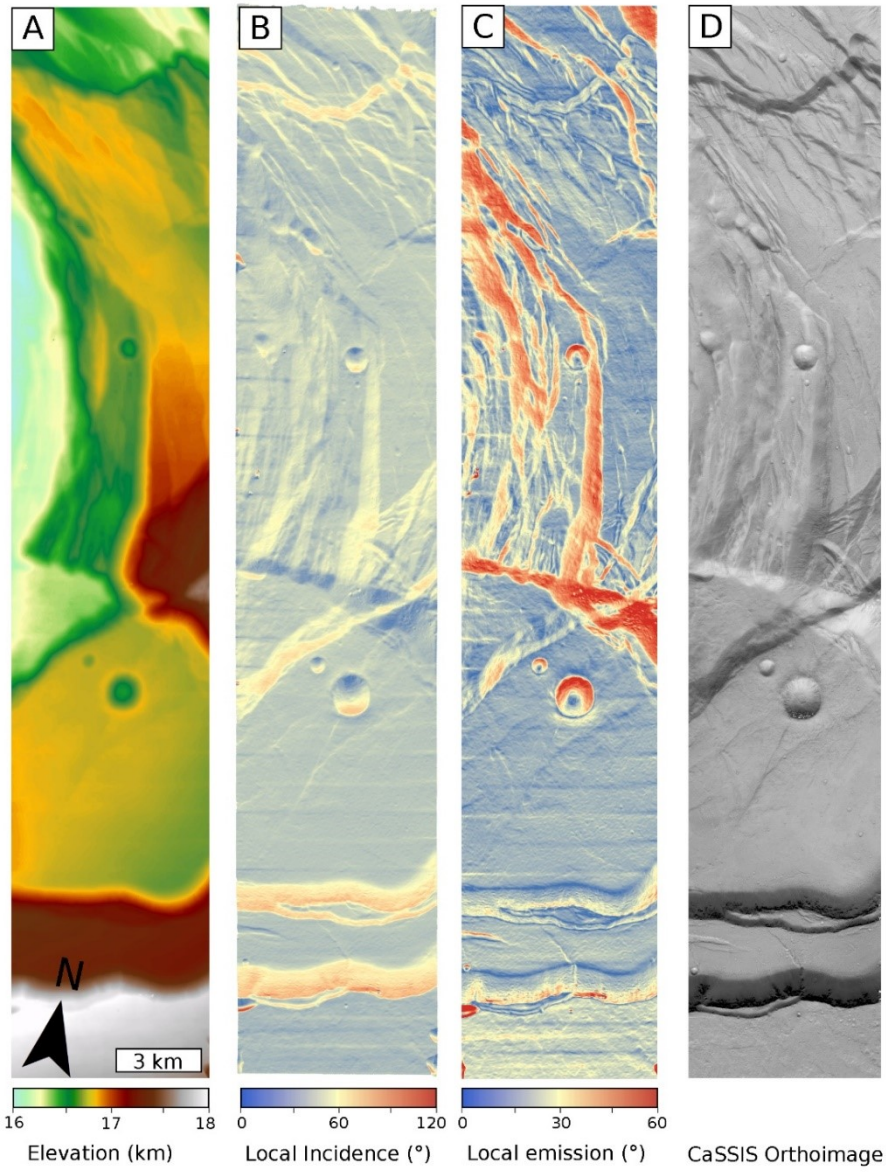

Figure 5.10: DTM of Ascraeus Mons caldera obtained from stereo pair MY34_004324_169_1. Elevations values are defined on the MOLA Datum (`https://pds-geosciences.wustl.edu/missions/mgs/megdr.html`) B) Local incidence and C) local emissions angle maps. D) CaSSIS orthoimage CAS-OTH-MY34_004324_169_1-OPD-03-02-PAN_1.

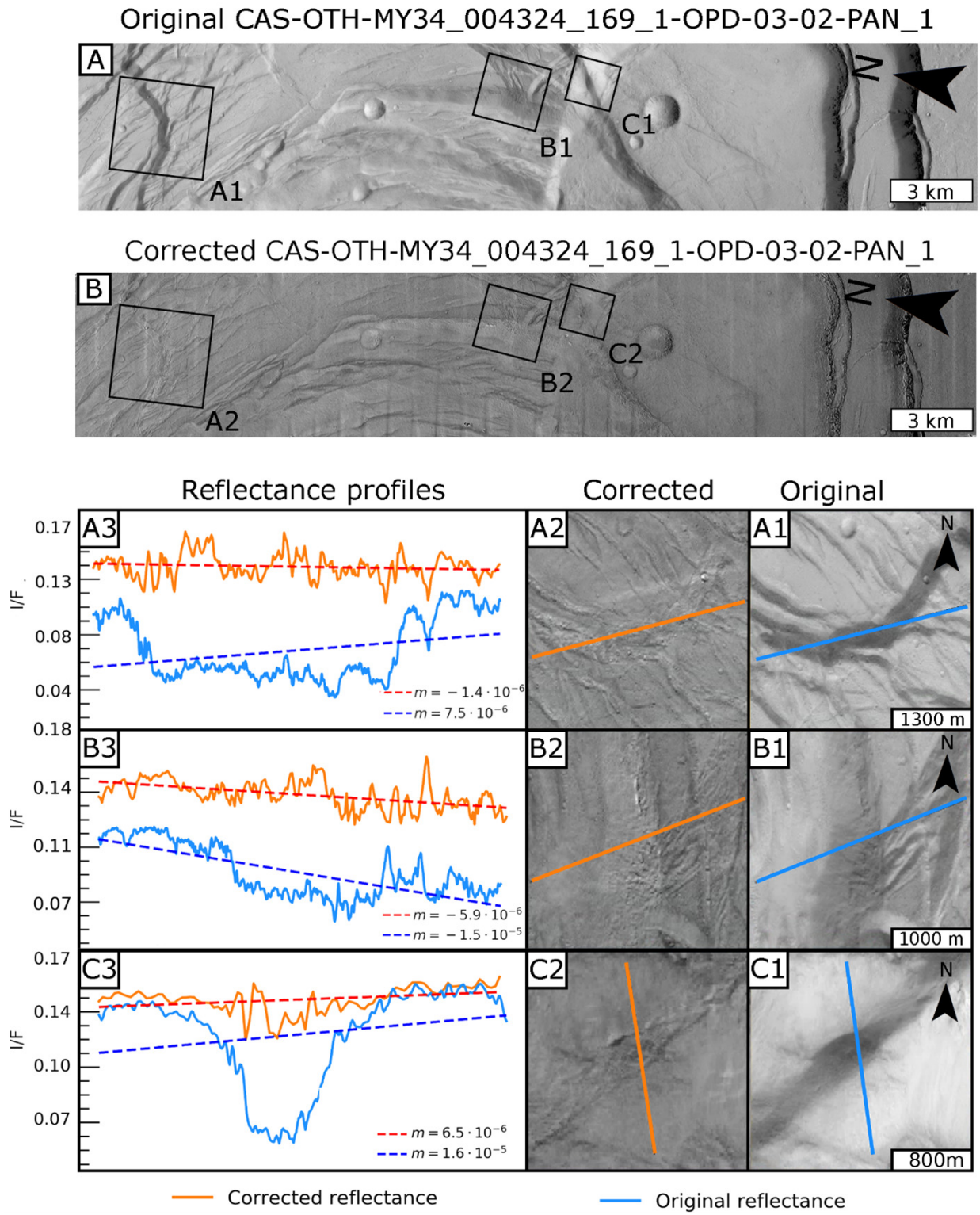

Figure 5.11: Topographic correction of the PAN filter of CaSSIS orthoimage CAS-OTH-MY34_004324_169_1-OPD-03-02-PAN_1. A) Original image. B) Lambert-corrected image. Examples of line profiles extracted from the black rectangles of the original (A1, B1 and C1) and corrected (A2, B2, C3) images. Panels (A3, B3 and C3) show the original (light blue) and corrected (orange) reflectance profiles extracted from each region. Red dashed lines represent linear fits to the corrected reflectance profiles. Blue dashed lines are linear fits to the original reflectance profiles. The m values are the linear slopes of each fit.

different relative albedo values, not compatible with the "true" ones. To further validate our method, in Fig. (5.7) we reproduced the same relative albedo evolution reported in Schaefer et al. (2019), but using the CON6 normalisation ROIs, which has different illumination conditions than the RSL and NEAR ROIs. In addition, in Fig. (5.7), we show that any of the CON1 to CON6 normalisation ROIs resulted in relative albedo values compatible with the "ground truth". This means that the method here presented can be used to perform photometric analyses of surface features, even when there are no normalisation regions having their same illumination and observation conditions. This capability allows to enlarge the applicability of this tool. For instance, this enables to extend the relative albedo analyses of RSL to a larger number of sites and investigate whether the same relative albedo evolution that occurs at Tivat crater applies to other locations. Another application here considered is the correction of HiRISE colour datasets. As shown in Fig. (5.8), the corrected IRB image appears "flatter" and more uniform that the original one, consistently with the successful removal of topographic shading in all bands. This is quantitatively confirmed by panels (A3, B3, A4, B4, A5, B5) of Fig. (5.8), where flatter corrected I/F profiles for each band and for both the investigated regions are outlined. The successful correction of HiRISE colour images is particularly interesting because, due to the relatively small colour swath of HiRISE, the probability of finding normalisation regions with the same illumination conditions of the feature of interest is even smaller than in the RED filter. This is the case of Tivat crater, where a ROI having the same illumination and observation conditions of the RSL features could not be found within the colour swath, in principle preventing relative albedo analyses in the NIR and BLU filters. On the contrary, the methodology here presented could be further used to correct images acquired in all filters and explore the relative albedo evolution of RSL and other albedo features throughout multiple Martian years. In Section (4.2) we provided an example of analysis that could be performed on a single HiRISE colour observation. In particular, Fig. (5.8) reports the results coming from the comparison of relative albedo of two RSL, one dust devil track and neighboring slopes in the BG, RED and NIR HiRISE filters. Consistently with previously reported RSL/adjacent slopes colour ratios (McEwen et al., 2011), we find no significant differences between colours of RSL and nearby slopes (orange and blue solid vs dashed lines in Fig. 5.8), further validating the applicability of our method to multiband datasets. In addition, we find that RSL and the dust devil track have a similar relative albedo behaviour in the HiRISE bands (orange and blue vs green solid lines in Fig. 5.8), even though RSL are systematically darker than dust devils. Although both features have a higher relative albedo in the RED and lower in the BG and NIR filters, these differences are within the measurement uncertainties, hence not robust. However, since dust devil tracks are well established dust-removed features, the fact that they have similar colour properties to RSL suggests that these are dust-removed too, consistently with independent conclusions of previous studies (Munaretto et al., 2020; Schaefer et al., 2019; Vincendon et al., 2019). The systematic difference in relative albedo between RSL and dust-devil tracks may be due to different amounts of dust deposited within the two features. In particular, RSL may be slightly more dust-depleted than dust-devil tracks, hence explaining the darker relative albedo. This picture is broadly consistent with the relative albedo measurement of dust deposition on Martian "dark areas" soil analogs, which are representative of typical RSL sites, as reported in (Wells et al., 1984).

Fig. (5.12), adapted from Fig. (5.3) of Wells et al. (1984), shows the relative albedo evolution of volcanic soil in response to progressive dust fallout. The measurements ofWells et al. (1984) are relative to a $BaSO_4$ paint standard, so only ratios of profiles in Fig. (5.12) can be compared in this discussion. From a qualitative point of view, the addition of dust has the main effect of increasing the relative albedo of the soil in the whole spectrum. A fallout of $6.4 \cdot 10^{-4}$ g/cm^2 of dust (less than a half of 1-year deposition on Mars) can increase the reflectance of a factor 4 (i.e. a relative darkening of 75%). A secondary effect is a slight increase in spectral slope shortward of 700 nm. Since we have a relatively small darkening of RSL with respect to dust-devil tracks and nearby regions ($\approx 10 - 25\%$), the amount of removed dust should be relatively small, meaning that RSL do not have an extremely lower amount of dust with respect to the nearby slopes. If this were not the case, we should observe a larger relative darkening. This is outlined in Fig. (5.12): "Deposit 1" has 7 times less dust than "Deposit 4" and shows a relative darkening of $\approx 50\%$ at wavelengths greater than 600 nm. "Deposit 2" has 4.2 times less dust than "Deposit 4" and shows a relative darkening of $\approx 30\%$. When comparing relative albedo profiles of features with small differences in deposited dust, the variation in spectral blue slope is very small and the main effect of the dust addition is to vertically shift the spectrum to higher reflectance. This is found for example when comparing the relative albedo profiles of the "Dust-free soil" with "Deposit 1", or "Deposit 1" with "Deposit 2". These are consistent with our results coming from the comparison between the relative albedo of the dust-devil track and the RSL in the HiRISE bands, hence further supporting RSL as dust-removed features as dust-devil tracks. It is also interesting to compare our relative albedo in the HiRISE bands with what would be expected by a difference in water content of the regolith. Fig. (5.11) of Pommerol et al. (2013) reports bidirectional reflectance spectra of dry and wet Martian soil analogs. In particular, we see that as soon as a liquid phase is present within the soil simulant the reflectance spectra has a lower spectral slope and lower reflectance. As water lowers the spectrum significantly more in the wavelengths corresponding to the HiRISE RED and NIR channels, we should therefore see a lower relative albedo in these two bands and a BG relative albedo close to unity. In contrast, we see a more uniform darkening in all bands, meaning that a higher hydration of RSL with respect to nearby slopes is not supported by our results. A more detailed analysis considering both the convolution of the measurements reported in Wells et al. (1984) and in Pommerol et al. (2013) with the HiRISE detector spectral response and the implementation of a more accurate atmospheric correction could provide a more quantitative assessment of this scenario. The last application of our method is the topographic correction of a CaSSIS orthoimage. At this stage, we only focus on the panchromatic filter using the available stereo observations of the Ascraeus Mons summit caldera complex and the DTM of the overlapping region (Fig. 5.10) produced to apply the topographic correction. The complex topography of this site yields a significant topographic shading, offering us a test-bench for our correction. The corrected orthoimage in Fig. (5.11B) shows a significantly more uniform surface brightness and flatter reflectance profiles than the original orthophoto (Fig. 5.10, 5.11), consistently with the proper removal of topographic shading

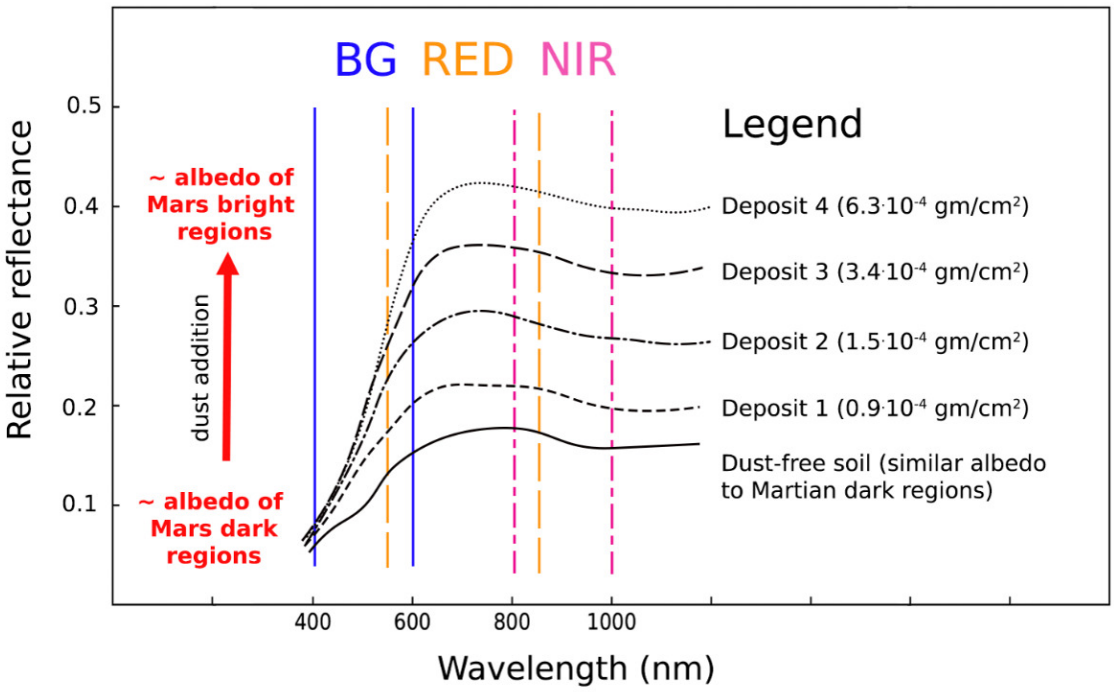

Figure 5.12: Effect of dust fallout on Mauna Kea volcanic soil (Readapted from Fig. (5.3) of Wells et al. (1984). Vertical lines represent the HiRISE BG, RED and NIR filters spectral ranges.

5.6 Conclusions

We presented a method to correct the topographic shading in HiRISE and CaSSIS images. Our approach is similar to the photometric correction usually performed on global mosaics or spectroscopic datasets, but it takes advantage of high resolution digital terrain models to compute with high accuracy the local illumination conditions of each pixel of the images. It evaluates the best disk functions among the Lambert, Akimov, Minnaert and Lommel-Seelinger photometric models. We validated our method performing relative albedo measurements of RSL at Tivat crater and getting results consistent with published measurements obtained at the same site. To highlight the scientific potential of our method, we applied it to colour HiRISE orthoimages of Tivat crater. Specifically, we used topographically corrected images to estimate the relative albedo of RSL and dust-devil tracks in all HiRISE filters. Our results are consistent with previous analyses based on RSL colour ratios, hence showing that this method is applicable to high-resolution multiband datasets. In addition, we find that RSL are darker than the analysed dust-devil track but they have similar colours, hence hinting a similar origin as dust-removed features. Further comparisons with multi-band relative albedo of different Martian albedo features and with laboratory experiments may better assess this scenario. We also corrected a CaSSIS panchromatic image of the Ascraeus Mons summit caldera complex. Since it has a very variable topography, this site displays a significant topographic shading and allowed us to test the performances of our method. In all the presented case studies, the corrected images showed more uniform brightness values, independently from the local illumination conditions, and flatter reflectance profiles than the original, uncorrected, images. Without requiring the presence of

normalisation regions having the same illumination conditions of the features of interest, our topographic correction allows to perform relative photometry analyses on a larger sample of datasets, including CaSSIS panchromatic and HiRISE colour images. It may also be used for other multispectral datasets, if a high-resolution DTM is available, required to compute the local incidence and emission angles with high accuracy. In particular, future CaSSIS stereo observations, providing both colour images and a DTM of the surface, will allow to extend our analysis to the remaining CaSSIS filters and better investigate the colour properties of Martian albedo features.

Chapter 6

Summary and future prospects for volatile-related Martian surface features research with CaSSIS

Throughout the first part of this Ph.D. thesis, we presented the work that was carried out to characterise the nature and formation mechanism of Martian RSL, exploiting new datasets and analyses available thanks to the CaSSIS stereocamera. At the start of this project, the origin of RSL and their relationship with liquid water was highly debated in literature. As already discussed in sections (1.6,3 and 4) initial studies and observations suggested that liquid water or brines may trigger RSL activity. However, more and more evidences towards dry mechanisms that do not require water are being put forward by recent studies, including the analyses presented in Chapters (3,5), published in Munaretto et al. (2020, 2021b), and the analysis in Chapter (4), currently under revision. This decade-old debate is the core and starting point of the Mars-related part of this work.

We decided to address the problem from an observational perspective, combining pre-existing HiRISE images of RSL with new observations from the CaSSIS camera. Both instruments have been described in Chapter (2). In particular, CaSSIS allowed, for the first time, to compare morning RSL observations with afternoon ones. The analysis and interpretation of such observations is presented in Chapter(3). Our results suggested that RSL do not show any significant relative albedo change from morning to afternoon. Combined with a thermal modeling approach, they also highlighted that the spatial distribution of RSL activity is different than what would be expected from brine melting or deliquescence. Instead, our results are consistent with dry flows, hence hinting that RSL may be dry surface features. To better characterise the RSL formation mechanism and further validate the results of Chapter (3) we improved our photometric approach. In particular, in Chapter (4) we extended the analysis to all the CaSSIS filters. This allowed to compare the spectrophotometric properties of RSL with those of other Martian albedo features that have a well-established formation mechanism. In particular, we considered dust-devil tracks (DDTs) and regions where the removal of dust from the surface was apparent. The remarkably similar relative albedo of all these features detected through CaSSIS suggested, once again, that RSL may be dust removed features. To

cross-check this we also considered reflectance spectra from laboratory experiments of Martian dust fallout on Martian soil analogs and photometric models of dry and wet Martian soils. We modeled this data to obtain the relative albedo that would be detected by CaSSIS when observing two surface having either a different amount of deposited dust or a variable amount of water in the regolith. We validated this approach applying it to dust devil and dust-poor regions, for which our "dust models" provided a better fit than the "water model", consistently with the physical origin of such features. The former provided a better fit than the latter even for RSL, confirming in an independent way the results of Chapter (3). Collectively, both analyses bring further evidences towards a dry dust origin for RSL, ruling out a significant relationship with liquid water or brines.

For the first two RSL studies that we carried out, presented in Chapters (3,4), we setup a methodology to derive relative albedo measurements of Martian surface features and convolve laboratory measurements within the CaSSIS photometric system. These methodologies have however one important constraint that limits their applicability. In order to measure the relative albedo of a surface feature, in fact, it is required to find another location on the image having the same illumination and observation conditions (i.e., the same orientation in 3D space). The latter is needed to factor out topographic shading. For example, in the measurements of Chapters (3,4) we divided the flux from the RSL pixels by the flux from a nearby region without RSL. Our relative albedo measurements were then naturally corrected for topographic shading. If no regions with the same local illumination and observation conditions exist, relative photometry cannot be performed. While this problem has a minor impact on observation of flat regions, it is significant at locations with a lot of topography. It is also a significant problem for using HiRISE colour images for photometric analyses, because the very small colour swath makes not probable to find such regions. Finally, besides relative photometry, using satellite images for photometric analyses of planetary surfaces bears the problem of topography, that introduces variations in surface brightness depending on the orientation of the terrain with respect to the Sun (i.e. sun-facing areas are brighter). These two problems lead us to develop in Chapter (5) what in the remote-sensing literature is called a *topographic correction* or *topographic normalisation* i.e., a methodology to model and remove brightness variations induced by topography. After validating it on pre-existing relative albedo measurements, we applied it to both HiRISE color datasets and CaSSIS panchromatic ones. This methodology allowed to both perform relative albedo analysis, again confirming a dry origin for RSLs, and obtain topographically corrected datasets. All these results have been published in Munaretto et al. (2021b).

The analyses and methodologies presented here represent a promising pathway for future analyses of CaSSIS and HiRISE images of Mars. In particular, additional RSL sites are under consideration for a comparative spectrophotometric analysis. While in Chapters (3) and (4) we focused only on a single site, Hale and Horowitz craters, respectively, we now have imaged more RSL sites with CaSSIS, allowing a broader spectrophotometric analysis. In particular, the comparison of CaSSIS spectra from different sites may give us insights on which dry mechanism explains better RSL activity. In addition, as soon as more early morning CaSSIS observations coordinated with the afternoon HiRISE ones will be available, it will be possible

to apply the techniques presented in Chapters (3,4,5) to further investigate diurnal processes occurring at the surface. In particular, very early local times are promising targets for future analyses as they are the optimal ones for studying volatiles release from the surface.

Chapter 7

Planet Mercury

In this section we provide a brief introduction about Mercury by reviewing the history of its exploration, its physical properties, the main geological units and surface features, as well as its geological history. Particular attention is given to the description of hollows, which are the prime scientific topic of this part of the thesis.
Mercury was already known as a planet since the Assyrians and Babylonians astronomers, which noted a rapidly moving celestial object in the night sky, particularly close to the Sun. As soon as the first telescopic observations we performed, starting from Galileo Galilei in the early 1600, it became possible to start the first quantitative studies about the planet. The first transit of Mercury was observed in 1677 by Edmond Halley. In 1880 the astronomer Giovanni Schiaparelli produced the first map of the hermean surface and estimated its orbital period of $\approx$ 88 solar days. He also proposed that the planet was in a synchronous rotation with the Sun, like the Moon with the Earth, until in 1965 the radar measurements of Pettengill and Dyce (1965) showed that the rotation period was $\approx$ 58 solar days. The Italian mathematician Giuseppe Colombo discovered that Mercury was in a 3:2 spin-orbit resonance with the Sun, meaning that a solar day on Mercury is two Mercury years long (Colombo, 1965). During the 19^{th} and 20^{th} centuries the first mass estimates were also performed, but provided inconsistent results. The only consensus was that the mass must have been very high, and given the small size of the planet that implied the presence of a highly dense metal core in its interior. The current knowledge of Mercury mainly comes from its explorations the NASA's Mariner 10 and the MErcury Surface, Space ENvironment, GEochemistry, and Ranging (MESSENGER) space missions, and by ground-based telescopes and radars. The first flyby of the planet by Mariner 10 on February 5th 1974 marked the beginning of its exploration. Two other flybys on September 21^{st} 1974 and March 16^{th} 1975 followed-up the first one and concluded the first ever mission to Mercury. The dataset returned by this mission allowed to make important and unexpected discoveries, like the presence of an internally generated magnetic field (Ness et al., 1974). This required a liquid iron core, against the predictions of a completely solid planet. Over 2000 images of the surface of Mercury were returned by the M10 Television experiment (Murray, 1975) at resolutions from 2 km/px up to 100 m/px. These covered almost all the illuminated side of the planet and allowed the geologists to identify the first surface features, define the first geological units and develop an initial stratigraphic system, i.e. a framework for assigning an age to all the geologic units on the surface. After Mariner10, Mercury will not receive any further visit by a space mission for the

next thirty years. During this time observations relied on ground-based facilities, mainly dedicated to the investigation of the exosphere and the surface at infrared wavelengths. In particular, ground-based radar observations evidenced the presence of radar-bright patches, which may be water ice (Harmon and Slade, 1992; Harmon et al., 2007). On March 18^{th} 2011, the MESSENGER mission entered in its orbit around Mercury. The datasets provided by this mission improved and extended the existing ones by Mariner10, leading to important discoveries and contributing to the current knowledge of Mercury. A brief overview of such discoveries is given in the next sections. The future discoveries and advances in the knowledge about the innermost planets will come from the ESA/JAXA BepiColombo mission (Benkhoff et al., 2010), which was launched on October 20^{th} 2018 and it is currently *en-route* to Mercury. A description of BepiColombo and its scientific context is given in Chapter (9).

7.1 Physical properties of Mercury

Mercury is the innermost planet, orbiting at $\approx$ 0.3 AU in a highly elliptic orbit. The close distance from the Sun and the 3:2 resonance result in the highest surface temperature range between day side and night side among the planets of the Solar System. Its density (5.43 g/cm^3 is very peculiar: even if it is slightly smaller than that of the Earth (5.52 g/cm^3), the small diameter of Mercury (4880 km) makes it relatively high. This is due to the presence of a layer of liquid iron within the core, which in turn generates a magnetic field. The internal structure of Mercury is differentiated into a $\approx$ 410 km thick solid outer shell, comprising the 20 to 80 km crust on the outer part, a few tens of km to 200 km thick inner solid FeS layer, a molten core and a solid inner core, which relative diameters are not known (Smith et al., 2012).

7.2 Mercury geologic units and surface features

Images returned by the Mariner 10 and MESSENGER missions allowed to map most of the planet at high resolution and in colors. This allowed to identify several geological units and surface features which are described in the following paragraphs.

7.2.1 Intercrater plains

The intercrater plains (ICP) were first identified in Mariner10 images and are defined as a flat or gently rolling ground between or around large craters and basins (Trask and Guest, 1975). This terrain has a high density of superposing craters, which implied an old age, and it is the most widespread geological unit on Mercury. The probable origin of the ICP is as remnants of volcanic flows (Murray, 1975; Strom, 1977; Trask and Guest, 1975; Whitten et al., 2014). The lower impact crater densities with respect to the Moon imply that during the formation of this unit there was an extensive resurfacing of the surface, due to extensive lava flooding by volcanism.

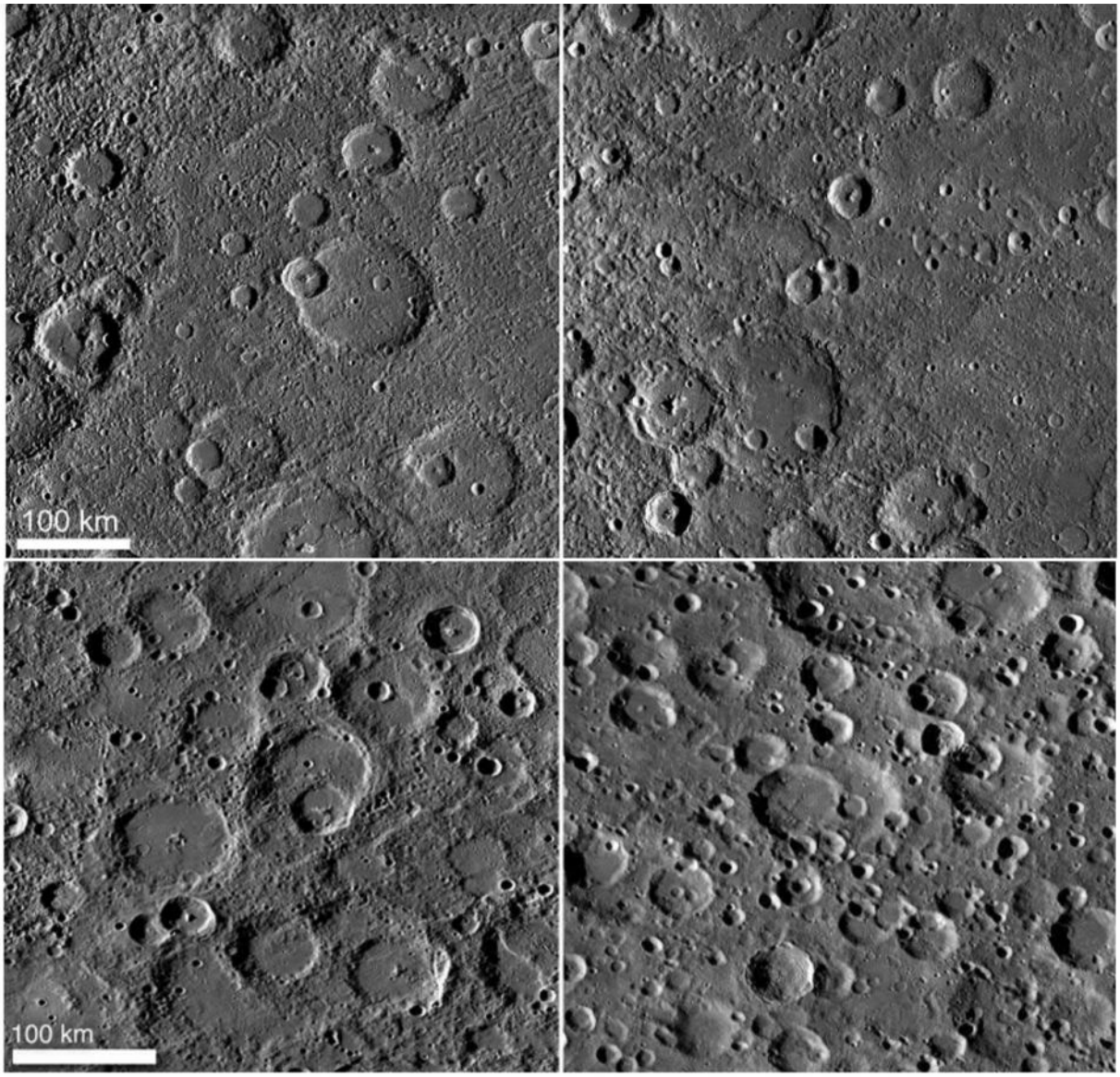

Figure 7.1: Example of intercrater plains from the monochrome global mosaic obtained by the MDIS instrument on board MESSENGER. Adapted from Fig. (6.3) of Denevi et al. (2018).

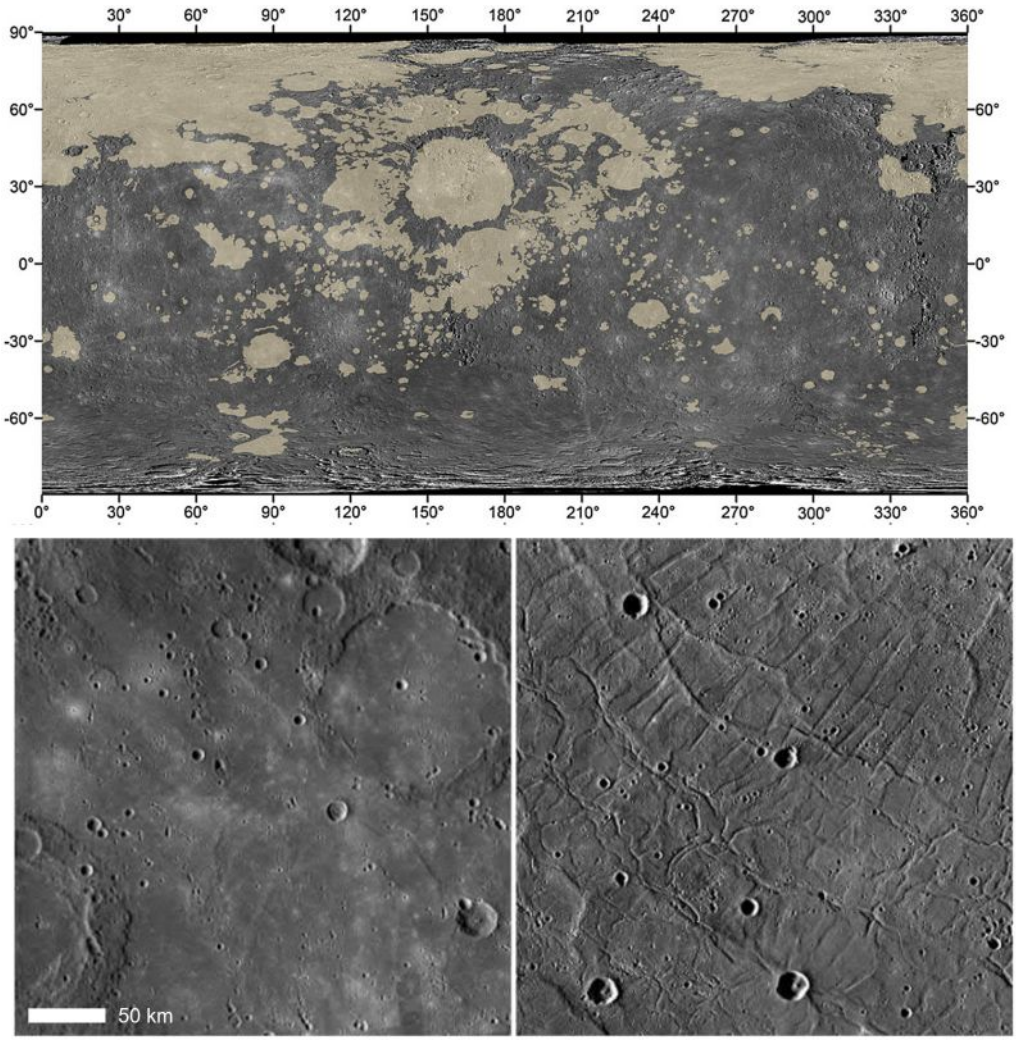

Figure 7.2: Top: distributions of smooth plains on Mercury (beige areas) in equirectangular projection. Image from Denevi et al. (2013). Bottom: examples of smooth plains terrain. Adapted from Denevi et al. (2018).

7.2.2 Smooth plains

In contrast to the widespread ICPs, the smooth plains are sparsely cratered deposits, showing clear boundaries with adjacent terrains and very flat or gently sloped surfaces (Trask and Guest, 1975). Two examples are shown in Fig. (7.2). They are cross-cut by contractional deformations like wrinkle ridges, scarps and high-relief ridges. The thickness of the smooth plains is estimated to range between 0.5 to $4km$. Smooth plains cover about 25% of Mercury (Denevi et al., 2013). Almost 30% of the smooth plains are in correspondence to the Caloris basin, but occurrences of this units have also been found without any association to impact craters (Denevi et al., 2009). For example, the northern hemisphere is covered by an extensive smooth plain deposit (Borealis planitia) that is not associated with any basin. Excluding the Caloris smooth plains and the Boralis planitia, the other smooth plain deposits are equally found on the northern and southern hemisphere. Their distributions is shown in Fig. (7.2).

7.2.3 Impact craters

Impact craters on the surface of Mercury shows different signs of degradation, which prompted many authors to link morphological evidence of degradation to the relative age of the surface (Trask and Guest, 1975). The current crater-degradation classification features five classes, from youngest to oldest. Class 1 represents the youngest craters with crisp rims, terraces and central peaks or peak rings, distinct contact between walls and floor, presence of hummocky material and smooth plains on the floor. They are also required to have well-defined, radially textured ejecta and fresh deposits of secondary crater. Finally, they exhibit high-reflectance proximal ejecta and distal rays. Class 2 includes craters similar to Class 1 but showing signs of degradation in the wall terraces, no high-reflectance ejecta or rays and a low density of superposed craters. Class 3 craters have continuous, rounded and degraded rims, lacking sharp and crisp morphologies. Wall terraces show slumping and the boundary between floor and wall is not well defined. They may have discontinuous ejecta and less visible secondaries. They are characterised by a low to moderate density of superposed craters. Class 4 crater and basins also show rounded rims, which can also be discontinuous. They show sometimes only remnant terraces, rarely central peaks and peak rings and crater floors filled with smooth plains material. They have a moderate density of superposed crater and a discontinuous ejecta. Class 5 comprises the oldest recognizable impacts on Mercury, having discontinuous and highly degraded rims, they lack terraces or wall structures and they have lost their central peak or peak ring and their ejecta. The floor is covered by smooth plain deposits and they have a high density of superposed craters.

7.2.4 Tectonic features

The surface of Mercury is covered by widespread tectonic landforms, in particular by contractional and extensional structures (Strom et al., 1975). The latter represent a minor percentage and are found within the largest basins. They are restricted to narrow grabens striking radially or concentrically from the basin center, formed by the dissipation of the mechanical loading of the crust after the impact event. On the other hand, contractional features are widespread. They can be divided into three types: wrinkle ridges, lobate scarps and high-relief ridges. Wrinkle ridges are defined as broad, low relief arches often superposed on a narrow ridge (Byrne et al., 2014), and usually form in correspondence with fault propagation or fault bend folding. Lobate scarps (or *rupes*) are steep scarps with a "gently sloping back limb" (Byrne et al., 2014) and with a asymmetrical cross-section. They are interpreted to be surface breaking thrust faults (Strom, 1977). High relief ridges (or *dorsum/dorsa*) are similar to lobate scarps but they have a symmetrical cross section. Examples of these tectonic features are shown in Fig. (7.3). The distribution of tectonic features on Mercury is deeply related to its evolution. Three main evolutionary frameworks responsible for the observed tectonic pattern have been proposed: the global contraction (Strom et al., 1975) due to the secular cooling of the planet's interior, the tidal despinning (Melosh and Dzurisin, 1978) or by mantle convection (King, 2008). The observed pattern of tectonic landforms is not compatible with any of the mechanism above, but with a combination of them. Tidal despinning occurred early, before the end of the Late Heavy Bombardment. After that, global contraction occurred, exploiting lithospheric weaknesses resulted from the tidal de-

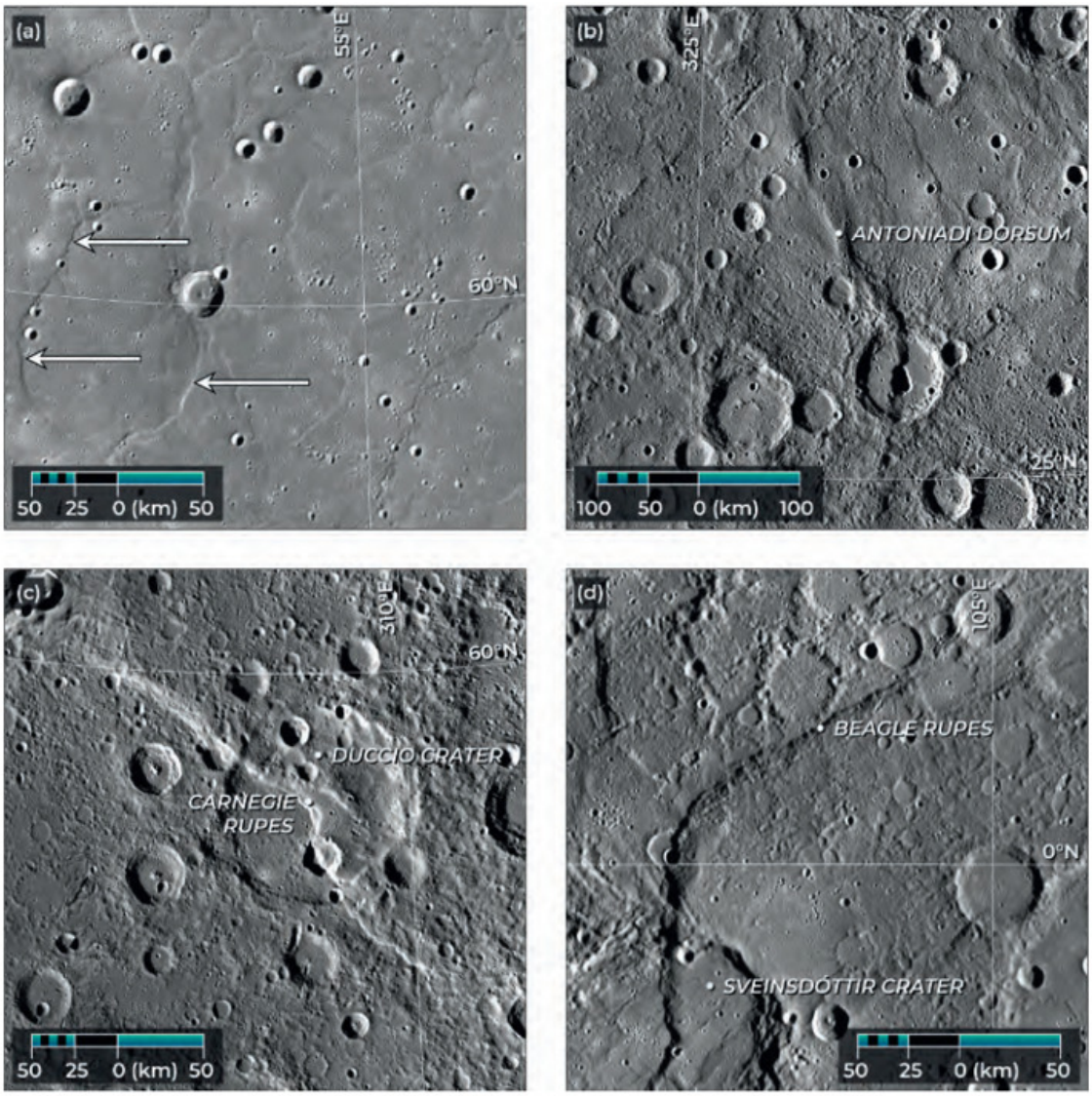

Figure 7.3: Summary of the most relevant tectonic features on Mercury. A) Example of wrinkle ridges on smooth plain terrain. B) Example of a high-relief ridge. C,D) examples of two lobate scarps. Image from Byrne et al. (2018).

spinning phase. Mantle dynamics also contributed throughout the planet's history by generated spatially concentrated faults (King, 2008; Watters et al., 2015).

7.2.5 Explosive volcanism

The surface of Mercury records evidences that explosive volcanism occurred during Mercury's history. These are several-km sized irregular, rimless depressions, often related to much more extended high-albedo, spectrally red diffuse haloes (called *faculae*) centered on the depression (Head et al., 2008). The depressions have been interpreted as volcanic vents, while the *faculae* as explosive volcanic deposits (Goudge et al., 2014; Head et al., 2008; Thomas et al., 2014). An example is shown in Fig. (7.4). Their observed association with impact craters and tectonic features suggested that these volcanic eruptions occurred by exploiting zones of lithopsheric weaknesses during the magma ascent phase (Jozwiak et al., 2018; Thomas et al., 2014).

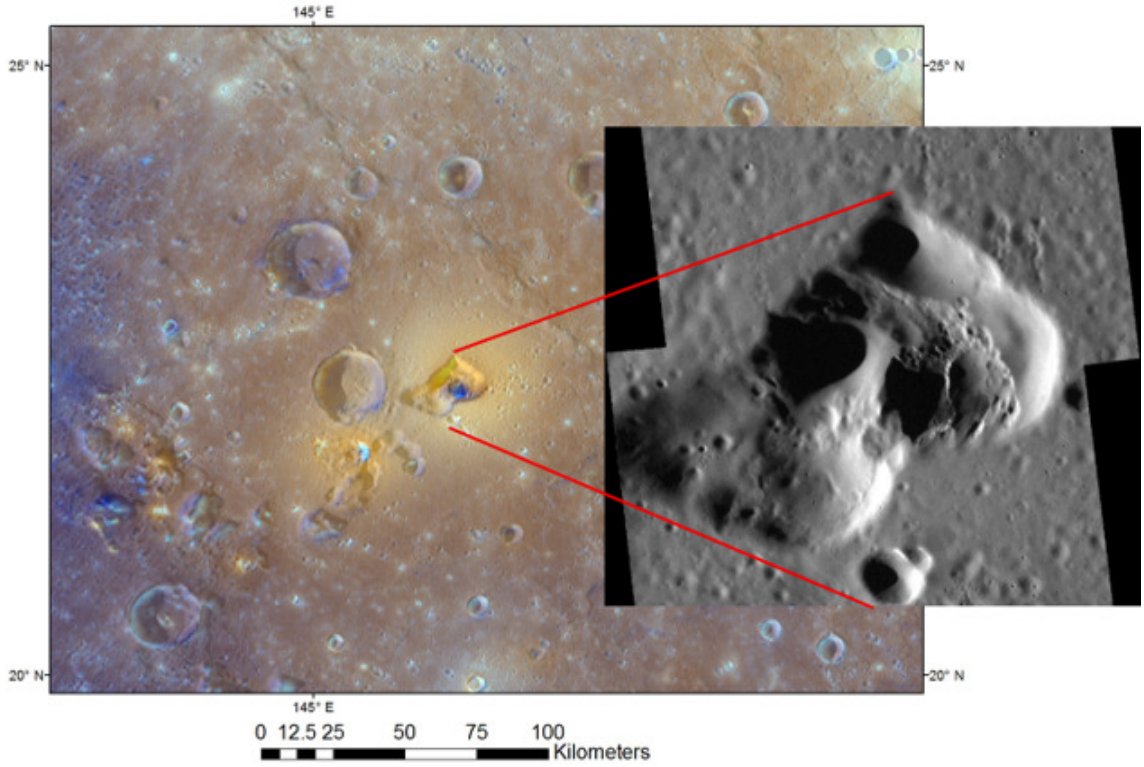

Figure 7.4: Main image: enhanced MESSENGER colour image of the Agwo Facula vent. The facula is the diffuse edged orange region surrounding the vent. The close-up shows a high resolution MESSENGER image of the vent. Image from Rothery et al. (2020).

7.2.6 Polar deposits

Between the Mariner10 and MESSENGER missions, Earth-based radar observations provided the first evidences of water ice at Mercury's poles (Harmon and Slade, 1992; Harmon et al., 2007). On the Moon, water ice was directly detected within permanently shadowed regions at the poles from the identification of absorption features in the $2.8 - 3.0\mu$m range (Colaprete et al., 2010; Pieters et al., 2009). However, this approach is not yet possible on Mercury due to the lack of spectral data at these wavelenghts. Instead, the presence of water was inferred from the detection of radar-bright patches showing a signal similar as the ice on the Galilean satellites (Campbell et al., 1978) and on the polar caps on Mars (Muhleman et al., 1991) and confirmed by the correlation with the permanently shadowed regions inside craters (Chabot et al., 2014, 2013, 2018b; Deutsch et al., 2016), from laser reflectance measurements (Deutsch et al., 2017) and from neutron spectrometry (Lawrence et al., 2013). An example is given in Fig. (7.5). The origin of these water ice deposits is not known yet, but four major mechanism have been proposed: interaction with the solar wind, outgassing from Mercury's interior, delivery by impact events or by micrometeoroids. Further research is still required in order to have a complete view on this open research topic.

7.3 Mercury's chronostratigraphic system

To assign ages defining the geological history of Mercury, geologists built a "chronostratigrpahic system" based on the relative ages of the different terrains identified on the surface. The latter are evaluated on the basis of superposition relationship (young terrains overlap old terrains) and the comparison of crater densities. On Mercury, four geological ages are defined: the pre-Tolstojan (> 3.9 Gyr), the Tolstojan ($3.9 - 3.8$ Gyr, the Calorian ($3.8 - 1.7$ Gyr), the Mansurian ($1.7 - 0.85$ Gyr) and the Kuiperian (0.13 Gyr-today) (Marchi et al., 2009). The pre-Tolstojan refers to the history of Mercury before the impact event that generate the Tolstoj basin. During this age, the surface of Mercury was dominated by a early crust that started being resurfaced by effusive volcanism which lead to the formation of the intercrater plains (Denevi et al., 2018). This process endured also in the Tolstojan period, but towards its end and the beginning of the Calorian period (determined by the Caloris impact event) it gradually changed and started to form smooth plains materials of intercrater plains. The Calorian period is also associated with the decrease of impactor flux due to the end of the late heavy bombardment phase. Soon after the beginning of the Calorian age, the majority of volcanism ended, possibly between $\approx 3.7 - 3.5$ Gyr ago, as a result of cooling of the planet and global contraction (Byrne et al., 2014). Rare, localized effusive volcanic activities continued in correspondence of young impact features such as Rachmaninoff basin before the onset of the Mansurian Period, when effusive volcanism had ceased entirely. As effusive volcanic activity waned, it left the stage to explosive volcanism leading to the formation of pyroclastic vents and deposits (Goudge et al., 2014; Thomas et al., 2014), most of which are found in Mansurian aged craters. The identification of pyroclastic vents in a few young old craters suggests that the explosive volcanism phase declined towards the end of the Mansurian period and a small fraction of it endured in the Kuiperian Period. During this period, the active geological processes on Mercury

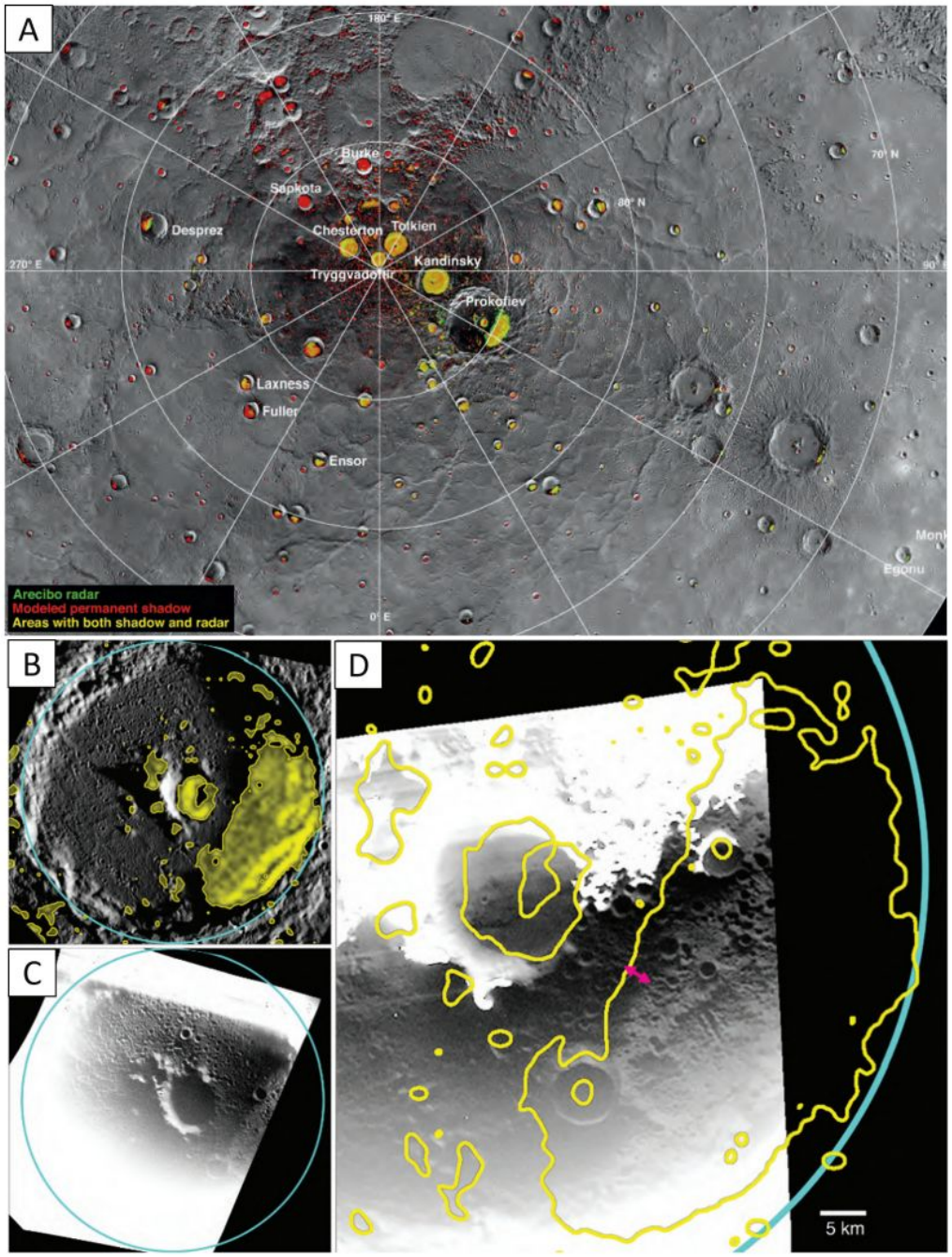

Figure 7.5: A) MESSENGER mosaic of Mercury's north pole, showing radar bright locations (green) from Arecibo observations (Harmon et al., 2011) and regions in permanent shadows (red) (Deutsch et al., 2016). Regions that are both in permanent shadow and radar-bright are colored yellow. Images from (Chabot et al., 2018a). Panel B) shows Prokofiev crater and its rim (cyan). The radar-bright patch from Arecibo observations is shown in yellow. Panels (B) and (C) show two WAC broadband images, EW1020581108B and EW1019169411B, respectively with sunlit portions are saturated in order to reveal the higher-reflectance surface associated to the polar iced deposit within the permanently shadowed, radar-bright region (Chabot et al., 2014). Pink arrows denote the $\approx$ 3-km offset between the outer boundaries of the radar-bright region and the higher-reflectance surface. Images from (Chabot et al., 2018a)

are the contraction of the planet, possibly still ongoing (Watters et al., 2015), the formation of impact craters and the formation of hollows. The latter are shallow, irregular rimless depressions surrounded by bright haloes (Blewett et al., 2011, 2018, 2013; Thomas et al., 2016, 2014) and are described in detail in section (7.5).

7.4 The Formation of Mercury

The fact that Mercury had a phase of explosive volcanism was a surprising discovery, because it implies that volatiles species were present in the magma, deep below the surface. This inference was fundamental to rule out some planetary formation paradigms invoked to explain the formation of Mercury that, to explain the large planet's iron core, advocated the vaporization of the outer layers due to giant impacts or high solar activity. These in fact would also have implied high temperatures leading to the loss of any volatile. Currently, the most favoured formation model for Mercury envisions the accretion of iron-rich material, favoured by solar magnetic field in the protoplanetary disk, followed by the accretion of chondritic, volatile-rich material (Peplowski et al., 2011; Weidenschilling, 1978).

7.5 Mercury's hollows: a decade old scientific puzzle

Hollows were first noticed in images returned by the Mariner 10 mission in the 70s as high-reflectance, anomalous blue colour patches on crater floors. However, they were not significantly studied until more than 30 years later, when the first flyby images of Mercury by the MDIS instrument on the MESSENGER mission led to the discovery of several impact craters with high-reflectance, relatively blue floors (Robinson et al., 2008). Further higher-resolution images were obtained during the MESSENGER mission, allowing to better investigate the morphology of these bright crater floors. In particular, it was possible to realize that they had a typical morphology, i.e. bright, often haloed, small, shallow, irregular, rimless and flat-floored depressions, leading to the name "hollow" (Blewett et al., 2018). The crisp morphologies associated with the hollows walls and the lack of superposing impact craters suggest a young relative to the whole Mercury's surface (Blewett et al., 2011, 2013). They mainly occur within impact crater and basins floors, walls, central peaks and ejecta (Blewett et al., 2011, 2018, 2013; Thomas et al., 2014), but can be found also on the walls of volcanic vents, in plains and rolling terrain, not associated with impacts, or within low-reflectance surface patches (Xiao et al., 2013). They can be found both as isolated or in clustered and coalescing depressions. Their depth ranges from 5 to 98 m with an average of 24 m and a standard deviation of 16 m (Blewett et al., 2016; Thomas et al., 2014). The geographical distributions of hollows on Mercury is rather widespread, with the greatest occurrence between 0° and 30° (Thomas et al., 2014). However, the lower number of hollows at higher latitudes can be also attributed to one or more observational biases. Observations at high latitudes were done at large solar incidence angle, making more difficult to detect hollow from their reflectance. This illumination geometry also implied larger shadows,that may have obscured several hollow sites. In addition, the southern hemisphere of Mercury was observed by MESSENGER with a coarser resolution.

Therefore, many southern latitude hollows may simply be undetected. Finally, the northern regions of Mercury are dominated by smooth plains, where hollows are not found, hence indicating the lack of a favourable substrate for their formation at high northern latitudes. Geographical analyses of hollows have also highlighted a weak tendency to form near longitudes 0° and 180° (Thomas et al., 2014). Due to the 3:2 spin-orbit resonance of Mercury these regions experience noon on successive perihelia and hence they receive greater levels of solar radiations. The correlation, even weak, between hollow formation and these "hot poles" suggest that high temperatures and solar fluxes favour the formation of hollows. This is also consistent with analysis at a local scale, where hollows are found preferentially on Sun facing slopes Blewett et al. (2011, 2013); Thomas et al. (2014) However, the areally largest ones are found outside these "hot poles", implying that other mechanism are at play, too. (Thomas et al., 2014). Other significant correlations are their association with the LRM, low reflectance blue plains and dark spots, with pyroclastic vents and with the so-called red pitted ground (i.e., shallow, irregular depression similar to hollows but made of a reddish material and more subdued than hollows) (Blewett et al., 2011, 2013; Thomas et al., 2014). Multiple evidences suggest that hollows are one of the youngest surface features on Mercury. In particular, they are found in correspondence of the youngest impact craters (Xiao et al., 2013), they lack impact-induced erosion and superposed crater (Blewett et al., 2013; Thomas et al., 2014), they have fresh and crisp morphologies and fine structures that would not be preserved in the severe space weathering environment of Mercury. In addition, if hollows within crater were formed soon after the impact, then older crater should display larger hollows. On the contrary, Thomas et al. (2014) showed that hollow size is uncorrelated with crater age, hence implying that their formation postdates significantly the impact event. The extensive analysis of hollows on Mercury and the documentation of their morphologies lead to the inferred development sequence in Fig. (7.6): small hollows first appear within a dark spot, they enlarge and/or multiple hollows coalesce and are surrounded by a bright halo, then the growth decreases and bright halo disappears. Eventually, growth stops, the hollow reflectance decreases, matching the surrounding terrain, and erosion gradually softens the overall morphology. (Blewett et al., 2011, 2018, 2013; Xiao et al., 2013).

7.5.1 Spectrophotometric analyses of hollows

Insights on the composition and formation of hollows also come from the analysis of the variation in surface reflectance with different viewing and illumination geometries. In particular, the phase angle, i.e. the angle between the direction of illumination and the direction pointing to the camera (c.f. Section 5.2) has a significant effect on the surface reflectance depending on the texture of the surface. Rough surfaces tend to be more reflective at low phase angles than smooth because of shadow hiding (Hapke, 2012). The ratio of two images taken at a low and high phase angles, called "phase ratio" is therefore an indicator of the surface texture. This techniques was used by Blewett et al. (2014), Thomas et al. (2016) Wang et al. (2020) to show that the floors of hollows are rougher than the surrounding crater floor, while the high-reflectance halos or newly formed hollows are rougher. The composition of hollows can be also studied by investigating their spectral reflectance. In particular, MESSENGER provided both multispectral images through

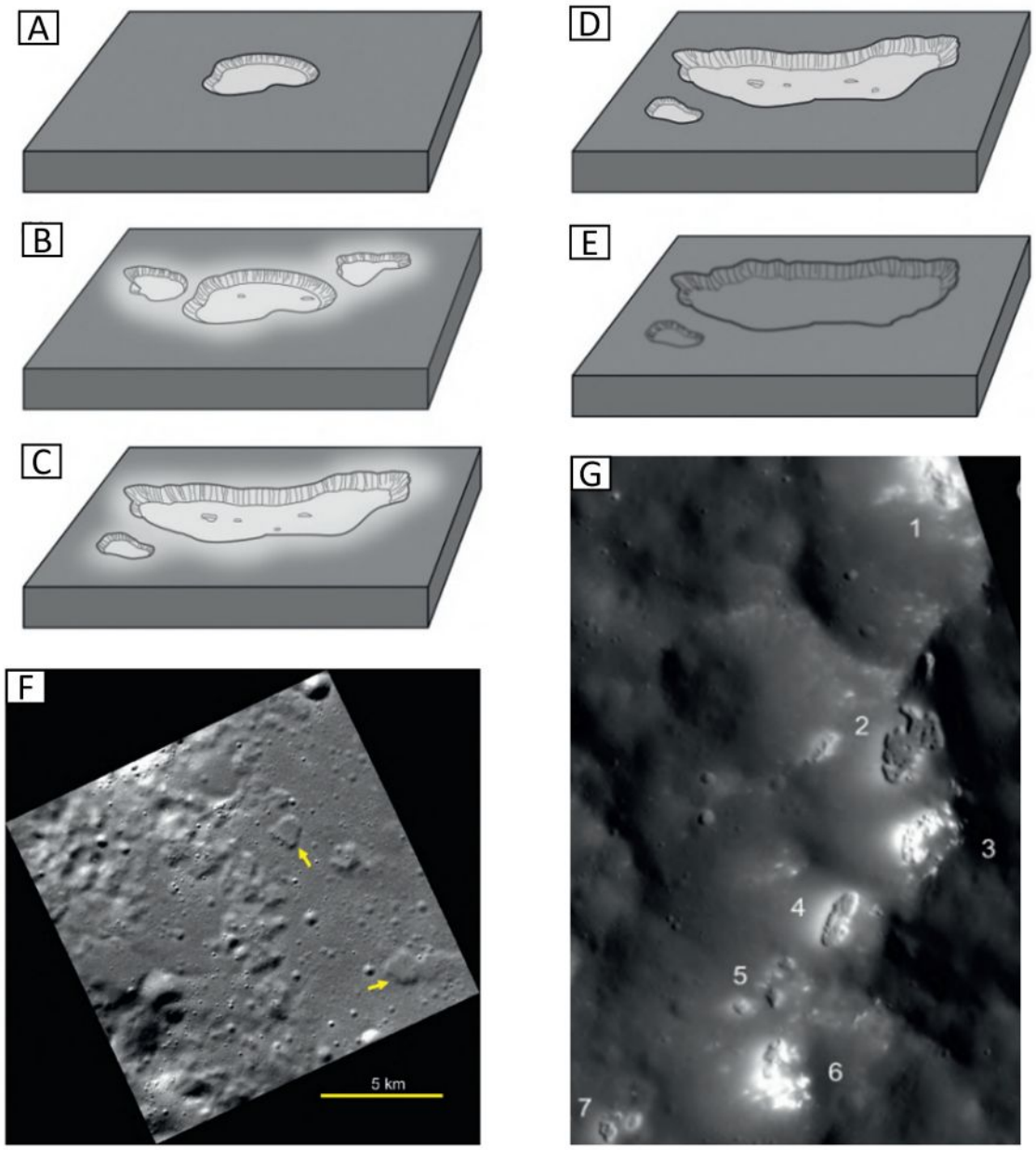

Figure 7.6: A to E) Hollow evolutionary sequence. A) Initiation. B) Enlargement and initiation of additional hollows, appearance of bright halo. C) Further enlargement and coalescence and additional initiation of new small hollows. D) Waning of activity leading to the disappearance of the bright halo. E) End of activity resulting into the hollows albedo matching the surroundings and erosion. F) Example of stage E) from NAC image EN0249182311M, 15 m/pixel, at location 62.9°N,118.3°E. G) Mosaic of NAC images EN0213851669M and EN0213851674M at 15 m/pixel showing a portion of the peak ring of Aksakov crater 34.4°N,282.1°E. Hollows (1,3,4,6) are examples of evolutionary phases between panels B) and C). Hollows (2,5,7), with faded or no high-reflectance haloed, are examples of evolutionary phases in panel D). Adapted from (Blewett et al., 2018).

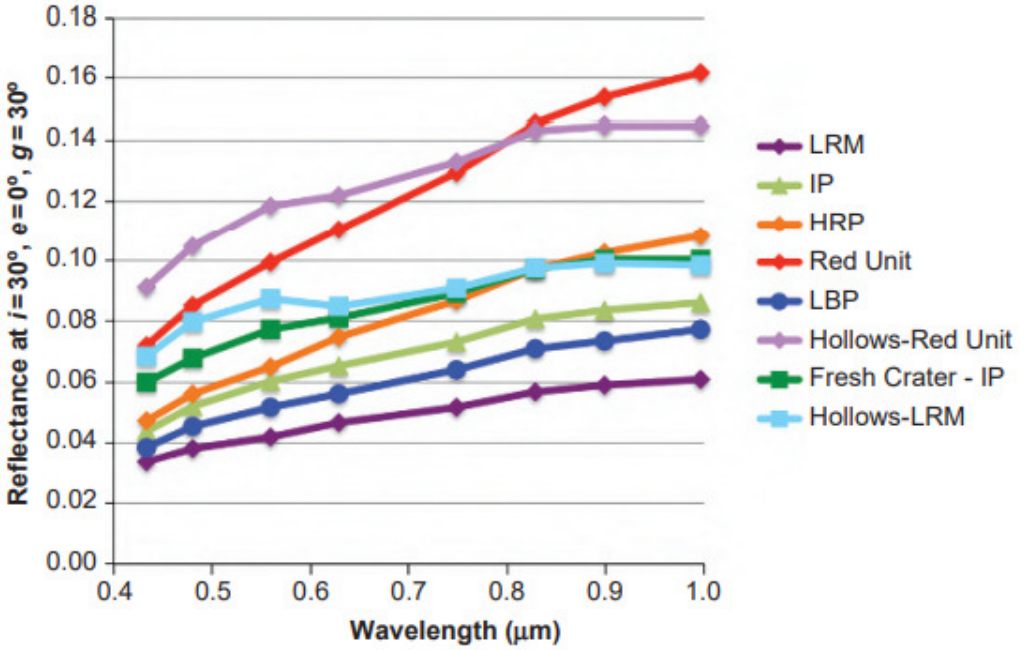

Figure 7.7: Adapted from Fig. 8.6a of (Blewett et al., 2018).MDIS/WAC spectra of several surface features on Mercury, including hollows.

the MDIS camera, and surface reflectance spectra through the VIRS Spectrograph on the MASCS instrument. However, the latter had a much lower resolution than the typical scale of hollows and a relatively low signal to noise. As a consequence, hollows are often not resolved by MASCS footprint, and/or have noisy spectra in the few cases in which they are resolved. For this reason, most of spectrophotometric analyses of hollows rely on MDIS 8-filter multispectral images. The latter allowed to highlight the relatively blue colour of hollows, which is due to the less steep spectral slope with respect to other materials on Mercury. MDIS Spectra of several surface features on Mercury, including hollows, are shown in Fig. (7.7). Hollows spectra are rather featureless, as most of materials of Mercury, with the exceptions of few absorption feature. In particular, they show an absorption feature near 600 nm, the same that is detected on the so called low-reflectance material (LRM, i.e dark material strongly concentrated on the floors and rims and in the ejecta of impact craters and basins) where it is possibly related to graphite (Murchie et al., 2015), the edge of the oxygen-metal charge-transfer UV band shortwards of 400 nm (Goudge et al., 2014; Izenberg et al., 2014) associated to pyroclastic deposits, and a decrease in reflectance from 629 and 749 nm attributed to the absorptions of Magnesium and/or Calcium rich sulfide minerals (Blewett et al., 2011, 2013; Lucchetti et al., 2018; Pajola et al., 2021; Phillips et al., 2021; Thomas et al., 2014; Xiao et al., 2013). In addition to sulfides minerals, hollows spectra also carry the signature of the material in which they were generated, such as pyroxenes or pyroclastic materials (Goudge et al., 2014; Izenberg et al., 2014; Lucchetti et al., 2018; Pajola et al., 2021). Finally, chloride volatiles have also been detected at Tyagaraja crater hollows (Lucchetti et al., 2021).

7.5.2 Elemental composition

A further tool to investigate the nature of hollows is given by the analysis of their elemental composition from the MESSENGER X-Ray (XRS), Gamma-Ray (GRS) and Neutron Spectrometers (NS). Although the resolution of these instruments was too coarse to resolve individual hollows, they were able to resolve the LRM, in which the hollows are seen to form. Therefore, understanding the composition of the LRM allows to have insights onto the hollows formation mechanism. In particular, the LRM appears to have a higher magnesium, calcium, sulfur than the average Mercury. In addition, the low reflectance of the LRM can be explained by the presence of a darkening agent. In particular, the presence of graphite has been inferred from the higher abundance of carbon in LRM with respect to other terrains detected from NS, GRS and MDIS spectral data (Murchie et al., 2015). The association between LRM and hollows suggests therefore that materials containing magnesium, calcium, sulfur and graphite could play an important role in the formation of hollows.

7.5.3 Hollows formation models and involved volatiles

The geomorphological, spectral and compositional properties of hollows gathered so far allowed to infer the formation sequence depicted in Fig. (7.6), in which after hollows activity initiates, it proceeds by scarp retreat, leading to enlargement and coalescence of individual hollow and emplacement of a bright halo and depositional lag. Finally, when activity wanes, the halo disappears and the fine and crisp hollow morphologies are softened by erosion. The similar depth of the hollow population on Mercury and the fact that the geological units in which hollows form are much thicker than the hollows themselves suggest that the emplacement of a sublimation lag protects the underlying material, coming from the thicker geological units in which activity is initiated, from being processed and sustain hollow formation. This acts as a thermophysical armor inhibiting further growth and leading to the final stages of hollow formation. While this model is now well accepted, many questions are still to be resolved. The precise identity of the lost volatiles leading to the hollows formation and the loss mechanisms are still debated. Proposed mechanism for the destruction of volatiles from the surface include sublimation due to its high temperature, space weathering, micrometeoroid impacts and ion bombardment sputtering. Laboratory experiments show that Calcium and Magnesium sulphides are promising candidates because they can decompose in the hermean thermal and radiation environment (Helbert et al., 2013). Graphite is also a promising candidate, because it can be sputtered by ion bombardment. In addition, graphite-bearing rocks exposed to solar-wind and/or energetic particles from the magnetosphere is converted in methane, which will escape disrupting the surface and leading to a scarp retreat. Due to its low albedo, the removal of graphite would also brighten the surface, explaining the higher reflectivity of hollows with respect to the surrounding surface (Blewett et al., 2016), although Thomas et al. (2016) argue that in order to explain the hollows spectral properties, the volatile removed from hollows should be redder than the LRM, hence favouring sulphides over graphite.
All hollows formation models envision a role of a volatiles phases, which loss from the surface causes a scarp retreat. In this context, is therefore pivotal to under-

stand if and where such volatiles are available on the hermean surface and if the geographical distribution of hollows is consistent with the availability of volatiles. The MESSENGER mission has collected evidences for sulfur and carbon-driven explosive volcanism, meaning that these volatiles are indeed sourced from volcanic activity. Two scenarios have been proposed to link them with hollows so far: the first assumes that a sulfide rich layer could form on the top of impact melts as a result of differentiation. The volatiles in this layer are then removed to form hollows. While this scenario explains the extensive presence of hollows on some crater floors, it has difficulties where they are found in unfavorable geologic settings, such as on central peaks. For this reason, another scenario has been proposed. In particular, the extensive presence of a rock-forming, volatile-rich phase has been proposed to explain the generic formation of isolated hollows in LRM. Both mechanism, however, could be at play in different geologic settings.

7.5.4 Hollows bright haloes and interiors

Finally, the nature of the bright interiors and haloes is still an open question. The higher reflectivity of the interiors have been imputed to five potential mechanisms: the presence of an alteration product, with different composition, the deposition of vapor coatings, the destruction of a darkening agent, differences in particle size, texture or scattering properties and the exposure of particles less affected by space weathering (Blewett et al., 2013). Concerning the bright haloes, further options envision generation of dust, thermal fracturing, recondensation of less-volatile component that were initially lost during the formation of the hollow, physical modification or chemical alteration of the surface by leftovers of the sublimation process.

Chapter 8

Exploring the spectrophotometric properties of hollows through multi-angular MESSENGER/MDIS observations

Hollows are one of the major puzzles about Mercury surface features and processes, with no equivalent on other planetary bodies. Therefore, they represent an interesting research topic that will be addressed by the BepiColombo mission once it will arrive on Mercury on December 2025. We therefore focus here on investigating the origin and formation mechanism of Mercury's hollows. We also focus on identifying investigation methodologies that will benefit from the future BepiColombo dataset and that will be useful for the analysis of such data. In particular, we mentioned in the previous section that the analysis of the variation in surface brightness with different viewing and illumination geometries can be helpful to provide insights on the hollows composition and surface properties. This has been investigated in literature through the phase ratio technique (Blewett et al., 2014; Thomas et al., 2016; Wang et al., 2020), but no further modeling has been attempted so far. On the contrary, photometric modeling of the surface of Mercury has been performed to produce global monochrome and colour mosaics (Domingue et al., 2019a,b, 2016, 2017, 2011a,b, 2010), but it has never been applied to local surface features. Since the latter a yet unexplored field of research, we here focus on the characterisation of the hollows scattering properties through a photometric modeling approach. The scope of such modeling is twofold: first, we aim to determine the models that best describe the photometric behaviour of hollows. This will be useful for future, updated, spectrophotometric analyses of hollows that will rely on dedicated photometric models instead of the ones that work for the average surface of Mercury. In addition, a model that can successfully describe the hollow scattering properties can be used to characterise the physical properties of their forming material. In this Chapter, we investigate the spectrophotometric properties of hollows located in the Tyagaraja and Canova craters on Mercury. Our analysis is presented as follows: in Section (8.1) we introduce the photometric models that have been applied to the surface of Mercury. In Section (8.2) we describe the study sites, the utilized datasets and our methodology. In Section (8.3) and (8.4) we present the performances of our

models and assess the quality of their parameter estimates, respectively. In section (8.5) we analyse the model parameters. In section (8.6) we discuss our results and in section 8.7 we draw our conclusions. Future development and perspectives are the object of the next Chapter.

8.1 Photometric modeling of the surface of Mercury

A photometric model is a mathematical equation that attempts to predict the light reflected by a surface as a function of the relative position of the observer and illumination source, often parametrized by the incidence, emission, phase and azimuth photometric angles, and depending on a certain number of parameters. We introduced this topic in Chapter (5) in the context of Martian photometry. However, the complications introduced by the complex martian environment prompted us to base our analysis on very simple photometric models with up to one parameter. Since Mercury is an atmosphereless planet, it is less affected by surface changes due the seasonal removal and deposition of dust. In addition, the lack of an atmosphere avoids the problem of taking into account the effect of aerosol scattering, a daunting task for martian surface photometry. We can therefore employ more complicated photometric models and investigate their parameter to have insights into the physical properties of the regolith. The models that we consider in this analysis are the same of the photometric analysis of the whole surface of Mercury of Domingue et al. (2016), i.e. the Hapke (Hapke, 1993, 2002a,b, 2012) and Kaasalainen–Shkuratov (KS) (Schröder et al., 2013; Shkuratov et al., 2011; Velikodsky et al., 2011; Wu et al., 2013) models.

8.1.1 The Hapke model

The Hapke model is probably the most common photometric model used in planetary photometry. It combines the equations of radiative transfer and geometry optics and it can take into account the effect of surface roughness, porosity, grain scattering properties. It can predict complex photometric phenomena, like the opposition surge, i.e. the rapid brightening of a surface at small phase angle. Multiple versions of this models have been defined so far, with the most advanced containing up to 9 parameters (Hapke, 1993, 2002a,b, 2012) In our analysis, we consider just the basic model. The rationale is that it was proven to perform better than its complicated versions (Domingue et al., 2016), and it has less parameters. The formulation of the basic Hapke reflectance model is the following:

$$r(i,e,g) = \frac{w}{4\pi}\frac{\mu_{0e}}{\mu_{0e}+\mu_e}\left\{[1+B(g)]p(g) + H\left(\mu_{0e}\right)H\left(\mu_e\right) - 1\right\}\mathrm{S}(i,e,g) \tag{8.1}$$

where w is the single scattering albedo, i.e. the ratio between the amount of light that is scattered vs the amount of light that is scattered and absorbed by the surface. i, e and g represent the local incidence, emission and phase angles. $B(g)$ represents the *shadow-hiding opposition effect function* and it is given by:

$$B(g) = \frac{B_0}{1+(1/h)\tan(g/2)} \tag{8.2}$$

where B_0 is the amplitude of the opposition effect and h is the angular half width of the peak (Domingue et al., 2016; Hapke, 1993).
$p(g)$ is the *phase function* and it is parametrized with a 2-term Henyey–Greenstein function:

$$p(g) = \frac{(1-c)\,(1-b^2)}{(1-2b\cos(g)+b^2)^{3/2}} + \frac{c\,(1-b^2)}{(1+2b\cos(g)+b^2)^{3/2}} \tag{8.3}$$

where b parametrizes the angular width of the scattering lobe: a high b means that light is scattered in a rather collimated fashion, while a low b means that scattering of light is isotropic. c parametrizes the partition of the scattered light into the forward (high c) or backward (low c) directions. The $H()$ function describes multiple scattering and it is given by:

$$H(x) = \left\{1 - \left[1-y^2\right] x \left[\left(\frac{1-y}{1+y}\right) + \left(\frac{1}{2} - x\left(\frac{1-y}{1+y}\right)\right)\ln\left(\frac{1+x}{x}\right)\right]\right\}^{-1} \tag{8.4}$$

where $\gamma = \sqrt{1-w}$. Finally, the $S(i,e,g)$ represents the effect of macroscopic roughness. This term depends on the parameter θ, i.e. the average surface tilt from the radiative transfer to the image resolution scales. A low value of this parameter implies a smooth surface, while a high value implies a rough surface. The expression of the macroscopic roughness term depends whether $i < e$ or $i > e$. In the first case ($i \leq e$) it is given by:

$$S(i,e,\psi,\bar{\theta}) = \frac{\mu_e}{\mu_e(0)}\frac{\mu_0}{\mu_{0e}(0)}\frac{\chi(\bar{\theta})}{1-f(\psi)+f(\psi)\chi(\bar{\theta})\left[\frac{\mu_0}{\mu_{0e}(0)}\right]} \tag{8.5}$$

with:

$$\mu_{0e} \simeq \chi(\bar{\theta})\left[\cos i + \sin i \tan\bar{\theta}\frac{\cos\psi E_2(e) + \sin^2(\psi/2)E_2(i)}{2 - E_1(e) - (\psi/\pi)E_1(i)}\right] \tag{8.6}$$

$$\mu_e \simeq \chi(\bar{\theta})\left[\cos e + \sin e \tan\bar{\theta}\frac{E_2(e) - \sin^2(\psi/2)E_2(i)}{2 - E_1(e) - (\psi/\pi)E_1(i)}\right] \tag{8.7}$$

The second case ($i > e$) is instead given by:

$$\mathrm{S}(i,e,\psi) \simeq \frac{\mu_e}{\mu_e(0)}\frac{\mu_0}{\mu_{0e}(0)}\frac{\chi(\bar{\theta})}{1-f(\psi)+f(\psi)\chi(\bar{\theta})\left[\mu/\mu_e(0)\right]} \tag{8.8}$$

with:

$$\mu_e \simeq \chi(\bar{\theta})\left[\cos e + \sin e \tan\bar{\theta}\frac{\cos\psi E_2(i) + \sin^2(\psi/2)E_2(e)}{2 - E_1(i) - (\psi/\pi)E_1(e)}\right] \tag{8.9}$$

$$\mu_{0e} \simeq \chi(\bar{\theta})\left[\cos i + \sin i \tan\bar{\theta}\frac{E_2(i) - \sin^2(\psi/2)E_2(e)}{2 - E_1(i) - (\psi/\pi)E_1(e)}\right] \tag{8.10}$$

The terms common to both cases are:

$$\mu_e(0) \simeq \chi(\bar{\theta})\left[\cos e + \sin e \tan\bar{\theta}\frac{E_2(e)}{2 - E_1(e)}\right] \tag{8.11}$$

$$\mu_{0e}(0) \simeq \chi(\bar{\bar{\theta}})\left[\cos i + \sin i \tan\bar{\theta}\frac{E_2(i)}{2 - E_1(i)}\right] \tag{8.12}$$

$$\chi(\bar{\theta}) = 1/\left(1 + \pi\tan^2\bar{\theta}\right)^{1/2} \tag{8.13}$$

$$E_1(x) = \exp\left(-\frac{2}{\pi}\cot\bar{\theta}\cot x\right) \tag{8.14}$$

$$E_2(x) = \exp\left(-\frac{1}{\pi}\cot^2\bar{\theta}\cot^2 x\right) \tag{8.15}$$

$$f(\psi) = \exp\left(-2\tan\frac{\psi}{2}\right) \tag{8.16}$$

with *psi* being the azimuth angle between the plane of illumination and scattering.

8.1.2 The Kaasalainen–Shkuratov models

The Kaasalainen-Shkruatov (KS) models represent a simpler alternative to the Hapke model. On the other hand they are more empirical, hence the interpretation of the model parameters is challenging. In the KS models, the dependence from the phase angle is decoupled from the dependence on incidence and emission angles (Kaasalainen et al., 2001; Schröder et al., 2013; Shkuratov et al., 2011). The general form of a KS reflectance model is given by:

$$\pi r(g, i, e, \lambda) = A_{eq}(g, \lambda)D(g, i, e, \lambda) \tag{8.17}$$

where $A_{eq}(g, \lambda)$ is called *equigonal albedo* and depends on phase angle and wavelength only. In particular, the equigonal albedo may be expressed as $A_{eq} = A_n(g_0, \lambda)f(g)$, i.e. the product between its value at zero phase angle ($A_n(g_0, \lambda)$ and a phase function $f(g)$. $D(g, i, e, \lambda)$ is a disk function that expresses the variation in surface reflectance due to the topography. We already used this formulation in Section (5.2) when modeling and correcting for the topographic shading in Eq. (5.2). However, at that stage we were dealing with only one image and we were focusing on relative photometry, hence the phase dependence could be ignored. Here instead, we have a multiangular dataset and therefore we can also account for the phase dependence. For each disk function among those in Section (5.2), or a combination of them, combined with a mathematical function represeting a *phase function*, we can obtain a different KS model. Basing on Domingue et al. (2016) we adopt the phase function:

$$f(g) = e^{-\mu g} \tag{8.18}$$

where μ is associated with surface roughness. This phase function was also used to model the photometric observations of Vesta (Schröder et al., 2013). Using this phase function, the KS models are:

$$\mathrm{KS}_1 = A_N e^{-g\mu}\frac{2\cos i}{\cos i + \cos e}, \tag{8.19}$$

$$\mathrm{KS}_2 = A_N e^{-g\mu}\cos\left(\frac{g}{2}\right)\cos\left[\frac{\pi}{\pi - g}\left(\gamma - \frac{g}{2}\right)\right]\frac{(\cos\beta)^{g/(\pi-g)}}{\cos\gamma}, \tag{8.20}$$

$$\mathrm{KS}_3 = A_N e^{-g\mu}\left[c_l\left(\frac{2\cos i}{\cos i + \cos e}\right) + (1 - c_l)\cos i\right], \tag{8.21}$$

$$\mathrm{KS}_4 = A_N e^{-g\mu}(\cos i)^k(\cos e)^{k-1} \tag{8.22}$$

$$\mathrm{KS}_5 = A_N e^{-g\mu}\cos\left(\frac{g}{2}\right)\cos\left[\frac{\pi}{\pi - g}\left(\gamma - \frac{g}{2}\right)\right]\frac{(\cos\beta)^{\eta g/(\pi-g)}}{\cos\gamma} \tag{8.23}$$

where c_l is a parameter which partition the scattering with a Lambert($c_l = 0$) and a Lommel-Seelinger ($c_l = 1$) disk function. k is the Minnaert exponent, as defined in Section (5.2). η is a parameter of the Akimov law (c.f. Section 5.2).

Filter Number	Central Wavelength nm	Bandpass nm	Filter name
6	433.2	18	F
3	479.9	8.9	C
4	558.9	4.6	D
5	628.7	4.4	E
1	698.8	4.4	A
2	700	600	B
7	749.0	4.5	G
12	828.6	4.1	L
10	898.1	4.3	J
8	948.0	4.9	H
9	996.8	12.0	I
11	1010	20	K

Table 8.1: MDIS/WAC Filter specification.

8.2 Datasets and modeling methodology

Our analysis relies on observations acquired by the Mercury Dual Imaging System (MDIS) (Hawkins et al., 2007) on board MESSENGER. It consisted of a monochrome narrow-angle camera (NAC) and a multispectral wide-angle camera (WAC) featuring 12 bands from 395 to 1040 nm. MDIS allowed the production of monochrome (166 m/px) and colour (665 m/px) global mosaics of Mercury. Details about the WAC filters are given in Table (8.1). We focus on the hollows located within the floors of Tyagaraja (3.89° N 211.1°) and Canova (25°N 3°E) craters, Mercury, and shown in Fig. (8.2). These two locations were selected because they have relatively large hollows and several WAC images in the 8 colour filters, hence allowing a proper sampling of the incidence, emission and phase angle space. We identified and downloaded all WAC images covering the Canova and Tyagaraja hollows using the Planetary Image Locator Tool (PILOT, `https://pilot.wr.usgs.gov/`). Specifically, the tool was used to convert the raw images to ISIS cubes, attach the geometric information about the position and pointing of the spacecraft and the Sun at the epoch of the observation contained in each observation SPICE kernels, perform the radiometric calibration and project the images on the surface of Mercury. In all this process, the USGS global DTM of Mercury was used as a shape model of Mercury. This DTM has a grid size of 665 m, and therefore all images were downsampled to this resolution. At this point, we used the *phocube* routine of the USGS ISIS software to compute incidence, emission, phase, subsolar ground azimuth and subspacecraft ground azimuth angles (c.f. Section (5.2)) for each pixel of the images. With this procedure, we obtained a datacube with flux (stored as I/F) and the photometric angles within his bands. The latter were computed in a similar manner as in Section (5.2) taking into account the effect of topography in tilting the surface by the slope and aspect angles. At this point, for each site we

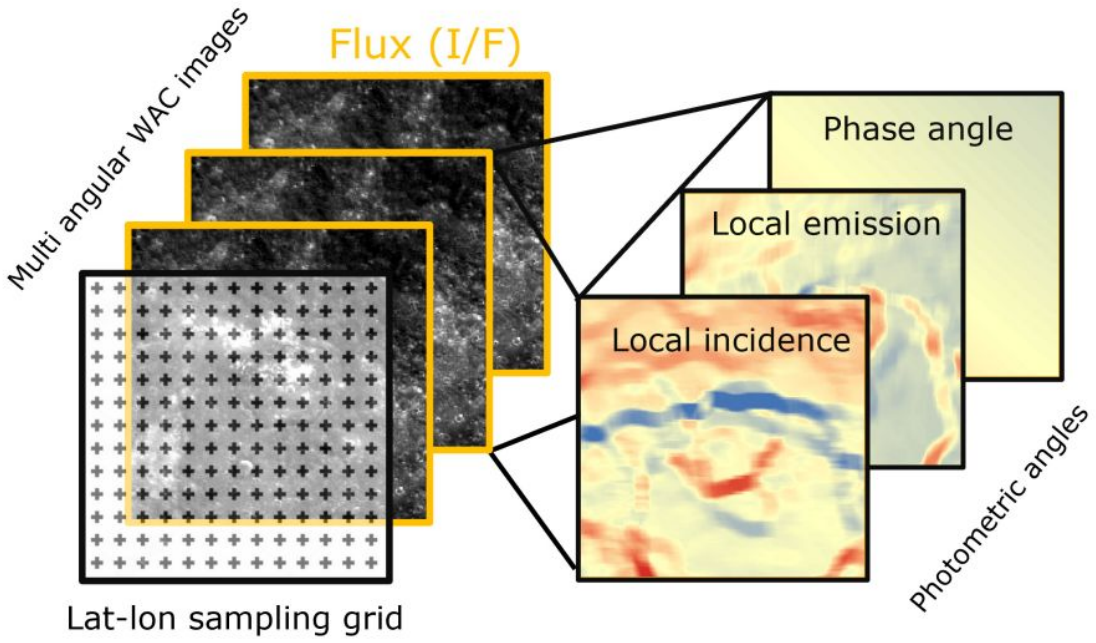

Figure 8.1: Sketch of our dataset for Canova crater. We show just 3 images and only the incidence, emission and phase photometric angle for simplicity.

defined a rectangular grid with a spacing of 665 m in latitude and longitude covering the Tyagaraja and Canova hollows and the immediate surroundings. The extent of such grid is shown as an orange rectangle in Fig. (8.2). In particular, at Tyagaraja we sampled the whole crater and part of the ejecta (Fig. 8.2a). At Canova, instead, image coverage and computational time restricted our grid to be within the rim of the Crater (Fig. 8.2b). For each WAC filter we sampled at each grid point all the flux and photometric angles coming from all the observations in that filter. A sketch of the whole dataset is shown in Fig. (8.1). Then, at each grid point we minimized all the photometric models in Section (8.2).

This task has been performed in literature with a grid-search approach where all the combinations of the parameters are tested and the one returning the lowest value of the *chi* metric was selected (Domingue et al., 2016). While this approach provided convincing result in past studies so far, it suffers from the problem that the final solution depends on the sampling of the parameter grid. In order to find a global minimum of the metric, a very fine grid must be used, translating in an exponential increase in the number of parameter combinations to be tested. As a consequence, the high computational time required for this approach renders it feasible when a limited number of fits has to be performed. In our case, we defined a 45×38 grid on Canova and a 292×294 grid on Tyagaraja. Taking into account all 8 filters and the 6 model considered, this results in $6 * 8 * (45 \times 38 + 292 \times 294) = 4202784$ fits. Such a number prevented the use of a grid-search approach. We instead opted for a numerical minimization approach, like in Munaretto et al. (2021b), of the χ function in Domingue et al. (2016) using the `minimize` routine provided by the `scipy` library of `Python` programming language and setting the initial parameter values to the ones in Domingue et al. (2016). We assess the performances of each model in each band by analysing the distributions of the ratio between the predicted I/F vs the observed

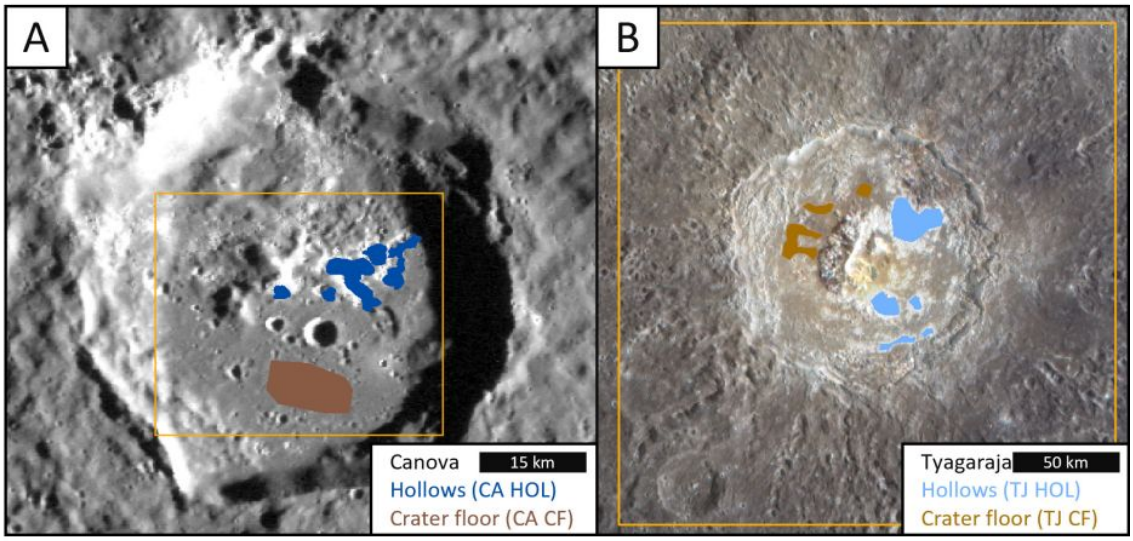

Figure 8.2: A) Canova crater as seen on the 166 m/px MDIS NAC basemap and the hollows (CA_HOL,blue) and the crater floor material (CA_CF,brown) ROIs.B) Tyagaraja crater as seen on the 665 m/px MDIS WAC colour mosaic overlain on the 166 m/px MDIS NAC basemap and the hollows (TJ_HOL, lightblue) and the crater floor material (CA_CF, gold) ROIs.

I/F, and we compare it with the results from Domingue et al. (2016). In particular, we consider the box and whisker plots of the ratios between the predicted and observed I/F. A box and whisker plot is a non parametric method used in descriptive statistic to display the variability in samples of a statistical population without assuming a particular distribution. The extent of the box equals the interquartile range (IQR), i.e. the samples between the 25th and 75th percentile of the population, while the whiskers are indicative of the variability of the dataset (i.e. $\approx \pm 3\sigma$ of a Gaussian distribution) and are equal to the 75th percentile +1.5IQR and to the 25th percentile −1.5IQR. Values outside the whiskers are usually considered outliers. We adopted this methodology because it is independent from the parameter distribution, which may not be Gaussian, and because the median is a much more robust indicator of central tendency than the average. An graphical explanation of these concepts is given in Fig. (8.3C), while a zoomed view of the box and whisker plots for the F band and KS3 model is shown in Fig. (8.3D). The shift from 1 of the median and the IQR are also reported. After the fitting assessment is completed, we generate parameter maps that are used for the subsequent analysis. In particular, we define the ROIs in Fig. (8.2) at both Canova and Tyagaraja covering the hollows (CA_HOL and TJ_HOL, respectively) and the surrounding crater floor materials (CA_CF and TJ_CF, respectively). These ROIs are used to extract statistics from the parameters maps for each model, and compare the hollows statistics between the two sites and with the crater floor material in which they formed. For the above mentioned reasons, we extract from each ROI the median value of each model parameter. The associated errors are given by the 25th percentile −1.5IQR and by the 75th percentile +1.5IQR, which is similar to the $\pm 3\sigma$ range of a Gaussian distribution.

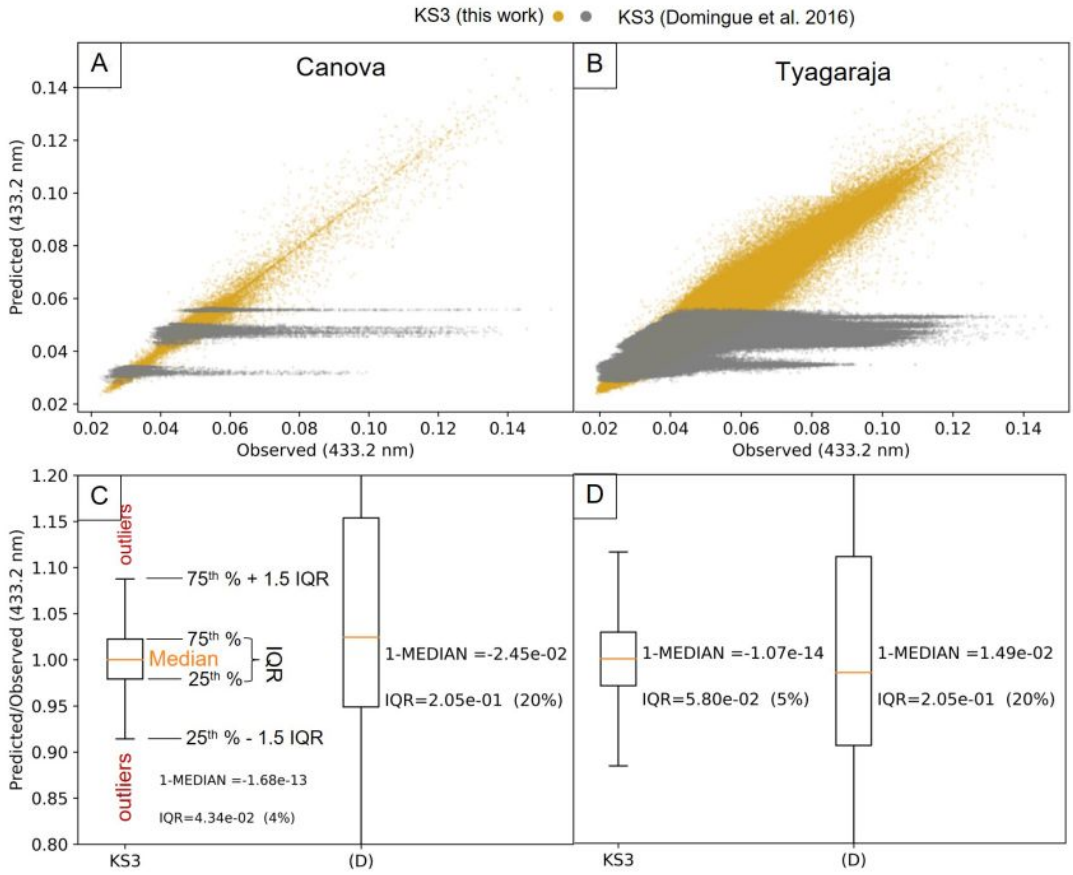

Figure 8.3: Comparison of predicted (y-axis) vs observed (x-axis) I/F for Canova (A) and Tyagaraja (B). Gold points represent our best-fit KS3 model, while the grey points represent the average Mercury KS3 model of Domingue et al. (2016). All datapoints are for the WAC F filter (433.2 nm). C) and D) represent box and whisker plots of the ratio between the y-axis and the x-axis of panels A) and B), respectively. The shift from 1 of the median and the IQR are also reported. Panel C) also indicates the various elements of a box and whisker plot.

8.3 Modeling accuracy assessment

After estimating the model parameters at each grid point for each WAC filter and for both our study sites, we assess the performances of our modeling by comparing the observed flux from the images with the predicted flux from our fitted models. In all WAC filters and for all the considered models, we could achieve a better prediction than the global Mercury photometric models in Domingue et al. (2016). An example for the KS3 model and the F filter (433.2 nm) is shown in Fig. (8.3), where we compare the predicted I/F vs the observed I/F. A perfect modeling would return a set of datapoints distributed around a 1:1 ideal relationship. While our modeling approximates this ideal behaviour, albeit with some scatter, the global Mercury model departs from it for bright fluxes. This is shown for all models and all filters in Fig. (8.4,8.5), where we report the. The box and whiskers plots in Fig. (8.4,8.5) highlight that in each band and for each model our approach represents an improvement with respect to the global solution. Since the grey-shaded band, representing a 10% variation around unity, is approximately consistent

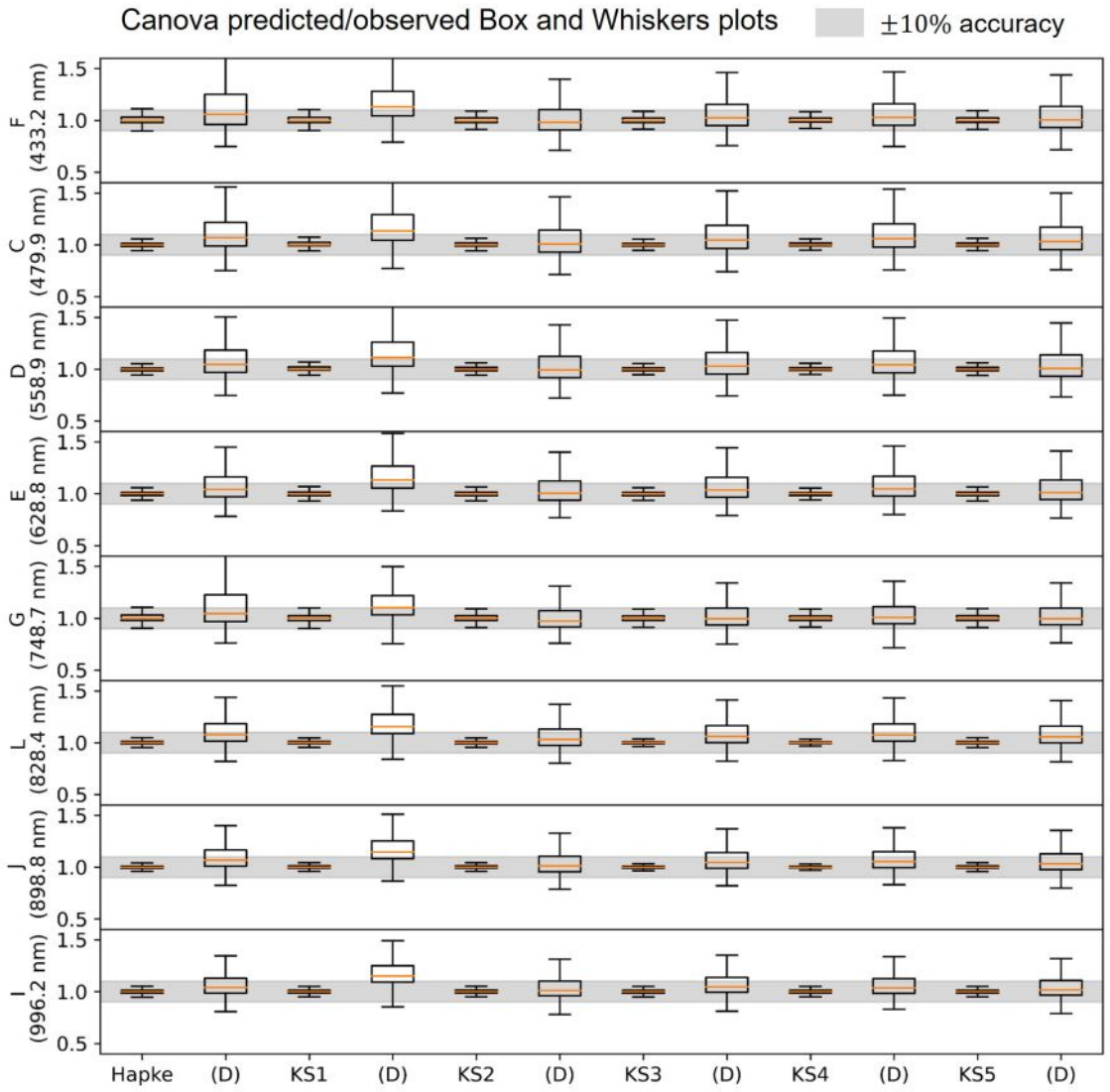

Figure 8.4: Box and whiskers plots of the ratios between the predicted and observed I/F for each WAC filter (y-axis) and each model (x-axis) at Canova crater. The (D) label indicates the version of Domingue et al. (2016). The grey shaded band indicate a spread of ±10% around 1.

with the extent of the whiskers, we estimate an accuracy higher than 10% at $\approx 3\sigma$. Quantitative values of the median and IQR are reported in Fig. (8.3C,D) and confirm this result.

8.4 Model parameters estimates

With our approach we derived disk resolved model parameter maps for both Tyagaraja and Canova crater at 665 m/px resolution. Our maps are reported in Fig. (8.6,8.7,8.8,8.9,8.10) for Canova and in Fig. (8.11,8.12,8.13,8.14,8.15) for Tyagaraja. While all models perform very well in reproducing the observed flux values with an accuracy better than $\approx$ 10% at 3σ, through the inspection of parameter maps we can assess the quality of estimation and identify potential nonphysical/unreliable

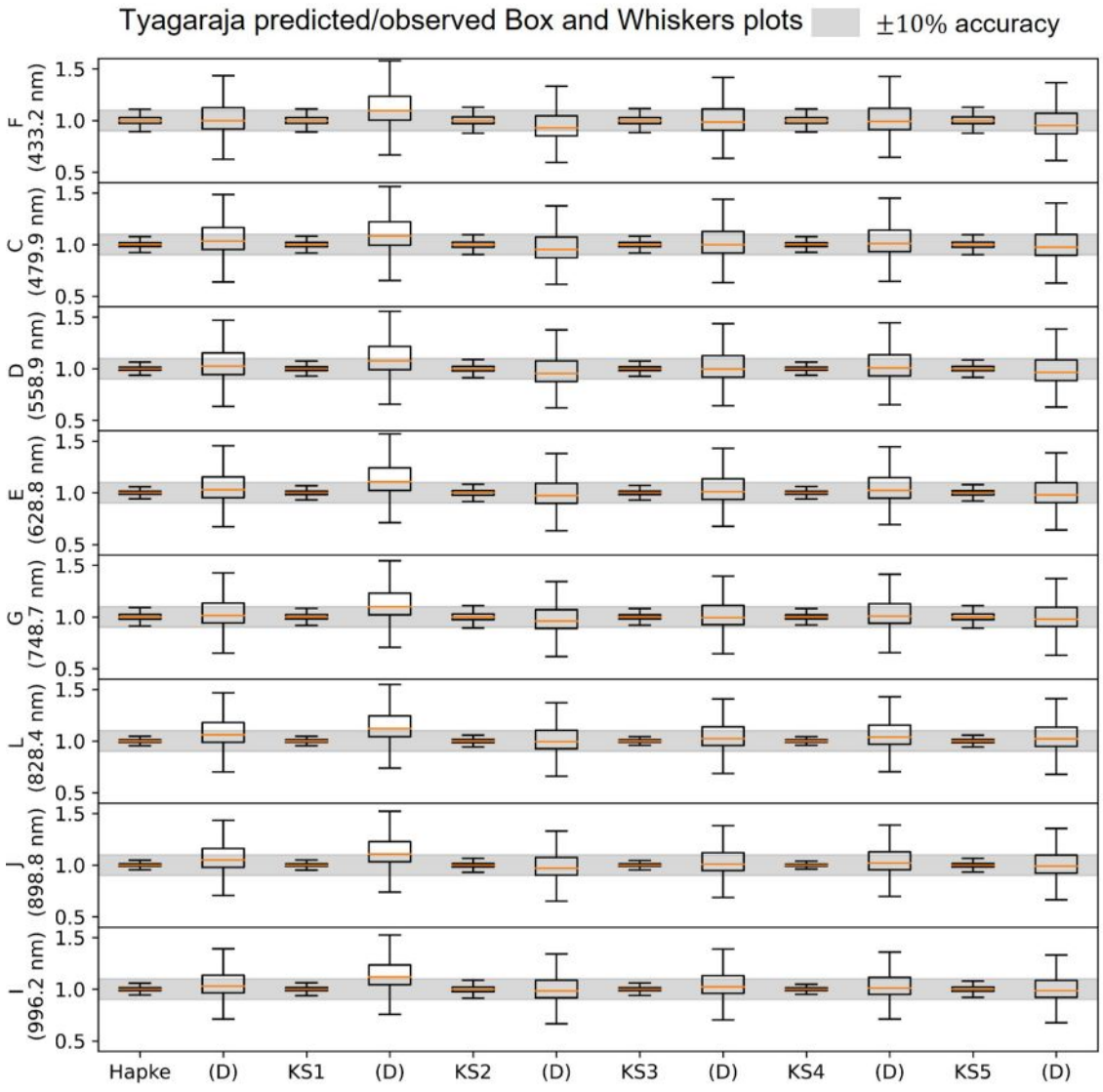

Figure 8.5: Box and whiskers plots of the ratios between the predicted and observed I/F for each WAC filter (y-axis) and each model (x-axis) at Tyagaraja crater. The (D) label indicates the version of Domingue et al. (2016). The grey shaded band indicate a spread of ±10% around 1.

estimates. In particular, a good photometric model should produce parameter maps that are correlated with surface composition and free of signs of residual topographic shading. While this is accomplished at Canova, the KS1, KS2 and KS5 models at Tyagaraja resulted in parameter maps which still carry a residual topographic shading. This is shown for example for the surface roughness μ in Fig. (8.16). While the nature of this residual is unclear, the fact that the KS3 and KS4 models did not show this feature even though they have the same parameter and were fitted with the same observations, suggest that it may be due to the model not being able to fully fit the observed fluxes. For this reason, we exclude the KS1, KS2 and KS5 from further analyses.

8.5 Model parameter analysis and interpretation

In this section we compare the model parameters of the Tyagaraja hollows with the Canova ones and then we compare, at each site, the hollows parameters with the respective crater floor materials.

8.5.1 Hapke parameters

The Hapke parameters have been often used to investigate the physical properties of the regolith. The HG Hapke parameters (b and c have been related to the internal structure of the regolith, while θ to its roughness. McGuire and Hapke (1995) and Souchon et al. (2011) related the b and c parameters to the internal texture and structure of the particles composing the light-scattering surface. Both studies found that the b and c Hapke parameters of artificial and natural particles lie on the so called "Hockey-Stick relation", a L-shaped curve in the c vs b parameter plot (also called the HG parameter plot), as depicted in Fig. (8.17). In particular, round particles with a complex internal structure (vesicles, inclusions, cavities, hollows) are more backscattering (high c and low b) than irregular but internally more uniform ones (low c, high b). We note that in literature there are several expressions for the 2 term Henyey-Greenstein function, leading to different expressions for c. In particular, in section (8.1.1) we adopted the notation used by Domingue et al. (2016). For better consistency with the work of McGuire and Hapke (1995), which introduced the Hockey-Stick relation, we now convert our c values to their notation. In particular, the new notation is given by $c = 1 - 2c_d$, where c_d is the notation of Domingue et al. (2016). Our estimates of the b and c parameters for hollows and crater floor materials at Canova and Tyagaraja are reported in the HG parameter plot in Fig. (8.17) along with the average parameters from Mercury (Domingue et al., 2016), the Moon (Sato et al., 2014), the artificial particles of McGuire and Hapke (1995) and the natural samples of Souchon et al. (2011). In particular, we note that all Mercury-related materials (average Mercury, hollows and crater floor materials) are all backscattering, and consistent with spherical particles with a high density of internal scatterers, following McGuire and Hapke (1995), or round, rough, opaque and hollowed particles according to Souchon et al. (2011). Another way to analyse the estimated Hapke parameters is to compare the two hollows and the hollows vs crater floors parameters as a function of wavelength, as shown in Fig. (8.18). We note that the Hake parameters for the Canova and Tyagaraja hollows are consistent one another, meaning that the hollow-forming material at the two sites has similar

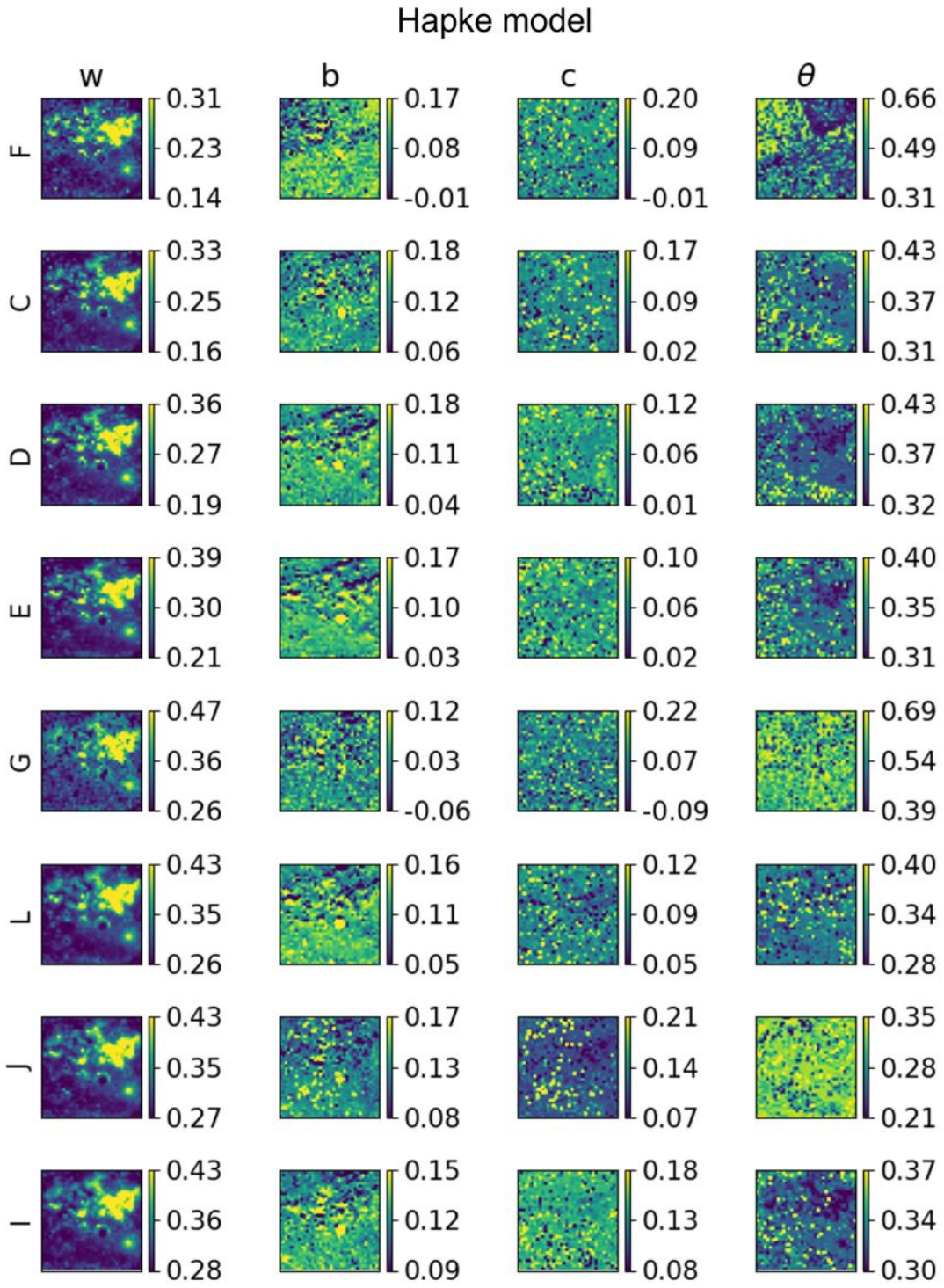

Figure 8.6: Hapke parameters maps for Canova crater in the 8 WAC colour filters.

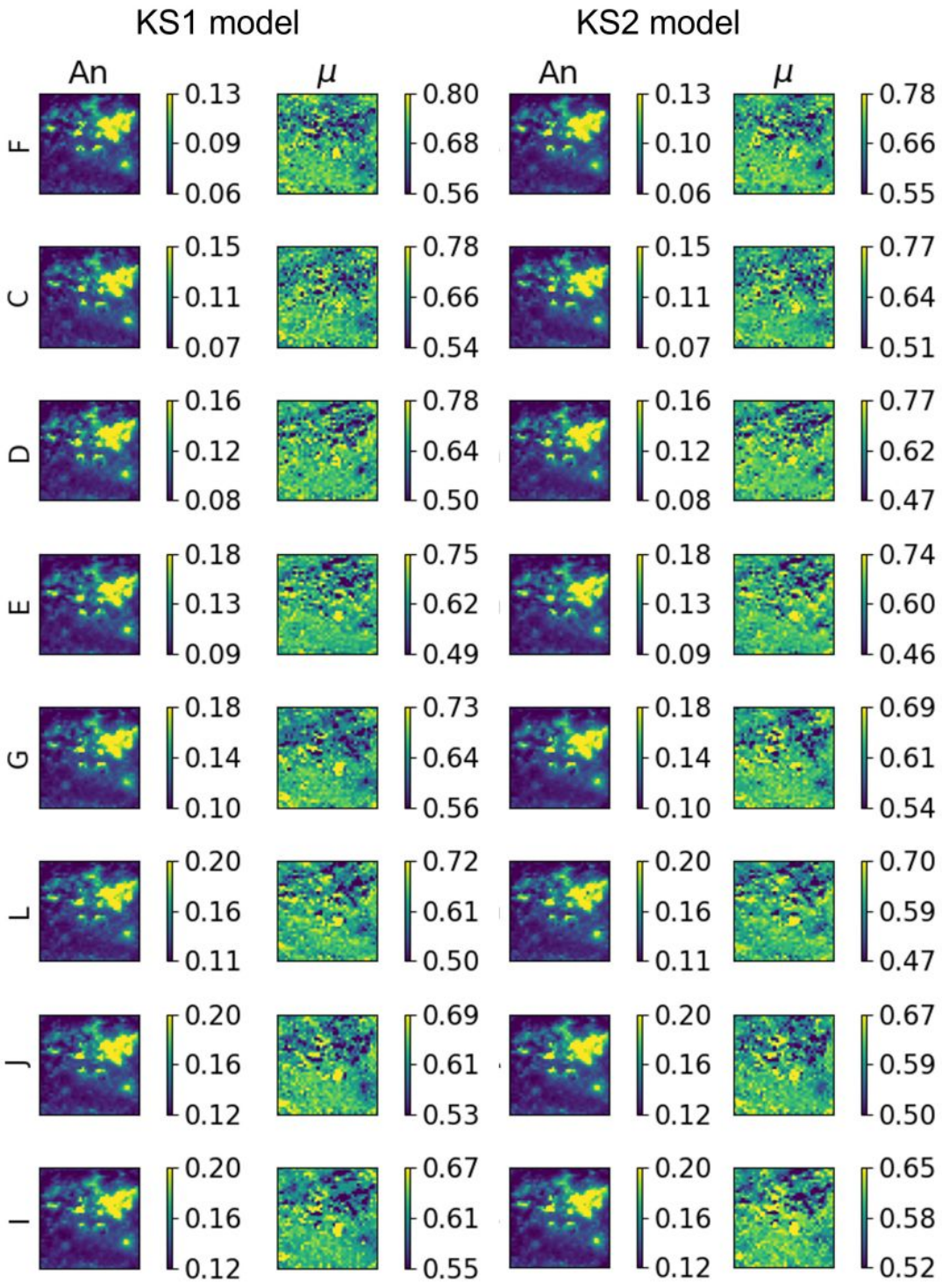

Figure 8.7: KS1 (left) and KS2 (right) parameters maps for Canova crater in the 8 WAC colour filters.

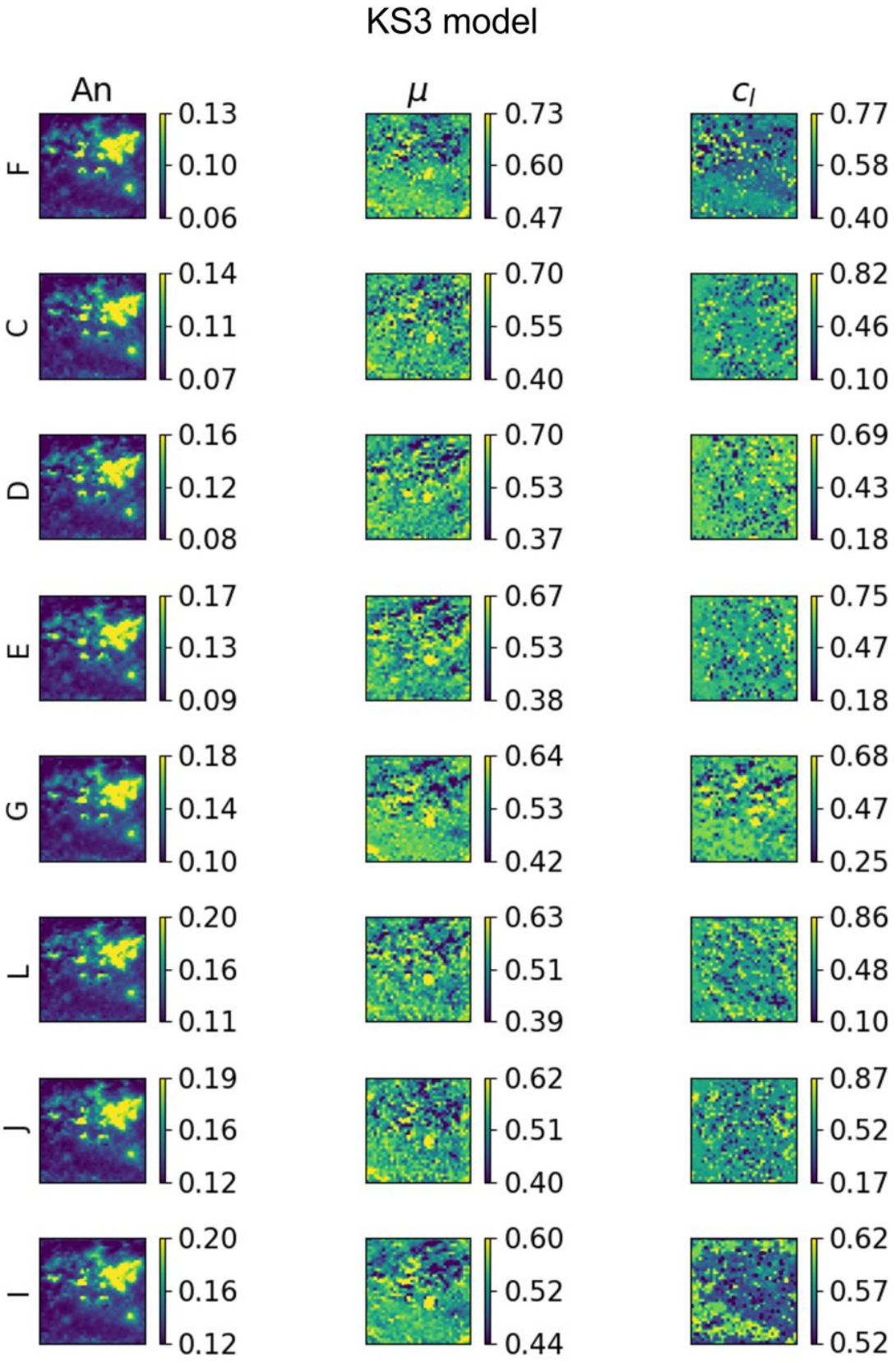

Figure 8.8: KS3 parameters maps for Canova crater in the 8 MDIS/WAC colour filters.

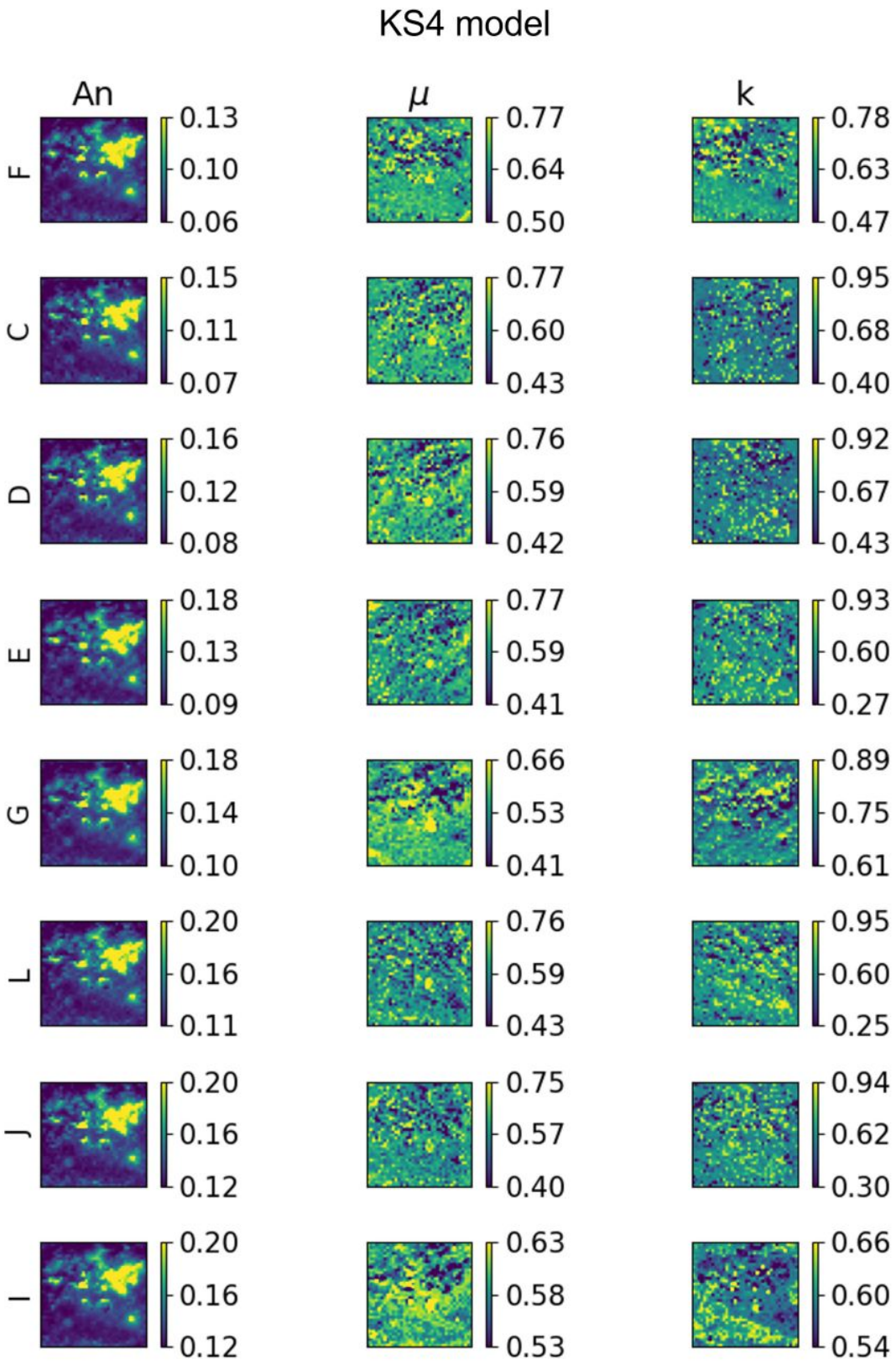

Figure 8.9: KS4 parameters maps for Canova crater in the 8 MDIS/WAC colour filters.

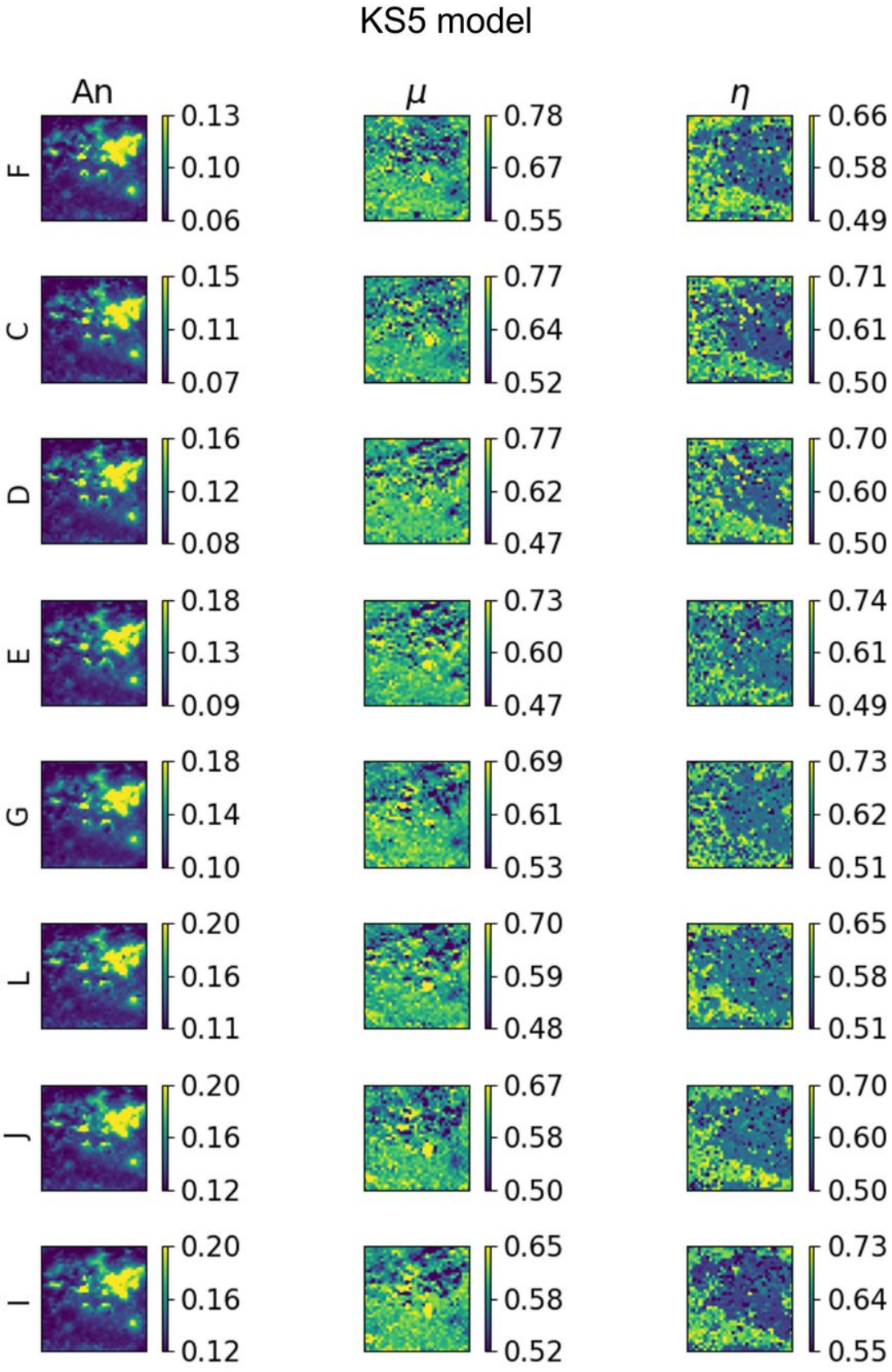

Figure 8.10: KS5 parameters fro Canova crater in the 8 MDIS/WAC colour filters.

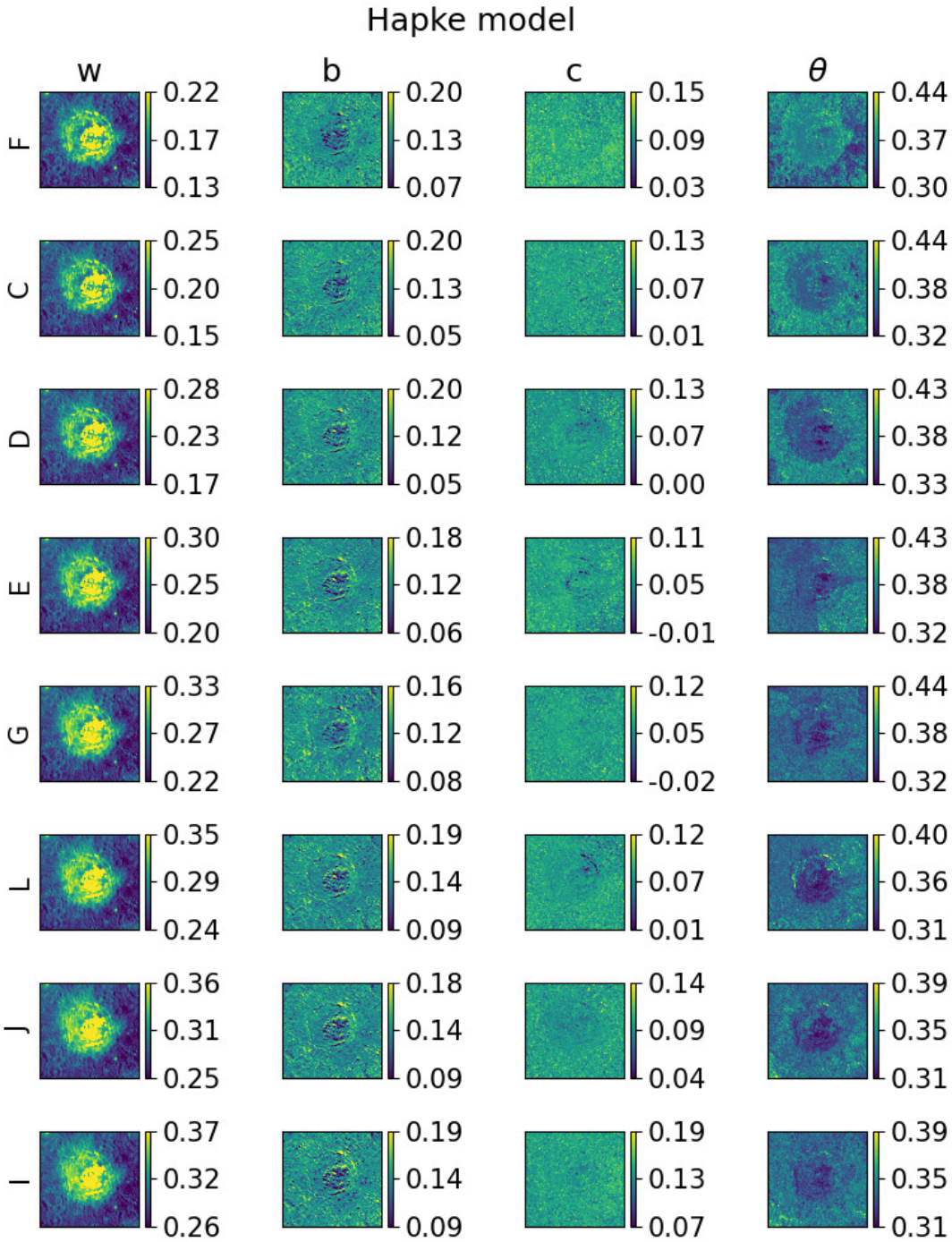

Figure 8.11: Hapke parameters maps for Tyagaraja crater in the 8 WAC colour filters.

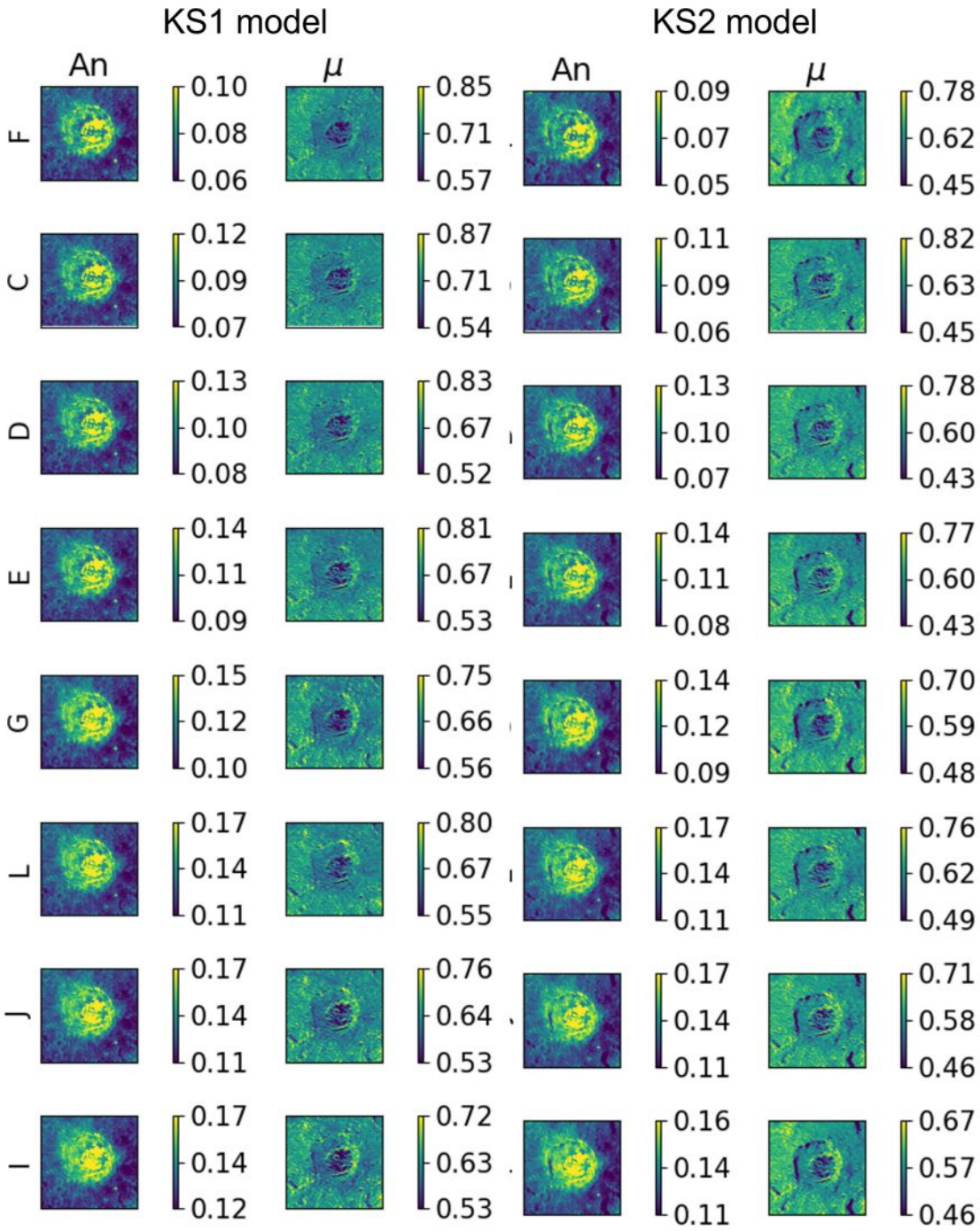

Figure 8.12: KS1 (left) and KS2 (right) parameters maps for Tyagaraja crater in the 8 WAC colour filters.

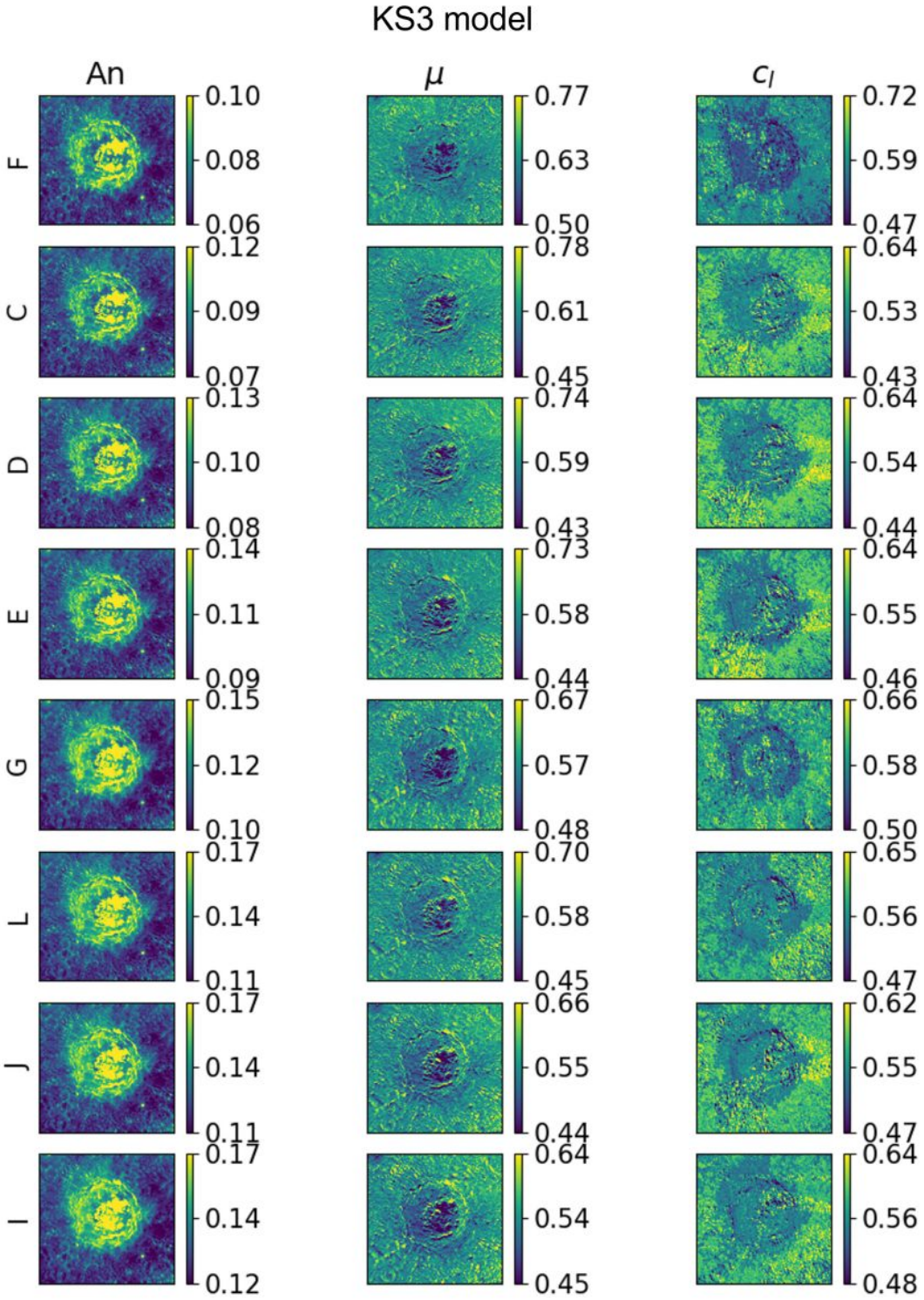

Figure 8.13: KS3 parameters maps for Tyagaraja crater in the 8 MDIS/WAC colour filters.

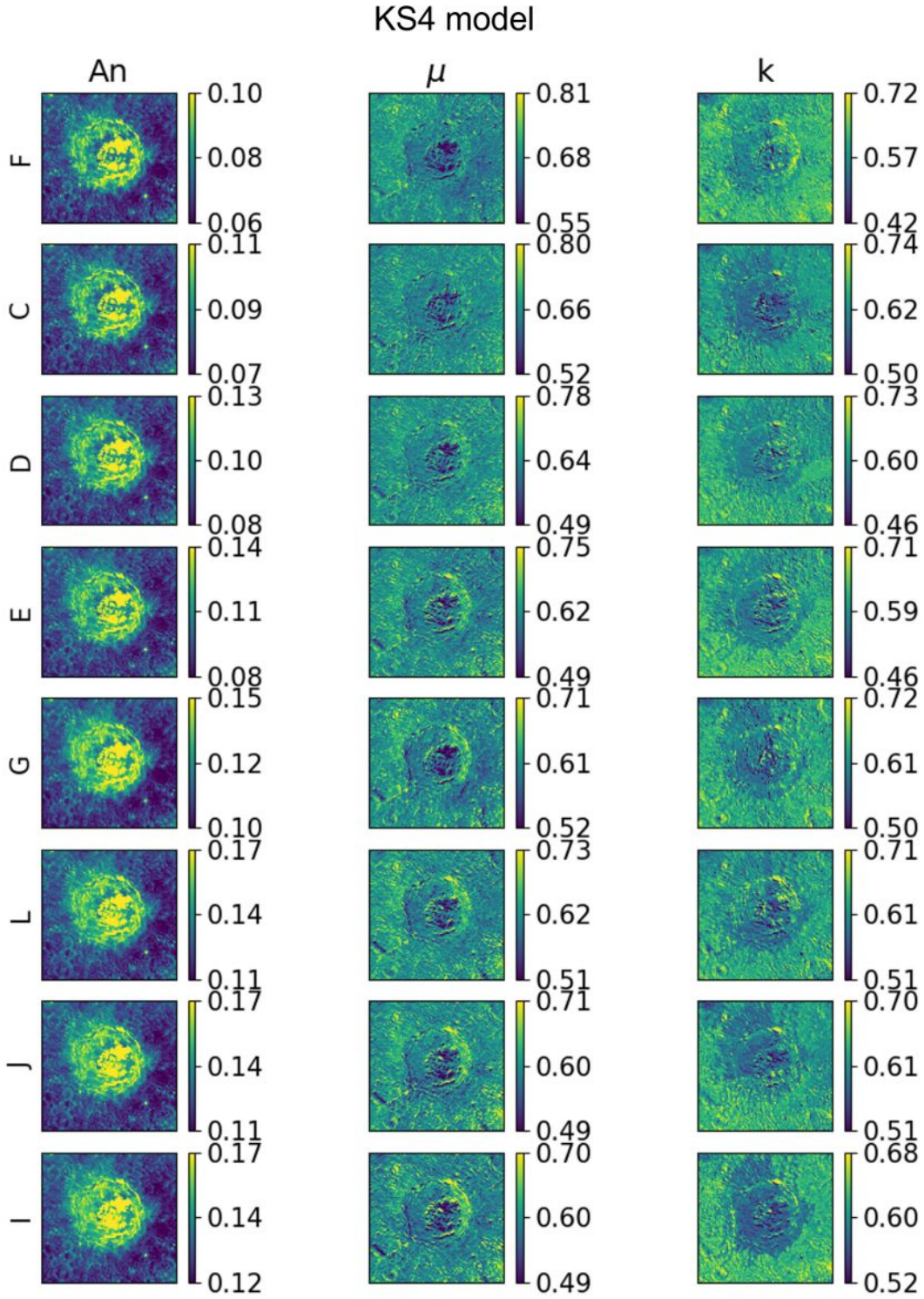

Figure 8.14: KS4 parameters maps for Tyagaraja crater in the 8 MDIS/WAC colour filters.

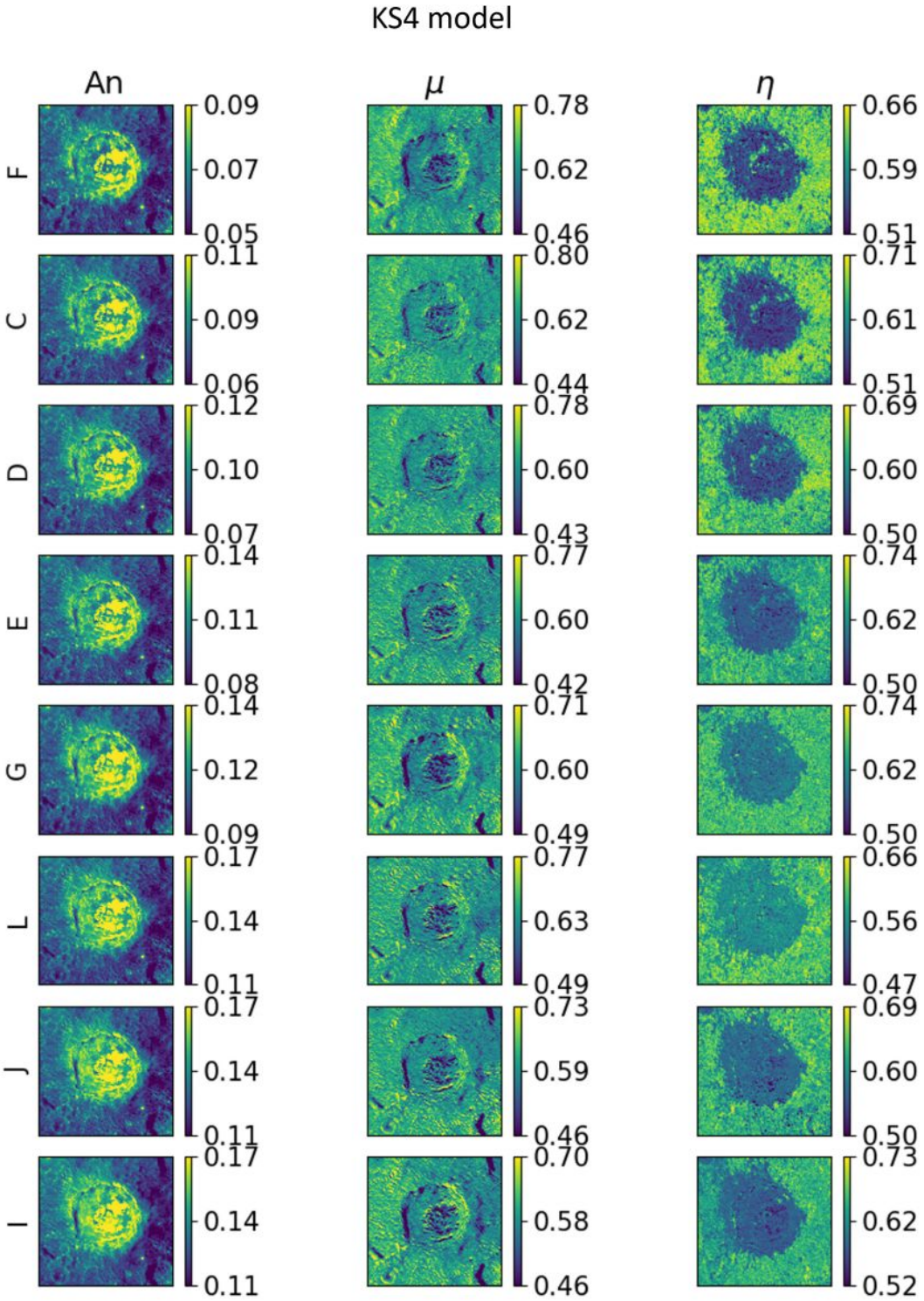

Figure 8.15: KS5 parameters fro Tyagaraja crater in the 8 MDIS/WAC colour filters.

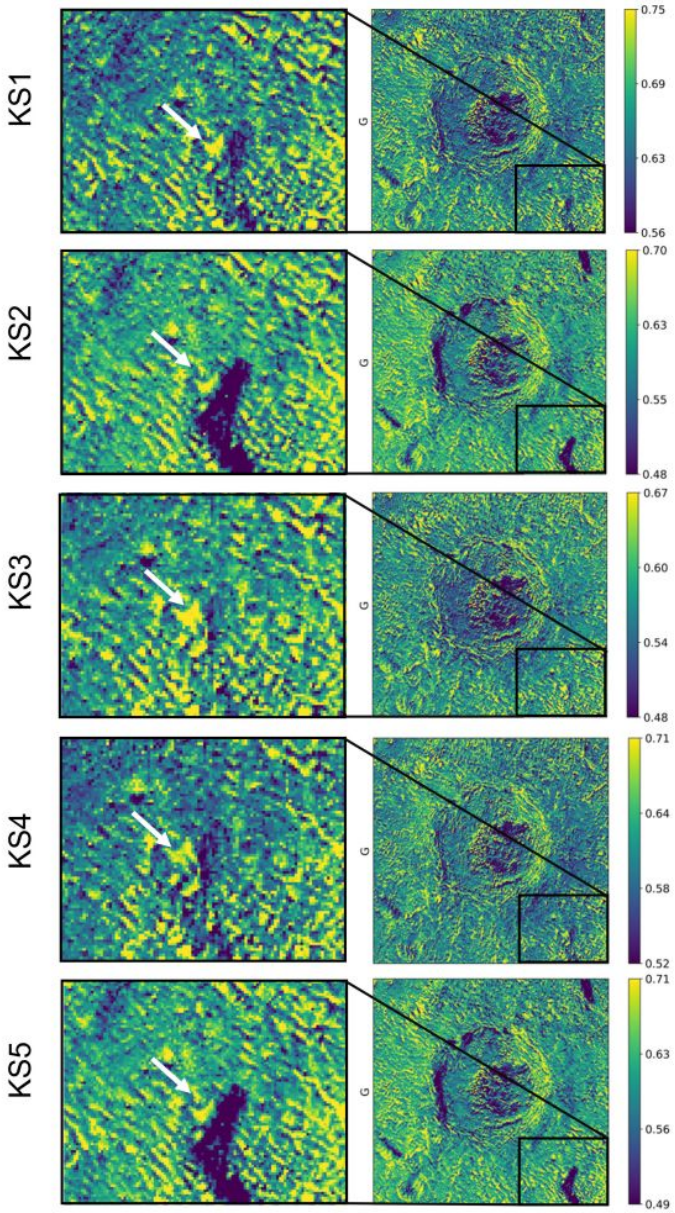

Figure 8.16: KS μ parameter maps of Tyagaraja crater in the G-band for each KS model (Right). The left column shows a closeup on a location with a residual topographic shading, indicated by white arrows. This residual is much less significant or absent in the KS3 and KS4 models.

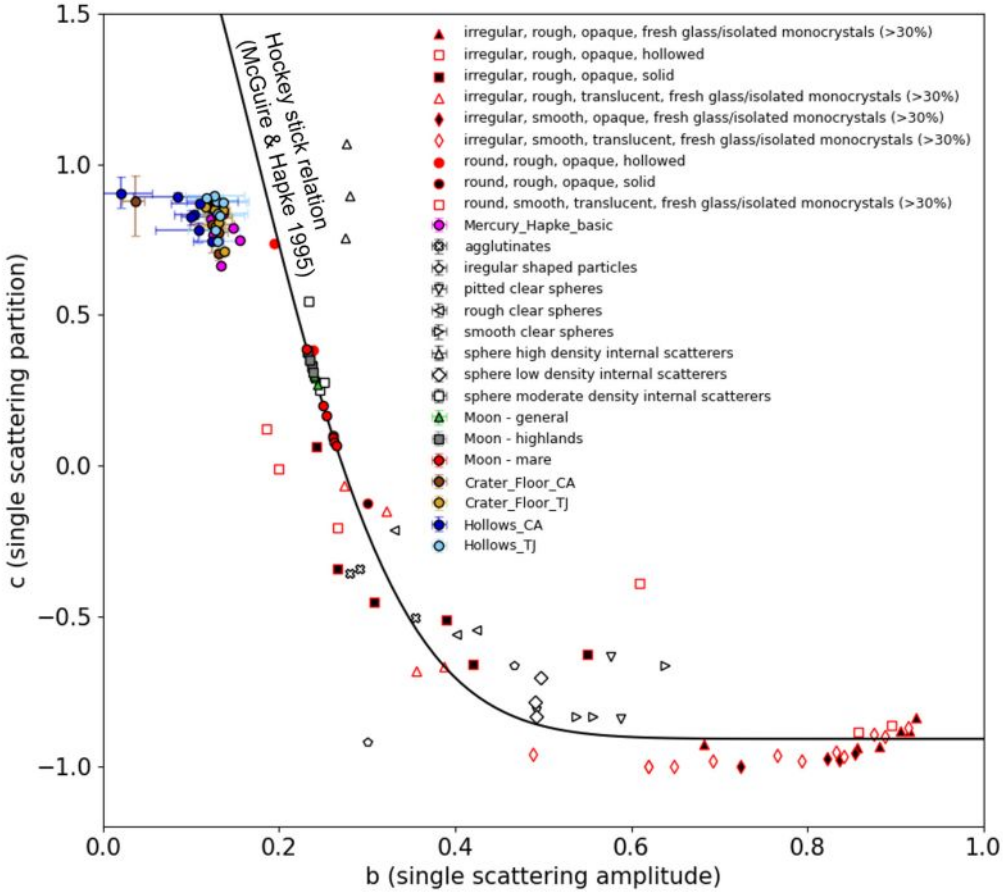

Figure 8.17: c vs b Hapke parameter plot and comparison with the Hockey-Stick relation (McGuire and Hapke, 1995) for different Materials. White markers are from McGuire and Hapke (1995). Red-bordered markers are from Souchon et al. (2011). The Moon data (red, green and grey markers) are from Sato et al. (2014).The pink markers represent the global mercury parameters from Domingue et al. (2016).

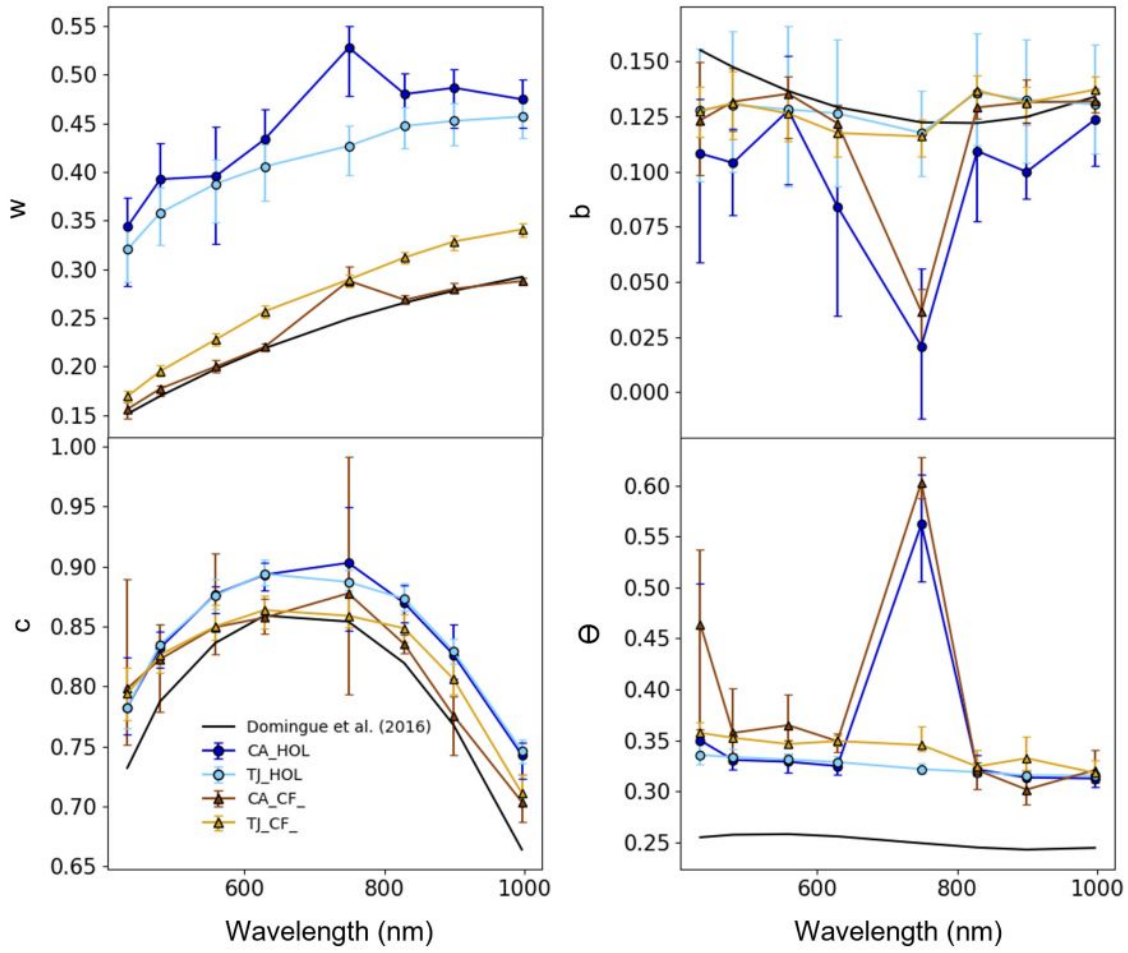

Figure 8.18: Hapke parameters for the Canova and Tjagaraya hollows (blue and light blue markers and lines) and crater floor material (brown and gold markers and lines) and for the average Mercury (black lines).

physical properties. The crater floor material is not too much dissimilar, but there is more variability than the two hollows samples, consistently with the different geological history of the two craters. Three main trend emerge from Fig. (8.18). From panel (A) we see that there is a significant difference in the hollows single scattering albedo from the other materials, which is expected since hollows are brighter than the surroundings. Panel (C) shows that hollows have systematically higher c with respect to the average Mercury and the crater floor material in which they form, implying a more backscattering behaviour and more hollowed/textured particles with a higher density of internal scatterers. This difference is not significant in the UV, specifically at 433.2 and 479.9 nm, meaning that at these wavelength the internal structure of the hollow-forming material is similar to the crater floor material. Panel (D) shows that hollows have a lower θ than the crater floor material, hence they are slightly smoother, although this difference is not significant in the near infrared. No particular trends emerge form the b parameters in panel (B). The parameter for the average Mercury, depicted with a black line in Fig. (8.18) are kept for reference. A comparison is not straightforward because of the different geological histories that characterise the Tyagaraja, the Canova and the regions used to derive the average global Hapke parameters for Mercury.

8.5.2 KS parameters

We here report the KS3 and KS4 parameters for the hollows and crater floor material as a function of wavelength at Canova and Tyagaraja crater. As we already mentioned in section (8.4), the KS1, KS2 and KS5 models provide poor parameter estimates and therefore are excluded from further analyses.

The KS3 model

The KS3 parameters in Fig. (8.19) show a normal albedo difference between the hollows and crater floor material, in agreement with the single scattering albedo, and consistent with the fact that hollows are brighter than the surrounding terrain. Hollows also have a lower surface roughens mu, meaning that they should be smoother, than the crater floor material in which they form. This is consistent with what suggested by the Hapke modeling, but the interpretation of the KS mu is more challenging. This parameter, in fact, is affected both by the surface roughness and the properties of the individual particles (shape, size, transparency, composition). Moreover, the differences in mu are almost comparable with the errors, unlike in the Hapke modeling, and may therefore be not significant. For these two reasons, we do not use the KS3 model to infer the physical properties of the regolith. Finally, both hollows and the crater floor material have the same c_l parameter, implying that they can be fitted by the same disk function.

The KS4 model

The analysis of the KS4 model parameters, which are shown in Fig. (8.20) is similar to those of the KS3 model. The major trend is in the normal albedo, consistent with the fact that hollows are brighter than the crater floor material. Again, the surface roughness is lower for hollows, but again this estimate suffers from all the problems of the KS3 model. Even if it is a little more significant, the challenges in its interpretation may prevent a robust link with the physical properties of the regolith. Finally, the Minnaert exponent (k) of hollows and the Tyagaraja crater floor material is similar, and a little smaller than the one for the Canova crater floor material. However, the error bars on the latter are quite large, meaning that this difference may not be significant.

8.6 Discussion

We performed a photometric modelings based on overlapping, multi angular observations instead of the commonly adopted approach to consider multiple ROIs of the same assumed composition (Domingue et al., 2016). In both tested locations, our approach resulted in more accurate photometric modeling than the global one, particularly for bright surfaces. This implies that future spectrophotometric analyses of Mercury may benefit from this methodology whenever the scientific target is highly reflective, like hollows, bright fresh crater rays and/or pyroclastic materials. Moreover, the resulting photometric models may be used to average all the overlapping observations and obtain higher signal to noise ratio MDIS spectra. We provide in Fig. (8.21) a further example showing the performances of our correction when mosaicking two images taken under different illumination and observation

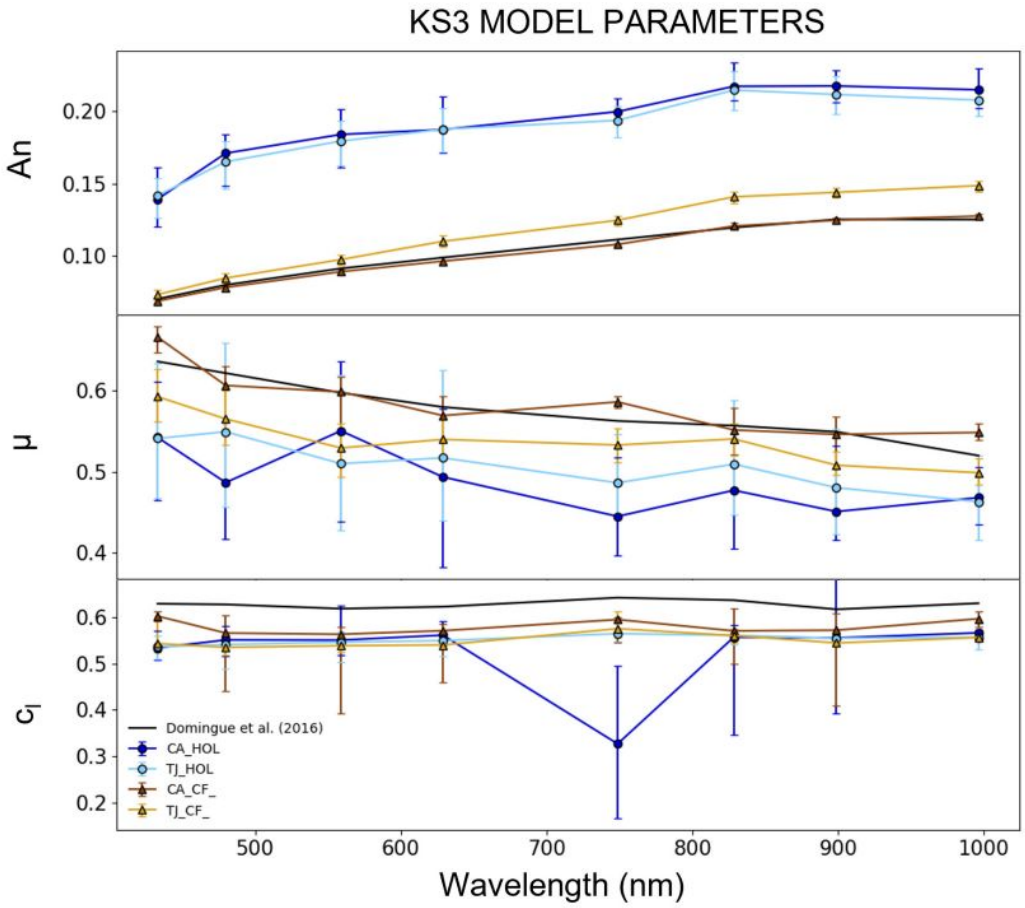

Figure 8.19: KS3 model parameters for the Canova and Tjagaraya hollows (blue and light blue markers and lines) and crater floor material (brown and gold markers and lines) and for the average Mercury (black lines).

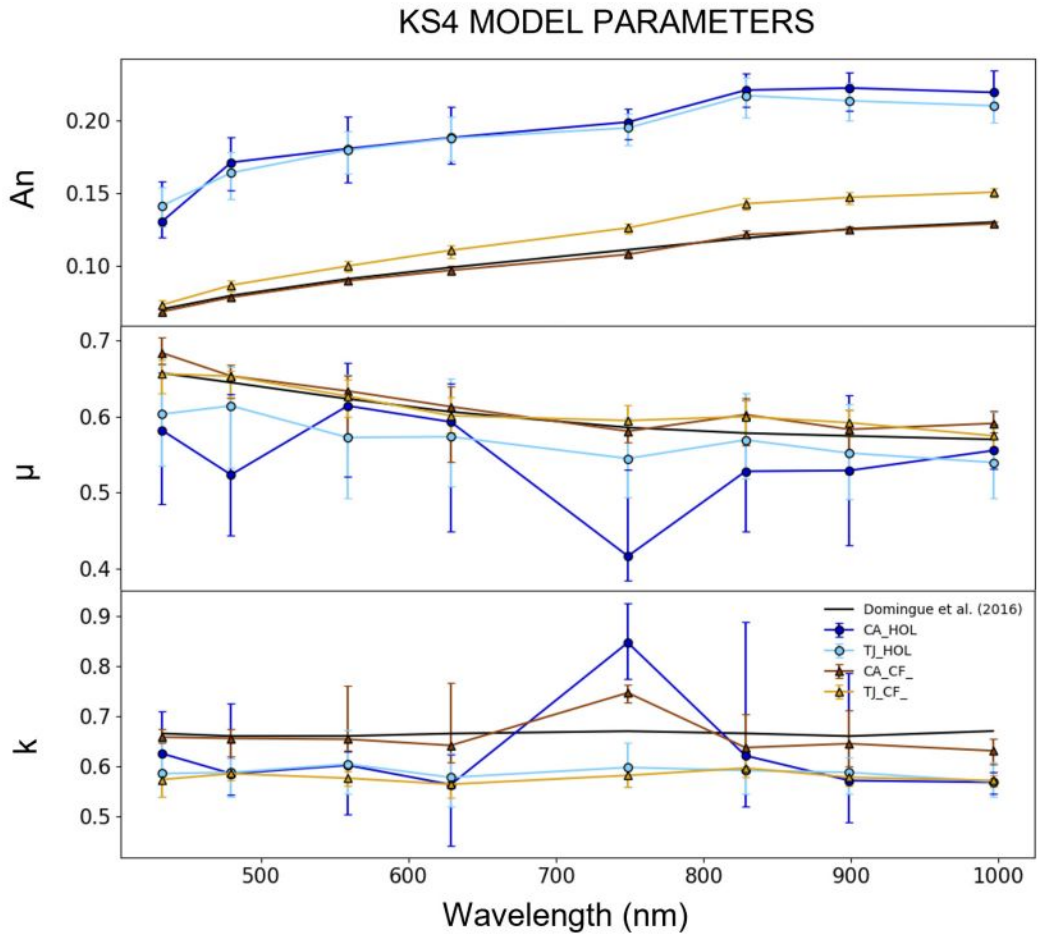

Figure 8.20: KS4 model parameters for the Canova and Tjagaraya hollows (blue and light blue markers and lines) and crater floor material (brown and gold markers and lines) and for the average Mercury (black lines).

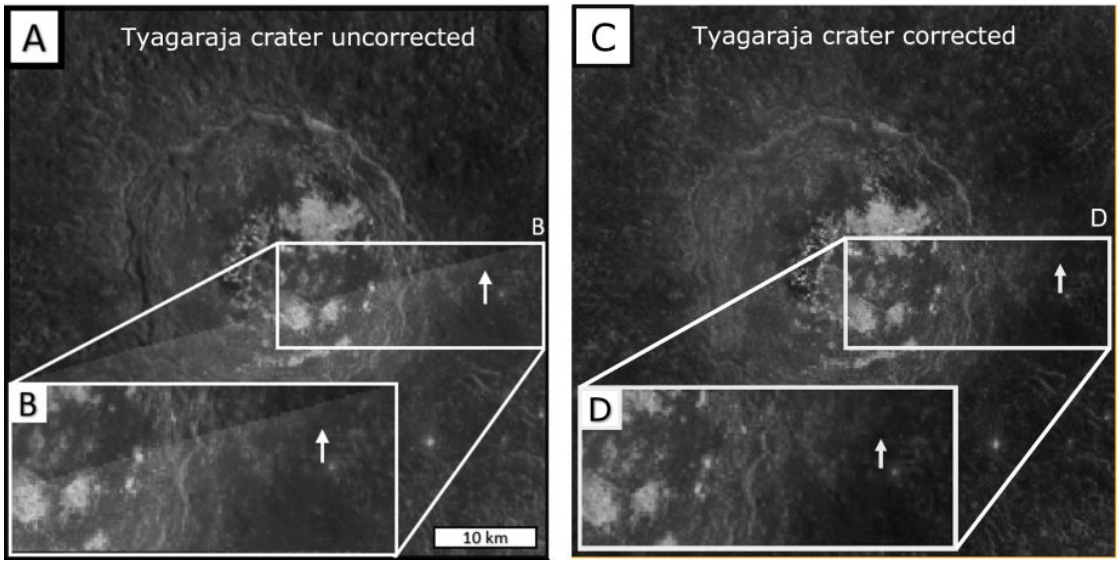

Figure 8.21: A) Mosaic of two MDIS/WAC images with different illumination and observation conditions. B) Closeup of the brightness difference between the two images. C) and D) are the same A) and B) but with the corrected images. White arrows points to the locations of the brightness difference that was completely removed by the correction.

conditions. The clear brightness difference between the two uncorrected images is completely absent in the mosaic of the two corrected observations. We quantified the accuracy of our modeling to be better than $\approx 10\%$ at 3σ. While all the tested models succeeded in predicting the observed flux values, some had partially unreliable parameter estimates. This is the case for the KS1, KS2 and KS5 models, which therefore were excluded from our analysis. On the contrary, the KS3, KS4 and Hapke models provided both high accuracy flux predictions and qualitatively reasonable and consistent parameter maps. In fact, all three models predict hollows to be smoother than the crater floor in which they form, although with a different degree of significance. Finally, the model parameters for the Tyagaraja and Canova hollows (which should be composed of the same particles even if they are from different location) match very well one another. Collectively, these results indicate that the parameter of at least the KS3, KS4 and Hapke models derived here are robust. Besides the applicability for updated and more accurate photometric correction, our modeling also allowed to characterise the scattering behaviour of the hollows and the crater floor material in which they formed. This was possible thanks to the Hapke model, while the interpretations of the KS model parameters are more challenging because they have no unique interpretation in terms of physical properties of the regolith. The HG parameter plot allowed to highlight the more back scattering nature of hollows with respect to the crater floors. This implies that the hollow-forming material is made of roundish particles with a high density of internal scatterers, which may be holes, vesicles, fractures, etc. This picture is consistent with the hollows being formed by the release of a volatile, that leaves behind holes and a possibly more fractured terrain, which serves as additional internal scatterers with respect to the original material. We also find that hollows are smoother than the surrounding terrain. This is consistent with the phase ratio analyses of newly formed hollows (like the ones in Canova) or near the walls of the hollows (that are

very common at Tyagaraja) (Blewett et al., 2014; Thomas et al., 2016; Wang et al., 2020). The fact that hollow walls are smoother fits rather well in the traditional hollows evolutionary scheme depicted in Fig. (7.6). During scarp retreat, in fact, loss of volatiles weakens the walls causing them to crumble and collapse towards the floor (Blewett et al., 2016). This mass wasting process occurring on the hollow may therefore bring the largest blocks of material downslope, accumulating them in the hollow floor (which is relatively small at Canova and Tyagaraja) and exposing relatively smoother material, made of smaller blocks or not-yet crumbled rocks. This would also imply the hollow floors to be rougher than the surrounding material, which is exactly what is inferred from phase ratio analyses (Blewett et al., 2014; Thomas et al., 2016; Wang et al., 2020). This smooth material would also carry the signs of devolatilization, hence displaying a lower θ with the increased back scattering behaviour. These results confirm in an independent way that hollows may be the result of a devolatilization process. The identity of the volatile phase is not constrained, but if a low albedo component is lost, like Graphite, then this would explain the higher single scattering and/or normal albedo of hollows. However, more in depth analyses should be performed to provide a robust conclusion.

8.7 Summary and Conclusions

We adapted the methodology of Domingue et al. (2016) to perform a photometric modeling of the hollows and the floor materials of the Canova and Tyagaraja craters, exploiting the presence of overlapping multiangular observations at these two sites. In particular, we consider the Hapke and multiple versions of the KS model. We show that fitting overlapping multi-angular observation can improve the photometric modeling accuracy, in particular for bright features, with respect to what is currently achieved by global models of Mercury. The derived resolved Hapke and KS parameter maps for the Tyagaraja and Canova craters can therefore be useful for future spectrophotometric analyses of these sites and/or of hollows, because they provide a more accurate photometric correction. They can also be useful for laboratory experiments that could try to simulate the processes driving the formation of hollows and match our estimated parameters. While all model provided a good topographic correction, the KS1, KS2 and KS5 showed not fully consistent model parameter maps and hence were excluded from the subsequent analysis. Our interpretation of the model parameters in terms of the physical properties of the scattering surface relies on the Hapke parameter. In fact, they have more well-established relationships with the properties of the reflecting particles, while while the interpretation of the KS parameters are more challenging and possibly affected by multiple factors that are difficult or impossible to disentangle. By comparing the hollows parameters with the crater floor material ones are that the former are smoother than the latter. This is challenging to interpret, but it is consistent with independent phase ratio analyses of hollows with a similar geologic context (i.e., dominated by walls, regions where scarp retreat is happening). It is also consistent with the general hollow evolution framework. During their formation, they increase their surface area by scarp retreat, i.e. the hollow-forming material collapses from the walls and it is deposited in the floor, allowing the depression to grow larger and larger. In this process, rough material is more likely to fall on the floor, while the smoothest particles tends to stick on the hollow walls. We also find that hollows

have a more back-scattering behaviour, which could be due to the forming material having a high density of internal scatterers (voids, vesicles, etc.). This picture is consistent with hollows being formed by a devolatilization process, where the internal scatterers represent a "scar" left by the loss of the volatile phase. Collectively, these results confirm that hollows may be the result of a devolatilization process, although the origin of the volatile phase is not constrained. Future photometric analysis of the surface of Mercury, and of hollows particular, represent a promising tool to better and further characterise their physical properties. As detailed in the next Chapter, this characterisation will be useful in perspective of the future datasets that will be available thanks to the SIMBIO-SYS suite of instruments on BepiColombo, currently *en-route* to Mercury.

Chapter 9

From MESSENGER to BepiColombo: imaging the hermean surface with SIMBIO-SYS

In this section we will describe the future exploration of Mercury, emphasizing synergies between the research work and methodologies presented in the previous Chapter and the scientific objectives of SIMBIO-SYS instrument on board BepiColombo. We start this discussion in Section (9.1) describing, very briefly, the BepiColombo mission. In Section (9.2) we describe the SIMBIO-SYS instrument and the scientific cases and puzzles that it will target. Finally, in Section (9.3) we discuss the perspectives and potentials of the research work presented in the previous Chapter in the framework of the future analysis of the hermean surface with SIMBIO-SYS.

9.1 BepiColombo: a two spacecraft mission to unveil the secrets of Mercury

The BepiColombo (Benkhoff et al., 2010) mission is a joint ESA-JAXA mission named in honor of the Italian mathematician Giuseppe (Bepi) Colombo (1920-1984), launched on 20 October 2018 and currently *en route* to Mercury. It consists of two spacecrafts, the Mercury Planetary Orbiter (MPO) and the Mercury Magnetospheric Orbiter (Mio,Murakami et al., 2020), stacked together within the Mercury Transfer Module (MTM) that it will carry them in proximity of the final orbit. Once they will be captured by the gravity of Mercury, the two spacecraft will separate from the MTM and continue together towards their dedicated orbits. Mio will be released first and reach a 590 km $\times$ 11640 km altitude polar orbit. The MPO will continue upon achieving its final orbit of 480 $\times$ 1500 km altitude polar orbit. With this two spacecraft design the mission will provide a complete view of the hermean environmens: from Mercury's internal structure, surface properties and near-surface exosphere and magnetosphere through MPO, and towards the magnetospheric, radiation, solar wind and interplanetary medium in-situ environments through Mio. In summary, BepiColombo will both follow-up and complement the analyses of MESSENGER, addressing the many outstanding questions raised from the latter.

9.1.1 The Mercury Magnetospheric Orbiter (Mio)

The BepiColombo Mio will provide in situ measurements of plasma and electromagnetic fields and waves while orbiting Mercury. It includes five instruments:

- MDM: the Mercury Dust Monitor (MDM,Nogami et al. (2010)) is designed to measure dust particles between 0.3 and 0.4 AU coming from the planet and from the interplanetary and interstellar space.
- MGF: the Magnetic Field Investigation (MGF, Baumjohann et al. (2010)) will study the planet's Magnetic field, magnetosphere and its interaction with the solar wind
- MPPE: the Mercury Plasma Particle Experiment (MPPE,Saito et al. (2010)) is set to investigate the plasma and particle and neutral atoms environment around Mercury
- MSASI: the Mercury Sodium Atmosphere Spectral Imager (MSASI, Yoshikawa et al. (2010)) will investigate the tenuous sodium exosphere of Mercury
- PWI: the Plasma Wave Instrument (PWI,Kasaba et al. (2010)) will provide the first electric field, plasma wave and radio wave data from the magnetosphere and solar wind.

9.1.2 The Mercury Planetary Orbiter (MPO)

The MPO features remote sensing information from a elliptical (480 $\times$ 1500 km) polar orbit. If accommodates 11 instruments:

- BELA, the BepiColombo Laster Altimeter (Gunderson and Thomas, 2010), will measure the figure, topography and surface morphology of Mercury, that will enable the creation of global digital terrain models.
- ISA, the Italian Spring Accelerometer (Iafolla et al., 2010), will measure non-gravitational perturbations acting on the MPO spacecraft and due to radiation from the Sun and the planet.
- MPO-MAG, the MPO Magnetometer (MPO-MAG,Heyner et al. (2021)), will study the Mercury planetary magnetic field and its source.
- MERTIS, the Mercury Thermal Infrared Spectrometer, (Hiesinger et al., 2020) will measure the spectral properties of the surface from 7 to 14 μm allowing to investigate its mineralogical composition.
- MGNS, the Mercury Gamma-ray and Neutron Spectrometer (Mitrofanov et al., 2010), will measure the elemental surface and subsurface composition over the entire surface of Mercury.
- MIXS stands for Mercury Imaging X-ray Spectrometer (Bunce et al., 2020), and will measure the X-ray flux from the planet to achieve complementary information about the composition of the surface.

- MORE, the Mercury Orbiter Radio Science Experiment (Iess et al., 2021), will investigate geodesy, geophysics and fundamental physics topics. It will help to characterise the planet's gravity field, infer its internal structure and it will test the general relativity theory.
- PHEBUS, the Probing of Hermean Exosphere by Ultraviolet Spectroscopy (Quémerais et al., 2020), will characterise the exosphere of Mercury with the aim of understanding its interaction with the surface and the magnetosphere.
- SERENA, the Search for Exosphere Refilling and Emitted Neutral Abundances (Orsini et al., 2021) will study the surface-exosphere-magnetosphere system and its interaction with the solar wind.
- SIXS, the Solar Intensity X-ray Spectrometer (Huovelin et al., 2020), will monitor Solar X-rays and energetic particles.
- SIMBIO-SYS, the Spectrometer and Imagers for MPO BepiColombo Integrated Observatory System (Cremonese et al., 2020), is an instrument suite containing a high-resolution imager, a stereocamera and and hyperspectral imager. It will study the geology and composition of the surface and it will contribute to geophysical studies of Mercury. A detailed description of this instrument is given in the next section.

9.2 SIMBIO-SYS: imaging composition and topography of the hermean surface

SIMBIO-SYS, on board the BepiColombo/MPO, is a suite of three instruments accommodating the High Resolution Imaging Camera (HRIC), the Visible and Infrared Hyperspectral Imager (VIHI) and the Stereo Channel (STC). During the first months of the mission, it will obtain a global mapping of the surface with STC and VIHI, hence delivering DTM at resolutions from 50 to 120m/px and compositional information at 480 m/px for the whole planet. After this it will obtain high resolution images ($5 - 12$ m/px) with HRIC, high spatial resolution spectra (120 m/px) with VIHI and 3-colour images with STC (< 120 m/px) for 20% of the surface (Cremonese et al., 2020).

9.2.1 Scientific Objectives

From a scientific standpoint, and in synergy with other instruments, SIMBIO-SYS will allow to answer several unresolved question concerning the geology and composition of the surface of Mercury that are briefly summarized hereafter.

Topography and morphology

The 3D information coming from STC, combined with the high resolution images from HRIC will allow the combined analysis of both surface morphology and topography, representing a significant step-forward in the geomorphological characterisation of the surface. This will allow to investigate the history and mechanisms of effusive and explosive volcanism. In fact, high resolution images will be useful

to investigate potential volcanic sources, while colour information and DTMs will allow to define different magmatic units. In addition, the widespread high resolution coverage will allow to better define cross-cutting relationship among the different geological units, hereby constraining the time evolution of the two styles of volcanism.

The enhanced morphological and topographic analysis that will be possible thanks to SIMBIO-SYS will be pivotal for progressing our knowledge about Mercury tectonic features. In particular, STC will enable a global assessment of fault geometries, timings, kinematics and their relationship with volcanic units at higher resolution than currently available, allowing to better understand Mercury's crustal mechanics. Finally, the production of geological maps from the SIMBIO-SYS data will enable the assessment of the interplay between impact craters, volcanism and tectonism.

Mineralogy

The limited S/N and short spectral range of the MASCS spectrometer on board MESSENGER, together with operational issues of the instrument and the intensive space weathering regime of the surface of Mercury represented a challenge in retrieving the mineralogy of the surface. The VIHI hyperspectral imaging system, with its high S/N (> 100) and broader spectral range should be able to overcome such challenges. This will be useful to understand the composition of effusive and explosive deposits, allowing to constrain the source of the magma and the consequent crustal formation and evolution. VIHI will also be able to distinguish lava flows from impact melts, allowing to identify volcanic sources of different ages and the amount of melt produced by impacts, and will be able to detect water ice. (Cremonese et al., 2020)

Volatiles

The surface expression of volatiles on Mercury is best expressed in three surface features: polar deposits, hollows and pyroclastic deposits. SIMBIO-SYS will play an important role in investigating the composition, distribution, thickness and origin of the polar deposits through imaging (STC, HRIC) and reflectance spectroscopy (VIHI). Representing a significant step forward with respect to MESSENGER in terms of coverage and resolution, it will also allow a direct confirmation of the presence of ice through its absorption bands within the VIHI spectral range. VIHI will also provide the first robust characterisation of the hollows spectral properties beyond 900 nm, where the currently available spectra from MASCS are noisy, allowing to better assess their composition. Moreover, STC and HRIC will enable high resolution geomorphological analyses of such features. In a similar way, SIMBIO-SYS is expected to reveal the compositional nature of pyroclastic deposits.

9.2.2 Mercury interior

Through its 120 m/px global DTM, STC will provide an extremely accurate global shape model of the planet (Cremonese et al., 2020). This information is critical to infer information about the planet interior, such as the extent and physical conditions of the core and the thicknesses of the mantle and the crust. Through HRIC, in

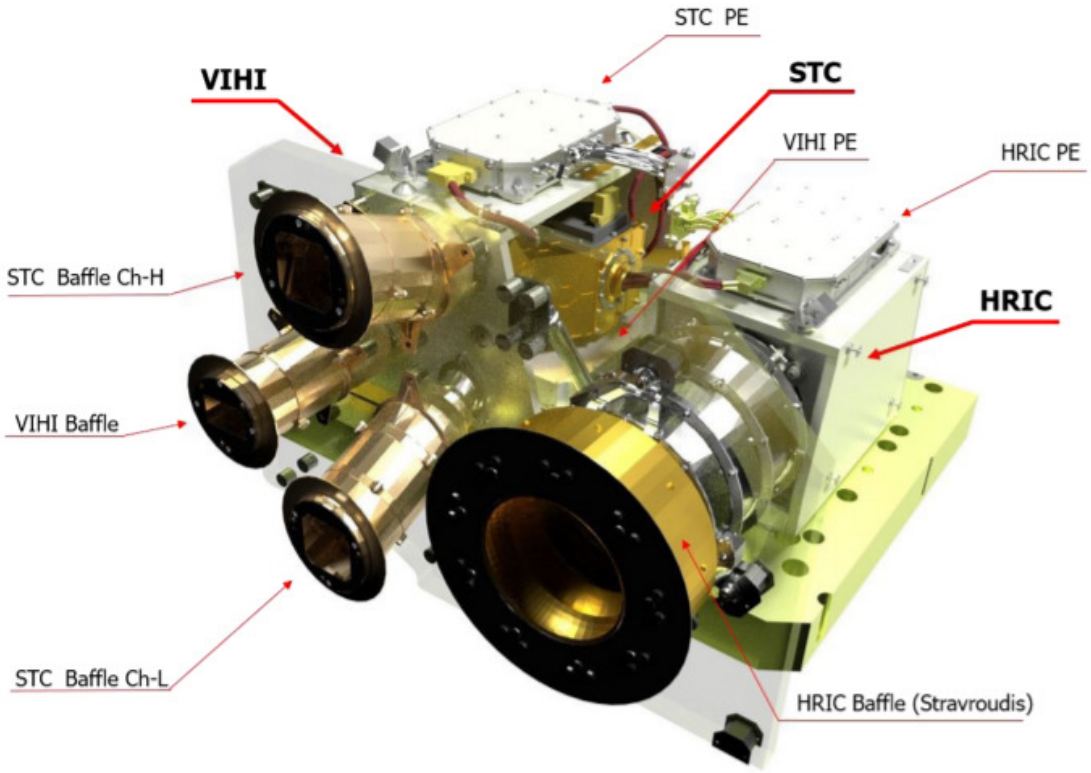

Figure 9.1: 3D rendering of SIMBIO-SYS from Cremonese et al. (2020).

addition, it will be possible to target the same surface features at different times of the mission. Their displacement can be used to inform about the planet and silicate shell moment of inertia, as well as its librations, in combination with the MORE and ISA instruments.

Surface Changes

By exploiting the high resolution provided by HRIC, SIMBIO-SYS will be able to image potential surface changes that occurred since the MESSENGER mission or during the BepiColombo mission itself. Surface changes are likely for hollows and pyroclastic activity if there is still some ongoing activity, ejecta blocks, which should change as a result of thermal stresses and loss of volatiles new impact craters and the site where MESSENGER impacted on Mercury.

9.2.3 Overview of the instrument

The SIMBIO-SYS suite of instrument is fully described in Cremonese et al. (2020), where we remind for further details. We only give here a short overview to frame the considerations of the next section. It consists of three independent optical head that share a common Main Electronics (ME) and gather light from the STC, VIHI and HRIC instruments. A 3D rendering of the instrument is shown in Fig. (9.1).

HRIC

HRIC is the high resolution multi-colour imager of SIMBIO-SYS and it will acquire images at resolutions as high as 6m/px with a S/N $\approx$ 100. The detector is the same that is mounted on CaSSIS (Thomas et al., 2017) and that it is used by STC. HRIC is equipped with four filters: a panchromatic (PAN,$400-900$ nm) that will provide the highest S/N ratio images, and three bandpasses centered at 550, 750 and 880 nm with 40 nm bandwidth for the acquisition of colour images.

STC

STC is a push-frame stereo camera. It has two channels looking with an angle of $\pm 20^{\circ}$ with respect to nadir that carry light towards the same detector, identical to the one used by HRIC. By taking advantage of the spacecraft motion, this allows to pass over the same surface region with a different viewing angle. The resulting stereo pairs can then be ingested into stereophotogrammetric pipelines to produce DTMs of the surface. STC provides six filters: two panchromatics (PAN, 699.5 nm and FWHM=204.3 nm) a 420.6 nm (FWHM=20.7 nm), a 550 nm (FWHM=20.4 nm), a 750 nm (FWHM=20.8 nm) and a 920 nm (923.8 nm) broad-bands. It will operate according two specific strategies, the Stereo Mapping and colour Mapping modes. During the Stereo Mapping, which will be performed in the first six months of the nominal mission, it will cover the whole surface with both PAN filters. After this, it will stitch to colour Mapping mode and will provide target-oriented multiband images with the four broad-bands.

VIHI

VIHI is an hyperspectral imager that will image the surface of Mercury from 400 nm to 2000 nm with a spectral sampling of 6.25 nm. Its operating principle is that the light collected by the telescope passes through a slit and is dispersed by a diffraction grating on the detector. This allows to acquire 2D images (of the slit) at each wavelength of the spectral range. In contrast to STC and HRIC, VIHI operates as a push-broom by taking advantage of the spacecraft motion to acquire overlapping images of the slit, which are then mosaicked to build the final image. This design will allow to perform a global spectral coverage of the planet during the first six months of the mission at 480 m/px resolution. The second six months of the nominal mission are instead dedicated to targeted acquisitions at its maximum resolution (120 m/px).

9.3 Future perspectives: spectrophotometric analysis of Mercury's surface with SIMBIO-SYS

As outlined in Chapter (8), the core of the research presented here about Mercury focuses on the characterisation of the spectrophotometric properties of hollows through a dedicated photometric modeling. This approach has been developed with the aim of identifying specific science questions that will be investigated in more details by SIMBIO-SYS, and specific methodologies that will be a) helpful in analysing its

future dataset and b) that will benefit from these dataset. In particular, our photometric modeling allowed to derive Hapke and KS parameters for hollows and crater floor materials at Canova and Tyagaraja crater. The consistency between the hollows parameters suggests that they may be used for any hollow site, or at least, since hollows are bright features, that they should be preferred over the global Mercury parameters. In particular, they can be very useful to carefully plan hollows observations with SIMBIO-SYS and maximize the S/N within the hollow terrain. Given that hollows are bright, the improvement offered by our photometric modeling in this range of reflectances implies a more accurate first guess of the exposure times, optimizing the quality and scientific return of the observations. In addition the parameters derived in this work can be used for the photometric correction of hollows images and spectra returned by SIMBIO-SYS, allowing more accurate spectral and spectrophotometric analyses.

On the other hand, the addition of the SIMBIO-SYS datasets to the pre-existing MESSENGER ones will allow to apply our photometric modeling approach to a much more broader ensemble of scientific cases. In fact, many (hollow and non-hollow) sites lack enough 8-filter images to provide a minimum sampling of the phase angle. With even a single observation, SIMBIO-SYS may fill the phase angle gaps of these observations and allow the photometric modeling of much more sites to be performed. This will be possible mainly with VIHI and STC, after proper convolution of the MDIS spectrophotometry in their respective photometric system (or vice-versa). A similar approach has been presented in Chapter (3) when simulating the signal of Martian soil analogs that would be observed by CaSSIS. As the mission progresses, observations of the same regions of the surface with different illumination and observation conditions will also provide multi-angular datasets, hence allowing this methodology to be applied solely to SIMBIO-SYS datasets. SIMBIO-SYS will also improve significantly the photometric modeling by providing high-resolution DTMs of the surface. This will allow to determine with higher accuracy the incidence and emission angles, hence directly improving the quality of the modeling. We highlight that solely with the global mapping DTM, an improvement of a factor 3 in terms of resolution is granted.

To conclude, the photometric modeling approach presented in this thesis will be useful in perspective of the analysis that will be performed with the images, DTM and spectra from SIMBIO-SYS and will directly benefit from the addition of such dataset, allowing a more accurate and widespread investigation of the photometric properties of the surface of Mercury.

Chapter 10

General summary and conclusions

The topic of this thesis is the analysis of surface processes on Mars and Mercury related to the (potential) release of volatiles, with the twofold aims of progressing our understanding of these processes and identifying research pathways for their future investigation.

As detailed at the beginning of this thesis, martian RSL were considered one of the most promising candidates for near-surface liquid water on Mars, although the scientific community is actively considering also dry options. Since CaSSIS started to acquire scientific images soon before the start of this Ph.D. project, we decided to exploit its new dataset and the novel analyses that they made possible. This allowed to study, for the first time, the RSL behaviour in terms of activity and albedo on a diurnal timescale. In addition, CaSSIS also allowed to investigate their spectrophotometric properties at higher resolution than in pre-existing analyses based on the CRISM spectrometer. Both these analyses allowed to gather evidences towards the a dry origin, implying that no or very little water is involved in the RSL formation process. These evidence joined those of other independent studies that have been put recently forward, that collectively shifted the paradigm of RSL formation from a potential liquid water source to a more likely aeolian feature. Nevertheless, further work is still needed for constraining the precise physical processes that originates these features. In this context, the comparison of AM-PM relative albedo and the multi-band photometry approaches that we presented in Chapters (3,4) represents promising research pathways that can be carried on with CaSSIS. Both analyses can be applied even to other surface feature on Mars to better understand their nature and formation mechanism. While developing these analyses, we realized that these required the presence of regions having the same illumination and observation conditions, limiting or preventing the analysis at locations where these could not be found. The reason for this lies in the presence, in any planetary images, of brightness differences due to topography, called topographic shading. We therefore devised, tested and validated a methodology to model and remove this effect, allowing more extended spectrophotometric analyses of the surface of Mars. This approach will be another future research pathway that can take advantage of both the 3D information and the colour capabilities of CaSSIS, maximizing the scientific return of its observations.

This decade of space exploration will see a new mission to the innermost planet

of the Solar System, Mercury. Since it is one of the less explored planets, Mercury is a very interesting celestial object. The MESSENGER mission revealed that its surface is unexpectedly rich in volatiles. It also identified puzzling bright depression, called *hollows*, that are thought to be the resulting from the release of a volatile into the exosphere. Many aspects of hollows are however still unclear, making it one of the most intriguing puzzles about Mercury. We decided to start investigating this feature with the datasets that we have from MESSENGER, aiming to understand more about the nature of the hollow forming material and their formation process, but also trying to identify specific ways in which hollows could be investigated by BepiColombo and future analytic approaches that will be in synergy with the mission. In particular, we performed a photometric modeling to analyze multi-angular observations from MESSENGER in 8 photometric bands. While this methodology was already used in the past to model the average photometric behaviour of Mercury, it always relied on collecting observations from multiple regions on the surface. In our case, instead, we collect the photometric observations at the same locations on Mercury from multiple, overlapping observations with variable illumination geometries and view angles. The resulting photometric models are therefore pertinent to each considered geographical location, in our case each point of a 665 m, regularly spaced grid, instead of the whole surface of Mercury, hence representing a step forward with respect to what is currently available in literature. The aims of this approach is twofold: a) establish the photometric behaviour of hollows to support future, updated, spectrophotometric studies of this features and b) gain insights about the nature of the hollow-forming material from established links between the photometric models parameters and their relationships with the physical properties of the reflecting surface. In particular, we derived model parameters maps at the Tyagaraja and Canova craters on Mercury, at a resolution of 665 m/px. These can be used for future spectrophotometric analyses of hollows, as they provide and improvement with respect to the current average photometric model of Mercury. In addition, since the model parameters of hollows at both locations matched each other, they can possibly be used for other locations as well and/or be used as a benchmark for laboratory experiments. These maps also allowed to infer some physical properties of the hollow-forming material. In particular, hollow would be composed of particles having a high density of internal scatterers, like internal voids, and smoother than the crater floor material in which they form. These results, that are currently being fully interpreted, are consistent with hollows being formed by a devolatilization process, although the precise identity of the volatile could not be constrained yet. Nevertheless, our methodology represent a promising tool that will be useful for future photometric analyses of the surface of Mercury. In particular, once BepiColombo will arrive at Mercury in 2025, it will be possible to take advantage of new hollows observations with SIMBIO-SYS. Combined with our photometric modeling approach, the latter are expected to significantly improve our results and their implications for the nature and formation mechanism of hollows.

Finally, although the methodologies developed in this thesis were tailored to specific science cases on Mars and Mercury, they have a wide range of applications, even on other planetary bodies. For example, high resolution topographic, imaging and multispectral datasets are available for the Moon, allowing future investigations to support the scientific and human lunar exploration over the next years.

Bibliography

Abotalib, A. Z. and Heggy, E. (2019). A deep groundwater origin for recurring slope lineae on Mars. *Nature Geoscience*, 12:235–241.

Abramov, O. and Kring, D. A. (2005). Impact-induced hydrothermal activity on early Mars. *Journal of Geophysical Research (Planets)*, 110:E12S09.

Altheide, T., Chevrier, V., Nicholson, C., and Denson, J. (2009). Experimental investigation of the stability and evaporation of sulfate and chloride brines on mars. *Earth and Planetary Science Letters*, 282(1):69–78.

Anderson, T. W. and Darling, D. A. (1954). A test of goodness of fit. *Journal of the American Statistical Association*, 49(268):765–769.

Bandfield, J. L., Glotch, T. D., and Christensen, P. R. (2003). Spectroscopic Identification of Carbonate Minerals in the Martian Dust. *Science*, 301(5636):1084–1087.

Bandfield, J. L., Hamilton, V. E., and Christensen, P. R. (2000). A Global View of Martian Surface Compositions from MGS-TES. *Science*, 287(5458):1626–1630.

Baumjohann, W., Matsuoka, A., Magnes, W., Glassmeier, K.-H., Nakamura, R., Biernat, H., Delva, M., Schwingenschuh, K., Zhang, T., Auster, H.-U., Fornacon, K.-H., Richter, I., Balogh, A., Cargill, P., Carr, C., Dougherty, M., Horbury, T. S., Lucek, E. A., Tohyama, F., Takahashi, T., Tanaka, M., Nagai, T., Tsunakawa, H., Matsushima, M., Kawano, H., Yoshikawa, A., Shibuya, H., Nakagawa, T., Hoshino, M., Tanaka, Y., Kataoka, R., Anderson, B. J., Russell, C. T., Motschmann, U., and Shinohara, M. (2010). Magnetic field investigation of Mercury's magnetosphere and the inner heliosphere by MMO/MGF. *Planet. Space Sci.*, 58(1-2):279–286.

Benkhoff, J., van Casteren, J., Hayakawa, H., Fujimoto, M., Laakso, H., Novara, M., Ferri, P., Middleton, H. R., and Ziethe, R. (2010). BepiColombo—Comprehensive exploration of Mercury: Mission overview and science goals. *Planet. Space Sci.*, 58(1-2):2–20.

Bibring, J.-P., Langevin, Y., Gendrin, A., Gondet, B., Poulet, F., Berthé, M., Soufflot, A., Arvidson, R., Mangold, N., Mustard, J., Drossart, P., OMEGA Team, Erard, S., Forni, O., Combes, M., Encrenaz, T., Fouchet, T., Merchiorri, R., Belluci, G., Altieri, F., Formisano, V., Bonello, G., Capaccioni, F., Cerroni, P., Coradini, A., Fonti, S., Kottsov, V., Ignatiev, N., Moroz, V., Titov, D., Zasova, L.,

Mangold, M., Pinet, P., Douté, S., Schmitt, B., Sotin, C., Hauber, E., Hoffmann, H., Jaumann, R., Keller, U., Duxbury, T., and Forget, F. (2005). Mars Surface Diversity as Revealed by the OMEGA/Mars Express Observations. *Science*, 307(5715):1576–1581.

Bibring, J.-P., Langevin, Y., Mustard, J. F., Poulet, F., Arvidson, R., Gendrin, A., Gondet, B., Mangold, N., Pinet, P., Forget, F., Berthé, M., Bibring, J.-P., Gendrin, A., Gomez, C., Gondet, B., Jouglet, D., Poulet, F., Soufflot, A., Vincendon, M., Combes, M., Drossart, P., Encrenaz, T., Fouchet, T., Merchiorri, R., Belluci, G., Altieri, F., Formisano, V., Capaccioni, F., Cerroni, P., Coradini, A., Fonti, S., Korablev, O., Kottsov, V., Ignatiev, N., Moroz, V., Titov, D., Zasova, L., Loiseau, D., Mangold, N., Pinet, P., Douté, S., Schmitt, B., Sotin, C., Hauber, E., Hoffmann, H., Jaumann, R., Keller, U., Arvidson, R., Mustard, J. F., Duxbury, T., Forget, F., and Neukum, G. (2006). Global mineralogical and aqueous mars history derived from omega/mars express data. *Science*, 312(5772):400–404.

Bibring, J. P., Soufflot, A., Berthé, M., Langevin, Y., Gondet, B., Drossart, P., Bouyé, M., Combes, M., Puget, P., Semery, A., Bellucci, G., Formisano, V., Moroz, V., Kottsov, V., Bonello, G., Erard, S., Forni, O., Gendrin, A., Manaud, N., Poulet, F., Poulleau, G., Encrenaz, T., Fouchet, T., Melchiori, R., Altieri, F., Ignatiev, N., Titov, D., Zasova, L., Coradini, A., Capacionni, F., Cerroni, P., Fonti, S., Mangold, N., Pinet, P., Schmitt, B., Sotin, C., Hauber, E., Hoffmann, H., Jaumann, R., Keller, U., Arvidson, R., Mustard, J., and Forget, F. (2004). OMEGA: Observatoire pour la Minéralogie, l'Eau, les Glaces et l'Activité. In Wilson, A. and Chicarro, A., editors, *Mars Express: the Scientific Payload*, volume 1240 of *ESA Special Publication*, pages 37–49.

Bierson, C. J., Tulaczyk, S., Courville, S. W., and Putzig, N. E. (2021). Strong marsis radar reflections from the base of martian south polar cap may be due to conductive ice or minerals. *Geophysical Research Letters*, 48(13):e2021GL093880. e2021GL093880 2021GL093880.

Bishop, J. L., Toner, J. D., Englert, P., Gulick, V. C., McEwen, A. S., Burton, Z. F. M., Thomas, M. F., Gibson, E. K., and Koeberl, C. (2019). Salty Solution to Slipping Soils on Martian Slopes. In *Lunar and Planetary Science Conference*, Lunar and Planetary Science Conference, page 1188.

Blewett, D. T., Chabot, N. L., Denevi, B. W., Ernst, C. M., Head, J. W., Izenberg, N. R., Murchie, S. L., Solomon, S. C., Nittler, L. R., McCoy, T. J., Xiao, Z., Baker, D. M. H., Fassett, C. I., Braden, S. E., Oberst, J., Scholten, F., Preusker, F., and Hurwitz, D. M. (2011). Hollows on Mercury: MESSENGER Evidence for Geologically Recent Volatile-Related Activity. *Science*, 333(6051):1856.

Blewett, D. T., Ernst, C. M., Murchie, S. L., and Vilas, F. (2018). *Mercury's Hollows*, pages 324–345.

Blewett, D. T., Levy, C. L., Chabot, N. L., Denevi, B. W., Ernst, C. M., and Murchie, S. L. (2014). Phase-ratio images of the surface of Mercury: Evidence for differences in sub-resolution texture. *Icarus*, 242:142–148.

Blewett, D. T., Stadermann, A. C., Susorney, H. C., Ernst, C. M., Xiao, Z., Chabot, N. L., Denevi, B. W., Murchie, S. L., McCubbin, F. M., Kinczyk, M. J., Gillis-Davis, J. J., and Solomon, S. C. (2016). Analysis of MESSENGER high-resolution images of Mercury's hollows and implications for hollow formation. *Journal of Geophysical Research (Planets)*, 121(9):1798–1813.

Blewett, D. T., Vaughan, W. M., Xiao, Z., Chabot, N. L., Denevi, B. W., Ernst, C. M., Helbert, J., D'Amore, M., Maturilli, A., Head, J. W., and Solomon, S. C. (2013). Mercury's hollows: Constraints on formation and composition from analysis of geological setting and spectral reflectance. *Journal of Geophysical Research (Planets)*, 118(5):1013–1032.

Boynton, W. V., Feldman, W. C., Squyres, S. W., Prettyman, T. H., Brückner, J., Evans, L. G., Reedy, R. C., Starr, R., Arnold, J. R., Drake, D. M., Englert, P. A. J., Metzger, A. E., Mitrofanov, I., Trombka, J. I., d'Uston, C., Wänke, H., Gasnault, O., Hamara, D. K., Janes, D. M., Marcialis, R. L., Maurice, S., Mikheeva, I., Taylor, G. J., Tokar, R., and Shinohara, C. (2002). Distribution of Hydrogen in the Near Surface of Mars: Evidence for Subsurface Ice Deposits. *Science*, 297:81–85.

Boynton, W. V., Taylor, G. J., Evans, L. G., Reedy, R. C., Starr, R., Janes, D. M., Kerry, K. E., Drake, D. M., Kim, K. J., Williams, R. M. S., Crombie, M. K., Dohm, J. M., Baker, V., Metzger, A. E., Karunatillake, S., Keller, J. M., Newsom, H. E., Arnold, J. R., Brückner, J., Englert, P. A. J., Gasnault, O., Sprague, A. L., Mitrofanov, I., Squyres, S. W., Trombka, J. I., d'Uston, L., Wänke, H., and Hamara, D. K. (2007). Concentration of H, Si, Cl, K, Fe, and Th in the low- and mid-latitude regions of Mars. *Journal of Geophysical Research (Planets)*, 112:E12S99.

Bramson, A. M., Byrne, S., Putzig, N. E., Sutton, S., Plaut, J. J., Brothers, T. C., and Holt, J. W. (2015). Widespread excess ice in Arcadia Planitia, Mars. *Geophys. Res. Lett.*, 42(16):6566–6574.

Brass, G. W. (1980). Stability of brines on mars. *Icarus*, 42(1):20–28.

Bunce, E. J., Martindale, A., Lindsay, S., Muinonen, K., Rothery, D. A., Pearson, J., McDonnell, I., Thomas, C., Thornhill, J., Tikkanen, T., Feldman, C., Huovelin, J., Korpela, S., Esko, E., Lehtolainen, A., Treis, J., Majewski, P., Hilchenbach, M., Väisänen, T., Luttinen, A., Kohout, T., Penttilä, A., Bridges, J., Joy, K. H., Alcacera-Gil, M. A., Alibert, G., Anand, M., Bannister, N., Barcelo-Garcia, C., Bicknell, C., Blake, O., Bland, P., Butcher, G., Cheney, A., Christensen, U., Crawford, T., Crawford, I. A., Dennerl, K., Dougherty, M., Drumm, P., Fairbend, R., Genzer, M., Grande, M., Hall, G. P., Hodnett, R., Houghton, P., Imber, S., Kallio, E., Lara, M. L., Balado Margeli, A., Mas-Hesse, M. J., Maurice, S., Milan, S., Millington-Hotze, P., Nenonen, S., Nittler, L., Okada, T., Ormö, J., Perez-Mercader, J., Poyner, R., Robert, E., Ross, D., Pajas-Sanz, M., Schyns, E., Seguy, J., Strüder, L., Vaudon, N., Viceira-Martín, J., Williams, H., Willingale, D., and Yeoman, T. (2020). The BepiColombo Mercury Imaging X-Ray Spectrometer: Science Goals, Instrument Performance and Operations. *Space Sci. Rev.*, 216(8):126.

Burrough, P. A. and McDonell, R. A. (1998). *Principles of Geographical Information Systems* . Oxford University Press, New York.

Byrne, P. K., Klimczak, C., Celâl Şengör, A. M., Solomon, S. C., Watters, T. R., and Hauck, Steven A., I. (2014). Mercury's global contraction much greater than earlier estimates. *Nature Geoscience*, 7(4):301–307.

Byrne, P. K., Klimczak, C., and Şengör, A. M. C. (2018). *The Tectonic Character of Mercury*, pages 249–286.

Byrne, P. K., van Wyk de Vries, B., Murray, J. B., and Troll, V. R. (2012). A volcanotectonic survey of Ascraeus Mons, Mars. *Journal of Geophysical Research (Planets)*, 117(E1):E01004.

Campbell, D. B., Chandler, J. F., Ostro, S. J., Pettengill, G. H., and Shapiro, I. I. (1978). Galilean satellites: 1976 radar results. *Icarus*, 34(2):254–267.

Carr, M. H. (2007). *The Surface of Mars*. Cambridge University Press.

Carr, M. H. and Clow, G. D. (1981). Martian channels and valleys: Their characteristics, distribution, and age. *Icarus*, 48(1):91–117.

Carr, M. H. and Head, J. W. (2010). Geologic history of mars. *Earth and Planetary Science Letters*, 294(3):185–203. Mars Express after 6 Years in Orbit: Mars Geology from Three-Dimensional Mapping by the High Resolution Stereo Camera (HRSC) Experiment.

Carter, J., Poulet, F., Bibring, J.-P., Mangold, N., and Murchie, S. (2013). Hydrous minerals on mars as seen by the crism and omega imaging spectrometers: Updated global view. *Journal of Geophysical Research: Planets*, 118(4):831–858.

Ceamanos, X., Douté, S., Fernando, J., Schmidt, F., Pinet, P., and Lyapustin, A. (2013). Surface reflectance of Mars observed by CRISM/MRO: 1. Multi-angle Approach for Retrieval of Surface Reflectance from CRISM observations (MARS-ReCO). *Journal of Geophysical Research (Planets)*, 118(3):514–533.

Chabot, N. L., Ernst, C. M., Denevi, B. W., Nair, H., Deutsch, A. N., Blewett, D. T., Murchie, S. L., Neumann, G. A., Mazarico, E., Paige, D. A., Harmon, J. K., Head, J. W., and Solomon, S. C. (2014). Images of surface volatiles in Mercury's polar craters acquired by the MESSENGER spacecraft. *Geology*, 42(12):1051–1054.

Chabot, N. L., Ernst, C. M., Harmon, J. K., Murchie, S. L., Solomon, S. C., Blewett, D. T., and Denevi, B. W. (2013). Craters hosting radar-bright deposits in Mercury's north polar region: Areas of persistent shadow determined from MESSENGER images. *Journal of Geophysical Research (Planets)*, 118(1):26–36.

Chabot, N. L., Lawrence, D. J., Neumann, G. A., Feldman, W. C., and Paige, D. A. (2018a). *Mercury's Polar Deposits*, pages 346–370.

Chabot, N. L., Shread, E. E., and Harmon, J. K. (2018b). Investigating Mercury's South Polar Deposits: Arecibo Radar Observations and High-Resolution Determination of Illumination Conditions. *Journal of Geophysical Research (Planets)*, 123(2):666–681.

Chen-Chen, H., Pérez-Hoyos, S., and Sánchez-Lavega, A. (2021). Dust particle size, shape and optical depth during the 2018/MY34 Martian global dust storm retrieved by MSL Curiosity rover Navigation Cameras. *Icarus*, 354:114021.

Chevrier, V. and Rivera-Valentin, E. (2012). Formation of recurring slope lineae by liquid brines on present-day Mars. *Geophysical Research Letters*, 39:L21202.

Chevrier, V. F. and Altheide, T. S. (2008). Low temperature aqueous ferric sulfate solutions on the surface of mars. *Geophysical Research Letters*, 35(22).

Chojnacki, M., McEwen, A., Dundas, C., Ojha, L., Urso, A., and Sutton, S. (2016). Geologic context of recurring slope lineae in melas and coprates chasmata, mars. *Journal of Geophysical Research: Planets*, 121(7):1204–1231.

Christensen, P. R., Bandfield, J. L., Bell III, J. F., Gorelick, N., Hamilton, V. E., Ivanov, A., Jakosky, B. M., Kieffer, H. H., Lane, M. D., Malin, M. C., McConnochie, T., McEwen, A. S., McSween, H. Y., Mehall, G. L., Moersch, J. E., Nealson, K. H., Rice, J. W., Richardson, M. I., Ruff, S. W., Smith, M. D., Titus, T. N., and Wyatt, M. B. (2003). Morphology and Composition of the Surface of Mars: Mars Odyssey THEMIS Results. *Science*, 300(5628):2056–2061.

Christensen, P. R., Jakosky, B. M., Kieffer, H. H., Malin, M. C., McSween, Harry Y., J., Nealson, K., Mehall, G. L., Silverman, S. H., Ferry, S., Caplinger, M., and Ravine, M. (2004). The Thermal Emission Imaging System (THEMIS) for the Mars 2001 Odyssey Mission. *Space Sci. Rev.*, 110(1):85–130.

Clancy, R. T., Sandor, B. J., Wolff, M. J., Christensen, P. R., Smith, M. D., Pearl, J. C., Conrath, B. J., and Wilson, R. J. (2000). An intercomparison of ground-based millimeter, MGS TES, and Viking atmospheric temperature measurements: Seasonal and interannual variability of temperatures and dust loading in the global Mars atmosphere. *Journal of Geophysical Research*, 105:9553–9572.

Colaprete, A., Schultz, P., Heldmann, J., Wooden, D., Shirley, M., Ennico, K., Hermalyn, B., Marshall, W., Ricco, A., Elphic, R. C., Goldstein, D., Summy, D., Bart, G. D., Asphaug, E., Korycansky, D., Landis, D., and Sollitt, L. (2010). Detection of Water in the LCROSS Ejecta Plume. *Science*, 330(6003):463.

Colombo, G. (1965). Rotational Period of the Planet Mercury. *Nature*, 208(5010):575.

Conway, S. J. and Balme, M. R. (2014). Decameter thick remnant glacial ice deposits on Mars. *Geophys. Res. Lett.*, 41(15):5402–5409.

Craddock, R. A. and Howard, A. D. (2002). The case for rainfall on a warm, wet early mars. *Journal of Geophysical Research: Planets*, 107("E11"):21–1–21–36.

Cremonese, G., Capaccioni, F., Capria, M. T., Doressoundiram, A., Palumbo, P., Vincendon, M., Massironi, M., Debei, S., Zusi, M., Altieri, F., Amoroso, M., Aroldi, G., Baroni, M., Barucci, A., Bellucci, G., Benkhoff, J., Besse, S., Bettanini, C., Blecka, M., Borrelli, D., Brucato, J. R., Carli, C., Carlier, V., Cerroni, P., Cicchetti, A., Colangeli, L., Dami, M., Da Deppo, V., Della Corte, V., De

Sanctis, M. C., Erard, S., Esposito, F., Fantinel, D., Ferranti, L., Ferri, F., FicaiÂ Veltroni, I., Filacchione, G., Flamini, E., Forlani, G., Fornasier, S., Forni, O., Fulchignoni, M., Galluzzi, V., Gwinner, K., Ip, W., Jorda, L., Langevin, Y., Lara, L., Leblanc, F., Leyrat, C., Li, Y., Marchi, S., Marinangeli, L., Marzari, F., MazzottaÂ Epifani, E., Mendillo, M., Mennella, V., Mugnuolo, R., Muinonen, K., Naletto, G., Noschese, R., Palomba, E., Paolinetti, R., Perna, D., Piccioni, G., Politi, R., Poulet, F., Ragazzoni, R., Re, C., Rossi, M., Rotundi, A., Salemi, G., Sgavetti, M., Simioni, E., Thomas, N., Tommasi, L., Turella, A., Van Hoolst, T., Wilson, L., Zambon, F., Aboudan, A., Barraud, O., Bott, N., Borin, P., Colombatti, G., ElÂ Yazidi, M., Ferrari, S., Flahaut, J., Giacomini, L., Guzzetta, L., Lucchetti, A., Martellato, E., Pajola, M., Slemer, A., Tognon, G., and Turrini, D. (2020). SIMBIO-SYS: Scientific Cameras and Spectrometer for the BepiColombo Mission. *Space Sci. Rev.*, 216(5):75.

Daubar, I. J., Dundas, C. M., Byrne, S., Geissler, P., Bart, G. D., McEwen, A. S., Russell, P. S., Chojnacki, M., and Golombek, M. P. (2016). Changes in blast zone albedo patterns around new martian impact craters. *Icarus*, 267:86–105.

Dehouck, E., Mangold, N., Le Mouélic, S., Ansan, V., and Poulet, F. (2010). Ismenius Cavus, Mars: A deep paleolake with phyllosilicate deposits. *Planet. Space Sci.*, 58(6):941–946.

Delamere, W. A., Tornabene, L. L., McEwen, A. S., Becker, K., Bergstrom, J. W., Bridges, N. T., Eliason, E. M., Gallagher, D., Herkenhoff, K. E., Keszthelyi, L., Mattson, S., McArthur, G. K., Mellon, M. T., Milazzo, M., Russell, P. S., and Thomas, N. (2010). Color imaging of Mars by the High Resolution Imaging Science Experiment (HiRISE). *Icarus*, 205(1):38–52.

Denevi, B. W., Ernst, C. M., Meyer, H. M., Robinson, M. S., Murchie, S. L., Whitten, J. L., Head, J. W., Watters, T. R., Solomon, S. C., Ostrach, L. R., Chapman, C. R., Byrne, P. K., Klimczak, C., and Peplowski, P. N. (2013). The distribution and origin of smooth plains on Mercury. *Journal of Geophysical Research (Planets)*, 118(5):891–907.

Denevi, B. W., Ernst, C. M., Prockter, L. M., and Robinson, M. S. (2018). *The Geologic History of Mercury*, pages 144–175.

Denevi, B. W., Robinson, M. S., Solomon, S. C., Murchie, S. L., Blewett, D. T., Domingue, D. L., McCoy, T. J., Ernst, C. M., Head, J. W., Watters, T. R., and Chabot, N. L. (2009). The Evolution of Mercury's Crust: A Global Perspective from MESSENGER. *Science*, 324(5927):613.

Deutsch, A. N., Chabot, N. L., Mazarico, E., Ernst, C. M., Head, J. W., Neumann, G. A., and Solomon, S. C. (2016). Comparison of areas in shadow from imaging and altimetry in the north polar region of Mercury and implications for polar ice deposits. *Icarus*, 280:158–171.

Deutsch, A. N., Neumann, G. A., and Head, J. W. (2017). New evidence for surface water ice in small-scale cold traps and in three large craters at the north polar region of Mercury from the Mercury Laser Altimeter. *Geophys. Res. Lett.*, 44(18):9233–9241.

Dickson, J. L., Fassett, C. I., and Head, J. W. (2009). Amazonian-aged fluvial valley systems in a climatic microenvironment on mars: Melting of ice deposits on the interior of lyot crater. *Geophysical Research Letters*, 36(8).

Dickson, J. L., Head, J. W., and Fassett, C. I. (2012). Patterns of accumulation and flow of ice in the mid-latitudes of Mars during the Amazonian. *Icarus*, 219(2):723–732.

Dickson, J. L., Head, J. W., and Marchant, D. R. (2010). Kilometer-thick ice accumulation and glaciation in the northern mid-latitudes of Mars: Evidence for crater-filling events in the Late Amazonian at the Phlegra Montes. *Earth and Planetary Science Letters*, 294(3-4):332–342.

Diniega, S., Hansen, C., McElwaine, J., Hugenholtz, C., Dundas, C., McEwen, A., and Bourke, M. (2013). A new dry hypothesis for the formation of martian linear gullies. *Icarus*, 225(1):526–537.

Domingue, D. L., D'Amore, M., Ferrari, S., Helbert, J., and Izenberg, N. R. (2019a). Analysis of the MESSENGER MASCS photometric targets part I: Photometric standardization for examining spectral variability across Mercury's surface. *Icarus*, 319:247–263.

Domingue, D. L., D'Amore, M., Ferrari, S., Helbert, J., and Izenberg, N. R. (2019b). Analysis of the MESSENGER MASCS photometric targets part II: Photometric variability between geomorphological units. *Icarus*, 319:140–246.

Domingue, D. L., Denevi, B. W., Murchie, S. L., and Hash, C. D. (2016). Application of multiple photometric models to disk-resolved measurements of Mercury's surface: Insights into Mercury's regolith characteristics. *Icarus*, 268:172–203.

Domingue, D. L., Hash, C. D., Denevi, B. W., and Murchie, S. L. (2017). Extending MESSENGER's Mercury dual imager's eight-color photometric standardization to cover all eleven filters. *Icarus*, 297:83–89.

Domingue, D. L., Murchie, S. L., Chabot, N. L., Denevi, B. W., and Vilas, F. (2011a). Mercury's spectrophotometric properties: Update from the Mercury Dual Imaging System observations during the third MESSENGER flyby. *Planet. Space Sci.*, 59(15):1853–1872.

Domingue, D. L., Murchie, S. L., Denevi, B. W., Chabot, N. L., Blewett, D. T., Laslo, N. R., Vaughan, R. M., Kang, H. K., and Shepard, M. K. (2011b). Photometric correction of Mercury's global color mosaic. *Planet. Space Sci.*, 59(15):1873–1887.

Domingue, D. L., Vilas, F., Holsclaw, G. M., Warell, J., Izenberg, N. R., Murchie, S. L., Denevi, B. W., Blewett, D. T., McClintock, W. E., Anderson, B. J., and Sarantos, M. (2010). Whole-disk spectrophotometric properties of Mercury: Synthesis of MESSENGER and ground-based observations. *Icarus*, 209(1):101–124.

Dundas, C. M. (2020). An aeolian grainflow model for martian recurring slope lineae. *Icarus*, 343:113681.

Dundas, C. M., Bramson, A. M., Ojha, L., Wray, J. J., Mellon, M. T., Byrne, S., McEwen, A. S., Putzig, N. E., Viola, D., Sutton, S., Clark, E., and Holt, J. W. (2018). Exposed subsurface ice sheets in the Martian mid-latitudes. *Science*, 359:199–201.

Dundas, C. M., Diniega, S., Hansen, C. J., Byrne, S., and McEwen, A. S. (2012). Seasonal activity and morphological changes in martian gullies. *Icarus*, 220(1):124–143.

Dundas, C. M., McEwen, A. S., Chojnacki, M., Milazzo, M. P., Byrne, S., McElwaine, J. N., and Urso, A. (2017). Granular flows at recurring slope lineae on Mars indicate a limited role for liquid water. *Nature Geoscience*, 10(12):903–907.

Edwards, C. S. and Piqueux, S. (2016). The water content of recurring slope lineae on Mars. *Geophysical Research Letters*, 43(17):8912–8919.

Edwards, C. S. and Piqueux, S. (2016). The water content of recurring slope lineae on Mars. *Geophysical Research Letters*, 43(17):8912–8919.

Efron, B. (1979). Bootstrap Methods: Another Look at the Jackknife. *The Annals of Statistics*, 7(1):1 – 26.

Ehlmann, B. L., Mustard, J. F., Fassett, C. I., Schon, S. C., Head, James W., I., Des Marais, D. J., Grant, J. A., and Murchie, S. L. (2008a). Clay minerals in delta deposits and organic preservation potential on Mars. *Nature Geoscience*, 1(6):355–358.

Ehlmann, B. L., Mustard, J. F., and Murchie, S. L. (2010). Geologic setting of serpentine deposits on Mars. *Geophysical Research Letters*, 37:L06201.

Ehlmann, B. L., Mustard, J. F., Murchie, S. L., Poulet, F., Bishop, J. L., Brown, A. J., Calvin, W. M., Clark, R. N., Des Marais, D. J., Milliken, R. E., Roach, L. H., Roush, T. L., Swayze, G. A., and Wray, J. J. (2008b). Orbital Identification of Carbonate-Bearing Rocks on Mars. *Science*, 322(5909):1828.

Fairbairn, M. B. (2005). Planetary Photometry: The Lommel-Seeliger Law. *JRASC*, 99(3):92.

Fassett, C. I. and Head, J. W. (2008a). The timing of martian valley network activity: Constraints from buffered crater counting. *Icarus*, 195(1):61–89.

Fassett, C. I. and Head, J. W. (2008b). The timing of martian valley network activity: Constraints from buffered crater counting. *Icarus*, 195(1):61–89.

Feldman, W. C., Prettyman, T. H., Maurice, S., Plaut, J. J., Bish, D. L., Vaniman, D. T., Mellon, M. T., Metzger, A. E., Squyres, S. W., Karunatillake, S., Boynton, W. V., Elphic, R. C., Funsten, H. O., Lawrence, D. J., and Tokar, R. L. (2004). Global distribution of near-surface hydrogen on Mars. *Journal of Geophysical Research (Planets)*, 109:E09006.

Fergason, R. L., Christensen, P. R., and Kieffer, H. H. (2006). High-resolution thermal inertia derived from the Thermal Emission Imaging System (THEMIS): Thermal model and applications. *Journal of Geophysical Research (Planets)*, 111(E12):E12004.

Fernando, J., Schmidt, F., Ceamanos, X., Pinet, P., Douté, S., and Daydou, Y. (2013). Surface reflectance of Mars observed by CRISM/MRO: 2. Estimation of surface photometric properties in Gusev Crater and Meridiani Planum. *Journal of Geophysical Research (Planets)*, 118(3):534–559.

Fischer, E., Martínez, G. M., Rennó, N. O., Tamppari, L. K., and Zent, A. P. (2019). Relative humidity on mars: New results from the phoenix tecp sensor. *Journal of Geophysical Research: Planets*, 124(11):2780–2792.

Franz, H. B., Trainer, M. G., Malespin, C. A., Mahaffy, P. R., Atreya, S. K., Becker, R. H., Benna, M., Conrad, P. G., Eigenbrode, J. L., Freissinet, C., Manning, H. L. K., Prats, B. D., Raaen, E., and Wong, M. H. (2017). Initial SAM calibration gas experiments on Mars: Quadrupole mass spectrometer results and implications. *Planet. Space Sci.*, 138:44–54.

Goldspiel, J. M. and Squyres, S. W. (2011). Groundwater discharge and gully formation on martian slopes. *Icarus*, 211(1):238–258.

Golombek, M. P., Grant, J. A., Crumpler, L. S., Greeley, R., Arvidson, R. E., Bell, J. F., Weitz, C. M., Sullivan, R., Christensen, P. R., Soderblom, L. A., and Squyres, S. W. (2006). Erosion rates at the Mars Exploration Rover landing sites and long-term climate change on Mars. *Journal of Geophysical Research (Planets)*, 111(E12):E12S10.

Goudge, T. A., Head, J. W., Kerber, L., Blewett, D. T., Denevi, B. W., Domingue, D. L., Gillis-Davis, J. J., Gwinner, K., Helbert, J., Holsclaw, G. M., Izenberg, N. R., Klima, R. L., McClintock, W. E., Murchie, S. L., Neumann, G. A., Smith, D. E., Strom, R. G., Xiao, Z., Zuber, M. T., and Solomon, S. C. (2014). Global inventory and characterization of pyroclastic deposits on Mercury: New insights into pyroclastic activity from MESSENGER orbital data. *Journal of Geophysical Research (Planets)*, 119(3):635–658.

Gough, R., Chevrier, V., and Tolbert, M. (2016). Formation of liquid water at low temperatures via the deliquescence of calcium chloride: Implications for Antarctica and Mars. *Planet. Space Sci.*, 131:79–87.

Gough, R., Primm, K., Rivera-Valentín, E., Martínez, G., and Tolbert, M. (2019). Solid-solid hydration and dehydration of mars-relevant chlorine salts: Implications for gale crater and rsl locations. *Icarus*, 321:1–13.

Gough, R. V., Nuding, D. L., Archer, P. D., Fernanders, M. S., Guzewich, S. D., Tolbert, M. A., and Toigo, A. D. (2020). Changes in Soil Cohesion Due to Water Vapor Exchange: A Proposed Dry-Flow Trigger Mechanism for Recurring Slope Lineae on Mars. *Geophys. Res. Lett.*, 47(11):e87618.

Grant, J. A., Irwin, Rossman P., I., Grotzinger, J. P., Milliken, R. E., Tornabene, L. L., McEwen, A. S., Weitz, C. M., Squyres, S. W., Glotch, T. D., and Thomson, B. J. (2008). HiRISE imaging of impact megabreccia and sub-meter aqueous strata in Holden Crater, Mars. *Geology*, 36(3):195–198.

Grimm, R. E., Harrison, K. P., and Stillman, D. E. (2014). Water budgets of martian recurring slope lineae. *Icarus*, 233:316–327.

Gross, J. and Ligges, U. (2015). *nortest: Tests for Normality*. R package version 1.0-4.

Gulick, V. C. (1998). Magmatic intrusions and a hydrothermal origin for fluvial valleys on Mars. *J. Geophys. Res.*, 103(E8):19365–19388.

Gulick, V. C., Glines, N., Hart, S., and Freeman, P. (2019). Geomorphological analysis of gullies on the central peak of Lyot Crater, Mars. *Geological Society of London Special Publications*, 467(1):233–265.

Gunderson, K., Lüthi, B., Russell, P., and Thomas, N. (2007). Visible/NIR photometric signatures of liquid water in Martian regolith simulant. *Planet. Space Sci.*, 55(10):1272–1282.

Gunderson, K. and Thomas, N. (2010). BELA receiver performance modeling over the BepiColombo mission lifetime. *Planet. Space Sci.*, 58(1-2):309–318.

Haberle, R. M., McKay, C. P., Schaeffer, J., Cabrol, N. A., Grin, E. A., Zent, A. P., and Quinn, R. (2001). On the possibility of liquid water on present-day mars. *Journal of Geophysical Research: Planets*, 106(E10):23317–23326.

Hamilton, V. E. and Christensen, P. R. (2005). Evidence for extensive, olivine-rich bedrock on Mars. *Geology*, 33(6):433.

Hansen, C. J., Byrne, S., Portyankina, G., Bourke, M., Dundas, C., McEwen, A., Mellon, M., Pommerol, A., and Thomas, N. (2013). Observations of the northern seasonal polar cap on Mars: I. Spring sublimation activity and processes. *Icarus*, 225(2):881–897.

Hapke, B. (1993). *Theory of reflectance and emittance spectroscopy*.

Hapke, B. (2002a). Bidirectional Reflectance Spectroscopy. 5. The Coherent Backscatter Opposition Effect and Anisotropic Scattering. *Icarus*, 157(2):523–534.

Hapke, B. (2002b). Bidirectional Reflectance Spectroscopy. 5. The Coherent Backscatter Opposition Effect and Anisotropic Scattering. *Icarus*, 157(2):523–534.

Hapke, B. (2012). Bidirectional reflectance spectroscopy 7. The single particle phase function hockey stick relation. *Icarus*, 221(2):1079–1083.

Harmon, J. K. and Slade, M. A. (1992). Radar Mapping of Mercury: Full-Disk Images and Polar Anomalies. *Science*, 258(5082):640–643.

Harmon, J. K., Slade, M. A., Butler, B. J., Head, J. W., Rice, M. S., and Campbell, D. B. (2007). Mercury: Radar images of the equatorial and midlatitude zones. *Icarus*, 187(2):374–405.

Harmon, J. K., Slade, M. A., and Rice, M. S. (2011). Radar imagery of Mercury's putative polar ice: 1999-2005 Arecibo results. *Icarus*, 211(1):37–50.

Hartmann, W. K. and Neukum, G. (2001). Cratering Chronology and the Evolution of Mars. *Space Sci. Rev.*, 96:165–194.

Hawkins, S. E., Boldt, J. D., Darlington, E. H., Espiritu, R., Gold, R. E., Gotwols, B., Grey, M. P., Hash, C. D., Hayes, J. R., Jaskulek, S. E., Kardian, C. J., Keller, M. R., Malaret, E. R., Murchie, S. L., Murphy, P. K., Peacock, K., Prockter, L. M., Reiter, R. A., Robinson, M. S., Schaefer, E. D., Shelton, R. G., Sterner, R. E., Taylor, H. W., Watters, T. R., and Williams, B. D. (2007). The Mercury Dual Imaging System on the MESSENGER Spacecraft. *Space Sci. Rev.*, 131(1-4):247–338.

Head, J. W. and Marchant, D. R. (2003). Cold-based mountain glaciers on Mars: Western Arsia Mons. *Geology*, 31(7):641.

Head, J. W., Murchie, S. L., Prockter, L. M., Robinson, M. S., Solomon, S. C., Strom, R. G., Chapman, C. R., Watters, T. R., McClintock, W. E., Blewett, D. T., and Gillis-Davis, J. J. (2008). Volcanism on Mercury: Evidence from the First MESSENGER Flyby. *Science*, 321(5885):69.

Head, J. W., Neukum, G., Jaumann, R., Hiesinger, H., Hauber, E., Carr, M., Masson, P., Foing, B., Hoffmann, H., Kreslavsky, M., Werner, S., Milkovich, S., van Gasselt, S., and HRSC Co-Investigator Team (2005). Tropical to mid-latitude snow and ice accumulation, flow and glaciation on Mars. *Nature*, 434(7031):346–351.

Helbert, J., Maturilli, A., and D'Amore, M. (2013). Visible and near-infrared reflectance spectra of thermally processed synthetic sulfides as a potential analog for the hollow forming materials on Mercury. *Earth and Planetary Science Letters*, 369:233–238.

Heyner, D., Auster, H. U., Fornaçon, K. H., Carr, C., Richter, I., Mieth, J. Z. D., Kolhey, P., Exner, W., Motschmann, U., Baumjohann, W., Matsuoka, A., Magnes, W., Berghofer, G., Fischer, D., Plaschke, F., Nakamura, R., Narita, Y., Delva, M., Volwerk, M., Balogh, A., Dougherty, M., Horbury, T., Langlais, B., Mandea, M., Masters, A., Oliveira, J. S., Sánchez-Cano, B., Slavin, J. A., Vennerstrøm, S., Vogt, J., Wicht, J., and Glassmeier, K. H. (2021). The BepiColombo Planetary Magnetometer MPO-MAG: What Can We Learn from the Hermean Magnetic Field? *Space Sci. Rev.*, 217(4):52.

Hiesinger, H., Helbert, J., Alemanno, G., Bauch, K. E., D'Amore, M., Maturilli, A., Morlok, A., Reitze, M. P., Stangarone, C., Stojic, A. N., Varatharajan, I., Weber, I., and Mertis Co-I Team (2020). Studying the Composition and Mineralogy of the Hermean Surface with the Mercury Radiometer and Thermal Infrared Spectrometer (MERTIS) for the BepiColombo Mission: An Update. *Space Sci. Rev.*, 216(6):110.

Hillel, D. (2004). *Introduction to environmental soil physics*. Elsevier Sicence & Technology.

Hoekzema, N., Garcia-Comas, M., Stenzel, O., Petrova, E., Thomas, N., Markiewicz, W., Gwinner, K., Keller, H., and Delamere, W. (2011). Retrieving optical depth from shadows in orbiter images of mars. *Icarus*, 214(2):447 – 461.

Holt, J. W., Safaeinili, A., Plaut, J. J., Head, J. W., Phillips, R. J., Seu, R., Kempf, S. D., Choudhary, P., Young, D. A., Putzig, N. E., Biccari, D., and Gim, Y. (2008). Radar Sounding Evidence for Buried Glaciers in the Southern Mid-Latitudes of Mars. *Science*, 322(5905):1235.

Huber, C., Ojha, L., Lark, L., and Head, J. W. (2020). Physical models and predictions for recurring slope lineae formed by wet and dry processes. *Icarus*, 335:113385.

Huovelin, J., Vainio, R., Kilpua, E., Lehtolainen, A., Korpela, S., Esko, E., Muinonen, K., Bunce, E., Martindale, A., Grande, M., Andersson, H., Nenonen, S., Lehti, J., Schmidt, W., Genzer, M., Vihavainen, T., Saari, J., Peltonen, J., Valtonen, E., Talvioja, M., Portin, P., Narendranath, S., Jarvinen, R., Okada, T., Milillo, A., Laurenza, M., Heino, E., and Oleynik, P. (2020). Solar Intensity X-Ray and Particle Spectrometer SIXS: Instrument Design and First Results. *Space Sci. Rev.*, 216(5):94.

Iafolla, V., Fiorenza, E., Lefevre, C., Morbidini, A., Nozzoli, S., Peron, R., Persichini, M., Reale, A., and Santoli, F. (2010). Italian Spring Accelerometer (ISA): A fundamental support to BepiColombo Radio Science Experiments. *Planet. Space Sci.*, 58(1-2):300–308.

Iess, L., Asmar, S. W., Cappuccio, P., Cascioli, G., De Marchi, F., di Stefano, I., Genova, A., Ashby, N., Barriot, J. P., Bender, P., Benedetto, C., Border, J. S., Budnik, F., Ciarcia, S., Damour, T., Dehant, V., Di Achille, G., Di Ruscio, A., Fienga, A., Formaro, R., Klioner, S., Konopliv, A., Lemaître, A., Longo, F., Mercolino, M., Mitri, G., Notaro, V., Olivieri, A., Paik, M., Palli, A., Schettino, G., Serra, D., Simone, L., Tommei, G., Tortora, P., Van Hoolst, T., Vokrouhlický, D., Watkins, M., Wu, X., and Zannoni, M. (2021). Gravity, Geodesy and Fundamental Physics with BepiColombo's MORE Investigation. *Space Sci. Rev.*, 217(1):21.

Ingersoll, A. P. (1970). Mars: Occurrence of liquid water. *Science*, 168(3934):972–973.

Ivanov, B. A. (2001). Mars/Moon Cratering Rate Ratio Estimates. *Space Sci. Rev.*, 96:87–104.

Izenberg, N. R., Klima, R. L., Murchie, S. L., Blewett, D. T., Holsclaw, G. M., McClintock, W. E., Malaret, E., Mauceri, C., Vilas, F., Sprague, A. L., Helbert, J., Domingue, D. L., Head, J. W., Goudge, T. A., Solomon, S. C., Hibbitts, C. A., and Dyar, M. D. (2014). The low-iron, reduced surface of Mercury as seen in spectral reflectance by MESSENGER. *Icarus*, 228:364–374.

Jaumann, R., Neukum, G., Behnke, T., Duxbury, T. C., Eichentopf, K., Flohrer, J., Gasselt, S. v., Giese, B., Gwinner, K., Hauber, E., Hoffmann, H., Hoffmeister, A., Köhler, U., Matz, K. D., McCord, T. B., Mertens, V., Oberst, J., Pischel, R., Reiss, D., Ress, E., Roatsch, T., Saiger, P., Scholten, F., Schwarz, G., Stephan, K., Wählisch, M., and HRSC Co-Investigator Team (2007). The high-resolution stereo camera (HRSC) experiment on Mars Express: Instrument aspects and experiment conduct from interplanetary cruise through the nominal mission. *Planet. Space Sci.*, 55(7-8):928–952.

Jozwiak, L. M., Head, J. W., and Wilson, L. (2018). Explosive volcanism on Mercury: Analysis of vent and deposit morphology and modes of eruption. *Icarus*, 302:191–212.

Kaasalainen, M., Torppa, J., and Muinonen, K. (2001). Optimization Methods for Asteroid Lightcurve Inversion. II. The Complete Inverse Problem. *Icarus*, 153(1):37–51.

Kasaba, Y., Bougeret, J. L., Blomberg, L. G., Kojima, H., Yagitani, S., Moncuquet, M., Trotignon, J. G., Chanteur, G., Kumamoto, A., Kasahara, Y., Lichtenberger, J., Omura, Y., Ishisaka, K., and Matsumoto, H. (2010). The Plasma Wave Investigation (PWI) onboard the BepiColombo/MMO: First measurement of electric fields, electromagnetic waves, and radio waves around Mercury. *Planet. Space Sci.*, 58(1-2):238–278.

King, S. D. (2008). Pattern of lobate scarps on Mercury's surface reproduced by a model of mantle convection. *Nature Geoscience*, 1(4):229–232.

Kirk, R. L., Howington-Kraus, E., Rosiek, M. R., Anderson, J. A., Archinal, B. A., Becker, K. J., Cook, D. A., Galuszka, D. M., Geissler, P. E., Hare, T. M., Holmberg, I. M., Keszthelyi, L. P., Redding, B. L., Delamere, W. A., Gallagher, D., Chapel, J. D., Eliason, E. M., King, R., and McEwen, A. S. (2008). Ultrahigh resolution topographic mapping of mars with mro hirise stereo images: Meter-scale slopes of candidate phoenix landing sites. *Journal of Geophysical Research: Planets*, 113(E3).

Klose, M., Jemmett-Smith, B. C., Kahanpää, H., Kahre, M., Knippertz, P., Lemmon, M. T., Lewis, S. R., Lorenz, R. D., Neakrase, L. D. V., Newman, C., Patel, M. R., Reiss, D., Spiga, A., and Whelley, P. L. (2016). Dust Devil Sediment Transport: From Lab to Field to Global Impact. *Space Sci. Rev.*, 203(1-4):377–426.

Kreslavsky, M. A. and Head, J. W. (2002). Mars: Nature and evolution of young latitude-dependent water-ice-rich mantle. *Geophys. Res. Lett.*, 29(15):1719.

Lauro, S. E., Pettinelli, E., Caprarelli, G., Guallini, L., Rossi, A. P., Mattei, E., Cosciotti, B., Cicchetti, A., Soldovieri, F., Cartacci, M., Di Paolo, F., Noschese, R., and Orosei, R. (2021). Multiple subglacial water bodies below the south pole of Mars unveiled by new MARSIS data. *Nature Astronomy*, 5:63–70.

Lawrence, D. J., Feldman, W. C., Goldsten, J. O., Maurice, S., Peplowski, P. N., Anderson, B. J., Bazell, D., McNutt, R. L., Nittler, L. R., Prettyman, T. H., Rodgers, D. J., Solomon, S. C., and Weider, S. Z. (2013). Evidence for Water Ice Near Mercury's North Pole from MESSENGER Neutron Spectrometer Measurements. *Science*, 339(6117):292.

Leask, E. K., Ehlmann, B. L., Dundar, M. M., Murchie, S. L., and Seelos, F. P. (2018). Challenges in the Search for Perchlorate and Other Hydrated Minerals With 2.1-μm Absorptions on Mars. *Geophys. Res. Lett.*, 45(22):12,180–12,189.

Levy, J. (2012). Hydrological characteristics of recurrent slope lineae on mars: Evidence for liquid flow through regolith and comparisons with antarctic terrestrial analogs. *Icarus*, 219(1):1 – 4.

Levy, J., Nolin, A., Fountain, A., and Head, J. (2014). Hyperspectral measurements of wet, dry and saline soils from the McMurdo Dry Valleys: soil moisture properties from remote sensing. *Antarctic Science*, 26(5):565–572.

Lucchetti, A., Pajola, M., Galluzzi, V., Giacomini, L., Carli, C., Cremonese, G., Marzo, G. A., Ferrari, S., Massironi, M., and Palumbo, P. (2018). Mercury Hollows as Remnants of Original Bedrock Materials and Devolatilization Processes: A Spectral Clustering and Geomorphological Analysis. *Journal of Geophysical Research (Planets)*, 123(9):2365–2379.

Lucchetti, A., Pajola, M., Poggiali, G., Semenzato, A., Munaretto, G., Cremonese, G., Brucato, J. R., and Massironi, M. (2021). Volatiles on mercury: The case of hollows and the pyroclastic vent of Tyagaraja crater. *Icarus*, 370:114694.

Madden, M. E., Bodnar, R. J., and Rimstidt, J. D. (2004). Jarosite as an indicator of water-limited chemical weathering on Mars. *Nature*, 431(7010):821–823.

Malin, M. C., Bell, J. F., Cantor, B. A., Caplinger, M. A., Calvin, W. M., Clancy, R. T., Edgett, K. S., Edwards, L., Haberle, R. M., James, P. B., Lee, S. W., Ravine, M. A., Thomas, P. C., and Wolff, M. J. (2007). Context Camera Investigation on board the Mars Reconnaissance Orbiter. *Journal of Geophysical Research (Planets)*, 112(E5):E05S04.

Malin, M. C., Danielson, G. E., Ingersoll, A. P., Masursky, H., Veverka, J., Ravine, M. A., and Soulanille, T. A. (1992). Mars Observer Camera. *J. Geophys. Res.*, 97(E5):7699–7718.

Malin, M. C. and Edgett, K. S. (2000). Evidence for recent groundwater seepage and surface runoff on mars. *Science*, 288(5475):2330–2335.

Mangold, N., Quantin, C., Ansan, V., Delacourt, C., and Allemand, P. (2004). Evidence for precipitation on mars from dendritic valleys in the valles marineris area. *Science*, 305(5680):78–81.

Marchi, S., Mottola, S., Cremonese, G., Massironi, M., and Martellato, E. (2009). A New Chronology for the Moon and Mercury. *AJ*, 137(6):4936–4948.

Marion, G., Catling, D., Zahnle, K., and Claire, M. (2010). Modeling aqueous perchlorate chemistries with applications to mars. *Icarus*, 207(2):675 – 685.

Massé, M., Conway, S. J., Gargani, J., Patel, M. R., Pasquon, K., McEwen, A., Carpy, S., Chevrier, V., Balme, M. R., Ojha, L., Vincendon, M., Poulet, F., Costard, F., and Jouannic, G. (2016). Transport processes induced by metastable boiling water under Martian surface conditions. *Nature Geoscience*, 9(6):425–428.

Massey, F. J. (1951). The kolmogorov-smirnov test for goodness of fit. *Journal of the American Statistical Association*, 46(253):68–78.

Mastropietro, M., Pajola, M., Cremonese, G., Munaretto, G., and Lucchetti, A. (2020). Boulder Analysis on the Oxia Planum ExoMars 2022 Rover Landing Site: Scientific and Engineering Perspectives. *Solar System Research*, 54(6):504–519.

McEwen, A. S. (1991). Photometric functions for photoclinometry and other applications. *Icarus*, 92(2):298–311.

McEwen, A. S., Dundas, C. M., Mattson, S. S., Toigo, A. D., Ojha, L., Wray, J. J., Chojnacki, M., Byrne, S., Murchie, S. L., and Thomas, N. (2014). Recurring slope lineae in equatorial regions of Mars. *Nature Geoscience*, 7(1):53–58.

McEwen, A. S., Eliason, E. M., Bergstrom, J. W., Bridges, N. T., Hansen, C. J., Delamere, W. A., Grant, J. A., Gulick, V. C., Herkenhoff, K. E., Keszthelyi, L., Kirk, R. o. L., Mellon, M. T., Squyres, S. W., Thomas, N., and Weitz, C. M. (2007). Mars Reconnaissance Orbiter's High Resolution Imaging Science Experiment (HiRISE). *Journal of Geophysical Research (Planets)*, 112(E5):E05S02.

McEwen, A. S., Ojha, L., Dundas, C. M., Mattson, S. S., Byrne, S., Wray, J. J., Cull, S. C., Murchie, S. L., Thomas, N., and Gulick, V. C. (2011). Seasonal flows on warm Martian slopes. *Science*, 333(6043):740–743.

McEwen, A. S., Schaefer, E. I., Dundas, C. M., Sutton, S. S., Tamppari, L. K., and Chojnacki, M. (2021). Mars: Abundant recurring slope lineae (rsl) following the planet-encircling dust event (pede) of 2018. *Journal of Geophysical Research: Planets*, 126(4):e2020JE006575. e2020JE006575 2020JE006575.

McEwen, A. S., Schafer, E., Sutton, S., and Chojnacki, M. (2019). Abundant Recurring Slope Lineae (RSL) Following the 2018 Planet-Encircling Dust Event (PEDE). In *Lunar and Planetary Science Conference*, Lunar and Planetary Science Conference, page 1376.

McGuire, A. F. and Hapke, B. W. (1995). An experimental study of light scattering by large, irregular particles. *Icarus*, 113(1):134–155.

Melosh, H. J. and Dzurisin, D. (1978). Mercurian Global Tectonics: A Consequence of Tidal Despinning? *Icarus*, 35(2):227–236.

Milliken, R. E., Grotzinger, J. P., and Thomson, B. J. (2010). Paleoclimate of Mars as captured by the stratigraphic record in Gale Crater. *Geophys. Res. Lett.*, 37(4):L04201.

Milliken, R. E., Mustard, J. F., and Goldsby, D. L. (2003). Viscous flow features on the surface of mars: Observations from high-resolution mars orbiter camera (moc) images. *Journal of Geophysical Research: Planets*, 108(E6).

Millot, C., Quantin-Nataf, C., Leyrat, C., and Enjolras, M. (2021). Local topography effects on the surface temperatures on mars – application to the case of recurring slope lineae (rsl). *Icarus*, 355:114136.

Minnaert, M. (1941). The reciprocity principle in lunar photometry. *ApJ*, 93:403–410.

Mitrofanov, I. G., Kozyrev, A. S., Konovalov, A., Litvak, M. L., Malakhov, A. A., Mokrousov, M. I., Sanin, A. B., Tret'ykov, V. I., Vostrukhin, A. V., Bobrovnitskij, Y. I., Tomilina, T. M., Gurvits, L., and Owens, A. (2010). The Mercury Gamma and Neutron Spectrometer (MGNS) on board the Planetary Orbiter of the BepiColombo mission. *Planet. Space Sci.*, 58(1-2):116–124.

Moratto, Z. M., Broxton, M. J., Beyer, R. A., Lundy, M., and Husmann, K. (2010). Ames Stereo Pipeline, NASA's Open Source Automated Stereogrammetry Software. In *Lunar and Planetary Science Conference*, volume 41 of *Lunar and Planetary Science Conference*, page 2364.

Morris, E. C. (1982). Aureole deposits of the Martian volcano Olympus Mons. *J. Geophys. Res.*, 87:1164–1178.

Muhleman, D. O., Butler, B. J., Grossman, A. W., and Slade, M. A. (1991). Radar Images of Mars. *Science*, 253(5027):1508–1513.

Munaretto, G., Pajola, M., Cremonese, G., Re, C., Lucchetti, A., Simioni, E., McEwen, A. S., Pommerol, A., Becerra, P., Conway, S. J., Thomas, N., and Massironi, M. (2020). Implications for the origin and evolution of Martian Recurring Slope Lineae at Hale crater from CaSSIS observations. *Planet. Space Sci.*, 187:104947.

Munaretto, G., Pajola, M., Lucchetti, A., G., C., Simioni, E., Re, C., Bertoli, S., Tornabene, L., McEwen, A. S., Becerra, P., G., R. V., Valantinas, A., Pommerol, A., Thomas, N., and Portyankina, G. (2021a). Multiband photometry of martian recurring slope lineae (rsl) and dust-removed features at horowitz crater, mars from tgo/cassis color observations. *in review for pss*.

Munaretto, G., Pajola, M., Lucchetti, A., Re, C., Cremonese, G., Simioni, E., Cambianica, P., and Thomas, N. (2021b). Topographic correction of HiRISE and CaSSIS images: Validation and application to color observations of Martian albedo features. *Planet. Space Sci.*, 200:105198.

Murakami, G., Hayakawa, H., Ogawa, H., Matsuda, S., Seki, T., Kasaba, Y., Saito, Y., Yoshikawa, I., Kobayashi, M., Baumjohann, W., Matsuoka, A., Kojima, H., Yagitani, S., Moncuquet, M., Wahlund, J.-E., Delcourt, D., Hirahara, M., Barabash, S., Korablev, O., and Fujimoto, M. (2020). Mio—First Comprehensive Exploration of Mercury's Space Environment: Mission Overview. *Space Sci. Rev.*, 216(7):113.

Murchie, S., Arvidson, R., Bedini, P., Beisser, K., Bibring, J.-P., Bishop, J., Boldt, J., Cavender, P., Choo, T., Clancy, R. T., Darlington, E. H., Des Marais, D., Espiritu, R., Fort, D., Green, R., Guinness, E., Hayes, J., Hash, C., Heffernan, K., Hemmler, J., Heyler, G., Humm, D., Hutcheson, J., Izenberg, N., Lee, R., Lees, J., Lohr, D., Malaret, E., Martin, T., McGovern, J. A., McGuire, P., Morris, R., Mustard, J., Pelkey, S., Rhodes, E., Robinson, M., Roush, T., Schaefer, E., Seagrave, G., Seelos, F., Silverglate, P., Slavney, S., Smith, M., Shyong, W.-J., Strohbehn, K., Taylor, H., Thompson, P., Tossman, B., Wirzburger, M., and Wolff, M. (2007). Compact Reconnaissance Imaging Spectrometer for Mars (CRISM) on Mars Reconnaissance Orbiter (MRO). *Journal of Geophysical Research: Planets*, 112(E5).

Murchie, S. L., Klima, R. L., Denevi, B. W., Ernst, C. M., Keller, M. R., Domingue, D. L., Blewett, D. T., Chabot, N. L., Hash, C. D., Malaret, E., Izenberg, N. R., Vilas, F., Nittler, L. R., Gillis-Davis, J. J., Head, J. W., and Solomon, S. C. (2015). Orbital multispectral mapping of Mercury with the MESSENGER Mercury Dual Imaging System: Evidence for the origins of plains units and low-reflectance material. *Icarus*, 254:287–305.

Murchie, S. L., Mustard, J. F., Ehlmann, B. L., Milliken, R. E., Bishop, J. L., McKeown, N. K., Noe Dobrea, E. Z., Seelos, F. P., Buczkowski, D. L., Wiseman, S. M., Arvidson, R. E., Wray, J. J., Swayze, G., Clark, R. N., Des Marais, D. J., McEwen, A. S., and Bibring, J.-P. (2009). A synthesis of Martian aqueous mineralogy after 1 Mars year of observations from the Mars Reconnaissance Orbiter. *Journal of Geophysical Research (Planets)*, 114(E2):E00D06.

Murray, B. (1975). The Mariner 10 pictures of Mercury: An overview. *J. Geophys. Res.*, 80(B17):2342–2344.

Mushkin, A., Gillespie, A. R., Montgomery, D. R., Schreiber, B. C., and Arvidson, R. E. (2010). Spectral constraints on the composition of low-albedo slope streaks in the Olympus Mons Aureole. *Geophys. Res. Lett.*, 37(22):L22201.

Mustard, J. F., Cooper, C. D., and Rifkin, M. K. (2001). Evidence for recent climate change on Mars from the identification of youthful near-surface ground ice. *Nature*, 412(6845):411–414.

Mustard, J. F., Ehlmann, B. L., Murchie, S. L., Poulet, F., Mangold, N., Head, J. W., Bibring, J.-P., and Roach, L. H. (2009). Composition, morphology, and stratigraphy of noachian crust around the isidis basin. *Journal of Geophysical Research: Planets*, 114(E2).

Mustard, J. F., Poulet, F., Head, J. W., Mangold, N., Bibring, J.-P., Pelkey, S. M., Fassett, C. I., Langevin, Y., and Neukum, G. (2007). Mineralogy of the nili fossae region with omega/mars express data: 1. ancient impact melt in the isidis basin and implications for the transition from the noachian to hesperian. *Journal of Geophysical Research: Planets*, 112(E8).

Möhlmann, D. (2011). Three types of liquid water in icy surfaces of celestial bodies. *Planetary and Space Science*, 59(10):1082–1086. Comparative Planetology: Venus-Earth-Mars.

Möhlmann, D. T. (2010). Temporary liquid water in upper snow/ice sub-surfaces on mars? *Icarus*, 207(1):140–148.

Ness, N. F., Behannon, K. W., Lepping, R. P., Whang, Y. C., and Schatten, K. H. (1974). Magnetic Field Observations near Mercury: Preliminary Results from Mariner 10. *Science*, 185(4146):151–160.

Neumann, G. A., Zuber, M. T., Wieczorek, M. A., McGovern, P. J., Lemoine, F. G., and Smith, D. E. (2004). Crustal structure of Mars from gravity and topography. *Journal of Geophysical Research (Planets)*, 109:E08002.

Niles, P. B., Catling, D. C., Berger, G., Chassefière, E., Ehlmann, B. L., Michalski, J. R., Morris, R., Ruff, S. W., and Sutter, B. (2013). Geochemistry of Carbonates on Mars: Implications for Climate History and Nature of Aqueous Environments. *Space Sci. Rev.*, 174(1-4):301–328.

Nogami, K., Fujii, M., Ohashi, H., Miyachi, T., Sasaki, S., Hasegawa, S., Yano, H., Shibata, H., Iwai, T., Minami, S., Takechi, S., Grün, E., and Srama, R. (2010). Development of the Mercury dust monitor (MDM) onboard the BepiColombo mission. *Planet. Space Sci.*, 58(1-2):108–115.

Nuding, D., Rivera-Valentin, E., Davis, R., Gough, R., Chevrier, V., and Tolbert, M. (2014). Deliquescence and efflorescence of calcium perchlorate: An investigation of stable aqueous solutions relevant to mars. *Icarus*, 243:420 – 428.

Ojha, L., McEwen, A., Dundas, C., Byrne, S., Mattson, S., Wray, J., Masse, M., and Schaefer, E. (2014). Hirise observations of recurring slope lineae (rsl) during southern summer on mars. *Icarus*, 231:365 – 376.

Ojha, L., Wilhelm, M. B., Murchie, S. L., McEwen, A. S., Wray, James J.and Hanley, J., Massé, M., and Chojnacki, M. (2015). Spectral evidence for hydrated salts in recurring slope lineae on Mars. *Nature Geoscience*, 8:829–832.

Orosei, R., Lauro, S. E., Pettinelli, E., Cicchetti, A., Coradini, M., Cosciotti, B., Di Paolo, F., Flamini, E., Mattei, E., Pajola, M., Soldovieri, F., Cartacci, M., Cassenti, F., Frigeri, A., Giuppi, S., Martufi, R., Masdea, A., Mitri, G., Nenna, C., Noschese, R., Restano, M., and Seu, R. (2018). Radar evidence of subglacial liquid water on Mars. *Science*, 361:490–493.

Orsini, S., Livi, S. A., Lichtenegger, H., Barabash, S., Milillo, A., De Angelis, E., Phillips, M., Laky, G., Wieser, M., Olivieri, A., Plainaki, C., Ho, G., Killen, R. M., Slavin, J. A., Wurz, P., Berthelier, J. J., Dandouras, I., Kallio, E., McKenna-Lawlor, S., Szalai, S., Torkar, K., Vaisberg, O., Allegrini, F., Daglis, I. A., Dong, C., Escoubet, C. P., Fatemi, S., Fränz, M., Ivanovski, S., Krupp, N., Lammer, H., Leblanc, F., Mangano, V., Mura, A., Nilsson, H., Raines, J. M., Rispoli, R., Sarantos, M., Smith, H. T., Szego, K., Aronica, A., Camozzi, F., Di Lellis, A. M., Fremuth, G., Giner, F., Gurnee, R., Hayes, J., Jeszenszky, H., Tominetti, F., Trantham, B., Balaz, J., Baumjohann, W., Brienza, D., Bührke, U., Bush, M. D., Cantatore, M., Cibella, S., Colasanti, L., Cremonese, G., Cremonesi, L., D'Alessandro, M., Delcourt, D., Delva, M., Desai, M., Fama, M., Ferris, M., Fischer, H., Gaggero, A., Gamborino, D., Garnier, P., Gibson, W. C., Goldstein, R., Grande, M., Grishin, V., Haggerty, D., Holmström, M., Horvath, I., Hsieh, K. C., Jacques, A., Johnson, R. E., Kazakov, A., Kecskemety, K., Krüger, H., Kürbisch, C., Lazzarotto, F., Leblanc, F., Leichtfried, M., Leoni, R., Loose, A., Maschietti, D., Massetti, S., Mattioli, F., Miller, G., Moissenko, D., Morbidini, A., Noschese, R., Nuccilli, F., Nunez, C., Paschalidis, N., Persyn, S., Piazza, D., Oja, M., Ryno, J., Schmidt, W., Scheer, J. A., Shestakov, A., Shuvalov, S., Seki, K., Selci, S., Smith, K., Sordini, R., Svensson, J., Szalai, L., Toublanc, D., Urdiales, C., Varsani, A., Vertolli, N., Wallner, R., Wahlstroem, P., Wilson, P., and Zampieri, S. (2021). SERENA: Particle Instrument Suite for Determining the Sun-Mercury Interaction from BepiColombo. *Space Sci. Rev.*, 217(1):11.

Osterloo, M. M., Anderson, F. S., Hamilton, V. E., and Hynek, B. M. (2010). Geologic context of proposed chloride-bearing materials on Mars. *Journal of Geophysical Research (Planets)*, 115(E10):E10012.

Osterloo, M. M., Hamilton, V. E., Bandfield, J. L., Glotch, T. D., Baldridge, A. M., Christensen, P. R., Tornabene, L. L., and Anderson, F. S. (2008). Chloride-Bearing Materials in the Southern Highlands of Mars. *Science*, 319(5870):1651.

Pajola, M., Lucchetti, A., Semenzato, A., Poggiali, G., Munaretto, G., Galluzzi, V., Marzo, G. A., Cremonese, G., Brucato, J. R., Palumbo, P., and Massironi, M. (2021). Lermontov crater on Mercury: Geology, morphology and spectral properties of the coexisting hollows and pyroclastic deposits. *Planet. Space Sci.*, 195:105136.

Pajola, M., Rossato, S., Baratti, E., Mangili, C., Mancarella, F., McBride, K., and Coradini, M. (2016a). The Simud-Tiu Valles hydrologic system: A multidisciplinary study of a possible site for future Mars on-site exploration. *Icarus*, 268:355–381.

Pajola, M., Rossato, S., Carter, J., Baratti, E., Pozzobon, R., Erculiani, M. S., Coradini, M., and McBride, K. (2016b). Eridania Basin: An ancient paleolake floor as the next landing site for the Mars 2020 rover. *Icarus*, 275:163–182.

Peplowski, P. N., Evans, L. G., Hauck, S. A., McCoy, T. J., Boynton, W. V., Gillis-Davis, J. J., Ebel, D. S., Goldsten, J. O., Hamara, D. K., Lawrence, D. J., McNutt, R. L., Nittler, L. R., Solomon, S. C., Rhodes, E. A., Sprague, A. L., Starr, R. D., and Stockstill-Cahill, K. R. (2011). Radioactive Elements on Mercury's Surface from MESSENGER: Implications for the Planet's Formation and Evolution. *Science*, 333(6051):1850.

Pettengill, G. H. and Dyce, R. B. (1965). A Radar Determination of the Rotation of the Planet Mercury. *Nature*, 206(4990):1240.

Phillips, M. S., Moersch, J. E., Viviano, C. E., and Emery, J. P. (2021). The lifecycle of hollows on Mercury: An evaluation of candidate volatile phases and a novel model of formation. *Icarus*, 359:114306.

Pieri, D. C. (1980). Martian Valleys: Morphology, Distribution, Age, and Origin. *Science*, 210(4472):895–897.

Pieters, C. M., Goswami, J. N., Clark, R. N., Annadurai, M., Boardman, J., Buratti, B., Combe, J. P., Dyar, M. D., Green, R., Head, J. W., Hibbitts, C., Hicks, M., Isaacson, P., Klima, R., Kramer, G., Kumar, S., Livo, E., Lundeen, S., Malaret, E., McCord, T., Mustard, J., Nettles, J., Petro, N., Runyon, C., Staid, M., Sunshine, J., Taylor, L. A., Tompkins, S., and Varanasi, P. (2009). Character and Spatial Distribution of OH/H_2O on the Surface of the Moon Seen by M^3 on Chandrayaan-1. *Science*, 326(5952):568.

Plaut, J. J., Safaeinili, A., Holt, J. W., Phillips, R. J., Head, J. W., Seu, R., Putzig, N. E., and Frigeri, A. (2009). Radar evidence for ice in lobate debris aprons in the mid-northern latitudes of Mars. *Geophys. Res. Lett.*, 36(2):L02203.

Pollack, J. B., Kasting, J. F., Richardson, S. M., and Poliakoff, K. (1987). The case for a wet, warm climate on early Mars. *Icarus*, 71:203–224.

Pommerol, A., Thomas, N., Cremonese, G., and Munaretto, G. (2021). In-flight photometric calibration of cassis images. *in review for pss.*

Pommerol, A., Thomas, N., Jost, B., Beck, P., Okubo, C., and McEwen, A. S. (2013). Photometric properties of mars soils analogs. *Journal of Geophysical Research: Planets*, 118(10):2045–2072.

Poulet, F., Bibring, J. P., Mustard, J. F., Gendrin, A., Mangold, N., Langevin, Y., Arvidson, R. E., Gondet, B., and Gomez, C. (2005). Phyllosilicates on Mars and implications for early martian climate. *Nature*, 438(7068):623–627.

Poulet, F., Mangold, N., Platevoet, B., Bardintzeff, J.-M., Sautter, V., Mustard, J., Bibring, J.-P., Pinet, P., Langevin, Y., Gondet, B., and Aléon-Toppani, A. (2009). Quantitative compositional analysis of martian mafic regions using the mex/omega reflectance data: 2. petrological implications. *Icarus*, 201(1):84–101.

Press, W. H., Teukolsky, S. A., Vetterling, W. T., and Flannery, B. P. (2002). *Numerical recipes in C++ : the art of scientific computing.*

Putzig, N. E., Barratt, E. M., Mellon, M. T., and Michaels, T. I. (2013). MARS-THERM: A Web-based System Providing Thermophysical Analysis Tools for Mars Research. In *AGU Fall Meeting Abstracts*, volume 2013, pages P43C–2023.

Quémerais, E., Chaufray, J.-Y., Koutroumpa, D., Leblanc, F., Reberac, A., Lustrement, B., Montaron, C., Mariscal, J.-F., Rouanet, N., Yoshikawa, I., Murakami, G., Yoshioka, K., Korablev, O., Belyaev, D., Pelizzo, M. G., Corso, A., and Zuppella, P. (2020). PHEBUS on Bepi-Colombo: Post-launch Update and Instrument Performance. *Space Sci. Rev.*, 216(4):67.

R Core Team (2019). *R: A Language and Environment for Statistical Computing.* R Foundation for Statistical Computing, Vienna, Austria.

Raack, J., Conway, S. J., Herny, C., Balme, M. R., Carpy, S., and Patel, M. R. (2017). Water induced sediment levitation enhances downslope transport on Mars. *Nature Communications*, 8:1151.

Rai Khuller, A. and Russel Christensen, P. (2021). Evidence of exposed dusty water ice within martian gullies. *Journal of Geophysical Research: Planets*, 126(2):e2020JE006539. e2020JE006539 2020JE006539.

Reiss, D., Fenton, L., Neakrase, L., Zimmerman, M., Statella, T., Whelley, P., Rossi, A. P., and Balme, M. (2016). Dust Devil Tracks. *Space Sci. Rev.*, 203(1-4):143–181.

Reiss, D., Zimmerman, M. I., and Lewellen, D. C. (2013). Formation of cycloidal dust devil tracks by redeposition of coarse sands in southern Peru: Implications for Mars. *Earth and Planetary Science Letters*, 383:7–15.

Renno, N., Bos, B., Catling, D., Clark, B., Drube, L., Fisher, D., Goetz, W., Hviid, S. F., Keller, H. U., Kok, J. F., Kounaves, S. P., Leer, K., Lemmon, M., Madsen, M. B., Markiewicz, W. J., Marshall, J., McKay, C., Mehta, M., Smith, M., Zorzano, M. P., Smith, P. H., Stoker, C., and Young, S. M. M. (2009). Possible physical and thermodynamical evidence for liquid water at the Phoenix landing site. *Journal of Geophysical Research (Planets)*, 114:E00E03.

Rivera-Valentin, E. G., Chevrier, V. F., Soto, A., and Martinez, G. (2020). Distribution and habitability of (meta)stable brines on present-day Mars. *Nature Astronomy*, 4:756–761.

Rivoldini, A., Van Hoolst, T., Verhoeven, O., Mocquet, A., and Dehant, V. (2011). Geodesy constraints on the interior structure and composition of Mars. *Icarus*, 213:451–472.

Robinson, M. S., Murchie, S. L., Blewett, D. T., Domingue, D. L., Hawkins, S. E., Head, J. W., Holsclaw, G. M., McClintock, W. E., McCoy, T. J., McNutt, R. L., Prockter, L. M., Solomon, S. C., and Watters, T. R. (2008). Reflectance and Color Variations on Mercury: Regolith Processes and Compositional Heterogeneity. *Science*, 321(5885):66.

Rogers, A. D. and Christensen, P. R. (2007). Surface mineralogy of martian low-albedo regions from mgs-tes data: Implications for upper crustal evolution and surface alteration. *Journal of Geophysical Research: Planets*, 112(E1).

Roloff, V., Pommerol, A., Gambicorti, L., Servonet, A., Thomas, N., Brändli, M., Casciello, A., Cremonese, G., Da Deppo, V., Erismann, M., Ficai Veltroni, I., Gerber, M., Gruber, M., Gubler, P., Hausner, T., Johnson, M., Lochmatter, P., Pelò, E., Sodor, B., Szalai, S., Troznai, G., Vernani, D., Weigel, T., Ziethe, R., and Zimmermann, C. (2017). On-Ground Performance and Calibration of the ExoMars Trace Gas Orbiter CaSSIS Imager. *Space Sci. Rev.*, 212(3-4):1871–1896.

Rothery, D. A., Massironi, M., Alemanno, G., Barraud, O., Besse, S., Bott, N., Brunetto, R., Bunce, E., Byrne, P., Capaccioni, F., Capria, M. T., Carli, C., Charlier, B., Cornet, T., Cremonese, G., D'Amore, M., De Sanctis, M. C., Doressoundiram, A., Ferranti, L., Filacchione, G., Galluzzi, V., Giacomini, L., Grande, M., Guzzetta, L. G., Helbert, J., Heyner, D., Hiesinger, H., Hussmann, H., Hyodo, R., Kohout, T., Kozyrev, A., Litvak, M., Lucchetti, A., Malakhov, A., Malliband, C., Mancinelli, P., Martikainen, J., Martindale, A., Maturilli, A., Milillo, A., Mitrofanov, I., Mokrousov, M., Morlok, A., Muinonen, K., Namur, O., Owens, A., Nittler, L. R., Oliveira, J. S., Palumbo, P., Pajola, M., Pegg, D. L., Penttilä, A., Politi, R., Quarati, F., Re, C., Sanin, A., Schulz, R., Stangarone, C., Stojic, A., Tretiyakov, V., Väisänen, T., Varatharajan, I., Weber, I., Wright, J., Wurz, P., and Zambon, F. (2020). Rationale for BepiColombo Studies of Mercury's Surface and Composition. *Space Sci. Rev.*, 216(4):66.

Saito, Y., Sauvaud, J. A., Hirahara, M., Barabash, S., Delcourt, D., Takashima, T., Asamura, K., and BepiColombo MMO/MPPE Team (2010). Scientific objectives and instrumentation of Mercury Plasma Particle Experiment (MPPE) onboard MMO. *Planet. Space Sci.*, 58(1-2):182–200.

Sato, H., Robinson, M. S., Hapke, B., Denevi, B. W., and Boyd, A. K. (2014). Resolved Hapke parameter maps of the Moon. *Journal of Geophysical Research (Planets)*, 119(8):1775–1805.

Schaefer, E. I., McEwen, A. S., and Sutton, S. S. (2019). A case study of recurring slope lineae (RSL) at Tivat crater: Implications for RSL origins. *Icarus*, 317:621–648.

Schmidt, F., Andrieu, F., Costard, F., Kocifaj, M., and Meresescu, A. G. (2017). Formation of recurring slope lineae on Mars by rarefied gas-triggered granular flows. *Nature Geoscience*, 10(4):270–273.

Schorghofer, N. (2020). Mars: Quantitative evaluation of crocus melting behind boulders. *The Astrophysical Journal*, 890(1):49.

Schorghofer, N., Levy, J., and Goudge, T. (2019). High-resolution thermal environment of recurring slope lineae in palikir crater, mars, and its implications for volatiles. *Journal of Geophysical Research: Planets*, 0(ja).

Schröder, S. E., Mottola, S., Keller, H. U., Raymond, C. A., and Russell, C. T. (2013). Resolved photometry of Vesta reveals physical properties of crater regolith. *Planet. Space Sci.*, 85:198–213.

Schwamb, M. E., Aye, K.-M., Portyankina, G., Hansen, C. J., Allen, C., Allen, S., Calef, F. J., Duca, S., McMaster, A., and Miller, G. R. M. (2018). Planet Four: Terrains - Discovery of araneiforms outside of the South Polar layered deposits. *Icarus*, 308:148–187.

Shapiro, S. S. and Wilk, M. B. (1965). An analysis of variance test for normality (complete samples). *Biometrika*, 52(3/4):591–611.

Shean, D. E., Arendt, A. A., Whorton, E., Riedel, J. L., O'Neel, S., Fountain, A. G., and Joughin, I. R. (2016). An automated, open-source (NASA Ames Stereo Pipeline) workflow for mass production of high-resolution DEMs from commercial stereo satellite imagery: Application to mountain glacies in the contiguous US. In *AGU Fall Meeting Abstracts*, volume 2016, pages EP24C–06.

Shkuratov, Y., Kaydash, V., Korokhin, V., Velikodsky, Y., Opanasenko, N., and Videen, G. (2011). Optical measurements of the Moon as a tool to study its surface. *Planet. Space Sci.*, 59(13):1326–1371.

Simioni, E., Re, C., Mudric, T., Cremonese, G., Tulyakov, S., Petrella, A., Pommerol, A., and Thomas, N. (2021). 3dpd: A photogrammetric pipeline for a push frame stereo cameras. *Planetary and Space Science*, 198:105165.

Simioni, E., Re, C., Mudric, T., Pommerol, A., Thomas, N., and Cremonese, G. (2017). a Photogrammetric Pipeline for the 3d Reconstruction of Cassis Images on Board Exomars Tgo. *ISPRS - International Archives of the Photogrammetry, Remote Sensing and Spatial Information Sciences*, 62W1:133–139.

Smith, D. E., Zuber, M. T., Phillips, R. J., Solomon, S. C., Hauck, S. A., Lemoine, F. G., Mazarico, E., Neumann, G. A., Peale, S. J., Margot, J.-L., Johnson, C. L.,

Torrence, M. H., Perry, M. E., Rowlands, D. D., Goossens, S., Head, J. W., and Taylor, A. H. (2012). Gravity Field and Internal Structure of Mercury from MESSENGER. *Science*, 336(6078):214.

Smith, I. B., Lalich, D. E., Rezza, C., Horgan, B. H. N., Whitten, J. L., Nerozzi, S., and Holt, J. W. (2021). A solid interpretation of bright radar reflectors under the mars south polar ice. *Geophysical Research Letters*, 48(15):e2021GL093618. e2021GL093618 2021GL093618.

Sori, M. M. and Bramson, A. M. (2019). Water on mars, with a grain of salt: Local heat anomalies are required for basal melting of ice at the south pole today. *Geophysical Research Letters*, 46(3):1222–1231.

Souchon, A. L., Pinet, P. C., Chevrel, S. D., Daydou, Y. H., Baratoux, D., Kurita, K., Shepard, M. K., and Helfenstein, P. (2011). An experimental study of Hapke's modeling of natural granular surface samples. *Icarus*, 215(1):313–331.

Steele, L. J., Balme, M. R., Lewis, S. R., and Spiga, A. (2017). The water cycle and regolith–atmosphere interaction at gale crater, mars. *Icarus*, 289:56 – 79.

Stillman, D. E., Bue, B. D., Wagstaff, K. L., Primm, K. M., Michaels, T. I., and Grimm, R. E. (2020). Evaluation of wet and dry recurring slope lineae (rsl) formation mechanisms based on quantitative mapping of rsl in garni crater, valles marineris, mars. *Icarus*, 335:113420.

Stillman, D. E. and Grimm, R. E. (2018). Two pulses of seasonal activity in martian southern mid-latitude recurring slope lineae (RSL). *Icarus*, 302:126–133.

Stillman, D. E., Michaels, T. I., and Grimm, R. E. (2017). Characteristics of the numerous and widespread recurring slope lineae (RSL) in Valles Marineris, Mars. *Icarus*, 285:195–210.

Stillman, D. E., Michaels, T. I., Grimm, R. E., and Hanley, J. (2016). Observations and modeling of northern mid-latitude recurring slope lineae (RSL) suggest recharge by a present-day martian briny aquifer. *Icarus*, 265.

Stillman, D. E., Michaels, T. I., Grimm, R. E., and Harrison, K. P. (2014). New observations of martian southern mid-latitude recurring slope lineae (RSL) imply formation by freshwater subsurface flows. *Icarus*, 233:328–341.

Strom, R. G. (1977). Origin and relative age of lunar and Mercurian intercrater plains. *NASA Technical Memo*, 3511:44–46.

Strom, R. G., Trask, N. J., and Guest, J. E. (1975). Tectonism and volcanism on Mercury. *J. Geophys. Res.*, 80(B17):2478–2507.

Tebolt, M., Levy, J., Goudge, T., and Schorghofer, N. (2020). Slope, elevation, and thermal inertia trends of martian recurring slope lineae initiation and termination points: Multiple possible processes occurring on coarse, sandy slopes. *Icarus*, 338:113536.

Thomas, N., Cremonese, G., Ziethe, R., Gerber, M., Brändli, M., Bruno, G., Erismann, M., Gambicorti, L., Gerber, T., Ghose, K., Gruber, M., Gubler, P., Mischler, H., Jost, J., Piazza, D., Pommerol, A., Rieder, M., Roloff, V., Servonet, A., Trottmann, W., Uthaicharoenpong, T., Zimmermann, C., Vernani, D., Johnson, M., Pelò, E., Weigel, T., Viertl, J., De Roux, N., Lochmatter, P., Sutter, G., Casciello, A., Hausner, T., Ficai Veltroni, I., Da Deppo, V., Orleanski, P., Nowosielski, W., Zawistowski, T., Szalai, S., Sodor, B., Tulyakov, S., Troznai, G., Banaskiewicz, M., Bridges, J. C., Byrne, S., Debei, S., El-Maarry, M. R., Hauber, E., Hansen, C. J., Ivanov, A., Keszthelyi, L., Kirk, R., Kuzmin, R., Mangold, N., Marinangeli, L., Markiewicz, W. J., Massironi, M., McEwen, A. S., Okubo, C., Tornabene, L. L., Wajer, P., and Wray, J. J. (2017). The Colour and Stereo Surface Imaging System (CaSSIS) for the ExoMars Trace Gas Orbiter. *Space Sci. Rev.*, 212(3-4):1897–1944.

Thomas, N., Pommerol, A., G., C., and Munaretto, G. (2021). Absolute calibration of the colour and stereo surface imaging system (cassis). *in review for pss*.

Thomas, R. J., Hynek, B. M., Rothery, D. A., and Conway, S. J. (2016). Mercury's low-reflectance material: Constraints from hollows. *Icarus*, 277:455–465.

Thomas, R. J., Rothery, D. A., Conway, S. J., and Anand, M. (2014). Hollows on Mercury: Materials and mechanisms involved in their formation. *Icarus*, 229:221–235.

Thuillier, G., Hersé, M., Labs, D., Foujols, T., Peetermans, W., Gillotay, D., Simon, P. C., and Mandel, H. (2003). The Solar Spectral Irradiance from 200 to 2400 nm as Measured by the SOLSPEC Spectrometer from the Atlas and Eureca Missions. *Sol. Phys.*, 214(1):1–22.

Toigo, A. D., Richardson, M. I., Wang, H., Guzewich, S. D., and Newman, C. E. (2018). The cascade from local to global dust storms on Mars: Temporal and spatial thresholds on thermal and dynamical feedback. *Icarus*, 302:514–536.

Toner, J. and Catling, D. (2018). Chlorate brines on mars: Implications for the occurrence of liquid water and deliquescence. *Earth and Planetary Science Letters*, 497:161 – 168.

Tornabene, L. L., Moersch, J. E., McSween, H. Y., Hamilton, V. E., Piatek, J. L., and Christensen, P. R. (2008). Surface and crater-exposed lithologic units of the Isidis Basin as mapped by coanalysis of THEMIS and TES derived data products. *Journal of Geophysical Research (Planets)*, 113(E10):E10001.

Tornabene, L. L., Seelos, F. P., Pommerol, A., Thomas, N., Caudill, C. M., Becerra, P., Bridges, J. C., Byrne, S., Cardinale, M., Chojnacki, M., Conway, S. J., Cremonese, G., Dundas, C. M., El-Maarry, M. R., Fernando, J., Hansen, C. J., Hansen, K., Harrison, T. N., Henson, R., Marinangeli, L., McEwen, A. S., Pajola, M., Sutton, S. S., and Wray, J. J. (2018). Image Simulation and Assessment of the Colour and Spatial Capabilities of the Colour and Stereo Surface Imaging System (CaSSIS) on the ExoMars Trace Gas Orbiter. *Space Science Reviews*, 214:18.

Trask, N. and Guest, J. (1975). Preliminary geologic terrain map of Mercury. *J. Geophys. Res.*, 80(B17):2461–2477.

Treiman, A. (2005). The nakhlite meteorites: Augite-rich igneous rocks from Mars. *Chemie der Erde / Geochemistry*, 65:203–270.

Velikodsky, Y. I., Opanasenko, N. V., Akimov, L. A., Korokhin, V. V., Shkuratov, Y. G., Kaydash, V. G., Videen, G., Ehgamberdiev, S. A., and Berdalieva, N. E. (2011). New Earth-based absolute photometry of the Moon. *Icarus*, 214(1):30–45.

Vincendon, M., Forget, F., and Mustard, J. (2010). Water ice at low to midlatitudes on mars. *Journal of Geophysical Research: Planets*, 115(E10).

Vincendon, M., Langevin, Y., Poulet, F., Bibring, J.-P., and Gondet, B. (2007). Recovery of surface reflectance spectra and evaluation of the optical depth of aerosols in the near-ir using a monte carlo approach: Application to the omega observations of high-latitude regions of mars. *Journal of Geophysical Research: Planets*, 112(E8).

Vincendon, M., Pilorget, C., Carter, J., and Stcherbinine, A. (2019). Observational evidence for a dry dust-wind origin of mars seasonal dark flows. *Icarus*, 325:115 – 127.

Viola, D. and McEwen, A. S. (2018). Geomorphological Evidence for Shallow Ice in the Southern Hemisphere of Mars. *Journal of Geophysical Research (Planets)*, 123(1):262–277.

Wang, A., Ling, Z., Yan, Y., McEwen, A. S., Mellon, M. T., Smith, M. D., Jolliff, B. L., and Head, J. (2019). Subsurface Cl-bearing salts as potential contributors to recurring slope lineae (RSL) on Mars. *Icarus*, 333:464–480.

Wang, Y., Xiao, Z., Chang, Y., and Cui, J. (2020). Lost Volatiles During the Formation of Hollows on Mercury. *Journal of Geophysical Research (Planets)*, 125(9):e06559.

Watters, T. R., Selvans, M. M., Banks, M. E., Hauck, S. A., Becker, K. J., and Robinson, M. S. (2015). Distribution of large-scale contractional tectonic landforms on Mercury: Implications for the origin of global stresses. *Geophys. Res. Lett.*, 42(10):3755–3763.

Weidenschilling, S. J. (1978). Iron Silicate Fractionation and the Origin of Mercury. *Icarus*, 35(1):99–111.

Wells, E. N., Veverka, J., and Thomas, P. (1984). Mars: Experimental study of albedo changes caused by dust fallout. *Icarus*, 58(3):331–338.

Whitten, J. L., Head, J. W., Denevi, B. W., and Solomon, S. C. (2014). Intercrater plains on Mercury: Insights into unit definition, characterization, and origin from MESSENGER datasets. *Icarus*, 241:97–113.

Wieczorek, M. A. and Zuber, M. T. (2004). Thickness of the Martian crust: Improved constraints from geoid-to-topography ratios. *Journal of Geophysical Research (Planets)*, 109:E01009.

Wilcoxon, F. (1945). Individual comparisons by ranking methods. *Biometrics Bulletin*, 1(6):80–83.

Wilson, J. T., Eke, V. R., Massey, R. J., Elphic, R. C., Feldman, W. C., Maurice, S., and Teodoro, L. F. A. (2018). Equatorial locations of water on Mars: Improved resolution maps based on Mars Odyssey Neutron Spectrometer data. *Icarus*, 299:148–160.

Wray, J. J., Squyres, S. W., Roach, L. H., Bishop, J. L., Mustard, J. F., and Noe Dobrea, E. Z. (2010). Identification of the Ca-sulfate bassanite in Mawrth Vallis, Mars. *Icarus*, 209(2):416–421.

Wu, Y., Besse, S., Li, J.-Y., Combe, J.-P., Wang, Z., Zhou, X., and Wang, C. (2013). Photometric correction and in-flight calibration of Chang' E-1 Interference Imaging Spectrometer (IIM) data. *Icarus*, 222(1):283–295.

Xiao, Z., Strom, R. G., Blewett, D. T., Byrne, P. K., Solomon, S. C., Murchie, S. L., Sprague, A. L., Domingue, D. L., and Helbert, J. (2013). Dark spots on Mercury: A distinctive low-reflectance material and its relation to hollows. *Journal of Geophysical Research (Planets)*, 118(9):1752–1765.

Yoshikawa, I., Korablev, O., Kameda, S., Rees, D., Nozawa, H., Okano, S., Gnedykh, V., Kottsov, V., Yoshioka, K., Murakami, G., Ezawa, F., and Cremonese, G. (2010). yThe Mercury sodium atmospheric spectral imager for the MMO spacecraft of Bepi-Colombo. *Planet. Space Sci.*, 58(1-2):224–237.

Zanetti, M., Hiesinger, H., Reiss, D., Hauber, E., and Neukum, G. (2010). Distribution and evolution of scalloped terrain in the southern hemisphere, Mars. *Icarus*, 206(2):691–706.

Zolotov, M. Y. and Mironenko, M. V. (2007). Timing of acid weathering on mars: A kinetic-thermodynamic assessment. *Journal of Geophysical Research: Planets*, 112(E7).